Triannual Report 2008 – 2010

Research Group “Scanning Probe Methods”

University of Hamburg
Institute of Applied Physics

Microstructure Advanced
Research Center Hamburg (MARCH)

Interdisciplinary Nanoscience Center
Hamburg (INCH)

Hamburg Cluster of Excellence
"NANOSPINTRONICS"

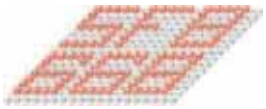

Sonderforschungsbereich 668
(DFG Collaborative Research Center)

ERC Advanced Grant Group
"FURORE"

Contact:
Prof. Dr. Roland Wiesendanger
Tel. (++49) 40-42838-5244 (direct)
(++49) 40-42838-3203/-7045 (secretary)
FAX (++49) 40-42838-6188
e-mail wiesendanger@physnet.uni-hamburg.de
WWW www.nanoscience.de

Contents

Chapter 1

Preface

This is the sixth triannual report of the research group "Scanning Probe Methods" at the Institute of Applied Physics of the University of Hamburg. Based on the strategic development of nanoscience-related infrastructure at the University of Hamburg over a time period of 18 years, several Centers and international networks of scientific excellence could be established in recent years and are recognized worldwide:

Since 2006 we have established a Collaborative Research Center, DFG-Sonderforschungsbereich (SFB 668), entitled "Magnetism from the single atom to the nanostructure" (chairman: Prof. Dr. Roland Wiesendanger). The SFB 668 is focussed on fundamental studies of magnetic properties of nanostructures in contact with a substrate, including spin structures in thermal equilibrium as well as transport and dynamic properties. It involves research groups from the Institute of Applied Physics, from the I. Institute of Theoretical Physics, from the Institute of Experimental Physics, from the Institute of Inorganic and Applied Chemistry (all from Hamburg University), and from the Institute of Experimental Physics of the University of Kiel. In total more than 100 researchers are working within the SFB 668. In 2009 the SFB 668 was evaluated with great success and received funding for a second 4-years period (2010 - 2013).

The research group "Scanning Probe Methods" was also engaged in the interdisciplinary Research Training Network on "Design and characterization of functional materials" which was funded by the DFG in the time period of 2001 - 2010 and coordinated by the Institute of Inorganic and Applied Chemistry. In 2006 another Research Training Network on "Tailored metal-semiconductor hybrid systems" (chairman: Prof. Dr. Ulrich Merkt) could be established with participation of groups from the departments of physics and informatics. It will continue to run till 2015. Within the framework of such Research Training Groups about 20 to 25 Ph.D. students obtain an excellent education and training in an interdisciplinary scientific environment.

In 2009 the State Government of the Free and Hanseatic City of Hamburg started an Excellence Initiative in order to support outstanding Research Clusters and Graduate Schools. We were successful in the competition and could establish a Cluster of Excellence in the topical field of "Nanospintronics" (chairman: Prof. Dr. Roland Wiesendanger). In total about 200 scientists from the University of Hamburg and the Helmholtz Centers DESY and Geesthacht are involved in this Cluster which receives funding for a time period of 3.5 years.

In Europe we have become partners within numerous research networks funded by the European Community in recent years. Moreover, an ERC Advanced Grant of the recently established European Research Council was awarded to Roland Wiesendanger in 2008 for "Fundamental studies and innovative approaches of research on magnetism". This new type of funding program allows individual researchers to build up a significant activity in an innovative field of science based on previous outstanding research achievements.

Together with colleagues from the US and Argentina, we were successful in the prestigious program "Partnerships for International Research and Education (PIRE)" funded by the NSF (only 17 out of 517 initiatives were successful in 2007). Moreover, we obtained funding by the DFG and JST for establishing a scientific cooperation between Hamburg University and the National Institute for Materials Science (NIMS) at Tsukuba (Japan) in the field of spin-dependent transport in nanostructures (2008 - 2010).

In the present triannual report 2008-2010 the scientific achievements of the research group "Scanning Probe Methods" are summarized covering the following topics: magnetic nanostructures, semiconductor quantum structures and hybrid systems, molecular systems, insulators, superconductors, and instrumental developments. The research activities of our group in the time period 2008-2010 resulted in 77 scientific publications (among them 6 in Science / Nature / Nature Nanotechnology / Nature Physics and 13 in "Physical Review Letters") as well as 325 presentations at conferences, colloquia or seminars (including 82 plenary and invited talks at international meetings). Several prizes and awards were given to members of our group in the past three years, including the ThyssenKrupp Dissertationspreis 2009 (Dr. Uwe Kaiser), the Jürgen-Geiger-Preis 2010 (Dr. Stefan Krause), the 1st Prize for "Understandable Science 2010" of the Helmholtz Center Geesthacht (Dr. Stefan Krause), and the Nanotechnology Recognition Award of the American Vacuum Society 2010 (Prof. Dr. Roland Wiesendanger). Furthermore, Roland Wiesendanger became Member of the "Deutsche Akademie der Technikwissenschaften" acatech (2008).

This research report provides a good opportunity to thank all funding agencies including the DFG, the EU, the Stifterverband für die Deutsche Wissenschaft, the

Alexander von Humboldt Foundation, the DAAD, the Konrad-Adenauer-Stiftung, the "Forschungs- und Wissenschafts-Stiftung Hamburg" as well as several industrial companies for their financial support of our research activities. In particular we would like to thank the Ministry of Science and Research (BWF) of the Free and Hanseatic City of Hamburg and the University of Hamburg for their continuous support of our activities in nanoscience and nanotechnology. I would also like to take the opportunity to thank all the past and present members of the research group "Scanning Probe Methods" for their strong devotion to scientific excellence. Finally, we gratefully acknowledge the great support by our central mechanical and electronic workshops, as well as by our secretaries and administration staff.

Hamburg, December 2010

Prof. Dr. Roland Wiesendanger

(Managing Director of the Institute of Applied Physics, Chairman of the DFG Collaborative Research Center SFB 668, Chairman of the Hamburg Cluster of Excellence NANOSPINTRONICS, and Scientific Coordinator of the Interdisciplinary Nanoscience Center Hamburg)

Chapter 2

Staff Members

Head

Prof. Dr. Roland Wiesendanger

Secretary

Andrea Beese
Ute Brenger
Sigrid Schmidtke

Public Relations Office

Dipl.-Chem. Heiko Fuchs

Technical Support

PTA Norbert Dix
Dipl.-Ing. Michael Langer

Senior Scientists

Dr. Makoto Ashino
Dr. Kirsten von Bergmann
Dr. Jessica Bickel
Dr. Shih-Hsin Chang (until May 2009)
Dr. Yingshuang Fu
Dr. Daniel Haude (until March 2008)
Dr. Germar Hoffmann (until December 2010)
Dr. Mahboubeh Hortamani
Dr. Uwe Kaiser (until January 2010)
Dr. Alexander Khajetoorians

Dr. Stefan Krause
Dr. André Kubetzka
Dr. Focko Meier (until October 2010)
Dr. Nikolai Mikuszeit (until December 2009)
Dr. Oswald Pietzsch
Dr. Robert Ravlić (until February 2008)
Dr. Alexander Schwarz
Dr. David Serrate (until January 2009)
Dr. Elena Vedmedenko
Dr. Marta Wasniowska
Dr. Jens Wiebe
Dr. Robert Wieser
Dr. Shiro Yamazaki
Dr. Yasuo Yoshida
Dr. Hai Zhong

Ph. D. Students

Henning von Allwörden
Jens Brede
Bruno Chilian
Liudmila Dzemiantsova
Thomas Eelbo
Andreas Eich
Mike Gyamfi
Gabriela Herzog
Stefan Kuck (until October 2009)
Knud Lämmle
Peter Löptien
Felix Marczinowski (until November 2010)
Stefan Meckler (until December 2010)
Matthias Menzel
Kai Ruschmeier
Anika Schlenhoff
René Schmidt
Jörg Schwöbel
Andreas Sonntag
Tobias Spitz
Martin von Sprekelsen
Thim Stapelfeldt
Kolja Them
Boris Wolter
Lihui Zhou

Diploma Students

André Engel
Sweetlana Fremy (until January 2009)
Josef Grenz
Christian Hanneken
Johannes Hattendorf (until July 2010)
Arne Köhler
Leonid Lichtenstein (until April 2009)
Jan Samuelsen (until November 2009)
Qingchui Zhu

Chapter 3

Research Activities 2008-2010

3.1 Overview

R. Wiesendanger

Our research activities are concentrated on nanometer-scale probe methods. In particular, emphasis is put on the investigation of the fundamental relationship between nanostructure and nanophysical properties. Scanning probe methods are ideally suited for such investigations because they provide atomic-scale spatial resolution combined with spectroscopical capabilities at low energy scales (down to micro-eV). By choosing an appropriate type of interaction between probe tip and sample, almost any kind of nanophysical property can be studied by scanning probe methods. We apply scanning probe methods (SPM) to various classes of materials, including metals, semiconductors, insulators, superconductors, magnetic materials, as well as organic thin films and molecular materials.

To be able to make significant contributions to this rapidly developing field, a major part of our activities is devoted to new developments or further improvements on SPM instrumentation, including the development of new positioning devices with nanometer-scale accuracy, the development of new types of sensors, or the development of dedicated SPM instruments which can operate under extreme conditions (e.g. UHV, low temperatures and high magnetic fields). Special emphasis is also put on the development of new experimental methods based on the local probe geometry, which usually requires adjustments of the hardware and software for SPM data acquisition. These developments are often made in close collaboration with European companies specialized in SPM instrumentation.

In the following, a brief summary of the highlights of our research activities in the time period of 2008 - 2010 is provided. For further information, please do not hesitate to contact us. We will be glad to provide reprints of publications on specific topics.

3.2 Magnetic nanostructures and thin film systems

3.2.1 Spin-polarized scanning tunneling microscopy (SP-STM) and spectroscopy (SP-STS) studies

R. Wiesendanger

In recent years great progress has been achieved in the preparation of self-organized and lithographically manufactured magnetic nanostructures. The structural properties of these nanostructures could routinely be investigated by high-resolution real-space imaging techniques like scanning electron microscopy (SEM) and scanning tunneling microscopy (STM) down to the atomic scale. In contrast, a detailed understanding of nanomagnetic properties has been hindered by the fact that experimental data have been obtained by methods which average over a fraction of the sample surface being much larger than the atomic length scale. So far, the limit of spatial resolution of the most advanced magnetic imaging techniques like magnetic force microscopy (MFM) and SEM with polarization analysis (SEMPA) has been on the order of ten nanometers (nm). Therefore, it has been proposed very early to make the tip of the STM sensitive to the spin of the tunneling electrons by illuminating GaAs tips with circularly polarized light or by using magnetic probe tips. Although spin-polarized electron tunneling in planar junctions is an established experimental technique it turned out that the realization of this idea is difficult. Spin-polarized tunneling using an STM has first been observed by Wiesendanger and co-workers in the early 1990s [1, 2]. In this experiment, CrO_2 thin film tips with a high degree of spin polarization were successfully used to detect periodic alternations of the measured monatomic step heights in constant-current images. The deviations of the measured step height values from the topographic monatomic step height could directly be related with the effective spin polarization of the tunnel junction. A drawback of this experimental approach was the superposition of topographic and magnetic structure information. As we have shown in the previous triannual reports of our research group we could overcome this problem by combining SP-STM with spectroscopic techniques [3, 4]. This allowed the successful separation of topographic, electronic and magnetic information thereby achieving magnetic domain and domain wall images of even micromagnetically complicated magnetic surfaces with subnanometer spatial resolution. On the other hand, spin-polarized scanning tunneling microscopy (SP-STM) performed in the constant-current mode is still the method of choice to resolve complex surface spin-structures, as, e.g., collinear or non-collinear antiferromagnetic structures, on the atomic scale [5–8].

References

[1] R. Wiesendanger, H.-J. Güntherodt, G. Güntherodt, R. J. Gambino, and R. Ruf, Phys. Rev. Lett. **65**, 247 (1990).

[2] R. Wiesendanger, D. Bürgler, G. Tarrach, A. Wadas, D. Brodbeck, H.-J. Gütherodt, G. Güntherodt, R. J. Gambino, and R. Ruf, J. Vac. Sci. Technol. **B9**, 519 (1991).

[3] M. Bode, M. Getzlaff, and R. Wiesendanger, Phys. Rev. Lett. **81**, 4256 (1998).

[4] M. Kleiber, M. Bode, R. Ravlić, and R. Wiesendanger, Phys. Rev. Lett. **85**, 4606 (2000).

[5] S. Heinze, M. Bode, O. Pietzsch, A. Kubetzka, X. Nie, S. Blügel, and R. Wiesendanger, Science **288**, 1805 (2000).

[6] A. Kubetzka, P. Ferriani, M. Bode, S. Heinze, G. Bihlmayer, K. von Bergmann, O. Pietzsch, S. Blügel, and R. Wiesendanger, Phys. Rev. Lett. **94**, 087204 (2005).

[7] M. Bode, E. Y. Vedmedenko, K. von Bergmann, A. Kubetzka, P. Ferriani, S. Heinze, and R. Wiesendanger, Nature Materials **5**, 477 (2006).

[8] M. Bode, M. Heide, K. von Bergmann, P. Ferriani, S. Heinze, G. Bihlmayer, A. Kubetzka, O. Pietzsch, S. Blügel, and R. Wiesendanger, Nature **447**, 190 (2007)

3.2.2 Non-collinear magnetic order in 3d monolayers on 5d substrates

K. von Bergmann, P. Ferriani, E. Y. Vedmedenko, M. Bode, M. Heide, G. Bihlmayer, S. Blügel, S. Heinze, and R. Wiesendanger

Magnetism in low-dimensions is a fascinating topic: Even in apparently simple systems –such as homoatomic monolayers– the nearest neighbor distance, the symmetry and the hybridization with the substrate can play a crucial role for the magnetic properties. This may lead to a variety of magnetic structures, from the ferromagnetic and antiferromagnetic state to much more complex spin structures. Spin-polarized scanning tunneling microscopy (SP-STM) combines magnetic sensitivity with high lateral resolution and therefore grants access to such complex magnetic order with unit cells on the nanometer scale. Different previously inconceivable magnetic structures are observed in pseudomorphic homoatomic 3d monolayers on late 5d transition metal substrates. As shown previously for the Mn monolayer on W(110) [1] the broken inversion symmetry due to the presence of the surface can induce the formation of spin spirals where the spin rotates from one atom to the next resulting in a nanometer sized magnetic period. The driving force for the canting of adjacent magnetic moments leading to such magnetic states is the Dzyaloshinskii-Moriya (DM) interaction and a unique rotational sense is found.

To investigate whether the DM interaction is generally to be considered when studying thin film magnetism we looked at other sample systems. As shown in Fig. 3.1(a) the Cr monolayer also grows pseudomorphically on W(110). The spin-resolved image in (b) shows stripes very similar to the ones observed in [1] indicating local antiferromagetic order as seen in the zoomed image (c) and the sketch in (d). Anyhow, the stripes in the large image (b) show a modulation along the [001] direction. Following the arguments of [1] we interpret this as a spin spiral propagating along the [001] direction. Though the experimental proof and ab-initio calculations are lacking for this system this indicates that again we have a cycloidal spin spiral with unique rotational sense due to the DM interaction. The propagation direction is perpendicular to that observed for the Mn monolayer which indicates a different easy magnetization axis for this system [2].

To study the influence of the symmetry of the atomic lattice on spin spiral states we investigated the pseudomorphic Mn monolayer on W(001) which has a four-fold symmetry. We again observe a spin spiral in spin-resolved measurements which has atoms with magnetization components in the surface plane (Fig. 3.2(a)) and normal to the surface (b). On a larger sized image (c) one can see a labyrinth pattern due to spin spirals propagating along the two equivalent <110> directions of the surface.

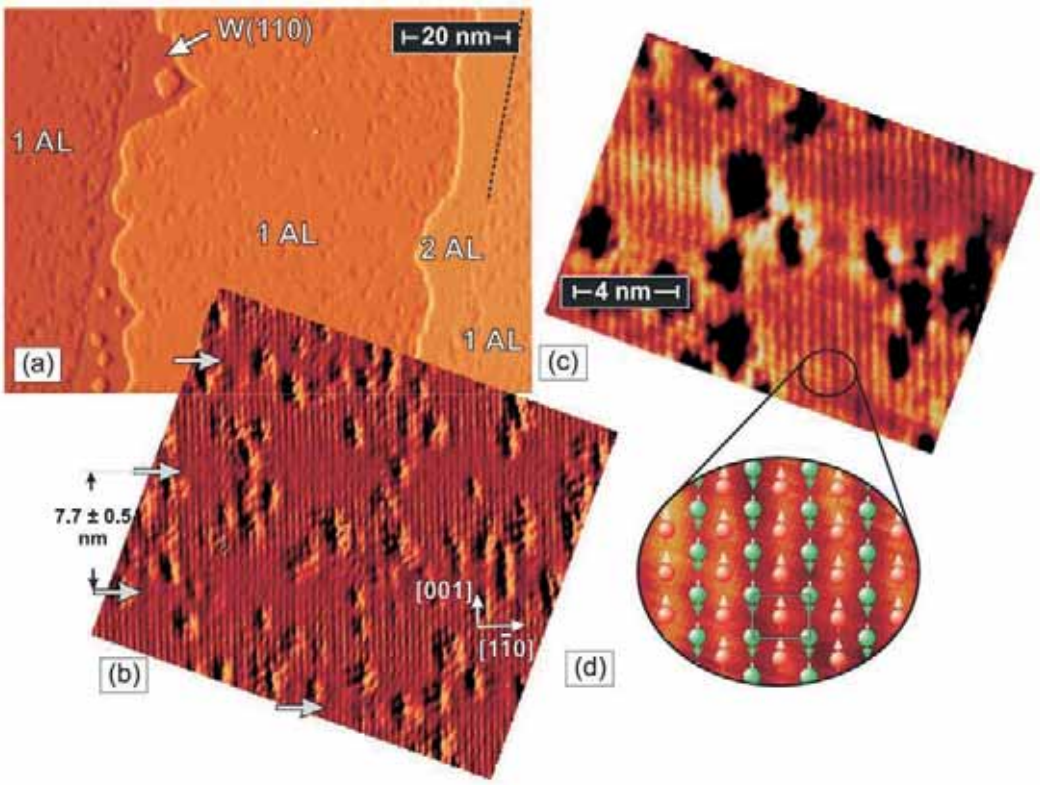

Figure 3.1: SP-STM images of 1.05 AL Cr/W(110) taken with a Fe-coated probe tip. (a) The overview shows that a small fraction of the substrate is still visible. The local Cr coverage is indicated. (b) Zooming on to an atomically flat terrace reveals stripes running along the [001] direction. A weak modulation of the magnetic signal with a periodicity of 7.7±0.5 nm can be recognized (gray arrows). (c) High-resolution SP-STM image of the Cr monolayer on W(110). The inter-stripe distance amounts to 4.6±0.2 Å, which is in reasonable agreement with the nominal periodicity of 4.48 Å. (d) Interpretation of the SP-STM in terms of the expected surface antiferromagnetic order from the ab initio calculation (the $p(2 \times 1)$ AFM unit cell is marked). The W atoms are shaded pink or green depending on their spin alignment.

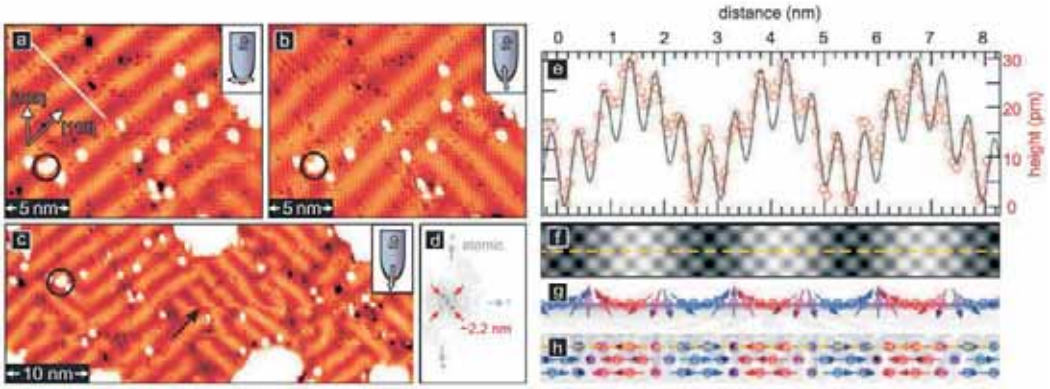

Figure 3.2: Spin-resolved STM measurements of 1 ML Mn/W(001). Constant-current image with magnetic tip sensitive to (a) the in-plane and (b),(c) the out-of-plane component of the sample magnetization (the black circle acts as position marker); (d) Fourier transform of a $\mathrm{d}I/\mathrm{d}U$ map (not shown) of a sample area with both rotational domains; (e) experimental (circles) and simulated (solid line) profile along the lines indicated in (a) and (f), respectively; (f) simulated SP-STM image, (g) side, and (h) top view of the corresponding model of the SS (colors represent the moment's in-plane component). The following values of bias voltage U and current I were used: (a) and (b) U = -0.1 V, I = 1 nA; (c) U = -0.1 V, I = 0.1 nA.

This gives rise to four spots in the Fourier transform of this image (d). Note that in addition to the magnetic signal we obtain atomic resolution for this sample system, which has proven to be very difficult for other systems studied so far. The experimental line profile indicated by the white line in (a) is shown in (e) as red open circles. The periodicity can be fitted to obtain a simulated SP-STM image (f). The underlying spin spiral is sketched as side (g) and top view (h), and ab-initio calculations have confirmed that it has a unique rotational sense due to the DM interaction [3].

References

[1] M. Bode, M. Heide, K. von Bergmann, P. Ferriani, S. Heinze, G. Bihlmayer, A. Kubetzka, O. Pietzsch, S. Blügel and R. Wiesendanger , Nature **447**, 190 (2007).

[2] B. Santos, J. M. Puerta, J. I. Cerda, R. Stumpf, K. von Bergmann, R. Wiesendanger, M. Bode, K. F. McCarty, and J. de la Figuera, Structure and magnetism of ultra-thin chromium layers on W(110), New J. Phys. **10**, 13005 (2008).

[3] P. Ferriani, K. von Bergmann, E.Y. Vedmedenko, S. Heinze, M. Bode, M. Heide, G. Bihlmayer, S. Blügel, and R. Wiesendanger, Atomic-scale spin spiral with a unique rotational sense: Mn monolayer on W(001), Phys. Rev. Lett. **101**, 027201 (2008).

3.2.3 Real-space observation of a right-rotating inhomogeneous cycloidal spin spiral by spin-polarized scanning tunneling microscopy in a triple axes vector magnet

S. Meckler, N. Mikuszeit, A. Preßler, E. Y. Vedmedenko, O. Pietzsch, and R. Wiesendanger

Recently, spin spirals at crystal surfaces were observed in the Mn monolayer (ML) on W(110) [1] and W(001) [2] using spin-polarized scanning tunneling microscopy (SP-STM). The formation of these spirals has been ascribed to strong spin-orbit coupling in the presence of broken inversion symmetry at the crystal surface leading to the Dzyaloshinskii-Moriya interaction (DMI) [3, 4]. Due to the strength of DMI the spin spirals are homogeneous, i.e. the angle between any two neighboring magnetic moments is constant along the propagation direction. The magnetic pattern of the Fe double layer (DL) on W(110) consists of a regular sequence of out-of-plane magnetized domains separated by domain walls [5–7]. The average distance between two walls amounts to about 20 nm. The pattern shows a unique sense of rotation and can thus also be described as a spin spiral propagating along the [001] direction. In contrast to the spirals described in Refs. [1, 2] the spin canting here does not occur at a fixed angle but is smaller in the domains and larger in the domain walls, the spiral thus being highly inhomogeneous. As for the spin spirals in the Mn ML on W(110) and W(001), the rotational sense of the spiral in the Fe DL on W(110) could not be measured so far because in the respective SP-STM experiments the azimuthal component of the tip magnetization was unknown. For the same reason it remained an open question whether the spiral is helical or cycloidal, i.e whether the domain walls are of Bloch- or Néel-type, cf. Fig. 3.3.

Starting from phenomenological Dzyaloshinskii-Moriya vectors [4] Monte-Carlo simulations (MCS) showed that the unique rotational sense can be explained as a consequence of DMI [8]. By density functional theory combined with micromagnetic calculations the DM vector was determined from first principles [9]. The magnetic ground state was predicted to be collinear although within numerical accuracy a non-collinear spin spiral ground state could not be ruled out. Two domains of opposite magnetization induced in this system by appropriate boundary conditions were shown to be separated by right-rotating ($\underline{\uparrow\nearrow\rightarrow\searrow\downarrow}$), in contrast to left-rotating ($\underline{\uparrow\nwarrow\leftarrow\swarrow\downarrow}$), Néel-type domain walls extending along the $[1\bar{1}0]$ axis.

In the following it is shown that the type of a spin spiral and its sense of rotation can be measured directly by SP-STM experiments performed in a triple axes vector magnet. The spin spiral in the Fe DL on W(110) is determined to be a right-rotating inhomogeneous cycloid. The non-collinear ground state is a consequence of interplaying Dzyaloshinskii-Moriya and dipolar energy contributions [10].

The SP-STM experiments were performed under ultra-high vacuum conditions at

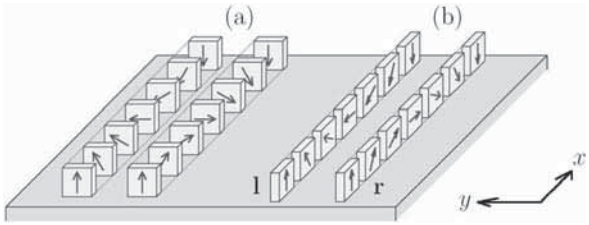

Figure 3.3: Left- and right-rotating spin spiral configurations of (a) helical, (b) cycloidal type. While the helical ones are mirror images of each other, hence being energetically degenerate, the cycloidal ones are not if the supporting surface is taken into account. Graphics from Ref. [9].

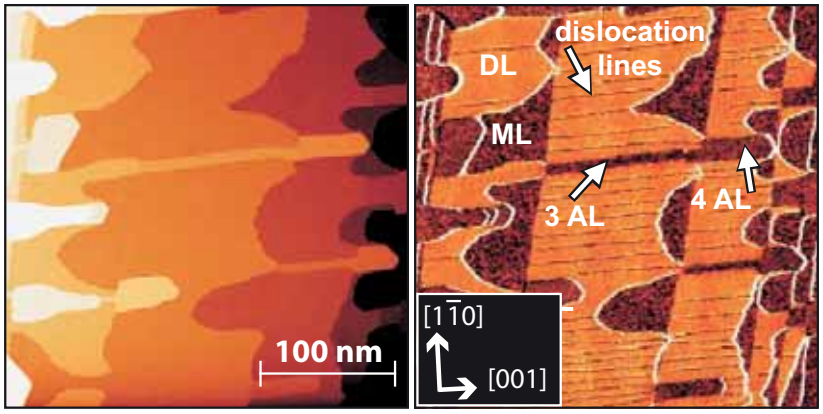

Figure 3.4: 1.7 atomic layers Fe on W(110) with local Fe coverages of 1-4 atomic layers. (a) Constant-currrent STM image showing the topography. (b) dI/dU map showing the details of the varying local coverage with dislocation lines in the double layer areas, and patches of the first, third and fourth atomic layers. Tunneling parameters: $I = 500$ pA, $U_{\mathrm{bias}} = 550$ mV.

$T = 4.7$ K in the magnetic field of a superconducting triple axes magnet [11]. Using this magnet to align the tip magnetization it is possible to do SP-STM experiments with the tip magnetization direction being well defined. The W(110) substrate was cleaned as described in [12]. 1.7 atomic layers (AL) of Fe were evaporated at a deposition rate of 0.6 AL per minute, with subsequent annealing at 500 K for five minutes. The tungsten tip was flashed to remove surface oxides and coated with about 50 AL of Fe resulting in an in-plane magnetic sensitivity.

Fig. 3.4 shows the morphology of the sample with various local Fe coverages. Regions of pseudomorphic ML and DL coverage coexist with patches of the third and fourth AL. To relief the strain resulting from the 9 % lattice mismatch between W and Fe, dislocation lines along the [001] axis are formed in the DL areas.

Fig. 3.5 presents a first field-dependent series of spin-polarized dI/dU maps showing the in-plane domain wall contrast in the DL areas. An external magnetic field was applied along different in-plane directions as indicated, to align the tip magnetization $\mathbf{m}_{\mathrm{t}}$ accordingly. This is a well established procedure for SP-STM experiments in

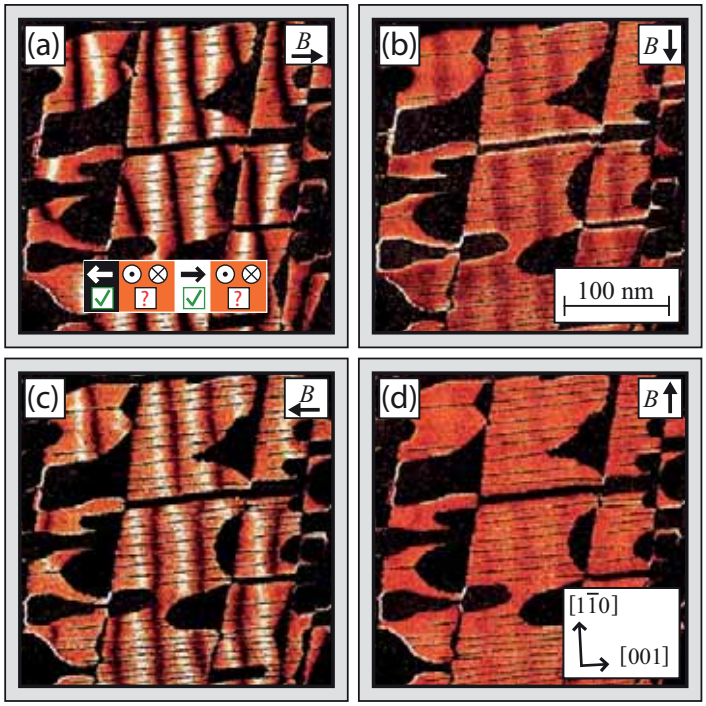

Figure 3.5: Spin-polarized dI/dU maps measured for different in-plane orientations of the external magnetic field $B = 150$ mT and the tip magnetization, respectively. (a, c) Domain walls showing up in the DL as black and white lines along the $[1\bar{1}0]$ axis with contrast inversion from (a) to (c). (b, d) Vanishing domain wall contrast. Inset: local orientation and color coding of the magnetic moments in the domain walls. Tunneling parameters: $I = 500$ pA, $U_{\mathrm{bias}} = 550$ mV.

fields oriented along the surface normal [7] which is generalized here to arbitrary field directions. The magnetic field $B = 150$ mT was chosen such that it is weak enough not to affect the magnetic structure of the sample but strong enough for the alignment of $\mathbf{m}_{\mathrm{t}}$. For $\mathbf{m}_{\mathrm{t}}$ pointing along the [001] axis (a,c) we observe a strong domain wall contrast (black and white lines along the $[1\bar{1}0]$ axis). By comparison of (a) and (c) one observes a contrast reversal due to the reversal of $\mathbf{m}_{\mathrm{t}}$. The domain wall contrast vanishes with $\mathbf{m}_{\mathrm{t}}$ being rotated by 90° (b,d) along the $[1\bar{1}0]$ axis. Instead, one observes a weak stripe-like pattern in the areas of the out-of-plane magnetized domains due to a residual perpendicular component of $\mathbf{m}_{\mathrm{t}}$. In conclusion, the magnetization in the domain walls rotates through the [001] rather than the $[1\bar{1}0]$ direction, proving that the domain walls are of Néel-type, i.e. the spiral is a cycloid.

Fig. 3.6 displays a second series of field dependent measurements to investigate the sense of rotation of the spin spiral. The measurements were done on the same sample and using the same tip, bias voltage and tunneling current as for the series shown in Fig. 3.5. Now, the field was applied normal to the sample surface and swept in the range $B_z = 0 - 350$ mT. In contrast to the measurement series shown in Fig. 3.5 now

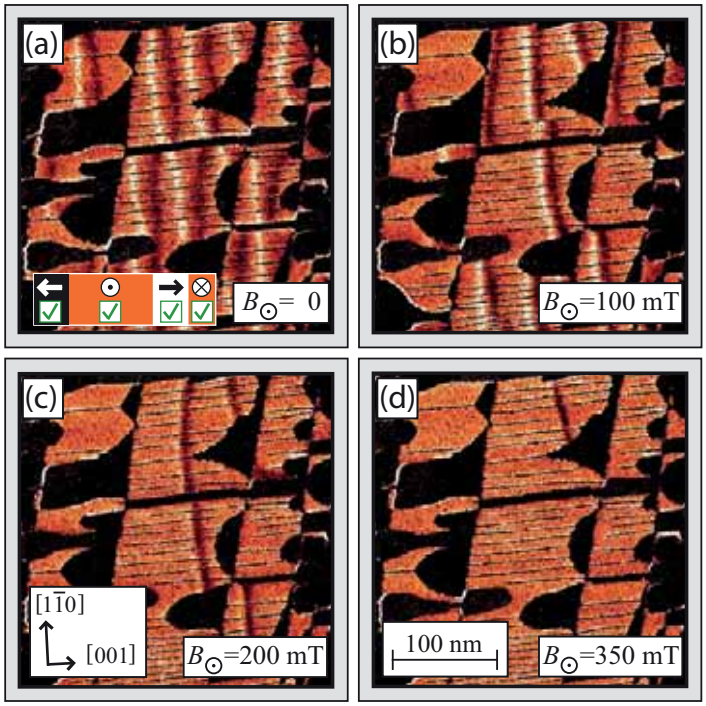

Figure 3.6: Spin-polarized dI/dU maps of the Fe DL on W(110) measured for variable field values applied normal to the surface plane. The domain sizes are affected by the external field indicating a local orientation of the magnetic moments in the domains as shown in the inset. The tip magnetization (and hence the magnetic sensitivity) is gradually rotated from in-plane to out-of-plane due to the field. Tunneling parameters: $I = 500$ pA, $U_{\mathrm{bias}} = 550$ mV.

both $\mathbf{m}_{\mathrm{t}}$ and the sample magnetization $\mathbf{m}_{\mathrm{s}}$ are affected by the external field. Domains with $\mathbf{m}_{\mathrm{s}}$ being parallel (antiparallel) to the field grow (shrink). Thus, the direction of $\mathbf{m}_{\mathrm{s}}$ can be identified for all domains as shown in the inset of Fig. 3.6(b). On the tip side, sweeping the field causes $\mathbf{m}_{\mathrm{t}}$ to increasingly rotate into the perpendicular direction. Consequently, the in-plane domain wall contrast gradually disappears and is eventually replaced by an out-of-plane contrast, allowing to image the domains rather than the domain walls (Fig. 3.6(c, d)). The large domains with $\mathbf{m}_{\mathrm{s}}$ being parallel to the field appear bright whereas residual domains, being shrunken to mere lines and with $\mathbf{m}_{\mathrm{s}}$ being antiparallel to the field, appear dark. This observation can be generalized such that for the tip-sample combination in our experiment, at the given bias voltage, bright colors (high dI/dU signal) indicate a parallel alignment of $\mathbf{m}_{\mathrm{s}}$ and $\mathbf{m}_{\mathrm{t}}$ while dark (low dI/dU signal) corresponds to an antiparallel alignment. Applying this result to the measurement shown in Fig. 3.5(a) one can identify the direction of $\mathbf{m}_{\mathrm{s}}$ also for the domain walls, as indicated in the inset. Combining this knowledge with that of the spin orientation in the domains (inset of Fig. 3.6(b)) allows the conclusion of a right-rotating cycloidal spin spiral propagating along the [001] axis.

In summary, the sense of rotation of a spin spiral, which so far had to be extracted

from theoretical calculations, was for the first time determined directly from a SP-STM experiment in a triple axes vector magnet.

References

[1] M. Bode, M. Heide, K. von Bergmann, P. Ferriani, S. Heinze, G. Bihlmayer, A. Kubetzka, O. Pietzsch, S. Blügel, and R. Wiesendanger, Nature **447**, 190 (2007).

[2] P. Ferriani, E. Y. Vedmedenko, S. Heinze, M. Bode, M. Heide, G. Bihlmayer, S. Blügel, and R. Wiesendanger, Phys. Rev. Lett. **101**, 027201 (2008).

[3] I. E. Dzyaloshinskii, Sov. Phys. JETP **5**, 1259 (1957).

[4] T. Moriya, Phys. Rev. **120**, 91 (1960).

[5] M. Bode, O. Pietzsch, A. Kubetzka, S. Heinze, and R. Wiesendanger, Phys. Rev. Lett. **86**, 2142 (2001).

[6] A. Kubetzka, M. Bode, O. Pietzsch, and R. Wiesendanger, Phys. Rev. Lett. **88**, 057201 (2002).

[7] A. Kubetzka, O. Pietzsch, M. Bode, and R. Wiesendanger, Phys. Rev. B **67**, 020401(R) (2003).

[8] E. Y. Vedmedenko, L. Udvardi, P. Weinberger, and R. Wiesendanger, Phys. Rev. B **75**, 104431 (2007).

[9] M. Heide, G. Bihlmayer, and S. Blügel, Phys. Rev. B **78**, 140403 (2008).

[10] S. Meckler, N. Mikuszeit, A. Preßler, E. Y. Vedmedenko, O. Pietzsch, and R. Wiesendanger, Phys. Rev. Lett. **103**, 157201 (2009).

[11] S. Meckler, M. Gyamfi, O. Pietzsch, and R. Wiesendanger, Rev. Sci. Instrum. **80**, 023708 (2008); see also Section 3.9.

[12] M. Bode, S. Krause, L. Berbil-Bautista, S. Heinze, and R. Wiesendanger, Surf. Sci. **601**, 3308 (2007).

3.3 Theoretical description of the interaction between domain walls and spin waves

3.3.1 Quantized spin waves in antiferromagnetic structures with domain walls

R. Wieser, E. Y. Vedmedenko, and R. Wiesendanger

Introduction

At the beginning of magnetic data storage it was important to understand spin wave excitations to minimize their disturbing influence or their assistance for the magnetization reversal [1]. More recent publications have shown that it is possible to use spin waves for logic devices [2, 3]. Another route for logic and data storage applications is based on the use of magnetic domain walls [4]. We propose to combine the advantages of these two directions. To make a first step towards future devices using a combination of spin waves and domain walls the interaction between domain walls and spin waves has to be understood.

Contemporary logic devices and data storage have mesoscopic dimensions, but in the future such devices might be realized on a much smaller length scale where not only ferromagnetic, but also antiferromagnetic and more complex spin structures are important. To study spin waves in those nanosystems we use a classical Heisenberg model. This representation is a good approximation to describe itinerant magnets with a ferromagnetic, antiferromagnetic, or complex spin structure on the atomic length-scale [5–7].

Model

The model we consider is a classical Heisenberg spin model with energy contributions from the exchange interaction and the magnetic anisotropy. As has been recently shown [8] the simple Heisenberg model with uniaxial anisotropy is well suited for the description of magnetic nanostructures. Such a spin model is on the one hand the classical limit of a quantum mechanical, localized spin model; on the other hand it might be interpreted as a rigid sphere approximation (RSA) of an itinerant magnet [9]. Here, we focus our attention on the second interpretation. The magnetic properties

are well described by the model Hamiltonian

$$\begin{aligned}\mathcal{H} &= J\sum_{\langle ij\rangle}\mathbf{S}_i\cdot\mathbf{S}_j - D_z\sum_i\left(S_i^z\right)^2 \\ &- \mu_s\sum_i\mathbf{B}_{\mathrm{RF}}\cos(\omega t)\mathbf{S}_i\ ,\end{aligned} \tag{3.1}$$

where $\mathbf{S}_i = \boldsymbol{\mu}_i/\mu_s$ is a three-dimensional magnetic moment of unit length on a simple cubic lattice with lattice constant a. The magnetic moment μ_s is given by $\mu_s = M_s a^3$, with the saturation magnetization M_s. The first sum in Eq. (3.26) is the exchange coupling between nearest neighbors with the coupling constant J. If $J > 0$ the coupling is ferromagnetic. In this case all magnetic moments have a parallel alignment. If $J < 0$ we have an antiferromagnetic coupling. In this case the system prefers an antiparallel orientation of the magnetic moments. The second sum represents a uniaxial anisotropy, favoring the z-direction as the easy axis of the system ($D_z > 0$). The last sum is the coupling of the spins to an oscillating field $\mathbf{B}_{\mathrm{RF}} \perp \mathbf{B}$ with the frequency ω.

The underlying equation of motion for magnetic moments which we consider is the Landau-Lifshitz-Gilbert (LLG) equation

$$\frac{\partial\mathbf{S}_i}{\partial t} = -\frac{\gamma}{(1+\alpha^2)\mu_s}\mathbf{S}_i\times\left[\mathbf{H}_i + \alpha\left(\mathbf{S}_i\times\mathbf{H}_i\right)\right]\ , \tag{3.2}$$

with the gyromagnetic ratio γ, the dimensionless Gilbert damping α, and the internal field $\mathbf{H}_i = -\partial\mathcal{H}/\partial\mathbf{S}_i$.

Solving of this equation leads to the time dependence of the magnetization and, hence, the spin wave excitations we are interested in. On the one hand the Landau-Lifshitz-Gilbert equation can be solved analytically in the framework of micromagnetic theory. This gives a good understanding of the physics but we are restricted to some approximations. On the other hand the Landau-Lifshitz-Gilbert equation can be solved numerically.

To study standing spin waves we calculate the absorbed power P at each lattice point i as

$$\begin{aligned}P_i &= -\left\langle\mu_s\left(\mathbf{S}_i\cdot\frac{\mathrm{d}\mathbf{B}(t)}{\mathrm{d}t}\right)\right\rangle \\ &= -\frac{\mu_s}{T}\int_0^T\mathbf{S}_i\cdot\frac{\mathrm{d}\mathbf{B}}{\mathrm{d}t}\mathrm{d}t\ .\end{aligned} \tag{3.3}$$

Physically P reflects the amount of energy (power) which is transformed into the spin wave excitations.

The numerical procedure is as follows: The simulations start with a relaxed saturated magnetic structure for given J and D_z values. In the next step, an oscillating magnetic field to all spins or one single spin is applied and the absorbed power is calculated at each site over the time interval $\mathcal{T}$. P_i is positive when both $S_i^B(t)$ and $\mathrm{d}\mathbf{B}(t)/\mathrm{d}t$

have the same sign and negative for the case of opposite signs. The sign of P_i reflects the phase of the excitation at site i. The maximum (minimum) means an oscillation in phase (anti-phase) with the time derivative of the oscillating field which corresponds to a phase shift of $+\pi/2$ $(-\pi/2)$ with respect to the oscillating field. $P_i = 0$ means no or no arranged oscillation. The values of P_i can be immediately plotted as a function of the distance vector and thus yield spatially resolved spin wave eigenmodes. The obtained patterns contain full information about the amplitude and the phase of an excitation. For larger time interval $\mathcal{T}$ the resolution of the normal modes is improved. To observe the absorbed power P as a function of frequency or an external field an averaging over the whole sample must be performed. The usual way of averaging is the integral response

$$P_{\mathrm{ir}} = \frac{1}{L} \sum_{i=1}^{L} P_i \; . \tag{3.4}$$

It is known, however, that the integral response signal P_{ir} does not show the whole spin wave mode spectrum due to the fact that the spatial average over antisymmetric waves is zero. Therefore, the averaged resolved P_{av} signal has been introduced:

$$P_{\mathrm{av}} = \frac{1}{L} \sum_{i=1}^{L} |P_i| \; . \tag{3.5}$$

With the help of Eq. (3.5) the power spectra, dispersion curves, and the field dependencies of normal modes can be easily calculated.

Quantized antiferromagnetic spin waves

To understand the interaction of spin waves with a domain wall one has first to understand the basic properties of the spin waves excited in confined magnetic structures. While the ferromagnetic spin waves have been broadly studied in confined ferromagnetic systems during last years, the investigations on magnetic excitation patterns in confined antiferromagnets are still very limited.

Finite chains of length up to $l = 100a$ lattice constants a have been simulated by solving the LLG equation. The calculations were performed with both fixed, both opened, and one fixed chain ends. The simulations were started with a relaxed magnetic configuration. Then an oscillating magnetic field was applied and the absorbed power was calculated. Fig. 3.7 shows the spatially resolved signal P_{av} as a function of frequency for a one-dimensional antiferromagnetic chain with one fixed end, while the inset shows the corresponding dispersion relation. Apart from the energy gap at zero wave-vector k one can recognize in Fig. 3.7 two groups of peaks, with larger and smaller peak-height. All peaks lie on the same straight dispersion line (see inset):

$$\frac{\hbar\omega}{J} = \sqrt{4\sin^2(ka) + 2\frac{D_z}{J}\left(2\frac{D_z}{J} + 4\right)} \; . \tag{3.6}$$

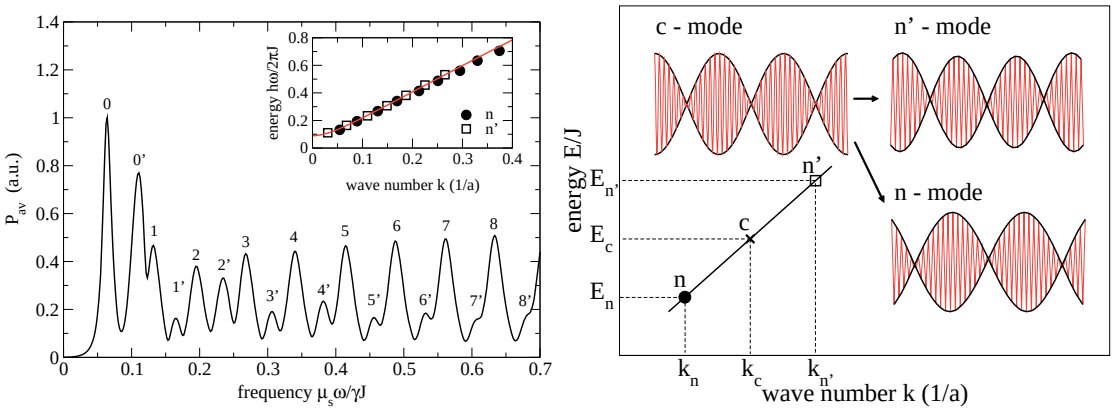

Figure 3.7: Left: Averaged signal P_{av} and dispersion of standing spin waves in an antiferromagnetic spin chain with one fixed end and anisotropy ($D_z/J = 0.001$). Right: Splitting of a conventional c-mode into n and n' modes in antiferromagnetic chains with open ends. A detailed description of the nomenclature is given in the text.

The main difference between a finite and an infinite system is the discrete character of $\hbar\omega = E(k)$ for finite antiferromagnets.

Mathematically, the two peak groups correspond to two solutions of the LLG equation. Physically, they correspond to two kinds of spin wave modes n and n'. The modes are defined by the number of nodes in a standing wave. The first six spin wave modes ($n = 0 \ldots 2,\ n' = 0 \ldots 2$) for a chain with a fixed end at $x = 0$ are shown in Fig. 3.7 (right). The fast oscillations correspond to the two sublattices with opposite orientation of magnetization, which rotate in opposite directions, while the envelope describes the standing wave. In the case of one or two open ends the n and n' differ by the character of the oscillation of the open end(s). As can be seen from Fig. 3.7 (right) the n-modes finish before the maximum, while the n' ones finish after the maximum.

The physical reason is the following: because of the existence of two sublattices two *different* solutions of the LLG equation are required. The two solutions may have identical energy. The identical energy for both sublattices (two possible solutions of the LLG) requires identical periodicity and phase of the sublattice standing waves, which is not allowed because of the orthonormality of two solutions. In order to relieve the degeneracy, two modes of identical periodicity but shifted in phase are formed. The average energy of these modes is equal to the energy of a conventional mode E_c ending at maximal amplitude $(E_n + E_{n'})/2 = E_c$ (see Fig. 3.7 (right)).

The case of a chain with two fixed ends is especially interesting as it includes two different realizations of boundary conditions: (i) both ends belong to the same sublattice; (ii) the ends belong to different sublattices. The chains belonging to the case (i) can be constructed only from an odd number of atomic sites. The dispersion curve and an example of a standing wave for antiferromagnetic chains of the case (i) are shown in Fig. 3.8 (left). A first remarkable feature of the standing wave is its asymme-

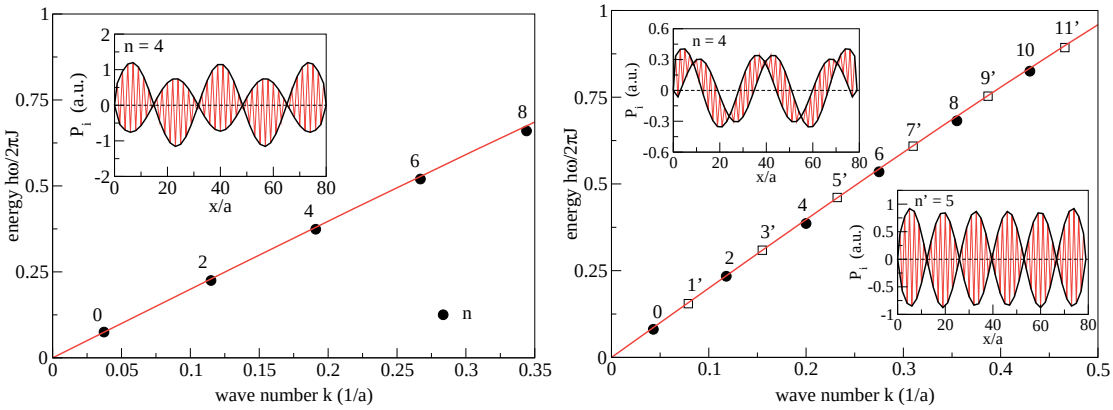

Figure 3.8: Left: Dispersion relation and standing spin wave of a chain with ends fixed at the same sublattice (case (i), $l = 78a$, i.e. 79 lattice sites). Right: Acoustic (even n, filled circles) and optical (odd n, open squares) standing antiferromagnetic spin waves in chains with ends fixed at different sublattices (case (ii), $l = 79a$, i.e. 80 lattice sites). The solid lines represent the analytical predictions.

try. Secondly, the dispersion curve does not show an energy splitting characteristic for chains with open ends; it means that n'-nodes are extinct. Thirdly, the edges pinned at the same sublattice cause a degeneracy of the two solutions: no odd modes can be found anymore (see Fig. 3.8) (left).

Chains of the type (ii) may only have an even number of atomic sites. For chains of type (ii) the nodes of the standing wave can easily form between two atomic sites. Therefore, both n- and n'-modes can be found (see Fig. 3.8 (right)). These two regimes can be regarded as antiferromagnetic acoustical and optical standing spin waves and can be visualized as a superposition of two ferromagnetic standing spin waves for different sublattices.

Spin waves in an antiferromagnetic system with a domain wall

In the following we present results for spin wave excitations in an one-dimensional antiferromagnetic systems with a 180° transverse domain wall. Such systems can be understood as prototypes of atomic chains or stripes. The profile of the transverse domain wall is given by:

$$S_y = \operatorname{sech}(x/\delta) \tag{3.7a}$$
$$S_z = -\tanh(x/\delta)\ , \tag{3.7b}$$

where δ is the domain wall width $\delta = \sqrt{Ja^2/2D_z}$.

We have performed both an analytical description as well as numerical simulations of standing spin waves in the presence of a transverse domain wall.

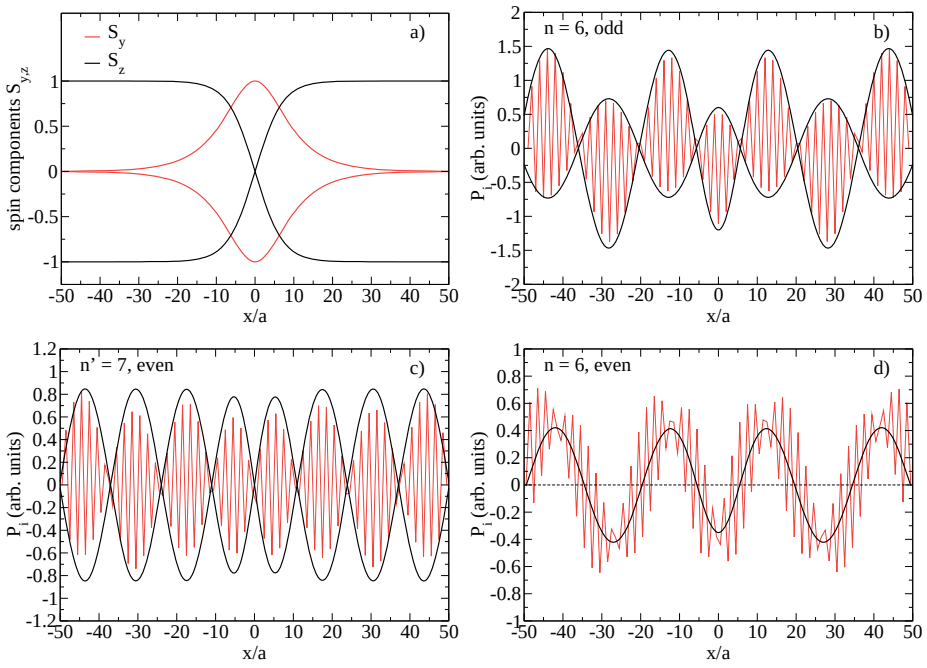

Figure 3.9: Domain wall profile (a) and standing spin wave modes in an antiferromagnetic spin chain with two fixed ends: both ends belong to the same sublattice (odd number of lattice sites) (b) or to different sublattices (even number of atoms) (c) and (d). $D_z/|J| = 0.01$ is assumed.

The analytical calculations lead to the following spin-wave solutions:

$$f_e(x) = N\left(\cos(k_x x) - \tanh\left(\frac{x}{\delta}\right)\frac{\sin(k_x x)}{k_x \delta}\right) \tag{3.8a}$$

$$f_o(x) = N\left(k_x \delta \sin(k_x x) + \tanh\left(\frac{x}{\delta}\right)\cos(k_x x)\right) \tag{3.8b}$$

The numerical procedure is identical to that of the previous subsection. We get similar discrete power spectra and shapes of spin waves. Here we limit our investigations to the mostly non-trivial case of an antiferromagnetic system with two fixed ends. In the first set of calculations both ends belong to the same sublattice. Due to the existence of the domain wall the magnetic moments at the ends are oriented in opposite directions. According to our simulations such a system exhibits standing spin waves with an odd number of nodes only. The envelope can be fitted with the even solution Eq. (3.8a) but with different amplitudes for different sublattices (see Fig. 3.9(b)). The wave number k_x is not affected by this asymmetry. The discrete energy values $\hbar\omega$ can be easily fitted by the well known dispersion relation Eq. (3.6).

In the second case, both ends belong to different sublattices. In this case the restriction of the boundary conditions is weaker and, therefore, it leads to the appear-

ance of both even and odd spin wave modes. Both types of modes can be fitted with the analytical solutions Eq. (3.8). The corresponding energy levels are well described by the dispersion relation of Eq. (3.6). While two enveloping curves of opposite signs Eq. (3.8b) exist in the case of an odd number of nodes the envelopes in the case of solutions Eq. (3.8a) have an identical sign but are shifted with respect to the initial curve. These two curves are visualized in Figure 3.9(c),(d) where the analytical solution without any displacement is also shown.

Spin waves in antiferromagnetic spin rings

Antiferromagnetic spin rings can be understood as a spin chain with periodic boundary conditions. The combination of periodic boundary conditions and an antiparallel alignment of the magnetic moments leads to the appearance of two cases depending on the chain length. If the number of lattice sites is even we end up with a non-frustrated spin ring with the well known Néel structure. For an odd number of lattice sites the antiferromagnetic structure is frustrated. Some of the nearest neighbors are oriented parallel to one another or in other words we find a domain wall.

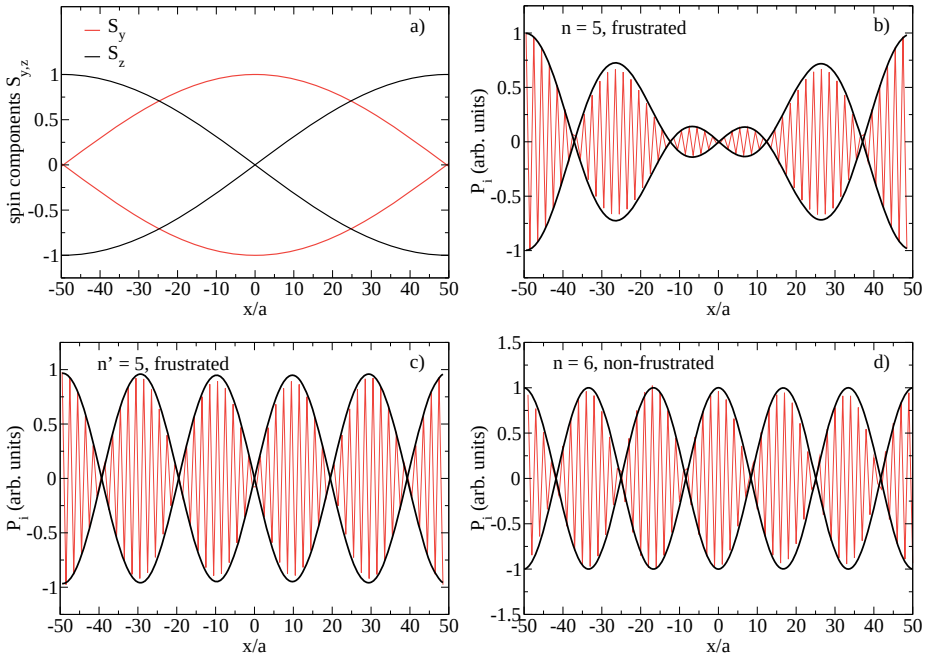

Figure 3.10: Profile of the frustrated antiferromagnetic spin ring (a) and the corresponding types of standing spin waves (b) and (c). Plot (d) shows the standing spin wave solution of the non-frustrated antiferromagnetic spin ring. $(D_z/|J| = 0)$ is assumed.

In the following, we investigate antiferromagnetic spin systems without anisotropy $(D_z/|J| = 0)$. If the number of lattice sites is even we end up with a non-frustrated

spin ring with the well known Néel structure. After the excitation of such a spin ring by an oscillating magnetic field as described above we find quantized spin waves with a simple cosine profile:

$$P_m = \pm\cos(k_x x)\ . \tag{3.9}$$

Due to the periodic boundary conditions an even number of nodes only (see Fig. 3.10(d)) may appear.

The relaxation of a ring with an odd number of lattice sites leads to an antiferromagnetic spin structure with a domain wall. For absent anisotropy of the profile the domain wall is described by

$$S_y = \pm\cos\left(\frac{x\pi}{L}\right) \tag{3.10a}$$

$$S_z = \pm\sin\left(\frac{x\pi}{L}\right)\ , \tag{3.10b}$$

with the domain wall width δ given by the chain length L divided by π (see Fig. 3.10(a)). Such magnetization configuration can be denoted as a magnetic Möbius stripe, because the ring should be rolled up twice to end up with the same orientation of the magnetization without abrupt changes.

Similarly to the antiferromagnetic spin chain we find in the second case (one lattice site more) two types of spin wave solutions which are given by the following expressions:

$$P_n = \pm N\left(\cos(k_x x) - \frac{L}{k_x\pi}\sin\left(\frac{x\pi}{L}\right)\cos(k_x x)\right) \tag{3.11a}$$

$$P_{n'} = \pm N\left(\frac{k_x L}{\pi}\sin(k_x x) + \sin\left(\frac{x\pi}{L}\right)\cos(k_x x)\right) \tag{3.11b}$$

where n, n' denote the number of nodes. Because of the periodic boundary conditions only odd number of nodes exist. Furthermore, for each n mode a corresponding n' spin wave mode with the same number of nodes has been found (see Fig. 3.10(b),(c)).

Summary

In summary we have demonstrated that quantized spin waves do exist in antiferromagnets. The characteristics of the antiferromagnetic standing waves have no equivalents neither in acoustics nor in ferromagnetic samples. Particularly, the discrete energy dispersion is splitted into n and n'-modes because of the existence of two sublattices. The splitting of the dispersion curve, the configuration of oscillations of individual sublattices as well as the symmetry of standing waves strongly depend on the boundary conditions. In chains with open boundaries we find spin wave modes of odd and even parity in n as well as in n' energy levels. The phases of oscillations in n- and n'-bands are shifted by one eighth of the wave vector, while the average energy of both

oscillations is equal to the energy of a conventional, unshifted mode. The chains with pinned ends can be subdivided into two main cases: those ones with both ends belonging to the same sublattice and that having the ends at different sublattices. In the first case the energy splitting does not appear and the n'-modes of odd parity do not exist. A very particular asymmetry of the envelope function has been observed for this geometry. In the second case the energy splitting is recovered, while the asymmetry of the oscillations disappears. Very peculiar acoustical and optical antiferromagnetic spin waves have been found if the two ends belong to the same sublattice. The unusual behavior is explained on the basis of symmetry considerations.

Spin waves in antiferromagnetic structures with a domain wall show a conventional antiferromagnetic dispersion relation and the characteristic antiferromagnetic spin wave patterns. Further, we have demonstrated that the spin waves can be described by analytical solutions which are well known from theory of solitons.

In the last section of the present study antiferromagnetic spin rings have been investigated. Similarly to the previous case different solutions have been found. If the number of lattice sites is even, the ground state is an ordinary Néel configuration. In this case only one type of spin wave modes with an even number of nodes can be excited. In the case of an odd number of lattice sites a frustrated ground state has been found which leads to a magnetic Möbius-like ground state for $D_z/|J| = 0$. In this case we find two types of odd spin wave modes, which are well described by the analytical solution if the domain wall profile is adjusted.

In conclusion, in all studied antiferromagnetic structures the presence of a transverse domain wall does not lead to a change of the dispersion curve, only the shape of the spin waves changes. The same is true for the ferromagnetic systems as well.

References

[1] Z. Z. Sun and X. R. Wang, Phys. Rev. B **74**, 132401 (2006).

[2] T. Schneider, A. A. Serga, B. Leven, B. Hillebrands, R. L. Stamps, and M. P. Kostylev, Appl. Phys. Lett. **92**, 022505 (2008).

[3] A. Khitun, B. Mingqiang, and K. L. Wang, IEEE Trans. Magn. **44**, 2141 (2008)

[4] D. A. Allwood, G. Xiong, C. C. Faulkner, D. Atkinson, D. Petit, and R. P. Cowburn, Science **309**, 1688 (2005)

[5] R. Wieser, E. Y. Vedmedenko, and R. Wiesendanger, Phys. Rev. B **77**, 064410 (2008)

[6] R. Wieser, E. Y. Vedmedenko, and R. Wiesendanger, Phys. Rev. Lett. **101**, 177202 (2008).

[7] R. Wieser, E. Y. Vedmedenko, and R. Wiesendanger, Phys. Rev. B **79**, 144412 (2009).

[8] P. Gambardella, Nature Mater. **5**, 431 (2006)

[9] V. P. Antropov, M. I. Katsnelson, B. N. Harmon, M. van Schilfgaarde, and D. Kusnezov, Phys. Rev. B **54**, 1019 (1996)

3.3.2 Domain wall motion damped by the emission of spin waves

R. Wieser, E. Y. Vedmedenko, and R. Wiesendanger

Introduction

Domain wall motion in magnetic nanowires has been extensively studied during the last years. The idea behind is to construct logic [1] and data storage devices [2, 3] based on domain wall motion. The physical picture of domain wall motion has been strongly influenced by the publications of L. R. Walker [4]. He demonstrated that above a critical field the domain wall starts to oscillate and, therefore, the velocity decreases with increasing field. Below this so-called Walker breakdown field one finds a steady domain wall motion with the velocity increasing with increasing field. The experimental proof of the existence of the Walker threshold [5] ensured the popularity of this theory. Recently, however, it has been demonstrated that the reality is much more complicated and the domain wall motion also depends on the shape and material of the wire. For instance while the transverse domain walls in thin film structures show the behavior described by Walker [6] one finds a totally different domain wall motion in cylindrical nanowires [7,8]. In this case the transverse domain wall shows a precessional motion and the Walker breakdown does not occur.

Further, it has been shown that vortex domain walls do not show a Walker breakdown [7]. Instead of a Walker breakdown the vortex domain wall starts to emit spin waves and its velocity decreases. A similar phenomenon is well known in the theory of Solitons [9], where this behavior is known as "Bremsstrahlung" [10]. Many analytical descriptions of this phenomenon based on a perturbation theory can be found in literature [11] but so far, there was neither a numerical proof nor a clear understanding of the reason for the spin wave emission. The dispersion relationship was unknown as well.

Model

We consider a classical Heisenberg model, which might be interpreted as rigid sphere approximation of an itinerant magnet [12]. The magnetic properties are described by the following biaxial Hamiltonian

$$\begin{aligned} \mathcal{H} = & - J\sum_n \mathbf{S}_n \cdot \mathbf{S}_{n+1} - \mu_s \mathbf{B} \cdot \sum_n \mathbf{S}_n \\ & + D_h \sum_n (S_n^x)^2 - D_e \sum_n (S_n^z)^2 \end{aligned} \tag{3.12}$$

where the $\mathbf{S}_n = \boldsymbol{\mu}_n/\mu_s$ are three dimensional magnetic moments of unit length on a simple cubic lattice with the lattice constant a.
The first term in Eq. (3.26) describes the exchange coupling between nearest neighbors with ferromagnetic coupling constant $J > 0$. The second sum is the so-called Zeeman term, which describes the coupling of the spins to an external magnetic field $\mathbf{B}$. The third sum describes an easy zy-plane or hard x-axis anisotropy ($D_h > 0$). The fourth sum gives an easy axis anisotropy ($D_e > 0$) in z-direction which breaks the easy plane symmetry.

In the following we investigate a transverse domain wall in linear magnetic chains oriented along the z-direction. Such chains can be interpreted as quasi 1D magnets [13] or as a cylindrical nanowire with a transverse domain wall [7,8].

The underlying equation of motion is the Landau-Lifshitz-Gilbert (LLG) equation,

$$\dot{\mathbf{S}}_n = -\frac{\gamma}{(1+\alpha^2)\mu_s}\mathbf{S}_n \times \mathbf{H}_n + \frac{\alpha\gamma}{(1+\alpha^2)\mu_s}\mathbf{S}_n \times (\mathbf{S}_n \times \mathbf{H}_n) \tag{3.13}$$

with the gyromagnetic ratio γ, the dimensionless Gilbert damping α, and the internal field given by the gradient $\mathbf{H}_n = -\partial\mathcal{H}/\partial\mathbf{S}_n$. The first term of the LLG equation describes the precessional motion of $\mathbf{S}_n$ and the second term the relaxation.

Domain wall deceleration by spin waves

According to the literature the assumption of a zero hard axis anisotropy $D_h/J = 0$ leads to the precessional domain wall motion during magnetization reversal [7,8]. The corresponding velocity equation

$$v_{\mathrm{S}} = \frac{\gamma B}{\alpha + \frac{1}{\alpha}}\sqrt{\frac{Ja^2}{2D_e}}\,, \tag{3.14}$$

for a constant domain wall width $\Delta = \sqrt{Ja^2/(2D_e)}$ and $1/\left(\alpha + 1/\alpha\right)$ velocity dependence has been derived by J. Slonczewski [14]. In the limit of zero damping ($\alpha = 0$) the velocity is zero and the magnetic moments inside the domain wall just precess around the z-axis. This behavior becomes obvious when one bears in mind that for $\alpha = 0$ the relaxation term in the LLG equation becomes zero.

If the hard axis anisotropy is finite the regime which was first described by L. R. Walker [4] is reached (see Fig. 3.3.2(b)). Here one finds a direct spin flip reversal of the magnetization during the domain wall motion which corresponds to a $1/\alpha$ behavior of the velocity:

$$v_{\mathrm{W}} = \frac{\gamma B}{\alpha}\sqrt{\frac{Ja^2}{2\left(D_e + D_h \sin^2\phi\right)}}\,. \tag{3.15}$$

The angle ϕ describes the angle between the plane where the spin motion takes place and the easy plane given by the hard axis anisotropy D_h. ϕ is constant in time but

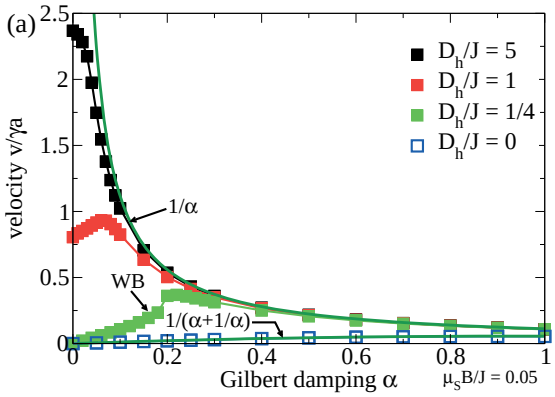

Figure 3.11: Velocity of a transverse domain wall with biaxial anisotropy (D_e and D_h) vs. Gilbert damping α (a). $D_e/J = 0.1$, $\mu_s B/J = 0.05$ is assumed.

depends on the external field B, the hard axis anisotropy D_h and the Gilbert damping α:

$$\phi = \frac{1}{2} \arcsin\left(\frac{\mu_s B}{\alpha D_h}\right) . \tag{3.16}$$

In the limit of infinite hard axis anisotropy $D_h/J \to \infty$ the angle ϕ becomes zero which corresponds to a magnetization reversal strictly in the easy axis (xy)-plane. In this limit the Eq. (3.15) becomes

$$v_{\mathrm{LL}} = \frac{\gamma B}{\alpha}\sqrt{\frac{Ja^2}{2D_e}} . \tag{3.17}$$

This equation has been derived by L. D. Landau and E. M. Lifshitz in 1935 [15] and gives the highest possible velocity of the domain wall.

Apart from the highest velocity Eq. (3.16) also defines the condition for a validity of the Walker formula. For a constant Gilbert damping α a maximum value B_{max} exists (or vice versa a minimum value of the Gilbert damping α_{min} exists for a constant external field B) beyond which the Eq. (3.16) is no longer fulfilled. This means that the spin motion is no longer restricted to a plane and an irregular precessional motion appears. This irregular precession in combination with an asymmetric oscillating force leads to a periodic change of the domain wall width and position [16] which corresponds to the Walker breakdown and leads to a decrease of the velocity as one could see in Fig. 3.3.2(a) and (b) for $D_h/J = 0.25$. In the limit of zero damping ($\alpha = 0$) one finds a periodic force and back motion of the domain wall with no effective wall displacement, which means that the time averaged velocity $\langle v \rangle$ vanishes.

A further increase of the hard axis anisotropy leads to the elimination of the Walker breakdown. Here one finds a finite velocity of the domain wall already for $\alpha = 0$ (see the $D_h/J = 1$ and $D_h/J = 5$ curves in Fig. 3.3.2(a)). This is still true for an infinite hard axis anisotropy. Here the velocity is well described by the formula of Walker

(Eq. 3.15) up to a maximum field value (Fig. 3.3.2(b)) or down to a minimum Gilbert damping α (Fig. 3.3.2(a)). Beyond these limiting values the domain wall starts to emit spin waves. One can recognize that by comparing the curves for $D_h/J = 1$ and $D_h/J = 5$ with their $D_h/J = 0.25$ counterpart in Fig. 3.3.2(a) and (b). In contrast to $v(\alpha)$ for $D_h/J = 0.25$ the $v(\alpha)$ dependencies for stronger anisotropies ($D_h/J = 1$ and $D_h/J = 5$) significantly deviate from the $1/\alpha$ behavior but the velocity does not vanish for vanishing α (see Fig. 3.3.2(a)). This behavior shows that there is a continuous crossover from Walker breakdown to a spin wave damped motion,

To understand the physics of domain wall deceleration by spin waves one has to answer the following two questions: What is the driving mechanism and is it possible to give a quantitative description of the spin wave emission?

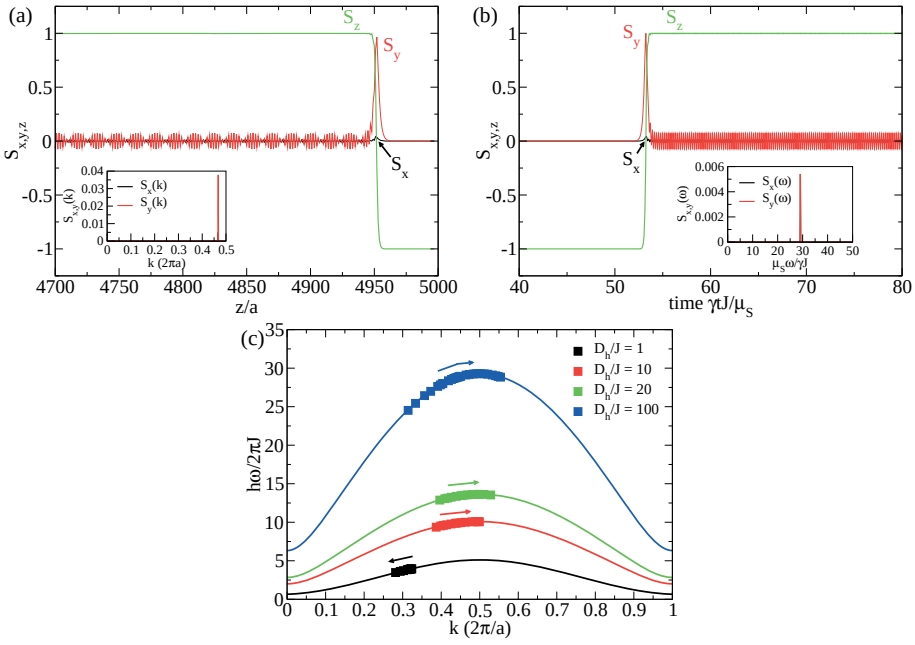

Figure 3.12: Spin wave behind a moving transverse domain wall: (a) magnetization as function of space (fixed time), (b) magnetization as function of time (fixed space). The insets show the corresponding Fourier transformations in k- respectively ω-space. (c) Magnetic spin wave dispersion. Solid lines are the analytical solutions given by Eq. (3.18). The arrows mark the direction of change (increasing / decreasing) of the wave number k with increasing applied field $\mu_s B/J$. $D_e/J = 0.01$, $D_h/J = 100$ (only (a) and (b)), $\alpha = 0$ and $\mu_s B/J = 0.005$ (only (a) and (b)), $\mu_s B/J$ between $1 \cdot 10^{-6}$ and 1 (only (c)) are assumed.

To answer these questions we repeat all calculations in the zero damping limit ($\alpha = 0$) in order to neglect the effect of all damping mechanisms which are included in the Gilbert damping term [17].

Our simulations show that the driving mechanism of the spin wave emission is the same as the wake behind a motorboat. This means that the spin wave is excited by

the magnetization reversal of the spins inside the domain wall. The energy comes from the external field. The unexpected result of our calculations is that the domain wall moves at a constant magnetic field despite the fact that the relaxation term in the LLG equation (Eq. (3.13)) is skipped if $\alpha = 0$. This effect can be understood taking into account the shape of the precessional motion of magnetic moments. For circular precession no domain wall motion could occur. This is the case for $D_h/J = 0$. In the general case however, the hard axis anisotropy distorts the shape of the orbit and makes it elliptic. The longer axis of the ellipse spans between the two minima of the easy axis anisotropy. That's why the switching between these two minima becomes possible. The exchange interaction ensures an energy transfer to the neighboring spins [18], i.e. makes the emission of spin waves behind the domain wall possible. The magnetic moments remain reversed.

For a quantitative description of the spin wave spectra the distance dependence of the spin wave at a fixed moment of time (Fig. 3.12(a)) and the time dependence at a fixed lattice point (Fig. 3.12(b)) have to be analyzed. For that purpose the Fourier transformation in space (see inset of Fig. 3.12(a)) and time (see inset of Fig. 3.12(b)) has to be performed [19]. In both cases distinct peaks in the Fourier spectra have been found. Using these peaks the spin wave dispersion can be plotted. The symbols in Fig. 3.12(c) are the numerical data for different hard axis anisotropies D_h and field values between $\mu_s B/J = 1 \cdot 10^{-6}$ and $\mu_s B/J = 1$. Each point corresponds to a single field value. The solid lines are the corresponding analytical curves given by the formula:

$$\frac{\hbar\omega}{J} = 2\mathcal{S}\sqrt{\left(1-\cos(ka)+\frac{D_e}{J}\right)\left(1-\cos(ka)+\frac{D_e}{J}+\frac{D_h}{J}\right)}\,. \tag{3.18}$$

Eq. (3.18) has been derived under the assumption of zero external field $\mathbf{B}$. In our simulations, however, one needs to apply a finite field in order to get domain wall motion. Therefore, each symbol in Fig. 3.12(c) corresponds to a certain field value $\mu_s B/J$.

The interesting point of the numerical solution is that the k-value has a non-trivial dependence on B. It increases with increasing field for higher values of D_h (the three upper curves in Fig. 3.12(c)), while decreases for weaker D_h (bottom curve in Fig. 3.12(c)). This is a direct consequence of an increasing / decreasing relaxation time. In other words the wave number k corresponds to the energy gained during the magnetization reversal.

Summary

We have investigated the domain wall motion of the field driven transverse domain walls in biaxial ferromagnets. We show that with increasing easy plane or hard axis anisotropy D_h different types of domain wall motion occur. In the limit of absent hard axis anisotropy ($D_h/J = 0$) the transverse domain wall shows a precessional motion.

Here, the velocity is well described by the equation given by J. Slonczewski. For finite hard axis anisotropy ($D_h/J \neq 0$) the transverse domain wall shows a steady state motion. For small anisotropies ($D_h > 0$) this velocity is limited by the occurrence of a Walker breakdown. For higher D_h the Walker breakdown is eliminated and a spin wave damped domain wall motion emerges. We have analyzed the emitted spin waves and calculated the spin wave dispersion numerically [20].

References

[1] D. A. Allwood, G. Xiong, C. C. Faulkner, D. Atkinson, D. Petit, and R. P. Cowburn, Science **309**, 1688 (2005)

[2] M. Hayashi, L. Thomas, R. Moriya, C. Rettner, and S. S. P. Parkin, Science **320**, 209 (2008).

[3] S. S. P. Parkin, M. Hayashi, and L. Thomas, Science **320**, 190 (2008).

[4] J. F. Dillon, in *Magnetism*, edited by G. T Rado and H. Suhl (Academic, New York, 1963), Vol. 1, p. 149.

[5] T. Ono , H. Miyajima, K. Shigeto, K. Mibu, N. Hosoito, and T. Shinjo, Science **284**, 468 (1999).

[6] A. Thiaville and Y. Nakatani, in *Spin dynamics in confined magnetic structures III*, edited by B. Hillebrands and A. Thiaville (Springer, Berlin, 2006).

[7] R. Wieser, U. Nowak, and K. D. Usadel, Phys. Rev. B **69**, 064401 (2004)

[8] R. Wieser, U. Nowak, and K. D. Usadel, Phase Transitions **78**, 115 (2005)

[9] R. Wieser, E. Y. Vedmedenko, and R. Wiesendanger, Phys. Rev. B **79**, 144412 (2009)

[10] G. Eilenberger, Z. Physik B **27**, 199 (1977)

[11] J. M. Winter, Phys. Rev. **124**, 452 (1961)

[12] V. P. Antropov, M. I. Katsnelson, B. N. Harmon, M. van Schilfgaarde, and D. Kusnezov, Phys. Rev. B **54**, 1019 (1996)

[13] H. J. Mikeska, J. Appl. Phys. **52**, 1950 (1981)

[14] A. P. Malozemoff and J. C. Slonczewski, in *Magnetic Domain Walls in Bubble Materials* (Academic, New York, 1979).

[15] D. L. Landau and E. Lifshitz, Phys. Z. Sowjetunion **8**, 153 (1935)

[16] N. L. Schryer and L. R. Walker, J. Appl. Phys. **45**, 5406 (1974)

[17] T. L. Gilbert, IEEE Trans. Magn. **40**, 3443 (2004)

[18] V. L. Safonov and H. N. Bertram, Phys. Rev. B **63**, 094419 (2001)

[19] O. Chubykalo, J. D. Hannay, M. Wongsam, R. W Chantrell, and J. M. Gonzalez, Phys. Rev. B **65**, 184428 (2002).

[20] R. Wieser, E. Y. Vedmedenko, and R. Wiesendanger, Phys. Rev. B **81**, 144412 (2010).

3.4 Dynamics and manipulation of magnetic nanostructures with SP-STM

3.4.1 Magnetization reversal of nano-scale islands: How size and shape affect the Arrhenius prefactor

S. Krause, G. Herzog, T. Stapelfeldt, L. Berbil-Bautista, M. Bode, E. Y. Vedmedenko, and R. Wiesendanger

The vast growth of storage density in magnetic media is closely connected to the miniaturization of bit size. Below a critical size, however, thermal agitation leads to a magnetization reversal of the grains that represent a bit, thereby destroying stored information. Therefore it is highly relevant to understand the underlying physical processes that favor or hinder magnetization reversal inside a nanomagnet.

In early theoretical approaches Néel [1] and Brown [2] calculated the switching probability for monodomain particles of uniaxial anisotropy. The mean lifetime $\bar{\tau}$ between consecutive switching events of a particle as a function of temperature T is characterized by its activation barrier E_b and attempt frequency ν_0,

$$\bar{\tau} = \nu_0^{-1} \exp\left(\frac{E_\mathrm{b}}{k_\mathrm{B}T}\right), \tag{3.19}$$

with k_B being the Boltzmann constant. In this model, magnetization reversal is realized by a coherent rotation of all magnetic moments inside the particle, with E_b given by the total magnetic anisotropy of the particle. The prefactor ν_0 is commonly related to Larmor precession, with $\nu_0 \approx 10^{10}\,\mathrm{Hz}$ [2].

Depending on the magnetic anisotropy, exchange parameter and size, a monodomain particle may reverse its magnetization via nucleation and propagation rather than by a coherent rotation. Like in the Néel-Brown model, an Arrhenius-like switching behavior is expected, now with E_b represented by the energy needed for the combined nucleation and domain wall formation. Whereas there are many studies focussing on the details of the energy barrier E_b and the microscopic processes for magnetization reversal, the fundamental physics of the prefactor ν_0 is not revealed. In general, ν_0 is considered to be a constant which only depends on material properties of the system, but size or shape effects have been neglected. A detailed study on the Arrhenius prefactor of nanomagnets that reverse their magnetization via nucleation and diffusion was lacking up to now, because laterally and time-averaging experimental techniques are not suitable to investigate the switching behavior of individual atomic-scale nanoobjects. However, spin-polarized scanning tunneling microscopy (SP-STM) serves as a unique tool to directly probe the magnetization of individual nanoislands.

Our studies using combined temperature-dependent SP-STM experiments and Monte-Carlo (MC) simulations reveal that monolayer iron islands on W(110) consisting of 30 atoms and more reverse their magnetization via the nucleation and propagation of a domain wall, whereas we have indications that for islands consisting of less than 30 atoms the reversal takes place via a coherent rotation of the magnetic moments. Although an Arrhenius-like switching has been observed, both the experimental and the theoretical investigations show that ν_0 strongly depends on the size and the shape of the nanoislands—which is not expected within the Néel-Brown model.

The experimental investigations were performed in an ultrahigh vacuum system that is equipped with a homebuilt spin-polarized scanning tunneling microscope for variable temperatures. Within our experimental setup, the entire microscope including the tip is cooled to minimize the thermal drift between tip and sample. While staying in tunneling contact, the temperature can be varied by more than 10 K without the nanoisland that is to be investigated drifting out of the tip scan range. The base pressure in both the preparation and the STM chamber is in the low 10^{-11} torr range. To exclude any unwanted dipolar tip-sample interaction, antiferromagnetic Cr coated tips were used that are sensitive to the in-plane component of the sample magnetization [3, 4].

A W(110) single crystal serves as substrate for our experiments. Its preparation is described in detail in Ref. [5]. Evaporating 0.14 atomic layers of iron onto the substrate held at room temperature leads to the formation of pseudomorphically grown nanoislands which have a typical diameter between 2 nm and 6 nm, thereby consisting of about 30–150 atoms. The thermal switching behavior of eleven nanoislands that differ in size and shape has been investigated in detail as a function of temperature. A topography patchwork of the nanoislands is shown in Fig. 3.13(a). All experiments have been performed at temperatures between $T = 30\,\mathrm{K}$ and $T = 80\,\mathrm{K}$. The magnetic probe tip has been positioned on top of the center of an individual island to record the temporal evolution of the differential conductance $\mathrm{d}I/\mathrm{d}U$, measured by adding a small ac modulation voltage ($U_{\mathrm{mod}} = 40\,\mathrm{mV}$) to the sample bias and detecting the resulting modulation of the tunneling current I by lock-in technique. The spin-dependent contribution to the $\mathrm{d}I/\mathrm{d}U$ signal scales with $\cos\alpha$, where α is the angle between the magnetization directions of the tip and sample [4].

In Fig. 3.13(b) a section of the telegraphic $\mathrm{d}I/\mathrm{d}U(t)$ signal is exemplarily shown for nanoisland "9" at a fixed temperature $T = 53.6\,\mathrm{K}$. The signal abruptly changes between two discrete levels, reflecting the island magnetization switching between two configurations with respect to the stable tip magnetization. From earlier investigations on the Fe/W(110) system it is known that the monolayer exhibits a uniaxial anisotropy with an easy axis of magnetization oriented along the $[1\bar{1}0]$ direction [6, 7], which is consistent with our observation. Plotting the histogram $h(\tau)$ of all the lifetimes τ between consecutive switching events, as shown in Fig. 3.13(c), reveals that the lifetime distribution can be described by an exponential decay law, and fitting the data results in the mean lifetime $\bar{\tau}(T)$. Approximately one thousand switching events

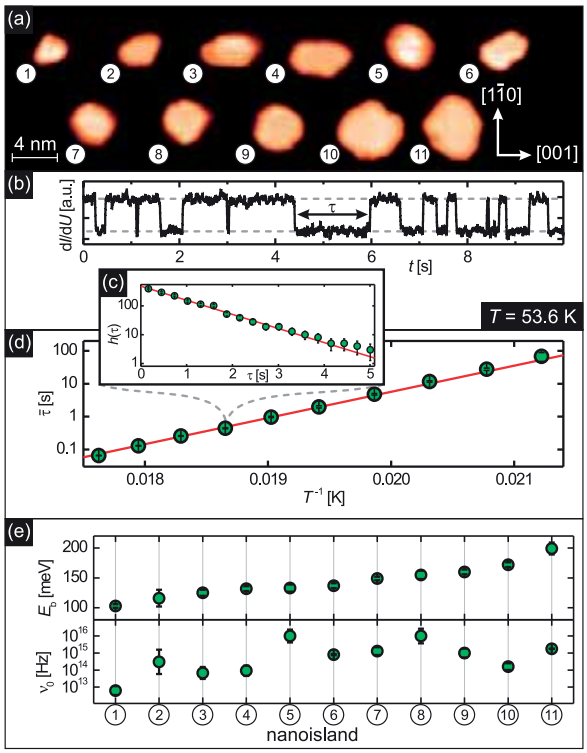

Figure 3.13: (a) Topography maps of all nanoislands investigated. (b) Section of the magnetic $\mathrm{d}I/\mathrm{d}U(t)$ signal as recorded above the center of an individual island. Every lifetime τ in between two consecutive switching events has been determined (see arrow). (c) Respective histogram $h(\tau)$ of the lifetimes τ. Fitting with a decay law results in the mean lifetime $\bar{\tau}$. (d) Mean lifetime $\bar{\tau}(T^{-1})$ as determined for different temperatures T. (e) Effective activation energy barrier E_b (top panel) and prefactor ν_0 (bottom panel) as determined for each of the nanoislands.

have been recorded to assure good statistics on the lifetime distribution. This procedure of mean lifetime determination was repeated at different temperatures on the same nanoisland. The result for the exemplary nanoisland is shown in Fig. 3.13(d). An Arrhenius-like behavior of $\bar{\tau}(T^{-1})$ is clearly visible, therefore it is reasonable to fit the data with Eq. 3.19, yielding the effective activation energy barrier E_b and the prefactor ν_0. The respective fitting parameters E_b and ν_0 for all investigated nanoislands are summarized in Fig. 3.13(e). Note that ν_0 is on the order of 10^{13} and 10^{16} Hz, whereas the observed switching frequencies are on the order of Hz—hence, the observed magnetization reversals are very rare events.

In Fig. 3.14(a), E_b is plotted as a function of the respective island length along the [1$\bar{1}$0] direction, $N_{[1\bar{1}0]}$, counted in atomic rows (AR). Obviously, E_b scales linearly with $N_{[1\bar{1}0]}$, whereas no clear dependence on the length along the [001] direction $N_{[001]}$ is visible, as can be seen in Fig. 3.14(b). The clear linear scaling behavior with $N_{[1\bar{1}0]}$ in Fig. 3.14(a) indicates that reversal takes place via the nucleation and propagation of

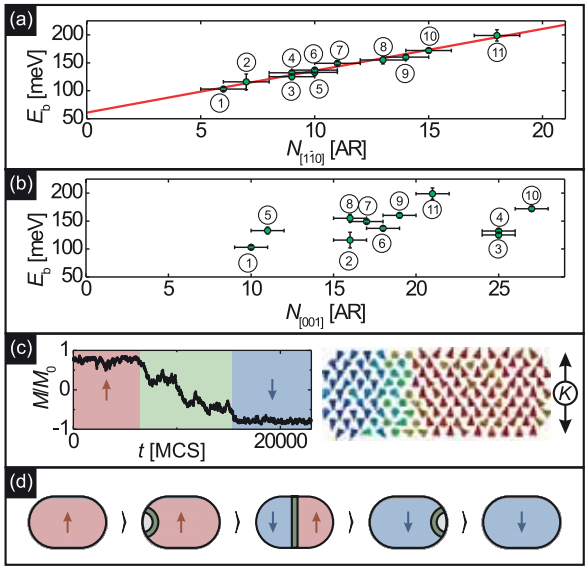

Figure 3.14: Activation energy barrier E_b plotted as a function of length N of the nanoisland along (**a**) the $[1\bar{1}0]$ direction and (**b**) the [001] direction. (**c**) Monte Carlo simulation: Evolution of the island magnetization M (M_0: saturation magnetization) for a typical switching event (left panel). Snapshot of the spin-configuration during reversal (right). Every cone represents one magnetic moment, while the color scheme denotes the orientation. (**d**) Model of magnetization reversal via nucleation and propagation of a domain wall.

a domain wall that aligns along the $[1\bar{1}0]$ direction and consequently moves along the [001] direction. As $N_{[1\bar{1}0]}$ increases, the respective length of the domain wall (and therefore its energy) increases accordingly. Fitting the experimentally obtained activation energy barriers $E_\mathrm{b}(N_{[1\bar{1}0]})$ in Fig. 3.14(a) to a linear function of the type

$$E_\mathrm{b}(N_{[1\bar{1}0]}) = E_0 + e_\mathrm{DW} \cdot N_{[1\bar{1}0]} \tag{3.20}$$

results in $E_0 = (61 \pm 5)\,\mathrm{meV}$ and $e_\mathrm{DW} = (7.5 \pm 0.4)\,\mathrm{meV/AR}$. The energy offset E_0 includes rim effects as well as the energy for the creation of a reversed nucleus. Within additional investigations on the Fe/W(110) closed monolayer system the domain wall width has been found to be $w = (2.15 \pm 0.35)\,\mathrm{nm}$. Using e_DW and w, the uniaxial anisotropy in the $[1\bar{1}0]$ direction, $K = (0.55 \pm 0.03)\,\mathrm{meV/atom}$, and the exchange stiffness component in the [001] direction, $A_{[001]} = (9.07 \pm 0.42)\,\mathrm{meV}$, have been derived.

Hence, two important issues have been experimentally revealed: a non-vanishing offset in the activation energy and an orientational preference of the domain walls. While similar effects have been discussed in the literature with respect to ground states of ultrathin films [8, 9] and quasi-static magnetization reversal [10], their role for the thermally induced switching behavior is unknown so far. To shed light on this important issue, MC simulations of thermally activated magnetization reversal in Fe/W(110) monolayer islands have been performed for different island sizes and shapes,

using the experimentally determined parameters $A_{[001]}$ and K. For the calculations the procedure described in [8] has been used, with the exchange interactions along the $[1\bar{1}0]$ direction taken to be twice as strong as those along the [001] direction, according to previous investigations [8, 9].

A typical switching event as calculated within the MC simulations is shown in Fig. 3.14(c). In contrast to the SP-STM experiment, the detailed magnetization reversal processes can be resolved at any given simulation time t. The snapshot in the right panel of Fig. 3.14(c) shows the magnetic configuration of the simulated island during reversal. It is clearly visible that a domain wall separates a spin-up domain from a spin-down domain. Composing a movie from many consecutive snapshots reveals that the domain wall propagates from one end of the island to the other, thereby leading to a reversal of the magnetization. Due to the strong anisotropy of the exchange stiffness tensor the domain walls have been found to be mainly oriented along the $[1\bar{1}0]$ axis independently of the sample shape. Because of this anisotropy, E_b scales linearly with $N_{[1\bar{1}0]}$, but does not depend on $N_{[001]}$. The detailed analysis of numerous switching events has shown that the magnetization reversal usually starts at one of the [001] ends of an island, whereas nucleation events taking place far away from the [001] ends are very rare. Consequently, the simulations support the experimental finding of temperature induced magnetization reversal via nucleation and propagation.

In Fig. 3.14(d), a detailed model for the magnetization reversal is developed. Initially, the island is in a monodomain state. The reversal starts by the coherent rotation of several magnetic moments within a small nucleus. This nucleus is confined by a domain wall that propagates along the [001] direction through the whole nanoisland with Boltzmann probability. Only a domain wall propagation from one end of the island to the other leads to a net magnetization reversal of the nanoisland, whereas the initial magnetic configuration is restored if the domain wall annihilates at the nucleation site.

The exciting question arises on how the size and shape of a nanoisland affects its switching rate. In Fig. 3.15(a), the experimentally determined prefactor ν_0 is plotted as a function of $N_{[001]}$ and $N_{[1\bar{1}0]}$. Adding a contour plot to the graph reveals that all data points (apart from the smallest nanoisland, labeled "1") seem to lie on a plane in the three-dimensional $(N_{[001]}, N_{[1\bar{1}0]}, \log_{10}[\nu_0/\nu_\mathrm{unit}])$ space ($\nu_\mathrm{unit} = 1\,\mathrm{Hz}$), as indicated by the interpolated color gradient ranging from high ν_0 values (red) on the upper left to low values (blue) on the lower right of the graph. The prefactor ν_0 of the smallest island considerably deviates from this scheme. We speculate that—due to its small size—this island reverses its magnetization via a coherent rotation of the magnetic moments rather than by a nucleation and propagation. The activation energy barrier E_b has been used to elaborate rim effects, resulting in the anisotropy of rim atoms $K_\mathrm{rim} \approx 5.6\,\mathrm{meV/atom}$. Fig. 3.15(a) shows that ν_0 should increase when increasing $N_{[1\bar{1}0]}$ while keeping $N_{[001]}$ constant, whereas ν_0 should decrease when increasing $N_{[001]}$ while keeping $N_{[1\bar{1}0]}$ constant.

In order to check this statement on a theoretical basis we performed MC simulations for islands of fixed $N_{[1\bar{1}0]}$ ($N_{[001]}$) while changing $N_{[001]}$ ($N_{[1\bar{1}0]}$), respectively. For

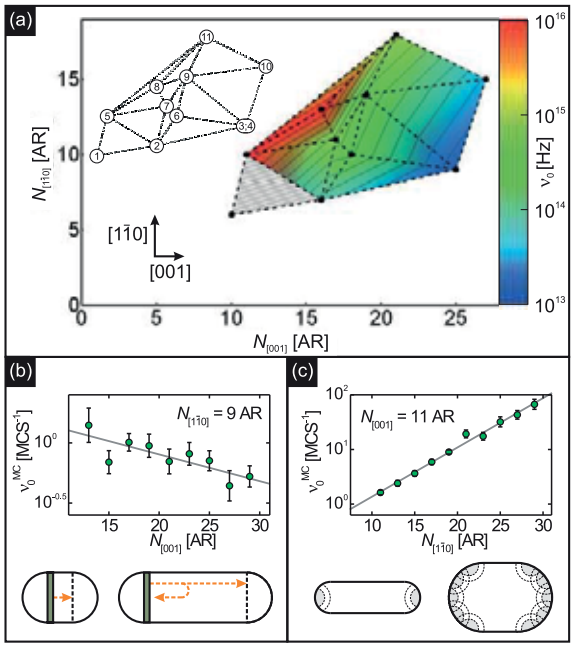

Figure 3.15: (**a**) Experimentally determined prefactor ν_0 as a function of island length $N_{[1\bar{1}0]}$ and $N_{[001]}$. See labeled mesh inset for island correlation. (**b**) Prefactor $\nu_0^{\mathrm{MC}}(N_{[001]})$ from Monte Carlo simulations for $N_{[1\bar{1}0]} = 9\,\mathrm{AR}$. A tendency of decreasing ν_0^{MC} with increasing $N_{[001]}$ is clearly visible. (**c**) Prefactor $\nu_0^{\mathrm{MC}}(N_{[1\bar{1}0]})$ from Monte Carlo simulations for $N_{[001]} = 11\,\mathrm{AR}$, revealing that ν_0^{MC} increases with increasing $N_{[1\bar{1}0]}$. Note that ν_0^{MC} is given in units of MCS^{-1}, whereas ν_0 is given in units of Hz. The lines within the graphs are guides for the eyes.

every island, the telegraphic signal of the magnetization $M(t)$ (t given by the Monte Carlo steps (MCS)) has been calculated for different temperatures T, resulting in numerous switching events. For every temperature, $M(t)$ has been analyzed in terms of switching frequency ν^{MC} (analog to the experimental data). An Arrhenius-like behavior is observed, and fitting the Néel-Brown model yields the activation energy barrier E_{b}^{MC} and the prefactor ν_0^{MC} of the respective simulated nanoisland. In Fig. 3.15(b), $\nu_0^{\mathrm{MC}}(N_{[001]})$ is shown for a fixed $N_{[1\bar{1}0]}$, revealing that ν_0^{MC} decreases with increasing $N_{[001]}$. In Fig. 3.15(c), $\nu_0^{\mathrm{MC}}(N_{[1\bar{1}0]})$ is shown for a fixed $N_{[001]}$. Here, ν_0^{MC} increases with increasing $N_{[1\bar{1}0]}$. Obviously, the simulations are in qualitative agreement with the experimental data.

The experimental as well as the simulation results can be understood in the framework of the following simple model. After the nucleation the domain wall can be described as a quasiparticle propagating through the nanoisland. Due to the absence of external forces (note that in our experiments no external magnetic field is applied), moving forward and backward is energetically degenerate. Following random walk theory for a particle moving along a line with absorbing ends [11], the mean distance

covered after n steps scales with $\sqrt{n}$. Thus, the probability of a domain wall successfully propagating from one end of the island to the other decreases with increasing $N_{[001]}$, as depicted in Fig. 3.15(b). For very elongated islands it is likely that the domain wall returns to its nucleation site and annihilates there, with no net magnetization reversal. This behavior is reflected by the decrease of ν_0 when increasing $N_{[001]}$ and keeping $N_{[1\bar{1}0]}$ constant. With increasing $N_{[1\bar{1}0]}$, the number of nucleation sites for magnetization reversal increases. Thus, every additional nucleation center increases the probability of magnetization reversal. Consequently, ν_0 increases when increasing $N_{[1\bar{1}0]}$ while keeping $N_{[001]}$ constant. Therefore, the prefactor ν_0 is determined by the probability of a domain wall to diffuse through the whole nanoisland and the number of nucleation sites.

In summary, we performed a combined experimental and theoretical study on the thermally induced magnetization reversal of atomic-scale monolayer iron nanoislands, thereby providing insight into the microscopic processes of magnetization reversal [12]. Even very small nanoobjects consisting of only a few atoms may switch their magnetization by nucleation and propagation. The Arrhenius prefactor is found to be strongly dependent on the morphology of each individual object: Tiny differences in size or shape can lead to a variation of the switching rate by orders of magnitude. Our studies help to systematically tailor future magnetic nanoobjects that hinder or favor magnetization reversal, which is important for the development of new types of data storage media or magnetic sensors at the nano-scale.

3.4.2 Heat assisted spin torque switching of quasistable nanomagnets across a vacuum gap

G. Herzog, S. Krause, and R. Wiesendanger

A spin-polarized current can transfer spin angular momentum to a ferromagnet and reverse the magnetization orientation by the exerted spin torque. The discovery of the spin transfer effect, first treated theoretically 1996 by Berger and Slonczewski [13, 14], lead to a variety of experiments [15–17] and technical applications like the development of spin-torque switched magnetic tunnel junctions for MRAM devices [18]. Utilizing a spin-polarized scanning tunneling microscope (SP-STM), it was recently demonstrated that it is possible to manipulate the thermally-activated magnetization of ferromagnetic nanostructures with high tunnel currents originating from an antiferromagnetic probe tip [19]. Three fundamental effects of the elevated spin-polarized current were thereby identified and quantified, i.e. spin torque, Joule heating and Oersted field contributions. However, there is still an open-ended question if it is possible to manipulate the static magnetization of nanostructures by SP-STM. In this paper, we show that spin-polarized tunnel current pulses across a vacuum gap can be utilized for magnetization reversal of individual thermally quasistable nanoislands. We demonstrate that

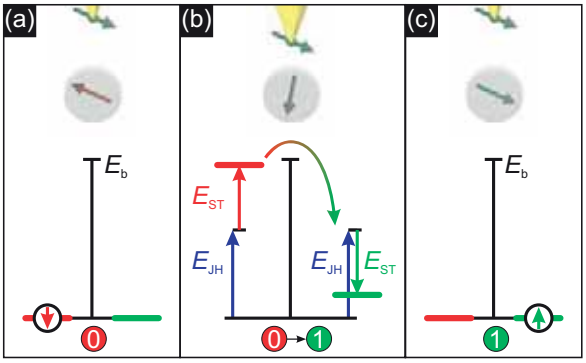

Figure 3.16: Basic principle of switching the magnetization of a nano-island by applying a short current pulse. Initial state (a): The nano-island's magnetization is in the state "0". The effective activation barrier E_b prevents the nano-island from switching. (b) Application of a high spin-polarized current pulse originating from a STM tip. Due to Joule heating and spin torque a magnetization reversal from state "0" to "1" is favored. (c) Final state. The magnetization has switched to state "1", and magnetization reversal is hindered again by E_b.

the switching results from the contributions of both Joule heating and spin torque, and determine critical currents necessary for reversal by sweeping the tunnel current.

Figure 3.16 illustrates the basic idea of current-induced magnetization switching: In the initial configuration the nano-island's magnetization is in one of its two stable magnetic states, here the state "0", reflected by the antiparallel alignment of tunnel current polarization and the magnetization of the nano-island. The state "1" is defined as parallel alignment, respectively. An effective activation energy barrier E_b has to be surmounted for reversal and is mainly related to the magnetic anisotropy of the nano-island which is typically on the order of 100 meV [12]. As a result of this energy barrier, thermal switching between these two states is hindered and both states exhibit long lifetimes. In order to reverse the magnetization to state "1", the SP-STM tip is shortly approached to the nano-island, as shown in Fig. 3.16(b), leading to a pulse of spin-polarized tunnel current. During the pulse Joule heating effectively lowers E_b for both states by E_{JH} and consequently decreases the lifetime of both states. Additionally, the spin torque lowers or elevates E_b by $\pm E_{ST}$, depending on the state. This results in a further lifetime decrease for state "0", but an increase in lifetime for state "1". If the pulse length is on the order of the modified lifetime, the nano-island's magnetization is likely to be reversed. By the asymmetry of the modified E_b it prevents the magnetization from switching back immediately into its initial configuration. Figure 3.16(c) shows the final configuration. After applying the pulse, the nano-island's magnetization is reversed. E_b again prevents the magnetization from reverting to its initial state. In order to switch the nano-island back into its initial state, the current polarity has to be reversed. This reverses the effect of the spin torque on E_b, therefore making it energetically favorable to revert the magnetization

to state "0" [14].

Our experiments were carried out in a multichamber system with base pressure below 1×10^{-8} Pa. The experiments have been performed using a home-built variable temperature STM. Both tip and sample were cooled by a continuous flow He cryostat which enables operation temperatures between $T = 20\,\mathrm{K}$ and $T = 300\,\mathrm{K}$. All measurements presented here were performed at $T = 31\,\mathrm{K}$. The nano-islands under investigation are Fe monolayer islands epitaxially grown on a W(110) substrate. These islands are known to exhibit an uniaxial magnetic anisotropy at low temperature with an in-plane easy axis along the $[1\bar{1}0]$ direction [20,21]. The W(110) surface was cleaned by subsequent cycles of oxygen annealing and flashing to $T \approx 2300\,\mathrm{K}$ [22]. Evaporating Fe onto the W(110) surface at room temperature leads to pseudomorphic growth of monolayer islands of various sizes and shapes [12]. A tungsten tip was flashed *in situ* to $T = 1500\,\mathrm{K}$, coated with chromium and annealed afterwards for 4 minutes at 550 K. This produces a magnetic tip with in-plane sensitivity [23].
A small AC modulation voltage ($U_{\mathrm{mod}} = 40\,\mathrm{mV}$) was added to the applied bias voltage U_{bias} in order to determine the differential conductance $\mathrm{d}I/\mathrm{d}U$ by lock-in technique. Positive bias voltages refer to electrons which tunnel from the tip to the sample (sample bias). All measurements were performed with the feedback loop closed, and the $\mathrm{d}I/\mathrm{d}U$ maps were acquired simultaneously during constant current imaging.

The utilized nano-island was thermally quasistable, which refers to an island with a long mean lifetime of $\tau \approx 30$ minutes. The tip was stabilized at a low tunnel current $I_{\mathrm{obs}} = 20\,\mathrm{nA}$ above the nano-island center to determine its initial state. A low (high) $\mathrm{d}I/\mathrm{d}U$ signal is related to state "0" ("1"). Figure 3.17(a) shows the $\mathrm{d}I/\mathrm{d}U$ signal as function of time t for two exemplary pulse applications at $t = 1\,\mathrm{s}$ and $t = 6\,\mathrm{s}$. At $t = 0\,\mathrm{s}$ the nano-island was in state "0". After the first pulse, the nano-island was switched to the state "1" and was reverted to state "0" after the second pulse. Every pulse was generated by setting the current feedback to $I_{\mathrm{pulse}} = 1.6\,\mu\mathrm{A}$ for a duration of τ_{pulse}. The pulse polarity was chosen depending on the respective state of the nano-island before the pulse was applied. For the nano-island in state "0" we applied a pulse at $U_{\mathrm{bias}} = +180\,\mathrm{mV}$ in order to switch the magnetization to the state "1". For the nano-island in state "1", a bias of $U_{\mathrm{bias}} = -180\,\mathrm{mV}$ was applied. The pulse polarity is illustrated by a green or red asterisk in Fig. 3.17(a). Since the lock-in parameters are optimized at the low current settings in order to differentiate between the two magnetic states, the signal is briefly saturated immediately after the applied pulse. Therefore, we cannot distinguish the state of the island for $\approx 0.5\,\mathrm{s}$ after pulse application. Figure 3.17(b) illustrates a series of five consecutive pulse applications with an interval of 5 s between the pulses, where each state is color coded (a green stripe refers to state "1", a red one to "0"). The signal was read out prior to each pulse.

Figure 3.17(c) shows the resultant evolution of the magnetization with varying pulse length τ_{pulse}. For every pulse length τ_{pulse} the bias-dependent probability p to switch the magnetization with one pulse has been defined as the number of successful switching events divided by the total number of applied pulses. This is further

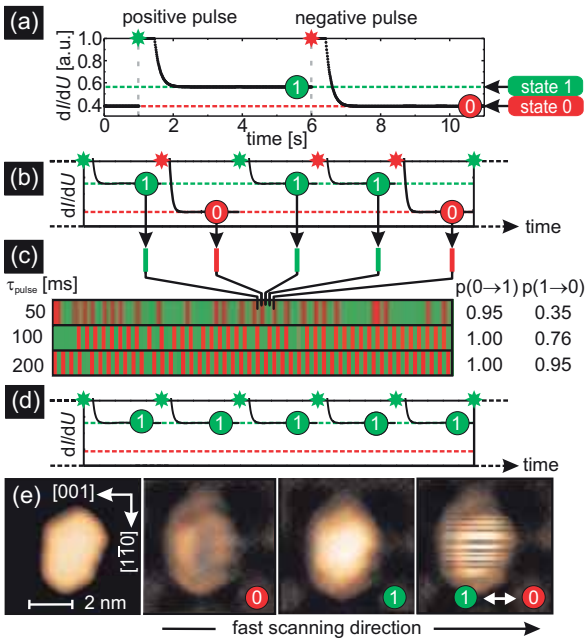

Figure 3.17: Current pulse experiments on a Fe ML nano-island on W(110). (a) The dI/dU signal as function of time t for two exemplary pulsing experiments with opposite pulse polarities (green and red asterisk for positive and negative pulse bias, respectively). After each pulse the dI/dU signal drops from saturation to state "1" or "0" level, indicating the nano-island's magnetization state after the respective pulse. (b) The dI/dU signal for five consecutive pulses. Right before each pulse the dI/dU signal is read out and the magnetic state is color coded. (c) Same color coding for experiments with different pulse lengths τ_{pulse} ($I_{\mathrm{pulse}} = 1.6\,\mu$A). Right hand side: Switching probabilities $p(0 \to 1)$ and $p(1 \to 0)$ to switch the magnetization with one pulse for the different pulse lengths τ_{pulse}. (d) Counter experiment for $\tau_{\mathrm{pulse}} = 200\,$ms at fixed bias $U_{\mathrm{pulse}} = +180\,$mV, revealing no switching event. (e) A topography image (left) of the nano-island under investigation ($I_{\mathrm{obs}} = 20\,$nA, $U_{\mathrm{bias}} = +180\,$mV). The three d$I$/d$U$ maps show the magnetic state of the nano-island: state "0", "1" and striped due to pulse application during scanning ($\tau_{\mathrm{pulse}} = 100\,$ms, $U_{\mathrm{pulse}} = \pm 180\,$mV).

illustrated in Fig. 3.17(c) where the probability to switch from the ith to jth state is referred to as $p(i \to j)$. The pulses were applied at even intervals. Therefore, uneven block widths indicate unsuccessful switching attempts. As can be seen in the figure, as the pulse width τ_{pulse} is increased, the probability to switch the island also increases. For pulse widths $\tau_{\mathrm{pulse}} = 200\,$ms, we observe that the island is reliably switched with $p \approx 1$ for both transitions. This indicates that the lifetime of the island is dramatically shortened by approximately five orders of magnitude which is an important consideration for future technological application.

In order to ascertain the roles of both Joule heating and spin torque, we applied pulses with the opposite polarity required to switch the island. Five positive pulses for the island initially in state "1" are shown in Fig. 3.17(d). None of the pulses we applied

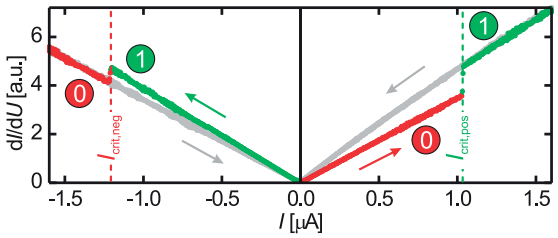

Figure 3.18: Switching the magnetization by increasing the tunnel current (sweeprate: 400 nA/s, $U = \pm 180\,\mathrm{mV}$). Ramping the current at positive bias (red arrow) forces the magnetization of the nano-island to switch from state "0" to state "1" when exceeding a critical current $I_{\mathrm{crit,pos}}$. When ramping the current at negative bias (green arrow) the magnetization of the nano-island switches back from state "1" to state "0" at $I_{\mathrm{crit,neg}}$. Decreasing the current from high values back to zero leads to no reversal (gray line).

($I_{\mathrm{pulse}} = 1.6\,\mu\mathrm{A}$, $\tau_{\mathrm{pulse}} = 200\,\mathrm{ms}$, 100 pulses for each configuration) led to a magnetization reversal. The effective Joule heating remains constant, since the total current is preserved. Consequently, the spin torque is the driving force for the magnetization reversal.

While the given pulses were applied to the island's center when the tip was stationary, it is also possible to switch the magnetization during conventional scanning. Figure 3.17(e) shows the topography image and three corresponding $\mathrm{d}I/\mathrm{d}U$ maps of the investigated nano-island: the foremost two $\mathrm{d}I/\mathrm{d}U$ maps show the island in its stable magnetic states "0" and "1", respectively. For the last $\mathrm{d}I/\mathrm{d}U$ map, the image was paused after every 20th scan, the tip was moved to the island center, and a pulse was applied. Again, the pulse polarity was chosen depending on the state of the island. The nano-island appears striped, indicating the scan line the pulses were initiated.

In order to determine the critical current necessary for magnetization reversal we applied triangular current sweeps to the nano-island. Figure 3.18 illustrates the $\mathrm{d}I/\mathrm{d}U$ signal as function of current I for one exemplary current sweep. Starting from low current ($I = +20\,\mathrm{nA}$), the island remains in its initial state "0" until a critical current $I_{\mathrm{crit,pos}}$ is reached and magnetization switching is triggered, as indicated by the jump in the $\mathrm{d}I/\mathrm{d}U(I)$ signal at $I_{\mathrm{crit,pos}}$. Ramping the current back from high to low values yields no switching event. Ramping from $I = -20\,\mathrm{nA}$ to $I = -1.6\,\mu\mathrm{A}$ leads to a magnetization reversal from "1" to "0" at $I_{\mathrm{crit,neg}}$. Repeating the sweep 25 times we determined the mean critical currents $\overline{I}_{\mathrm{crit}}$ for switching back and forth: $\overline{I}_{\mathrm{crit,pos}} = (1.0 \pm 0.1)\,\mu\mathrm{A}$ and $\overline{I}_{\mathrm{crit,neg}} = (-1.2 \pm 0.2)\,\mu\mathrm{A}$. These values correspond to local current densities of $j \approx 10^8\,\mathrm{A/cm^2}$ and are slightly higher than those utilized in nanopillar experiments [24], probably due to the inhomogeneous current density distribution on the nano-island in our experiments.

In summary, we demonstrated the capability to switch the magnetization of quasistable magnetic nanostructures by the injection of high spin-polarized currents [25]. The combination of Joule heating and spin torque enables the manipulation of magnetism on the local scale reliably and reversibly, making the usage of external nonlocal magnetic fields dispensable. We find that the chosen pulse length τ_{pulse} is of crucial

importance as demonstrated in experiments with nanopillar spin valves of larger dimensions. In addition we introduced the possibility to sweep the injected current to determine the critical currents necessary for magnetization reversal.

References

[1] M. L. Néel, Ann. Géophys. **5**, 99 (1949).

[2] W. F. Brown, Phys. Rev. **130**, 1677 (1963).

[3] A. Kubetzka, M. Bode, O. Pietzsch, and R. Wiesendanger, Phys. Rev. Lett. **88**, 057201 (2002).

[4] A. Wachowiak, J. Wiebe, M. Bode, O. Pietzsch, M. Morgenstern, and R. Wiesendanger, Science **298**, 577 (2002).

[5] M. Bode, S. Krause, L. Berbil-Bautista, S. Heinze, and R. Wiesendanger, Surf. Sci. **601**, 3308 (2007).

[6] M. Pratzer, H. J. Elmers, M. Bode, O. Pietzsch, A. Kubetzka, and R. Wiesendanger, Phys. Rev. Lett. **87**, 127201 (2001).

[7] M. Pratzer and H. J. Elmers, Phys. Rev. B **67**, 094416 (2003).

[8] E. Y. Vedmedenko, A. Kubetzka, K. von Bergmann, O. Pietzsch, M. Bode, J. Kirschner, H. P. Oepen, and R. Wiesendanger, Phys. Rev. Lett. **92**, 077207 (2004).

[9] R. B. Muniz, A. T. Costa, and D. L. Mills, J. Phys.: Condens. Matter **15**, S495 (2003).

[10] J. Vogel, J. Moritz, and O. Fruchart, C. R. Physique **7**, 977 (2006).

[11] G. Ehrlich, J. Chem. Phys. **44**, 1050 (1965).

[12] S. Krause, G. Herzog, T. Stapelfeldt, L. Berbil-Bautista, M. Bode, E. Y. Vedmedenko, and R. Wiesendanger, Phys. Rev. Lett. **103**, 127202 (2009).

[13] L. Berger, Phys. Rev. B **54**, 9353 (1996).

[14] J. C. Slonczewski, J. Magn. Magn. Mater. **159**, L1 (1996).

[15] I. N. Krivorotov, Science **307**, 228 (2005).

[16] E. B. Myers, D. C. Ralph, J. A. Katine, R. N. Louie, and R. A. Buhrman, Science **285**, 867 (1999).

[17] R. Koch, G. Grinstein, G. Keefe, Y. Lu, P. Trouilloud, W. Gallagher, and S. Parkin, Phys. Rev. Lett. **84**, 5419 (2000).

[18] J. Katine and E. E. Fullerton, J. Magn. Magn. Mater. **320**, 1217 (2008).

[19] S. Krause, L. Berbil-Bautista, G. Herzog, M. Bode, and R. Wiesendanger, Science **317**, 1537 (2007).

[20] U. Gradmann, G. Liu, H. J. Elmers, and M. Przybylski, Hyperf. Interact. **57**, 1845 (1990).

[21] H. J. Elmers, J. Hauschild, H. Höche, U. Gradmann, H. Bethge, D. Heuer, and U. Köhler, Phys. Rev. Lett. **73**, 898 (1994).

[22] M. Bode, S. Krause, L. Berbil-Bautista, S. Heinze, and R. Wiesendanger, Surface Science **601**, 3308 (2007).

[23] A. Kubetzka, M. Bode, O. Pietzsch, and R. Wiesendanger, Phys. Rev. Lett. **88**, 057201 (2002).

[24] G. D. Fuchs, N. C. Emley, I. N. Krivorotov, P. M. Braganca, E. M. Ryan, S. I. Kiselev, J. C. Sankey, D. C. Ralph, R. A. Buhrman, and J. A. Katine, Appl. Phys. Lett. **85**, 1205 (2004).

[25] G. Herzog, S. Krause, and R. Wiesendanger, Appl. Phys. Lett. **96**, 102505 (2010)

3.5 Atomic spins and dilute chains

This chapter describes investigations of the magnetism of individual 3d atoms adsorbed onto surfaces of different materials. In view of future applications in storage, information processing or even quantum computation technology, the fundamental magnetic properties to be characterized are (i) the magnetic moment of the atom, (ii) the magnetic anisotropy which stabilizes the atom's magnetization into certain directions and (iii) the character and lifetime of excitations of the atom's magnetization. These three properties crucially depend on the chemical composition, symmetry, and conduction electron density of the substrate and on the strength and character of hybridization of atomic states with the surface electronic states. In order to investigate these dependencies systematically, magnetic atoms on substantially different substrates have been investigated: (i) non-magnetic metallic surfaces; (ii) semiconducting surfaces and (iii) magnetic surfaces.

We have used different scanning tunneling spectroscopy based methods in order to study these fundamental magnetic properties. Firstly, by using STM tips coated with ferromagnetic thin films and performing spin-resolved scanning tunneling microscopy and spectroscopy (SP-STM/-STS) on antiferromagnetic samples in an external magnetic field, the tip can be aligned along certain directions while the sample magnetization remains unaffected. This can be used to image different projections of the sample magnetization. Secondly, using STM tips coated with anti-ferromagnetic thin films, measurement of the spin-resolved differential conductance on individual paramagnetic atoms as a function of an external magnetic field results in the so-called single-atom magnetization curve. Analysis of such curves reveals the direction of the magnetic anisotropy and the size of the magnetic moment of the atom. Thirdly, the differential conductance measured with a high energy resolution around the Fermi energy contains the excitations of the magnetic atoms in form of symmetric steps around zero voltage. This so called inelastic scanning tunneling spectroscopy (ISTS) mode is complementary to SP-STS and reveals the energy and lifetime of the magnetic excitations of the atom. Finally, in case of the semiconducting substrates which have spin-resolvable Landau levels, the substrate serves as a source for spin-polarized electrons and therefore, single-atom magnetization curves can be recorded with non-magnetic tips.

The newly developed scheme of SP-STS based single-atom magnetometry not only has a sensitivity of a single Bohr magneton (μ_B), which is by far exceeding the sensitivity of state-of-the-art nanoSQUID magnetometry. Moreover, due to the atomic spatial resolution of this technique, we were able to measure interactions between individual magnetic atoms, and down to on energy scale of only tens of micro-electronvolts using a sub-kelvin STM [1]. This allowed us to acquire atomically resolved maps of the substrate-electron mediated Ruderman-Kittel-Kasuya-Yosida (RKKY)-type exchange interaction between pairs of atoms adsorbed on metallic surfaces. Finally, it has been demonstrated, that the method of SP-STS can be combined with tip-induced lateral manipulation of the atom position. This allows us to construct artificial structures with atomic precision and then image their magnetic configuration. Thus, the first

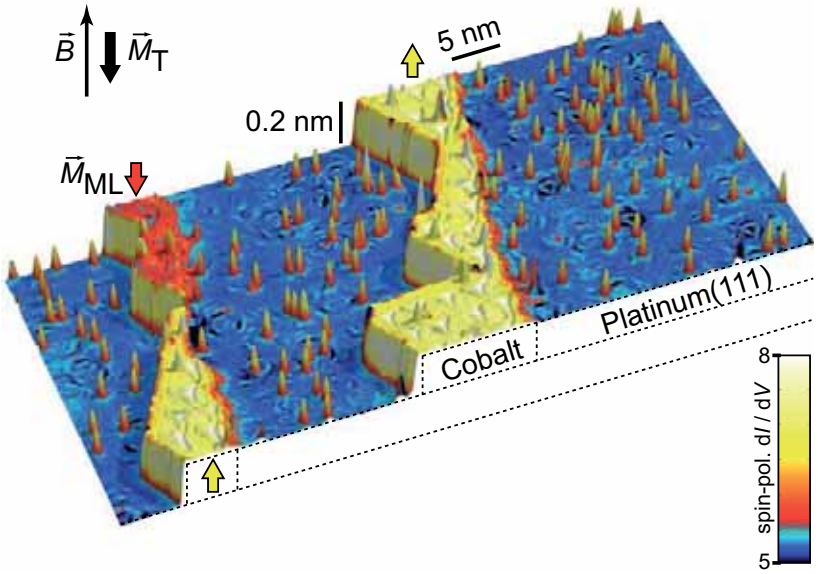

Figure 3.19: Overview of the sample of individual cobalt adatoms on the platinum(111) surface (blue) and cobalt monolayer (ML) stripes (red and yellow) attached to the step edges (STM topograph colorized with the simultaneously recorded spin-polarized $\mathrm{d}I/\mathrm{d}V$ map measured with a chromium coated STM tip magnetized antiparallel to the surface normal). An external magnetic field $\vec{B}$ can be applied perpendicular to the sample surface in order to change the magnetization of adatoms $\vec{M}_{\mathrm{A}}$, ML stripes $\vec{M}_{\mathrm{ML}}$, or tip $\vec{M}_T$. The ML appears red (yellow) when $\vec{M}_{\mathrm{ML}}$ is parallel (antiparallel) to $\vec{M}_T$. (Tunneling parameters: I = 0.8 nA, V = 0.3 V, V_{mod} = 20 mV, T = 0.3 K.)

step towards the exploitation of the knowledge about atomic-scale magnetism for the realization of magnetic nanostructures with interesting and useful properties has been made.

3.5.1 Spin-resolved scanning tunneling spectroscopy on individual atoms and dimers on nonmagnetic metallic substrates

F. Meier, L. Zhou, J. Wiebe, and R. Wiesendanger

We chose the sample system of cobalt atoms adsorbed on the (111) surface of platinum for our first attempt of the application of SP-STS to individual magnetic atoms on a non-magnetic metallic substrate [2,3]. For this purpose, the sample system has several advantages: (i) it has been extensively characterized by spatially averaging techniques, (ii) the magnetic moment of the Co atom is large ($m \approx 5\,\mu_{\mathrm{B}}$) and (iii) it

has a large uniaxial magnetic anisotropy of $K \approx 9\,\mathrm{meV}$ which forces the atomic spin of the Co to point perpendicular to the (111) surface (out-of plane) [4]. Figure 3.19 shows an overview of the sample. It has been prepared in two steps. First, Co was deposited at room temperature, resulting in step flow growth and thus stripes of monolayers (ML) of Co are attached to the step edges of the Pt(111) surface. The ML stripes exhibit a dislocation network induced by the coexistence of face-centered cubic (fcc) and hexagonal closed-packed (hcp) stacked areas [5]. Second, the sample was cooled to $T < 25\,\mathrm{K}$ and Co was again deposited resulting in a statistical distribution of Co atoms on Pt(111) as well as on the ML. The advantage of the additional deposition of Co ML stripes is twofold: First, it serves to measure the magnetic interaction between the stripes and the individual Co atoms. Second, the ML stripes can serve as calibration standard for the magnetic properties of the SP-STM tip since their magnetization $\vec{M}_{\mathrm{ML}}$ is perpendicular to the surface [5]. Using out-of-plane oriented (chromium coated) tips the up and down domains exhibit a different spin-resolved $\mathrm{d}I/\mathrm{d}V$ signal as visible in Fig. 3.19. Thereby, it is possible to characterize the spin polarization and magnetization $\vec{M}_T$ of the foremost tip atom acting as a detector for the magnetization of the atom on the surface $\vec{M}_{\mathrm{A}}$.

The statistical distribution of the Co atoms on this surface results in a variety of different adsorption sites. Firstly, we can find isolated Co atoms on Pt(111) which can sit either on the fcc or on the hcp lattice site. Secondly, Co atoms are adsorbed on the hcp or fcc areas of the Co ML. Thirdly, we also find close-packed Co dimers, as well as pairs, triplets or even larger ensembles with different inter-atomic distances. All these different geometries are investigated concerning their magnetic properties in the following Sections. In the remaining part of this section, we focus on the characterization of the Co atoms on the bare Pt(111) and on the ML as well as of the close-packed dimers using SP-STS.

To gain information about the local electronic density of states (LDOS) $\rho_S(E, \vec{R}_T)$ *above* the sample and the DOS of the tip $\rho_T(E_F)$, as well as their spin polarizations P_S and P_T defined as the difference between the majority and minority density of states normalized by the sum of them, *i.e.* $P = (\rho^{\uparrow} - \rho^{\downarrow})/(\rho^{\uparrow} + \rho^{\downarrow})$, the spin-resolved differential tunneling conductance $\mathrm{d}I/\mathrm{d}V$ was measured in the spectroscopic mode. For a small voltage range around the Fermi energy, it is approximately given by

$$dI/dV(x, y, V) \propto \rho_T(E_F) \cdot \rho_S(E_F + eV, \vec{R}_T) \cdot \Big(1 + P_T(E_F) \cdot P_S(E_F + eV, \vec{R}_T) \cos\theta\Big), \tag{3.21}$$

where $\vec{R}_T$ is the position of the foremost tip atom and θ is the angle between its magnetization $\vec{M}_T$ and that of the sample $< \vec{M}_S >$ [6]. Since the tip electrode material is Cr, which has a relative large coercivity, the external magnetic field $\vec{B}$ can be used to align the two electrodes parallel ($\uparrow\uparrow$) or antiparallel ($\uparrow\downarrow$) resulting in the spin-resolved differential tunneling conductance $\mathrm{d}I^{\uparrow\uparrow}/\mathrm{d}V(V)$ and $\mathrm{d}I^{\uparrow\downarrow}/\mathrm{d}V(V)$. Assuming a constant distance between the tip and sample for the two cases ($\uparrow\uparrow$, $\uparrow\downarrow$), the product of the two electrodes' spin-polarizations can be deduced from the magnetic asymmetry

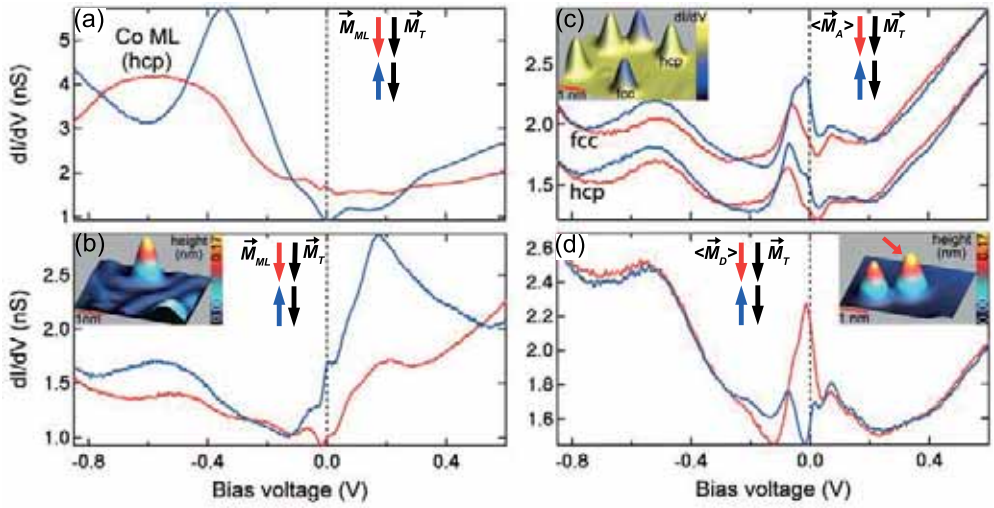

Figure 3.20: (a) Spin-resolved dI/dV curves acquired over an hcp area of a ML as illustrated in the inset of (b). (b) Spin-resolved dI/dV curves acquired over a single atom on an fcc region of a ML. Inset: Topograph of the area with the single atom sitting on the ML. The dislocation network on the ML surface is visible. (c) Spin-resolved dI/dV curves acquired over single atoms sitting on fcc and hcp lattice sites on a Pt terrace. (Curves from fcc atoms are vertically offset by 0.5 nS for clarity) Inset: Topograph colored with the simultaneously recorded dI/dV map at $I_{\mathrm{stab}} = 0.3\,\mathrm{nA}$ and $V_{\mathrm{stab}} = -0.1\,\mathrm{V}$ of an area with several fcc (purple) and hcp (gold) atoms (vertical scale from 0 to 0.17 nm). (d) Spin-resolved dI/dV curves acquired over the center of a dimer with both atoms sitting on nearest neighbouring fcc sites on a Pt terrace. Inset: Topograph of the area with a single atom and the compact dimer (arrow). Curves in (a)-(d) change with the relative orientation of sample and tip magnetizations as indicated. (Tunneling parameters: $I_{\mathrm{stab}} = 1.0\,\mathrm{nA}$, $V_{\mathrm{stab}} = 0.6\,\mathrm{V}$, $V_{\mathrm{mod}} = 10\,\mathrm{mV(rms)}$.)

$$A_{mag}(V) \equiv \left(dI^{\uparrow\uparrow}/dV - dI^{\uparrow\downarrow}/dV\right) / \left(dI^{\uparrow\uparrow}/dV + dI^{\uparrow\downarrow}/dV\right) = P_T(E_F)\cdot P_S(E_F+eV, \vec{R}_T). \tag{3.22}$$

Thus the sample's spin-polarization can be extracted only with the knowledge of the tip's spin-polarization. We can achieve this by measuring the voltage dependent A_{mag} on the Co MLs with well-known $P_S(E_F + eV, \vec{R}_T)$ [5] to calibrate P_T and then using exactly the same tip to characterize the Co adatoms with unknown $P_S(E_F + eV, \vec{R}_T)$.

Figure 3.20(a)-(d) show the dI/dV spectra using the same tip but measured on the Co ML (a), a Co atom on a Co ML (b), a Co atom on Pt(111) (c) and a Co dimer on Pt(111) (d) in (↑↑) and (↑↓) configurations. Figures 3.21(a)-(d) show A_{mag} calculated from Fig. 3.20(a)-(d), respectively. As shown in the topograph colored with the dI/dV map simultaneously recorded at -0.1 V (Fig. 3.20(c) inset), two types of atoms are found on Pt(111) with identical height but distinct spectroscopic signature. This spectroscopic signature is induced by the two possible binding sites, fcc and hcp, and can be traced back to a slight shift of a pronounced peak at -0.05 V in their LDOS

in the vacuum (Fig. 3.20(c)).

To calibrate P_T, we first characterized the Co ML with different relative orientation of sample and tip magnetizations (Fig. 3.20(a)). These spectra were recorded over the hcp area of the ML depicted in the inset of Fig. 3.20(b). As seen from Fig. 3.21(a), the tunneling junction has a large positive A_{mag} at E_F, i.e. $P_T(E_F) \cdot P_S^{ML}(E_F, \vec{R}_T) > 0$. The spin-resolved LDOS *above* Co ML on Pt(111) was recently studied using SP-STS and first-principles calculations showing that $P_S^{ML}(E_F, \vec{R}_T) < 0$ [5]. Therefore, it is immediately clear that our tip also has a negative spin polarization at E_F, i.e. $P_T(E_F) < 0$. This conclusion is consistent with the fact that Cr is negatively polarized around E_F. Note that A_{mag} changes the sign between E_F and -0.35 V, which indicates a reversal of the Cr-tip's spin-polarization around $-0.1\,\mathrm{V}$. By comparing A_{mag} of the Co atom on the ML (Fig. 3.21(b)) to that of the monolayer (Fig. 3.21(a)) we see that now the sign of the spin polarization around E_F is reversed and a dominance of majority electrons is found instead. Thus, one main finding of this Section is that even one atomic protrusion at the interface of a magnetic tunnel junction can reverse the sign of the spin polarization.

As seen in Fig. 3.20(c) and (d), the magnetization orientation of the atom and of the dimer on Pt(111) can be aligned parallel or antiparallel relative to the tip magnetization by changing the orientation of $\vec{B}$. As a consequence, the intensity of the measured $\mathrm{d}I/\mathrm{d}V$ signal changes in a large energy interval around the Fermi energy. This signal change is used to record the magnetization curves of single atoms on Pt(111) as described in the following. Furthermore, a detailed comparsion of the measured magnetic asymmetries of Co atoms and dimers on Pt(111) in Fig. 3.21(c,d) with that of the Co ML in Fig. 3.21(a) leads to the following conclusion. While near E_F the electronic states in the vacuum above Co atoms on Pt(111) are dominated by majority electrons (as in the case of Co atoms on Co ML), minority states are dominant above the Co dimer (as in the case of the closed Co ML). This result suggests that the dominance of majority electrons might be unique for atomic protrusions on otherwise atomically flat surfaces which could be an effect due to the reduced coordination and thereby enhanced symmetry.

3.5.2 Single-atom magnetization curve measurements

F. Meier, L. Zhou, J. Wiebe, and R. Wiesendanger

We developed a new SP-STS based technique to measure the local magnetization curve of a single atom adsorbed on a nonmagnetic substrate. As shown in Sec. 3.5.1, the differential conductance $\mathrm{d}I/\mathrm{d}V$ measured on top of such an atomic spin varies in intensity in a wide voltage range around E_F as a function of the saturation of the atom magnetization by an external magnetic field. If we take Eq. 3.21 and (i) postulate that $\mathrm{d}I/\mathrm{d}V$ is measured at a particular energy on the same atom at the same tip-sample

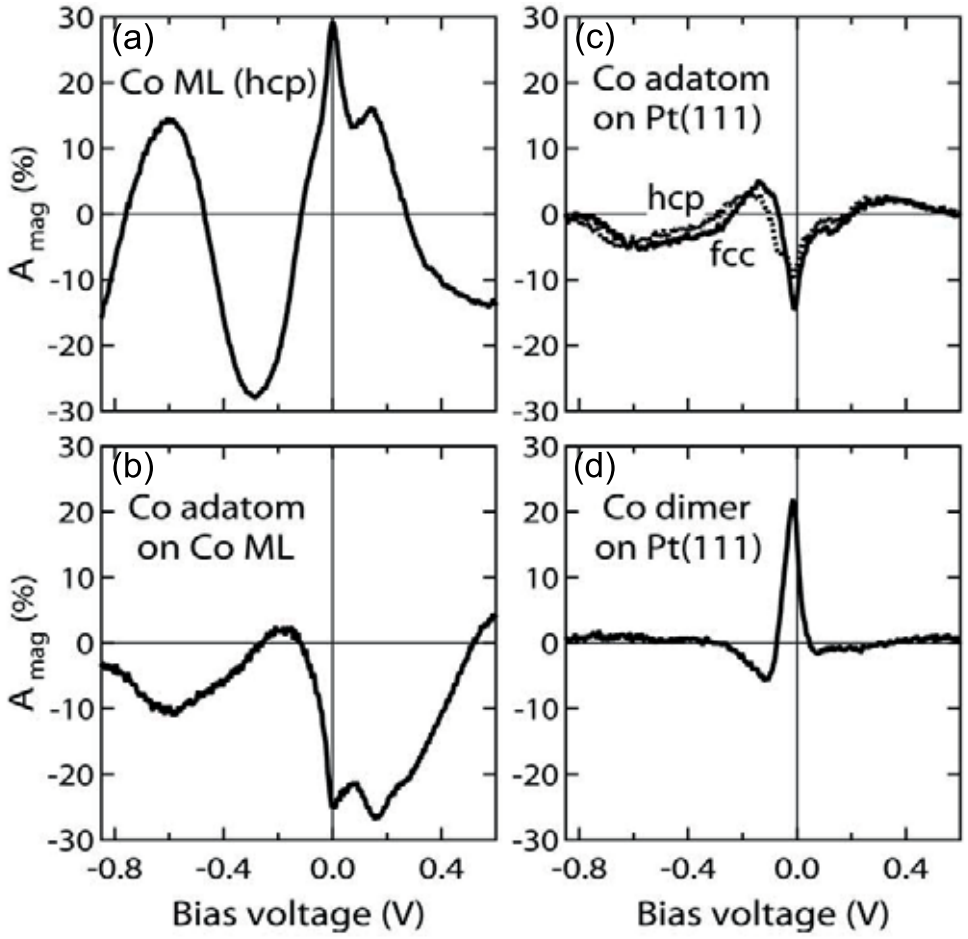

Figure 3.21: (a)-(d). Magnetic asymmetry A_{mag} calculated from the spin-resolved $\mathrm{d}I/\mathrm{d}V$ curves in Figs. 3.20(a)-(d), respectively. Note that the tip's spin-polarization is negative around E_F and has a sign reversal around $-0.1\,\mathrm{V}$.

distance, (ii) that the tip is not affected by the external magnetic field (which is fulfilled for most of our anti-ferromagnetically coated tips), and (iii) consider, that the time resolution of SP-STS is much worse than the time scale of the magnetization switching of the paramagnetic atom, then $P_T(E_F) \cdot P_S(E_F + eV, \vec{R}_T)cos\theta$ is proportional to the scalar product of the tip magnetization vector with the time average of the adatom magnetization vector:

$$dI/dV \propto (dI/dV)_0 + (dI/dV)_{SP}\vec{M}_{\mathrm{T}} \cdot \langle \vec{M}_{\mathrm{A}} \rangle \left(\vec{B}\right) , \tag{3.23}$$

In words, the measurement of $\mathrm{d}I/\mathrm{d}V$ as a function of the external magnetic field results in a measurement of the projection of the time-average of the atom magnetization onto the tip magnetization direction.

In practice, we record a series of $\mathrm{d}I/\mathrm{d}V$ maps using a chromium tip that is magnetized perpendicular to the surface as a function of an out-of-plane field $\vec{B}$ in a hysteresis loop measurement on an area with several adatoms as shown in Figs. 3.22(A,B). Then, the single-atom magnetization curves of each atom in this area are received by plotting the corresponding $\mathrm{d}I/\mathrm{d}V$ value averaged on top of each individual atom as a function of B. This is shown in Figs. 3.22(C,D) for several different atoms (on fcc and hcp stacking position) and at the two different temperatures $T = 4\,\mathrm{K}$ and $T = 0.3\,\mathrm{K}$. As a result we can conclude that the Co atom behaves paramagnetic and its magnetic energy and magnetization curve can be nicely fitted in the following continuum model [4]:

$$E\,(\theta, B) = -mBcos\theta - K(cos\theta)^2 \tag{3.24}$$

$$\langle M_{\mathrm{A}} \rangle \propto \frac{\int d\theta \sin\theta e^{\frac{-E(\theta,B)}{k_{\mathrm{B}}T}}}{\int d\theta e^{\frac{-E(\theta,B)}{k_{\mathrm{B}}T}}} \tag{3.25}$$

Here, m is the effective magnetic moment of the atom and K is its uniaxial magnetic anisotropy energy in the direction of $\vec{B}$. The fitted curves, shown in Figs. 3.22(C,D) on top of the measured curves, can be used to extract the effective m of each individual atom. As shown in the resulting histograms in the inset of Fig. 3.22(C), the average values are $m_{hcp} = (3.9 \pm 0.2)\mu_B$ and $m_{fcc} = (3.5 \pm 0.2)\mu_B$ for the hcp and the fcc adatoms, respectively, which is comparable to the values from XMCD measurements [4]. Most importantly, there is a strong scattering of m which is due to residual magnetic interaction from the background of statistically distributed atoms.

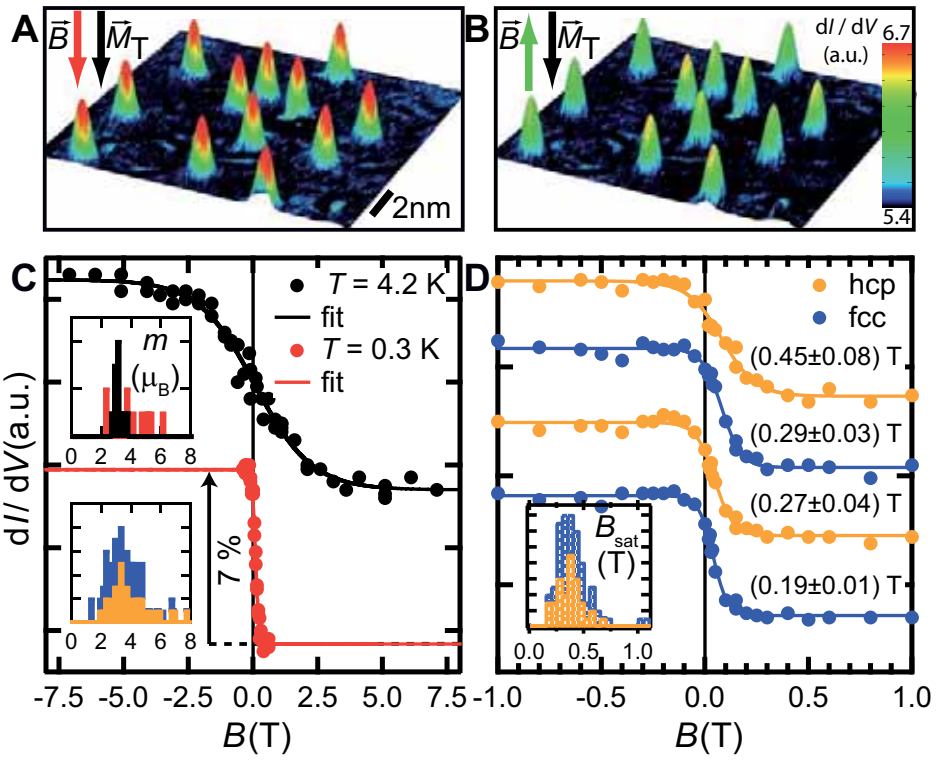

Figure 3.22: (**A**),(**B**) Topographs of an area with several Co adatoms on Pt(111) colorized with the spin-polarized dI/dV map at $\vec{B}$= -0.5 T parallel to the tip magnetization $\vec{M}_{\mathrm{T}}$ (A) and $\vec{B}$= +0.5 T antiparallel to $\vec{M}_{\mathrm{T}}$ (B). (**C**) Magnetization curves from an individual adatom taken at different temperatures as indicated (dots). The solid lines are fits to the data (see text). The insets show the resulting histograms of the fitted magnetic moments (in μ_B) for the same 11 adatoms at $T = 4.2$ K (black) and at 0.3 K (red) (upper histogram) and for 38 hcp (orange) and 46 fcc (blue) adatoms at 0.3 K (lower histogram, fcc bars stacked on hcp). (**D**) Magnetization curves of four adatoms at 0.3 K with fit curves and resulting $\vec{B}_{\mathrm{sat}}$ of 99% saturation. The inset shows the histogram of $\vec{B}_{\mathrm{sat}}$ (in Tesla) for the same adatoms used in the lower histogram in (C) (fcc bars stacked on hcp). (Curves in (C) and (D) are offset for clarity. Tunneling parameters: I = 0.8 nA, V = 0.3 V, V_{mod} = 20 mV.)

3.5.3 Measuring interactions using single atom magnetization curves

F. Meier, L. Zhou, E. Vedmedenko, S. Lounis, P. H. Dederichs, S. Blügel, J. Wiebe, and R. Wiesendanger

Single-atom magnetization curves not only can be used to reveal the magnetic anisotropy and moment of individual atoms, but also to study their magnetic interactions as will be shown in the following [7].

Interaction between atoms and ML stripes

Figures 3.23(A-C) illustrate magnetization curves that have been recorded on one of the cobalt ML stripes of the sample of Fig. 3.19 and on three Co atoms on Pt(111) with different separations from the stripe. The coercive field of the ML stripe is 0.5 T. The magnetization curves measured on the three atoms show hysteresis due to interaction with the ML. From the symmetry of the magnetization curves we can conclude, that the interaction oscillates between ferromagnetic and anti-ferromagnetic coupling. The corresponding exchange bias fields B_{ex} can be transformed into the absolute value of the interaction energy using $J = mB_{\mathrm{ex}}$, plotted in Fig. 3.23(D) as a function of distance d of the atom from the ML stripe. It shows an oscillatory damped behaviour which is reminiscent of the substrate-electron mediated Ruderman-Kittel-Kasuya-Yosida (RKKY) interaction. Therefore, we used isotropic models of the asymptotic RKKY interaction $J(d) = J_0 \cdot cos(2k_F d)/(2k_F d)^D$ with the Fermi wavevector k_F and different assumed dimensionalities D to fit the data as shown in Fig. 3.23(D). D is determined by the dimensionality of the electrons that induce the interaction, which is not known a priori, since it depends on the localization character of the underlying substrate-electron states that induce the interaction. The best fit is found for $D = 1$ which lead to the conclusion that the responsible substrate-electron states are strongly localized in the surface and have a Fermi wavelength of $\lambda_F = 2 - 3\,\mathrm{nm}$.

Interaction in pairs of atoms

Examples of isolated atom pairs with decreasing separations between 2 to 5 lattice constants are shown in Figs. 3.24(A) to (E). Their lattice sites given in Figs. 3.24(L) to (P) can be extracted without ambiguity and we focus on fcc atoms. Using Cr-coated probe tips sensitive to the out-of-plane magnetization we measure $\mathrm{d}I/\mathrm{d}V$ of both atoms in order to access their out-of-plane components of the time-averaged magnetization $\langle M_i^z \rangle$ $(i = 1, 2)$ in each pair as a function of the applied external magnetic field $\vec{B}$. The corresponding curves are shown in Figs. 3.24(F) to (K). Their shape can be interpreted in terms of the magnetic interactions between the Co atoms by a fit to a model using

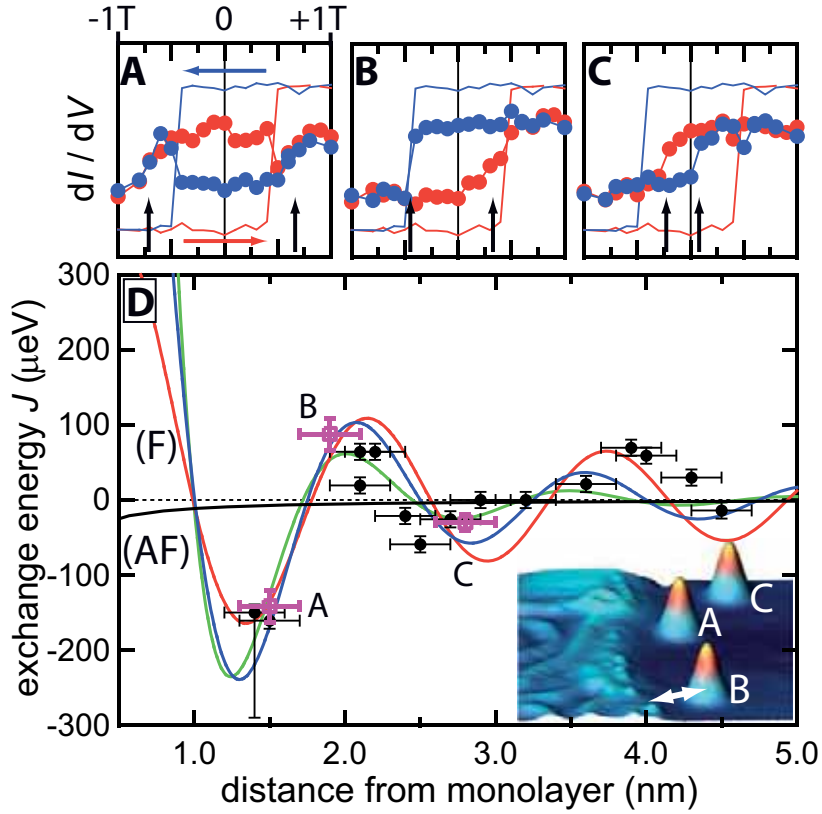

Figure 3.23: Magnetic exchange between Co atoms on Pt(111) and a ML stripe. (**A**),(**B**),(**C**) Magnetization curves measured on the ML (straight lines) and on the three atoms (dots) A, B and C visible in the inset topograph of (D). The blue (red) colour indicates the down (up) sweep from $\vec{B} = +1$ T to -1 T (-1 T to $+1$ T) ($\mathrm{d}I/\mathrm{d}V$ signal on ML inverted for clarity). The vertical arrows indicate the exchange bias field $\vec{B}_{\mathrm{ex}}$ which is converted into the exchange energy (using $m = 3.7\mu_B$) for the corresponding magenta points in the plot (D). (Tunneling parameters for magnetization curves: $I_{\mathrm{stab}} = 0.8\,\mathrm{nA}$, $V_{\mathrm{stab}} = 0.3\,\mathrm{V}$, $V_{\mathrm{mod}} = 20\,\mathrm{mV}$, $T = 0.3\,\mathrm{K}$.) (**D**) Dots: measured exchange energy as a function of distance as indicated by the arrow in the inset (about 50° to $[11\bar{2}]$). The black line is the dipolar interaction calculated from the stray field of a 10 nm wide stripe with saturation magnetization $1.3 \cdot 10^6$ A/m. The red, blue and green lines are fits to 1D, 2D and 3D range functions for indirect exchange (see text).

the following Hamiltonian

$$\begin{aligned}\mathcal{H} &= -\frac{1}{2}\sum_{i,j(i\neq j)} J_{ij}\left(\vec{r}_{ij}\right)\vec{S}_i\cdot\vec{S}_j - K\sum_i \left(S_i^z\right)^2 \\ &- \sum_i m_i\vec{S}_i\cdot\vec{B} \end{aligned} \tag{3.26}$$

where $i(j)$ numbers the atoms in the pair, $\vec{S}_i = \vec{M}_i/m_i$ are normalized magnetic moments, and m_i are their absolute values (in μ_B). The first sum describes the distance dependent exchange interactions. The second sum describes a uniaxial anisotropy favoring an out-of-plane (z) orientation of magnetization for positive K (per atom), and the third sum is the Zeeman energy. We apply two different models: (i) an Ising limit ($\vec{S}_i = \pm 1\cdot\vec{e}_z$) and (ii) a quasi-classical Heisenberg limit. The expectation values of the atom magnetizations $\langle M_i^z\rangle$ have been calculated exactly and in case (ii) additionally by Monte-Carlo simulations assuming a temperature of $T = 0.3$ K and an anisotropy of $K = 9.3$ meV. We vary m_1, m_2 and J_{12} to fit the measured magnetization curves. We find that the two different models are undistinguishable within the experimental error because of the large anisotropy which forces the magnetization to point out-of-plane. Therefore, the results from the most instructive Ising model are shown. The fitted curves and the corresponding m's and J's are given in Figs. 3.24(F) to (P) demonstrating an excellent reproduction of the measured data. Obviously, for antiferromagnetic interaction between two atoms with magnetic moments m_1 and m_2 ($m_1 \leq m_2$, w.l.o.g.) the coupling can be broken if the external magnetic field gets larger than $|B^z_{\text{crit}}| = -J_{12}/m_1$.

We performed fits for about 10 pairs with different distances d placed at different locations on the bare Pt(111) substrate. The resulting interaction energies $J(d)$ are shown in Fig. 3.25(A) together with the relative position of the two atoms on the lattice in panel (C). The J's from adatom triplets are also included (corresponding magnetization curves not shown here). Measurements of the local electronic density of states reveal that the atoms in pairs with a separation of larger than one lattice constant are sufficiently separated to exclude a strong overlapping of the electronic orbitals. Thus, there is no direct exchange interaction. Furthermore, dipolar interaction is at least three times smaller than the measurement temperature. Consequently, the extracted J's are dominated by RKKY interaction.

Note that the orientation of the pairs relative to the underlying Pt(111) lattice is changing, when the distance in the pairs is increased. Our measurements show, that the RKKY interaction is ferromagnetic for small distances, gets maximally antiferromagnetic for a distance of three lattice spacings in the $[1\bar{1}0]$ direction ($J \approx -250\mu$eV), and then shows a damped oscillation between ferromagnetic and antiferromagnetic coupling. However, there is no well defined wavelength. The data of the pairs along the closed packed direction ($[1\bar{1}0]$) may be fitted to a 2D isotropic and continuous RKKY model $J(d) \propto \cos(2k_F d)/(2k_F d)^2$ using a Fermi wavelength $\lambda_F = 2\pi/k_F = 2 \pm 0.5$nm (Fig. 3.25(A)) which is consistent to the wavelength from the interaction with the

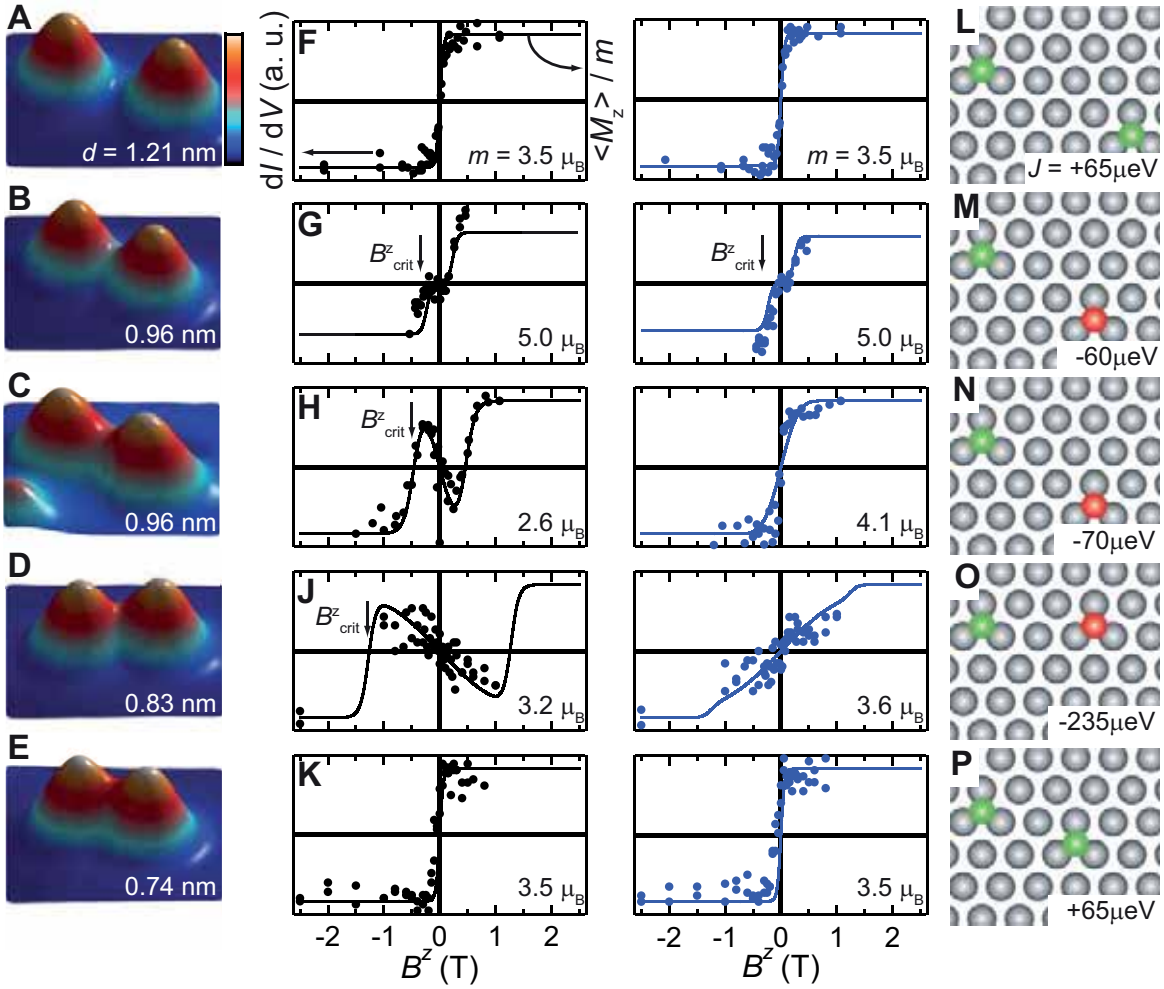

Figure 3.24: Magnetization curves of Co pairs on Pt(111). (**A** to **E**) Topographs (2.1 nm × 2.1 nm) of Co pairs with decreasing distance as indicated (vertical scale from 0 to 0.15 nm). (**F** to **K**) Single-atom magnetization curves measured on the left atom (black dots) and on the right atom (blue dots) of each pair. The curves are vertically normalized to the saturation magnetization and horizontally offset to compensate for the effective tip field $\vec{B}_{\mathrm{T}}$. The straight lines are calculated from the Ising model assuming magnetic moments m given in each curve. (**L** to **P**) Ball models of the atomic configuration in the pairs and J resulting from the Ising model fit. Same color indicates ferromagnetic coupling, different color indicates antiferromagnetic coupling. (Tunneling parameters: stabilization current I_{stab} = 0.8 nA, stabilization voltage V_{stab} = 0.3 V, modulation voltage V_{mod} = 20 mV (rms).)

ML stripes (see above). But, for slightly different orientations, the isotropic model fails, and a strongly different wavelength has to be assumed (cyan-colored, yellow and red data points). This proves a strong directionality of the RKKY interaction on the atomic scale. We propose, that an upward dispersing surface resonance crossing the Fermi energy at $\lambda_F \approx 1.6$ nm with an effective mass of about 1.5 m_e could be mediating the observed RKKY interaction [8].

To explore the directionality further, we calculated the interaction energy J of adatom pairs using density functional theory in connection with the KKR method. The calulated $J(d)$ (Fig. 3.25(B)) reveals the same direction dependency as the measured data with a maximum in the antiferromagnetic coupling for a distance of three lattice spacings in $[1\bar{1}0]$ direction. The values are a factor of about three times larger than the experimental ones. Given the small absolute values of J of only several tens of a microelectronvolt, the correspondence is remarkably good. Figure 3.25(D) shows a different view of the calculated J's in a 3D plot which highlights the strong anisotropy of the RKKY interaction at the surface when being compared to a similar plot of the 2D isotropic RKKY model in Fig. 3.25(E). The strongest variation of J with increasing interatomic distance is observed along $[1\bar{1}0]$ while it is weaker along $[11\bar{2}]$.

In conclusion, it has been shown that the magnetization of an atom adsorbed to a metallic surface can be stabilized by RKKY interaction to patches of ferromagnetic monolayers. Moreover, the same interaction interconnects and communicates the spin state between two atoms. From the knowledge of the atomic maps of these interactions it will be possible to design artificial nanostructures of a larger number of atoms with interesting functionalities, which can be built via STM-tip induced atom manipulation.

3.5.4 Induced spin-polarization in Pt(111) in the proximity to magnetic layers

F. Meier, S. Lounis, J. Wiebe, L. Zhou, S. Heers, P. Mavropoulos, P. H. Dederichs, S. Blügel, and R. Wiesendanger

In order to further study the origin of the RKKY interaction described in the previous section, we measured maps of the magnetic asymmetry A_{spin} above the Pt(111) surface in the vicinity of a Co ML stripe by SP-STS [9]. Such maps have been calculated as the difference image from two $\mathrm{d}I/\mathrm{d}V$ maps recorded for parallel and antiparallel alignment of tip and ML magnetization according to Eq. 3.22. The result is shown in Fig. 3.26 (a). The Co stripe shows a strong negative A_{spin} while on the Pt terrace far from the stripe A_{spin} is zero. Above the Pt close to the Co stripe an area with positive A_{spin} is visible which fades out for an increasing distance from the nanostripe. The decay is further analyzed in Fig. 3.26 (b) which shows A_{spin} values below the section line in Fig. 3.26 (a) as a function of the distance d from the Co nanostripe. In order to quantify the decay behavior the graph has been fitted to a

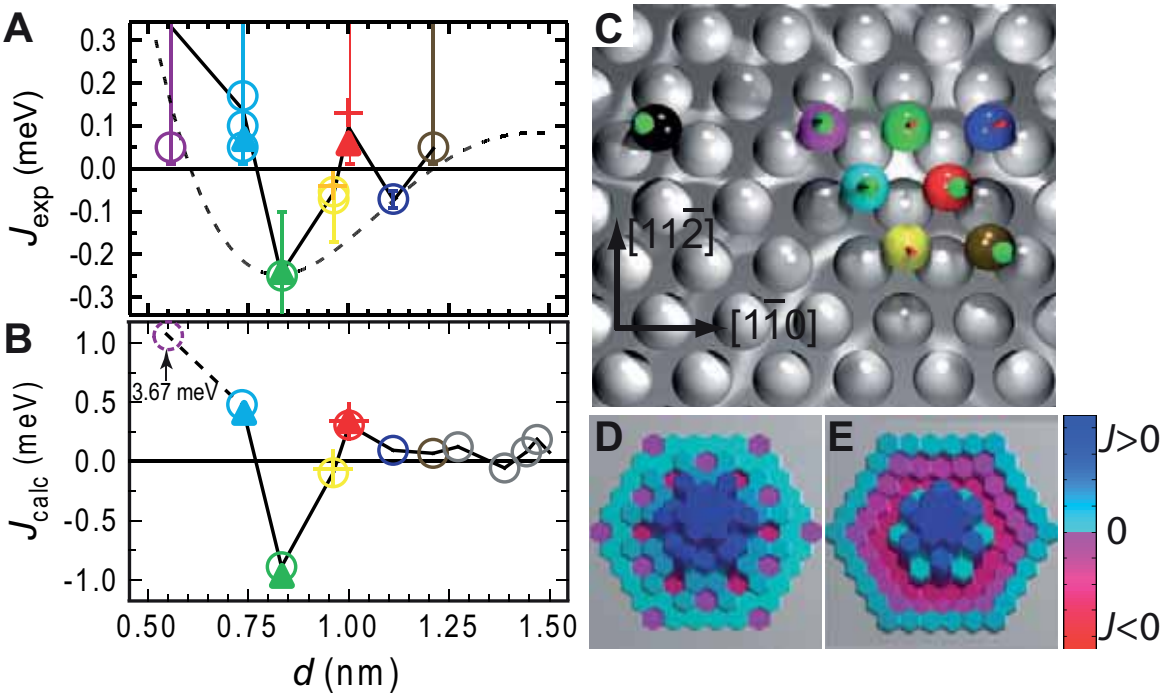

Figure 3.25: Distance dependency and directionality of RKKY interaction of Co pairs on Pt(111). (**A**), (**B**) Measured J_{exp} and calculated J_{calc} in Co pairs (circles) and triplets (triangles: triangular triplet, crosses: straight triplet) as a function of distance d. The data points are colored corresponding to the lattice positions of the adatoms in the pairs shown in (**C**) (first atom: black ball with spin up; second atom: colored ball with spin direction as indicated by the arrow). Values in (A) are extracted from the magnetization curves by fitting to the Ising model. The error bars are calculated from the uncertainty in the magnetic moments. The dotted line is a fit to the data of the pairs oriented along [1$\bar{1}$0] using a 2D isotropic and continuous RKKY model. (**D**) Plot of the calculated J's of (B) as a function of position in the (111) plane. Each hexagon corresponds to the lattice site of the second atom in a specific pair with the first atom fixed in the center. The height and color of each hexagon corresponds to the size of J. (**E**) Same as (D), but with J's from the 2D isotropic RKKY model evaluated on the discrete lattice.

simple exponential function resulting in decay lenths in the range from $\lambda = 0.9$ nm to $\lambda = 1.2$ nm. This corresponds to more than three next nearest neighbor distances within the Pt lattice. We observe the same quantitative behavior in A_{spin} calculated from $\mathrm{d}I/\mathrm{d}V$ maps recorded at $V_{stab} = -0.1\,\mathrm{V}$ (cp. inset Fig. 3.26(b)). We conclude that the observed spin-polarization above Pt is present in a large energy window around the Fermi energy.

Figure 3.26 (b) also includes the experimentally obtained indirect exchange energies, J, between the Co ML stripe and single Co atoms. The damped oscillatory exchange interaction which can be described by a one-dimensional isotropic RKKY model to a good approximation is present in the same range where the exponentially decaying Pt vacuum spin-polarization is measured. These observations raise the question, how exactly the measured Pt spin-polarization is linked to the induced magnetization within the Pt surface.

In order to answer this question we performed calculations of the induced magnetization M_{Pt} within the Pt(111) as well as of the vacuum spin-polarization, which can be directly compared to the measured magnetic asymmetry, using the KKR method within the framework of Density Functional Theory. These calculations led to the following conclusions. We find that M_{Pt} is oscillating between parallel and antiparallel alignment relative to the magnetic moment of the Co ML stripe consistent with the measured oscillating exchange interaction between the atom and the ML stripe shown in Fig. 3.26(b). The sign as well as the strength of M_{Pt} is additionally highly influenced by the strong anisotropy of the Fermi surface of Pt. The apparent contradiction of the measured monotonously decaying A_{spin} in the vacuum and the calculated oscillating M_{Pt} can be explained by local changes of the electronic structure of the Pt atoms close to the embedded ML stripe. It is evident also that the hybridization between the Pt and the Co states changes with increasing the distance from the chain. Therefore, also the spin-averaged LDOS changes laterally. According to [6] the measured spin-resolved $\mathrm{d}I/\mathrm{d}V$ signal and the deduced magnetic asymmetry is a measure of the energy dependent spin-polarization of the sample. *This quantity is only a measure for the magnetization, which is an integrated quantity of majority and minority states up to the Fermi energy, if the spin-averaged LDOS is constant.* Therefore the induced magnetization of the Pt cannot be deduced from the experimentally detected vacuum spin-polarization in the Pt only.

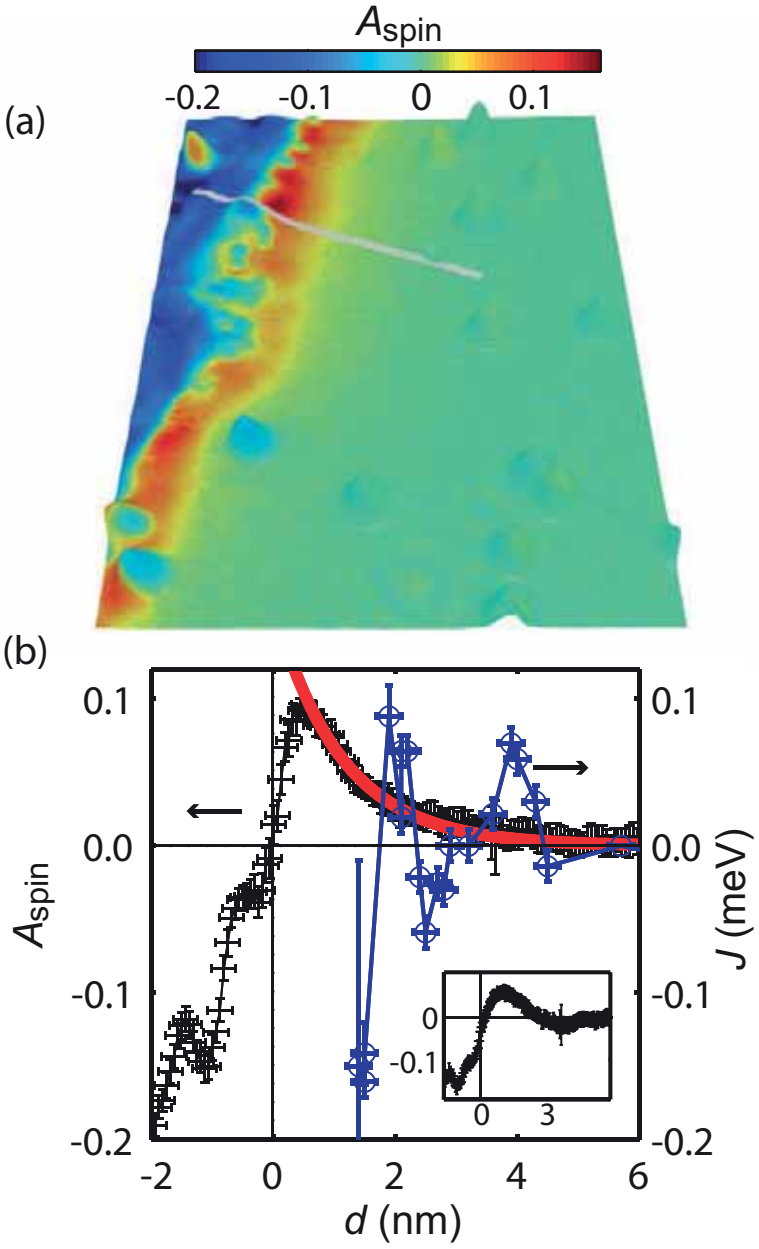

Figure 3.26: (a) STM topograph in 3D view colorized with the measured asymmetry map of Pt(111) in the vicinity to the Co ML, obtained from local magnetization curves ($V_{\mathrm{stab}} = 0.3\,\mathrm{V}$). (b) Crosses: asymmetry values below line section indicated in (a). Open circles: magnetic exchange energy J for the coupling between Co ML stripe and individual Co atoms taken from Sec. 3.5.3. '0' indicates the border between Co ML stripe and Pt layer. The red line shows an exponential fit to $f = Ce^{-x/\lambda}$ with $\lambda = 1.05 \pm 0.15\,\mathrm{nm}$. Inset: asymmetry values as in (a) for $V_{\mathrm{stab}} = -0.1\,\mathrm{V}$.

References

[1] J. Wiebe, A. Wachowiak, F. Meier, D. Haude, T. Foster, M. Morgenstern, and R. Wiesendanger, Rev. Sci. Instrum. **75** 4871 (2004).

[2] F. Meier, L. Zhou, J. Wiebe, and R. Wiesendanger, Science **320**, 82 (2008).

[3] F. Meier, L. Zhou, J. Wiebe, and R. Wiesendanger, Phys. Rev. B **82**, 012409 (2010).

[4] P. Gambardella, S. Rusponi, M. Veronese, S. S. Dhesi, C. Grazioli, A. Dallmeyer, I. Cabria, R. Zeller, P. H. Dederichs, K. Kern, C. Carbone, and H. Brune, Science **300**, 1130 (2003).

[5] F. Meier, K. von Bergmann, P. Ferriani, J. Wiebe, M. Bode, K. Hashimoto, S. Heinze, and R. Wiesendanger, Phys. Rev. B **74**, 195411 (2006).

[6] D. Wortmann, S. Heinze, Ph. Kurz, G. Bihlmayer, and S. Blügel, Phys. Rev. Lett. **86**, 4132 (2001).

[7] F. Meier, L. Zhou, E. Vedmedenko, S. Lounis, P. H. Dederichs, S. Blügel, J. Wiebe, and R. Wiesendanger, Nature Physics **6**, 187 (2010).

[8] J. Wiebe, F. Meier, K. Hashimoto, G. Bihlmayer, S. Blügel, P. Ferriani, S. Heinze, and R. Wiesendanger , Phys. Rev. B **72**, 193406 (2005).

[9] F. Meier, S. Lounis, J. Wiebe, L. Zhou, S. Heers, P. Mavropoulos, P. H. Dederichs, S. Blügel, and R. Wiesendanger, Phys. Rev. B, accepted (2010).

3.5.5 Imaging and manipulating the spin direction of Co atoms on Mn/W(110)

D. Serrate, P. Ferriani, Y. Yoshida, S.-W. Hla, M. Menzel, K. von Bergmann, S. Heinze, A. Kubetzka, and R. Wiesendanger

Single magnetic atoms on surfaces are the smallest conceivable units for two-dimensional magnetic data storage. An ideal tool to investigate and build atomic-scale structures is the scanning tunnelling microscope (STM). Previous experiments have investigated magnetization curves [1, 2], the many-body Kondo effect, and magnetic excitations in quantum spin systems [3,4], but a stable magnetization has not yet been detected for an atom on a non-magnetic surface in the absence of a magnetic field. The spin direction of a single magnetic atom can be fixed by coupling it to an underlying magnetic substrate via the exchange interaction [5,6], but then it is difficult to differentiate between the magnetism of the atom and the surface. Here we exploit the orbital symmetry of the spin-polarized density of states of single cobalt atoms to unambiguously determine their spin direction in real space using a combination of spin-resolved scanning tunnelling microscopy experiments and *ab initio* calculations. By laterally moving atoms on our non-collinear magnetic template [7] the spin direction can also be controlled while maintaining magnetic sensitivity, thereby providing an approach for constructing and characterising artificial atomic-scale magnetic structures. While both spin-resolution down to the atomic scale with magnetic tips [8] and atom manipulation with normal metallic tips [9] have been demonstrated separately and are well-established techniques, the combination of these two intriguing methods is still an experimental challenge. We have chosen the well-characterized atomic layer of Mn on W(110), which exhibits a spin spiral ground state [7], as our magnetic template for single Co atom adsorption. This template serves both as a reference to monitor the tip's magnetization in our spin-polarized scanning tunnelling microscopy (SP-STM) measurements, as well as a magnetic backbone to fix the spin of the adatoms by direct magnetic exchange interaction [10].

Figure 3.27 presents SP-STM constant-current images of single Co atoms adsorbed on Mn/W(110) obtained with an out-of-plane sensitive tip (see Methods). As sketched at the bottom of Fig. 3.27b the Mn layer exhibits a robust cycloidal spin spiral induced by the Dzyaloshinskii-Moriya interaction, propagating along the [1–10] direction with an angle of $\approx 173^\circ$ between magnetic moments of adjacent atomic rows. This spin spiral gives rise to periodic stripes on the Mn layer along the [001] direction (Fig.3.27a,b) reflecting the almost antiferromagnetic order on the atomic scale. This apparent height contrast vanishes approximately every 6 nm along the [1–10] direction where the local Mn moments lie in the plane. Thus, the Mn layer not only has nearly opposite magnetic moments between neighbouring sites but also their orientation varies gradually as one laterally moves across the surface.

The adsorbed Co atoms reside in hollow sites (cf. Fig.3.28a) and display varying heights and shapes that strongly depend on their lateral position with respect to the underlying spin spiral (Fig. 3.27a,b). Three distinct cases are marked by boxes in Fig. 3.27a: The Co atoms appear higher when they are located on bright Mn atom rows (top) and lower on dark Mn rows (bottom). At sites where the spin spiral contrast vanishes (Mn moments are in plane) the Co atoms have an intermediate height (right). In addition to these height variations, the shape of the atoms appears different on bright and dark Mn rows. Fig. 3.27c shows a magnified view of two Co atoms on positions where the Mn magnetic moments underneath point exactly upwards and downwards. Depending on the two possible orientations, the Co atom appears either rotationally symmetric with its maximum height at its centre (left) or elongated with two lobes along the [1–10] direction and a central minimum (right). Since in equivalent images acquired with a non-magnetic W tip all Co atoms appear identical these variations in height and shape can only be of magnetic origin.

To explain such a dramatic change in appearance, we have performed density functional theory calculations [11,12] for this system in a geometry as depicted in Fig. 3.28a. The calculations do not include the small deviation of $\approx 7^\circ$ from the collinear antiferromagnetic state since our focus here is on the local electronic structure of the Co atoms. The calculated results reveal that the Co atom gains an energy of 145 meV by coupling ferromagnetically to the nearest Mn atoms (along the [001] direction) as compared to the antiferromagnetic case. In the limit of low bias voltage, only states close to the Fermi energy E_F contribute to the tunnel current. The tip's spin-polarization $P_\mathrm{T} = (n_\mathrm{T}^\uparrow - n_\mathrm{T}^\downarrow)/(n_\mathrm{T}^\uparrow + n_\mathrm{T}^\downarrow)$, and the angle θ between tip and local sample magnetization at position $\mathbf{r}$ determine whether the majority ($n^\uparrow$) or the minority states ($n^\downarrow$) of the sample (S) at E_F dominate the tunnel current $I(\mathbf{r})$, according to the following expression derived from the spin-polarized Tersoff-Hamann model [13]:

$$I(\mathbf{r}) \propto (1 + P_\mathrm{T} \cos\theta(\mathbf{r}))\, n_\mathrm{S}^\uparrow(\mathbf{r}) + (1 - P_\mathrm{T} \cos\theta(\mathbf{r}))\, n_\mathrm{S}^\downarrow(\mathbf{r}). \tag{3.27}$$

The calculated local density of states (LDOS) for the Co atom in the vicinity of E_F displays a nearly circular shape for the majority channel, whereas the minority channel shows two lobes along the [1–10] direction with a minimum above the atom (Fig. 3.28b,c top and cross-sectional view), in excellent agreement with the SP-STM images in Fig. 3.27c. The different symmetries can be explained as follows: In the majority channel, the Co atom possesses a state composed of s, p_z, and d_{z^2} orbitals, all of them rotationally symmetric normal to the surface with a maximum above the Co atom. For the minority channel, the LDOS is mainly given by a d_{xz} state which exhibits a node at the Co atom centre and an overall reduced electron density. In an SP-STM experiment with $\theta = 0^\mathrm{o}$ the majority channel ($n_\mathrm{S}^\uparrow$) contributes predominantly to the tunnel current, while at $\theta = 180^\mathrm{o}$ the contribution of $n_\mathrm{S}^\uparrow$ is sufficiently suppressed and the d_{xz} character of $n_\mathrm{S}^\downarrow$ becomes visible. For a spin-averaging W tip ($P_T = 0$) $n_\mathrm{S}^\uparrow$ dominates the vacuum LDOS and the d_{xz} orbital remains hidden.

As a function of lateral position the spin of the Co atoms can be set to any direction

which is available on the Mn spin spiral, which can be viewed as a process of writing information. Fig. 3.29 shows equally spaced Co atoms, which were positioned using an Fe coated W tip. The spin-polarization of the tip is preserved throughout the atom manipulation process, and thus the magnetic superstructure of the spin spiral could be used as a grid to precisely position the atoms. Figures 3.29a and b show the change in topographic appearance of the atoms in the chain when the tip magnetization is reversed (see Methods). As illustrated in Fig. 3.29c, the Co atoms are separated by six atomic rows in the [1–10] direction and four rows in the [001] direction which results in a nominal angle of $\approx 42^\circ$ between adjacent Co moments, derived from the measured period of the spin spiral. The Co atoms in the chain display a gradual transition from a majority dominated appearance (rotational symmetry) to a minority dominated one (d_{xz} symmetry) via asymmetric states (Fig. 3.29a,b). Each angle θ of the Co moments with respect to the tip magnetization corresponds to a specific height and shape in the SP-STM measurement. Line profiles across the atomic centres along the [1–10] direction are displayed in Fig. 3.29d, positioned as a function of the angle θ. Though the height at the atomic centres (crosses) roughly follows a cosine (dot-dashed line), better agreement can be achieved with a higher order correction, mixing 36% of a $\cos^2\,\theta$ (solid line). Reasons might be the effect of spin-orbit coupling [14] onto the charge distribution or the constant current measuring mode, since the $\cos\,\theta$ in equation (3.27) is exact only at constant height.

The asymmetric shapes of Co atoms, which are observed in SP-STM images when their magnetic moments are non-collinear to the tip magnetization ($\theta \neq 0^o$, 180^o), cannot be explained based on electronic states with a single quantization axis. If both states, $n_S^{\uparrow}$ and $n_S^{\downarrow}$, are mirror symmetric (cf. Fig. 3.28), this symmetry is preserved by Eq. (3.27) for any angle θ, in contrast to the experiment. The missing ingredient is the non-collinear magnetization of the Mn template underneath the Co atom which is a vector field rotating $\approx 173^\circ$ between adjacent atomic rows [7]. Since the local magnetization density above the Co atom, which extends roughly over three Mn rows, must connect smoothly to the one above the Mn/W(110) surface, it is also non-collinear, i.e. $\theta(\mathbf{r})$ changes significantly within the extent of the Co states. Therefore, for a spin-polarized tip the two sides of the Co states are not equivalent and atoms with angles $+\theta$ and $-\theta$, can be distinguished. This means that while the height of the atoms allows a determination of the absolute value $|\theta|$, the degree of asymmetry provides information about the angle θ itself.

This work demonstrates not only direct access to the spin direction via differently shaped spin-polarized orbitals but also the feasibility of performing atom manipulation with a spin-sensitive tip, thereby opening a novel route of research investigating bottom-up structures at an atomic level with spin sensitivity.

Methods

The experiments were conducted with a home-built STM at $T = 10$ K in ultrahigh vacuum [15]. The Co atoms were deposited *in situ* onto the magnetic template at $T <$ 20 K to prevent diffusion. Magnetic tips were prepared by deposition of 30-40 atomic

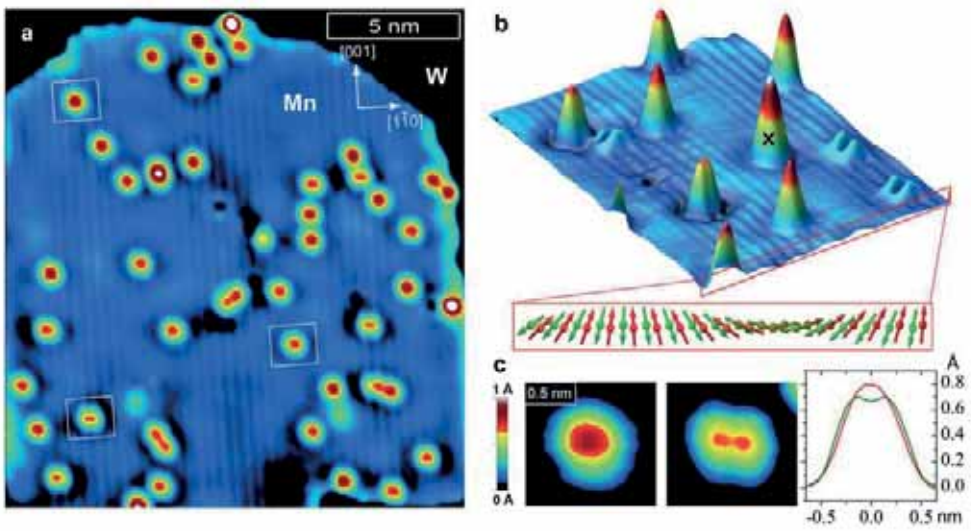

Figure 3.27: SP-STM measurements of single Co atoms on one atomic layer of Mn on W(110) with a tip sensitive to the out-of-plane magnetization. (a) Constant-current image (U = –50 mV, I = 2 nA). Periodic stripes along [001] indicate magnetic contrast of adjacent atomic rows. Height and shape of the Co atoms depend critically on their position on the Mn spin spiral. (b) Perspective view of a different sample area (U = –10 mV, I = 2 nA) and sketch of the Mn spin spiral (side view). A Co dimer has been indicated by a black cross. (c) Two particular cases (Co magnetic moment up and down) and the respective line profiles taken along the [1–10] direction.

layers of iron onto a W tip [8]. The spin-resolved measurements presented here were performed in magnetic fields of $|B| \geq 2$ T applied perpendicular to the sample surface, which aligns the tip magnetization resulting in magnetic out-of-plane sensitivity (Fig. 3.27: B = +2 T, Fig. 3.29a: +2.5 T; Fig. 3.29b: –2.5 T). The magnetic state of the Mn layer is unaffected by these low fields, because its spatially averaged magnetization is zero. Atom manipulation was performed by approaching the STM tip towards the atom and then moving the tip laterally at constant current (pulling mode) [9]. We found that the Co atoms can be moved reliably along ⟨111⟩ in-plane directions, i.e. parallel to the close-packed Mn rows, using tunnelling parameters of U = 2 mV and I = 50 nA [16].

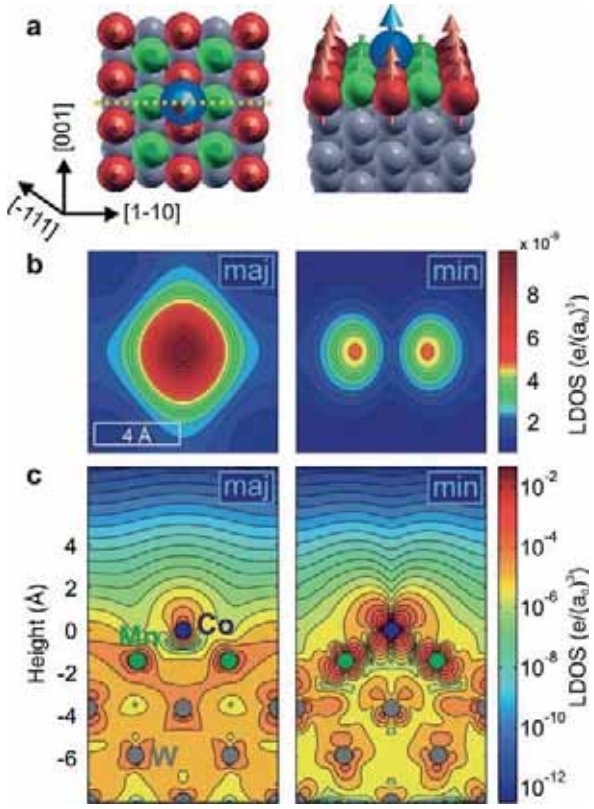

Figure 3.28: Calculated spin-resolved local density of states of a Co atom on Mn/W(110). (a) Top and perspective view of the unit cell used in the calculations. Red and green spheres represent Mn atoms with magnetization parallel and antiparallel to the Co atom (blue), respectively. (b) LDOS in the energy interval between E_F and E_F + 10 meV for majority (maj) and minority (min) electrons in a plane parallel to the surface 5.2 Å above the Co atom (a_0 is the Bohr radius). (c) Same as (b) for a cross section perpendicular to the surface along the dashed line in (a). The positions of Co, Mn, and W atoms are marked for clarity.

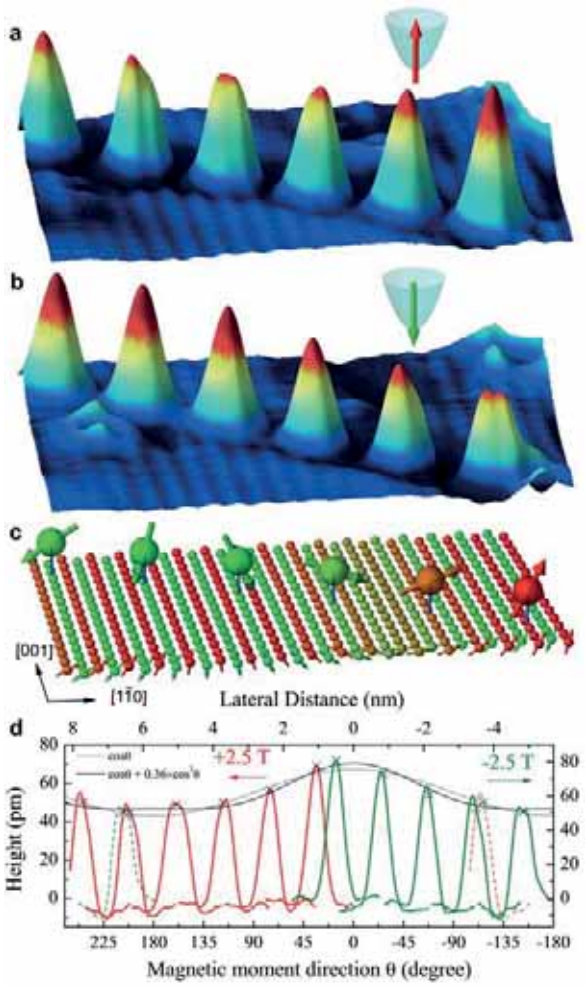

Figure 3.29: Chain of Co atoms constructed by atom manipulation while maintaining spin resolution measured with up and down magnetized tip. (a,b) Perspective views of SP-STM images (U = –10 mV, I = 2 nA) taken with (a) upwards and (b) downwards pointing tip magnetization (see insets), thereby reversing the spin sensitivity. Raw data has been smoothed with a Gaussian to reduce noise. (c) The atoms within the chain are equally spaced with a nominal angle of $\approx 42°$ between adjacent Co moments. (d) Line profiles across the Co atoms in (a) and (b) taken along the [1–10] direction and positioned as a function of θ, determined from fits to the spin spiral. Different left and right axes are due to a slight tip change in-between measurements. The apparent height at the atomic centres (crosses) has been fitted with a cos θ (dot-dashed line) and the function $a_1 \cos\theta + a_2 \cos^2\theta$ (solid line).

References

[1] P. Gambardella, S. Rusponi, M. Veronese, S. S. Dhesi, C. Grazioli, A. Dallmeyer, I. Cabria, R. Zeller, P. H. Dederichs, K. Kern, C. Carbone, and H. Brune, Science **300**, 1130-1133 (2003).

[2] F. Meier, L. Zhou, J. Wiebe, and R. Wiesendanger, Science **320**, 82-86 (2008).

[3] A.J. Heinrich, J.A. Gupta, C.P. Lutz, and D.M. Eigler, Science **306**, 466-469 (2004).

[4] C.F. Hirjibehedin, C.P. Lutz, and A. J.Heinrich, Science **312**, 1021-1024 (2006).

[5] Y. Yayon, V.W. Brar, L. Senapati, S.C. Erwin, and M.F. Crommie, Phys. Rev. Lett. **99**, 067202 (2007).

[6] C. Iacovita, M. V. Rastei, B. W. Heinrich, T. Brumme, J. Kortus, L. Limot, and J. P. Bucher, Phys. Rev. Lett. **101**, 116602 (2008).

[7] M. Bode, M. Heide, K. von Bergmann, P. Ferriani, S. Heinze, G. Bihlmayer, A. Kubetzka, O. Pietzsch, S. Blügel, and R. Wiesendanger, Nature **447**, 190-193 (2007).

[8] S. Heinze, M. Bode, A. Kubetzka, O. Pietzsch, X. Nie, S. Blügel, and R. Wiesendanger, Science **288**, 1805-1808 (2000).

[9] D.M. Eigler and E.K. Schweizer, Nature **344**, 524-527 (1990).

[10] D. Serrate, P. Ferriani, Y. Yoshida, S.-W. Hla, M. Menzel, K. von Bergmann, S. Heinze, A. Kubetzka, and R. Wiesendanger, Nature Nanotechn. **5**, 350 (2010).

[11] P. Hohenberg and W. Kohn, Phys. Rev. **136**, B864-B871 (1964).

[12] Y. Zhang and W. Yang, Phys. Rev. Lett. **80**, 890 (1998).

[13] D. Wortmann, S. Heinze, Ph. Kurz, G. Bihlmayer, and S. Blügel, Phys. Rev. Lett. **86**, 4132-4135 (2001).

[14] M. Bode, S. Heinze, A. Kubetzka, O. Pietzsch, X. Nie, G. Bihlmayer, S. Blügel, and R. Wiesendanger, Phys. Rev. Lett. **89**, 237205 (2002).

[15] O. Pietzsch, A. Kubetzka, D. Haude, M. Bode, and R. Wiesendanger, Rev. Sci. Instr. **71**, 424-430 (2000).

[16] S.-W. Hla, K.-F.Braun, and K.-H. Rieder, Phys. Rev. B **67**, 201402(R) (2003).

3.6 Semiconductors

This section deals with the investigation of semiconductor surfaces as substrates for magnetic atoms. The (110) surface of narrow band-gap III-V semiconductors as indium arsenide or indium antimonide is especially well suited for an SP-STS study of electron or hole systems of different dimensions and of magnetic dopants at the surface due to three reasons: (i) as it is the natural cleavage plane, a largely defect free and flat surface which typically shows no steps over several hundreds of nanometers can easily be prepared in ultra high vacuum; (ii) STS is usually sensitive to the local electron density-of-states (LDOS) *at* the surface. However, since the (110) surface has no intrinsic surface states in a range of ± 1 eV arround the band edges which is the relevant window for STS, the electronic states of the bulk [1] or of dopants lying up to ten layers below the surface [2,3] are still detectable; (iii) confined electron systems of lower dimensionality can be obtained by depositing adsorbates (2DES) [4–9], below step edges (1DES) [10], or just below the local gate built by the tip of the STM (0DES) [11]. Thus, the local magnetic and electronic properties of surface dopants coupled to electron systems in all dimensions can be studied on the atomic scale.

Section 3.6.1 focuses on the real-space investigation of the electron states of the cesium-induced 2DES in InSb as a function of an external magnetic field. In particular, we were able to observe the evolution from localized drift states in the insulating phases to branched extended drift states at the quantum critical point. The microscopic behavior close to the extended state indicates points of localized quantum tunneling, which are considered to be decisive for a quantitative description of the transition.

Importantly, the g-factor of the 2DES electrons in InSb is so huge, that the Landau levels are already strongly spin-split at moderate magnetic fields of $B = 6\,\mathrm{T}$. Thus, for particular bias voltages of the tunnel junction, the 2DES may serve as a source for 100 % spin-polarized electrons. As shown in Sec. 3.6.2 this principle indeed can be used to measure single-atom magnetization curves of iron atoms doped into the surface of InSb by STS, i.e. without spin-polarization of the tip. Furthermore, we were able to detect the spin-flip excitations of the Fe dopants by ISTS. Together with the help of the magnetization curves, the corresponding excitation energies were used to pinpoint the spin quantum number and the magnetic anisotropy of the Fe dopant. The result is corroborated by first principles calculations.

Finally, we also revisited the electronic structure of the 7×7 reconstruction of Si(111) as a possible future template for magnetic adatoms. Interestingly, we observed the opening of an energy gap in the ground state of this surface at $T = 0.3\,\mathrm{K}$ (Sec. 3.6.3).

3.6.1 Observation of the quantum Hall transition in real space

K. Hashimoto, C. Sohrmann, J. Wiebe, T. Inaoka, F. Meier, Y. Hirayama, R. A. Römer, M. Morgenstern, and R. Wiesendanger

The 2DES in this section was prepared in ultrahigh vacuum (UHV) by depositing 0.01 monolayer Cs on cleaved n-InSb(110). STS was performed with a carefully selected W-tip exhibiting a minimum of tip-induced band-bending by trial and error [12]. Figure 3.30 (a) shows a color scale plot of the local differential conductivity $\mathrm{d}I/\mathrm{d}V(V_s)$ of the 2DES measured along a straight line across the sample (left) at $B = 0$ T (sample voltage: V_s). The corresponding spatially averaged $\mathrm{d}I/\mathrm{d}V$ curve is shown on the right. They represent the energy dependence of the LDOS (energy-position plot) and of the macroscopically averaged LDOS, i.e. the DOS. The energy-position plot shows two apparent boundaries coinciding with two step-like features in the averaged $\mathrm{d}I/\mathrm{d}V$ curve at V_s = -115 meV and -47 meV. They are signatures of the first (E_1) and second (E_2) subband edges and are in excellent agreement with the subband energies resulting from a self-consistent calculation (Fig. 3.30 (b)).

Figure 3.30 (c) shows a set of $\mathrm{d}I/\mathrm{d}V$ curves measured at the same position at different B-fields. Already at $B = 6$ T, the $\mathrm{d}I/\mathrm{d}V$ curve exhibits distinct LLs with a pronounced twofold spin splitting. Repeating the measurement using more B-field steps reveals the continuous evolution of the spin-split LLs, i.e. the LL fan diagram (Fig. 3.30 (d)). The green (red) dashed lines mark the four (two) spin-down LLs of the 1st (2nd) subband. The accompanying spin-up LLs are visible at correspondingly higher energies as marked by blue spin arrows for the lowest LL.

From the distances of the peaks in the spectra, we deduce the effective mass $m^\star$ and the absolute value of the g-factor $|g|$ via $\Delta E_{LL} = \hbar eB/m^\star$ ($\hbar$: Planck's constant, e: electron charge) and $\Delta E_{\uparrow\downarrow} = |g|\mu_B B$ (μ_B: Bohr magneton), to be $m^\star/m_e = 0.019 \pm 0.001$ and $|g| = 39 \pm 2$ for the lowest energy peaks at $B = 6$ T. This is close to the known values at the band edge $m^\star/m_e = 0.014$ and $|g| = 51$ with slight deviations due to the non-parabolicity of the InSb conduction band and the increased energetic distance to the spin-orbit split valence band. The large $|g|$-factor and low $m^\star$ inherent to InSb are the key to a direct measurement of spin-resolved LLs by STS.

Now we address the real-space behavior of the LDOS across a quantum-Hall transition. Figures 3.31 (a)-(g) present the $\mathrm{d}I/\mathrm{d}V$ images recorded at different V_s in the lowest spin-down LL at $B = 12$ T. The corresponding, spatially averaged $\mathrm{d}I/\mathrm{d}V$ curve is shown in Fig. 3.31 (h). In the low-energy tail of the LL at V_s = -116.3 mV (Fig. 3.31 (a)), we observe spatially isolated closed-loop patterns. The averaged FWHM of the closed loop in the top right of Fig. 3.31 (a) is 6.9 nm close to the cyclotron radius $r_c = 7.4$ nm. Thus, we attribute the isolated patterns to localized spin-down drift states aligning along the equipotential lines around a potential minimum. Accordingly, at slightly higher energy (Fig. 3.31 (b)), the area encircled by the drift states increases indicating that the drift states probe a longer equipotential line at higher energy within the potential valley. In contrast, the ring patterns at the

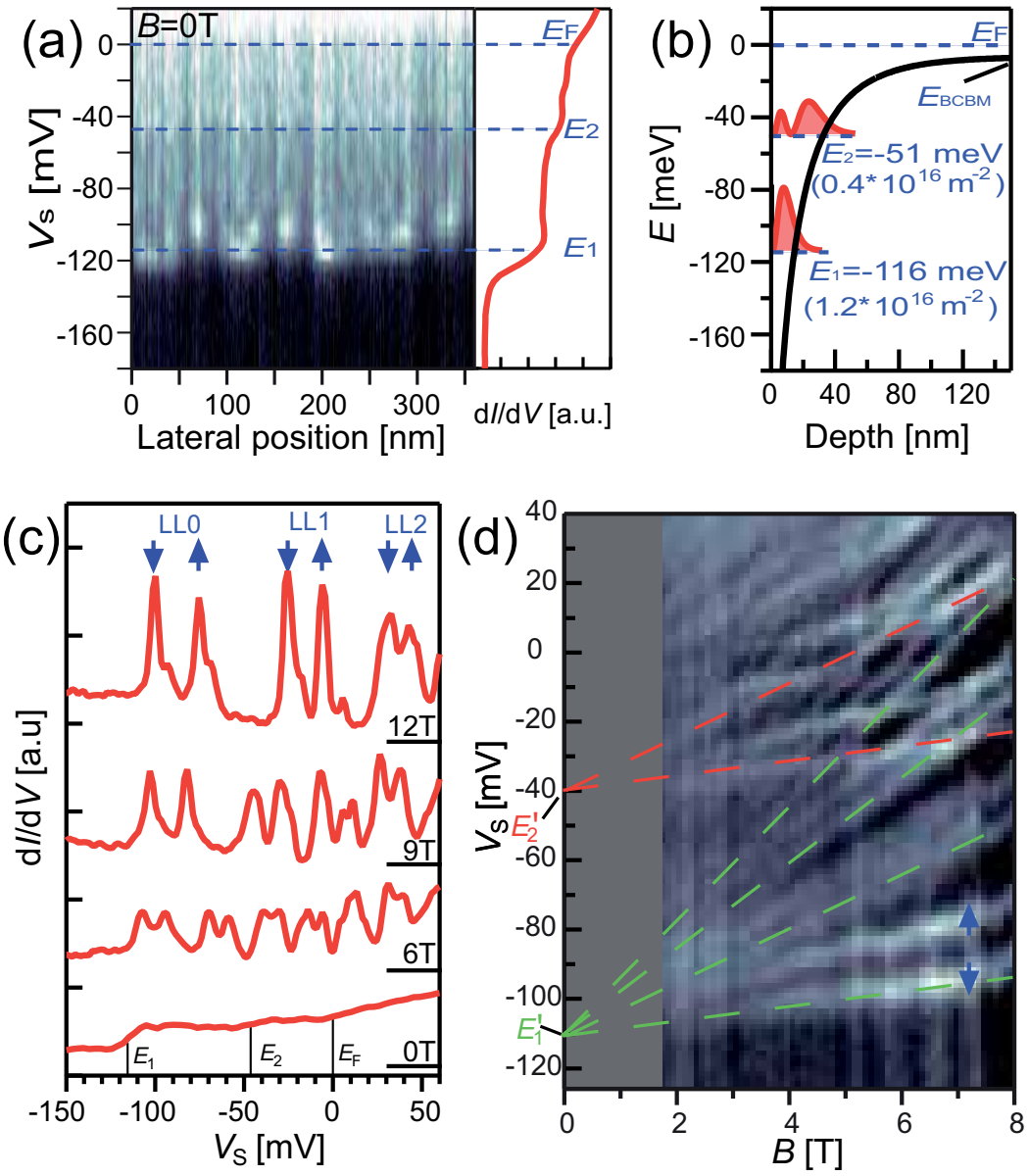

Figure 3.30: STS of Cs induced 2DES in InSb ($I_{\mathrm{stab}} = 0.13$ nA (a),(c), and 0.10 nA (d), $V_{\mathrm{stab}} = 150$ mV, $V_{\mathrm{mod}} = 2.0$ mV (a), 1.5 meV(d)) (a) Color scale plot of $\mathrm{d}I/\mathrm{d}V$ (V_s) measured along a straight line at $B = 0$ T (left), and corresponding spatially averaged $\mathrm{d}I/\mathrm{d}V$ curve (right). Blue lines: E_F and subband energies of the 2DES (E_1, E_2). (b) Self-consistently calculated band bending (black solid line) and confined states (red areas). Resulting E_i and corresponding electron densities n_i are marked. (c) $\mathrm{d}I/\mathrm{d}V$ curves at different B-fields recorded at the same lateral position ($V_{\mathrm{mod}} = 2.0$ mV (0 T), 1.3 mV (6 T), 1.0 mV (9 T) and 0.9 mV (12 T)). E_1, E_2 and E_F (bottom), ($\mathrm{d}I/\mathrm{d}V = 0$)-lines (right), as well as LLs with index and spin directions (top) are marked. (d) Experimentally determined Landau fan diagram (see the text). Green (red) dashed lines: Spin-down LLs of the 1st (2nd) subband. Arrows: different spin levels of the lowest LL.

high-energy LL tail marked by green arrows in Figs. 3.31 (f) and (g) encircle an area decreasing in size with increasing voltage. They are attributed to localized drift states around potential maxima. When the voltage is close to the LL center (Figs. 3.31 (c) and (e)), adjacent drift states become partly connected (probably at saddle points of the potential) and a dense network is observed directly at the LL center (Fig. 3.31 (d)). Figure 3.31 (j) shows another extended state recorded on a larger area at different B. This corresponds exactly to the expected behavior of an extended drift state at the integer quantum-Hall transition which carries the current through the whole sample.

Interestingly, the extended drift states indicate quantum tunneling at the saddle points of the potential. As an example, the red and yellow arrows in Fig. 3.31 (c) and (e) mark the same connection point at V_s = -104.4 mV and -99.2 mV. LDOS is faintly visible at both positions in both images and surprisingly rotates by about 90° between the images. The reason is simply that the tunneling interconnection mediates between valley states at energies below the LL center and between hill states at energies above the LL center, while hills and valleys are connected via nearly orthogonal lines. The weak links are also reproduced by Hartree-Fock calculations taking the disorder into account as marked by red arrows in Fig. 3.31 (i), which represents the LDOS including an extended state.

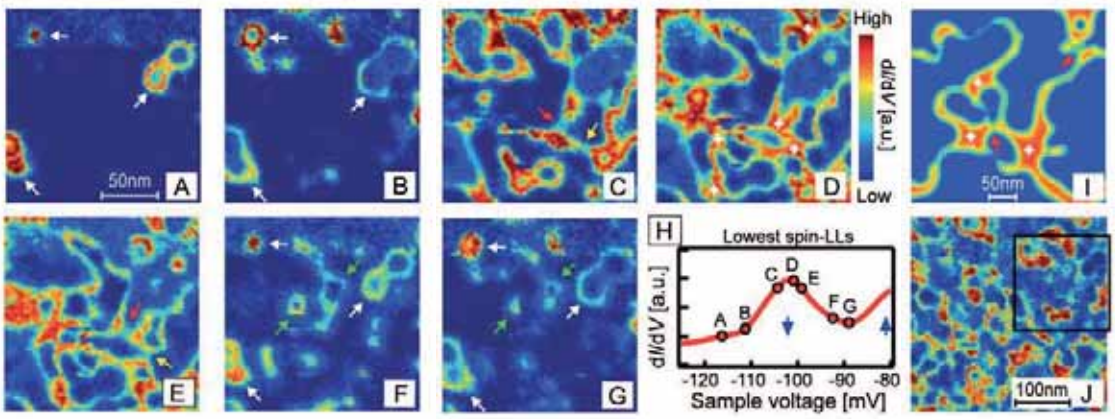

Figure 3.31: Real-space LDOS at the lowest LL of the Cs induced 2DES in InSb. (a)-(g) Measured dI/dV images at B = 12 T and V_s = -116.3 mV (a), -111.2 mV (b), -104.4 mV (c), -100.9 mV (d), -99.2 mV (e), -92.4 mV (f) and -89.0 mV (g) ($I_{\rm stab}$ = 0.10 nA, $V_{\rm stab}$ = 150 mV, $V_{\rm mod}$ = 1.0 mV). The same dI/dV-color scale is used for each image. Green (white) arrows mark drift states encircling potential maxima (minima) [(a), (b), (f), and (g)]. Red and yellow arrows mark tunneling connections existing at the identical position in (c) and (e). Crosses mark extended LDOS areas at the saddle points (d). (h) Spatially averaged dI/dV curve with circles marking V_s corresponding to (a)-(g). (i) Calculated LDOS at the center of the spin-down LL0 (B = 12 T). Red arrows mark tunneling connections at the saddle points. Crosses mark extended areas. (j) dI/dV image measured at B = 6 T and V_s = -99 mV close to the center of spin-up LL0. The image includes the area of (a)-(g) within the marked rectangle.

3.6.2 Magnetic excitation and read out of Fe in InSb(110)

A. A. Khajetoorians, B. Chilian, J. Wiebe, S. Schuwalow, F. Lechermann, and R. Wiesendanger

A similar 2DES as in the case of Cs/InSb(110) is formed by the charge transfer of a dilute density of deposited Fe atoms. It also has two occupied subbands, but with slightly different subband energies of $E_1 = -80 \pm 20$ meV and $E_2 = -25 \pm 20$ meV below the Fermi energy E_F ($V = 0$ V) indicating less band bending. However, the resulting effective mass $m^\star \approx 0.02 m_\mathrm{e}$ and Landé g-factor $g_\mathrm{InSb} \approx -45$ of the 2DES electrons is almost the same. In contrast to the case of Cs, the Fe atoms aditionally act as localized atomic spins which may weakly couple to the 2DES. Here, the coverage is low enough (0.1 Fe/nm^2) such that single Fe spins behave as isolated entities [13].

To detect the spin excitations of the Fe atom, we acquired differential conductance spectra with high energy resolution ($V_\mathrm{mod} = 40\mu$V rms) in a narrow bias voltage range ($\pm$10 meV) around E_F, which are shown in Fig. 3.32 (a). While such spectra measured on the substrate are largely flat and featureless, spectra taken with the same tip above the Fe atom show two distinct steps at both positive and negative sample bias ($V \approx \pm 0.5$ meV and $V \approx \pm 1.5$ meV) which are symmetric to E_F. The intensity of each step amounts to about 25% of the signal at zero bias voltage. These steps are due to magnetic excitations of the Fe atom by the tunneling electrons and can be well described within a relatively simple model as shown in the following.

For the description of the Fe spin we use the "giant spin" approximation:

$$\hat{H} = g_\mathrm{Fe}\mu_\mathrm{B}\vec{B}\cdot\vec{\hat{S}} + D\hat{S}_z^2 + E\left(\hat{S}_x^2 - \hat{S}_y^2\right) \tag{3.28}$$

The first term is the Zeeman splitting resulting from an external magnetic field $\vec{B}$ with the vector spin operator $\vec{\hat{S}} = \left(\hat{S}_x, \hat{S}_y, \hat{S}_z\right)$, the Landé g-factor of the Fe atom g_Fe, and the Bohr magneton μ_B. The second and the third term describe the so called magnetic anisotropy energy. It takes into account the spin-orbit interaction in harmonic approximation, and energetically forces the spin to point along certain lattice directions, which are *a priori* unknown. Diagonalization of the Hamiltonian yields the eigenstates and eigenenergies as a function of $\vec{B}$. The steps in the conductance in Fig. 3.32 (a) appear at bias voltages equal to the energetic separations between the ground state and the excited states at $\vec{B} = 0$ T which are determined by the two parameters D and E. To calculate the step heights which represent the transition probabilities the exchange interaction between the tunneling electron spin and the atom spin has to be considered. We use the model from [14]. The inelastic tunneling spectra are calculated by assuming different values for the atom spin and for D and E. We find that out of all possible spin values ($1/2$, 1,$3/2$, 2, $5/2$) only $S = 1$ properly reproduces both the experimentally observed number of steps as well as the overall intensity of each step as shown by comparison to the normalized spectra in Fig. 3.32 (b). In

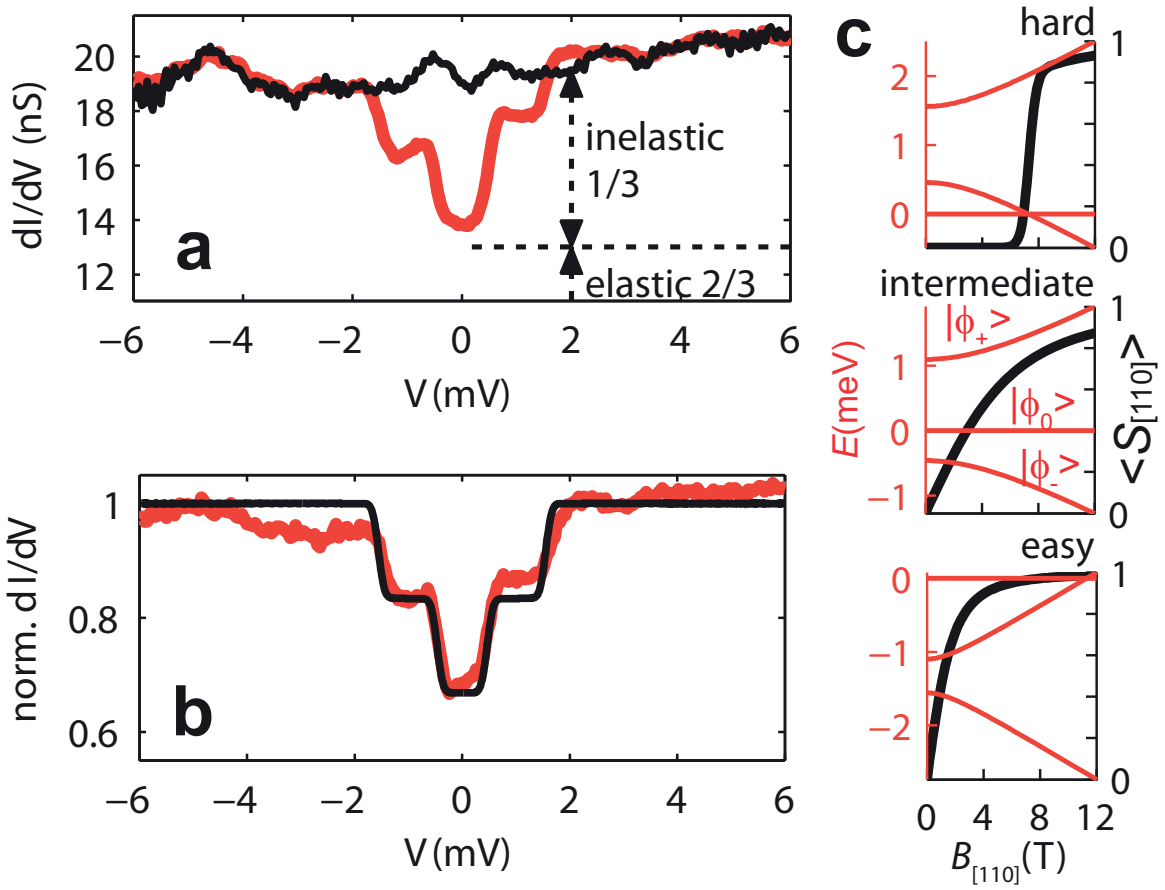

Figure 3.32: Inelastic electron tunneling spectra of Fe dopants in the surface of InSb. (**a**) The spectra ($I_{\mathrm{stab}} = 0.16$ nA, $V_{\mathrm{stab}} = 6$ mV, $V_{\mathrm{mod}} = 40$ μV (rms), T = 0.3 K) were taken with the tip positioned above the Fe atom (red curve) and above the bare substrate (black curve). The elastic and inelastic contributions are indicated. (**b**) Normalized differential conductance (red curve) calculated by dividing the spectrum from the Fe atom by that from the substrate measured with the same tip ($I_{\mathrm{stab}} = 0.32$ nA, $V_{\mathrm{stab}} = 10$ mV, $V_{\mathrm{mod}} = 40$ μV (rms), T = 0.3 K, different data set than in a). The black curve shows the conductance spectrum calculated from the quantum mechanical model (see text) with $S = 1$ and D and E extracted from best fit. (**c**) Energies of the three eigenstates (red) and expectation value of the [110] component of the spin (black) calculated from the Hamiltonian ($S = 1$, eq. 3.28) as a function of the strength of a magnetic field in [110] direction for the three possible cases with [110] being the hard axis, the intermediate axis, and the easy axis, respectively.

order to substantiate this result we calculated the magnetic moment by density functional theory (DFT) with the result of $2.0\mu_{\mathrm{B}}$. This confirms the experimental result $S = 1$ if we assume $g_{\mathrm{Fe}} = 2.0$.

By analyzing the step positions in the spectra of several equivalent atoms on different samples, we deduce the following average values for the magnetic anisotropy parameters: $D = -1.4 \pm 0.3$ meV and $E = 0.22 \pm 0.06$ meV. Note, that this choice satisfies the convention to maximize $|D|$ and have $E > 0$, but there are six possible cases corresponding to the orientation of the axes in Eq. 3.28 with respect to the three lattice directions ($[1\bar{1}0]$, [001] and [110]). The usual way to experimentally distinguish between these cases is to detect the evolution of the excitation energies as a function of a magnetic field. The eigenenergies of the three eigenstates $|\phi_+\rangle$, $|\phi_-\rangle$ and $|\phi_0\rangle$ in a magnetic field $B_{[110]}$ (along [110]) for the three cases with [110] being the most unfavored "hard" axis (x), the "intermediate" axis (y), or the favored "easy" axis (z), respectively, are shown in Fig. 3.32 (c). For this particular system, the excitations are strongly masked by the Landau levels emerging in the conductance spectra with the application of a magnetic field. In the following we will show that the energetic separation of tunneling electrons with different spin states resulting from spin-splitting of the Landau levels acts as a spin-polarized source which allows us to measure the expectation value of the spin-component along the applied magnetic field (magnetization curve) of the Fe atom. The shape of the magnetization curve indicated in Fig. 3.32 (c) is strongly sensitive to the orientation of the easy axis, thus allowing us to unequivocally identify the proper anisotropy case.

Fig. 3.33 (a) shows conductance spectra taken on and off an Fe atom in a wider voltage range as a function of $B_{[110]}$. As expected for a 2DES, the spectra reveal sharp peaks with energy spacings corresponding to the separation of the Landau levels (LL) and the resultant spin-splitting (see Sec. 3.6.1). While both peaks for the lowest LL (LL0) corresponding to spin up (↑, left) and spin down (↓, right) have nearly the same intensity on the substrate, the ↓ peak has a larger intensity than the ↑ peak on the Fe atom. A quantitative measure for this asymmetry is obtained by fitting the two peaks to a sum of two Lorentzians with amplitudes a_{right} and a_{left} and defining $A_{\mathrm{LL0}} = (a_{\mathrm{right}} - a_{\mathrm{left}}) \,/\, (a_{\mathrm{right}} + a_{\mathrm{left}})$. The dependency of A_{LL0} on $B_{[110]}$ measured at $T = 0.3$ K and $T = 4$ K for different atoms using different non-magnetic tips is shown in Fig. 3.34 (a) together with the substrate asymmetry. Obviously, the Fe atom which is magnetized by the external magnetic field acts as a spin-filter for tunneling electrons as sketched in the inset of Fig. 3.33 (a).

A proof of the interpretation of the observed LL asymmetry as being due to the spin-filter effect of the atom comes from experiments with spin-polarized tips. Fig. 3.33 (b) shows the conductance spectra of the lowest LL (LL0) taken at up- and downwards pointing $B_{[110]}$ using a tip coated with several tens of monolayers chromium. Such tips are known to act as filters for electrons with a spin component in the axis of the tip ([110]) (Sec. 3.5.1). Consequently, the spectra taken on the substrate already show a considerable asymmetry of $A_{\mathrm{LL0}} \approx 30\%$ which directly measures the

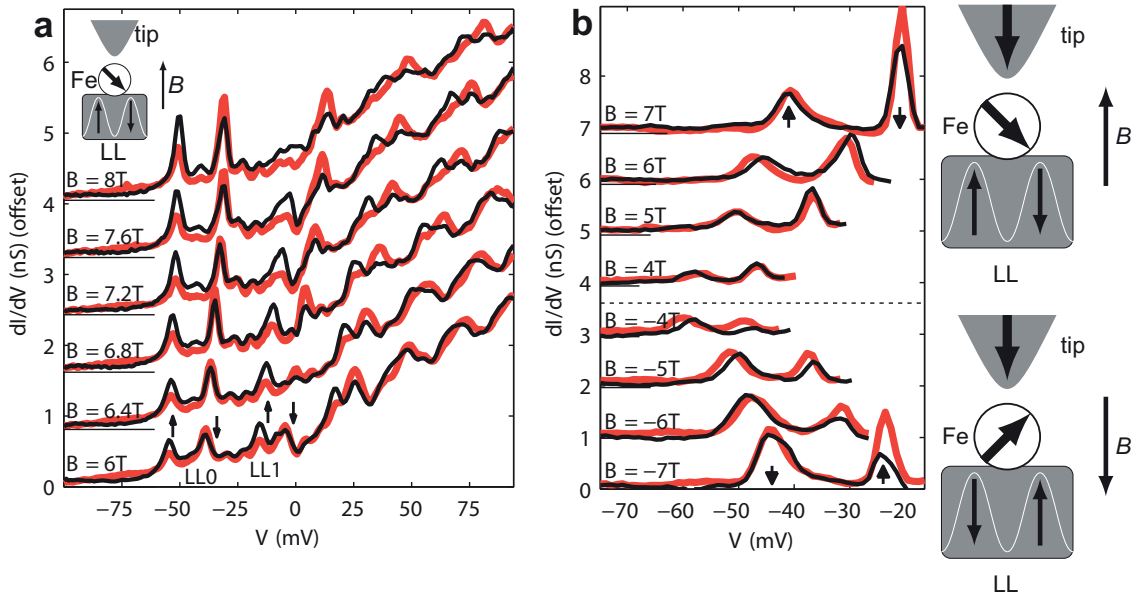

Figure 3.33: Spin resolved Landau-level spectroscopy of Fe dopants in the surface of InSb. The spectra ($I_{\mathrm{stab}} = 0.3$ nA, $V_{\mathrm{stab}} = 100$ mV, $V_{\mathrm{mod}} = 1$ mV (rms), T = 0.3 K) were taken with the tip positioned above the Fe atom (red curves) and above the bare substrate (black curves) with $\vec{B}$ oriented along the surface normal [110] (curves are offset for clarity as indicated by vertical zero lines). (**a**) Spectra taken with a nonmagnetic tip. Inset: Sketch of the directions of the spin in each Landau level (LL) and of the majority electrons in Fe (resulting from the direction of $\vec{B}$). (**b**) Spectra of the lowest spin-split LL (LL0) taken with a magnetic tip. Insets: Sketches of the directions of the spin in each LL and of the majority electrons in Fe and in the foremost tip atom for the two cases $B_{[110]} > 0$ (top) and $B_{[110]} < 0$ (bottom).

spin polarization of the tip within the energy range corresponding to LL0. When the direction of $B_{[110]}$ is switched, the substrate asymmetry changes sign proving that the tip magnetization is not reversed up to $B_{[110]} = \pm 7$ T. The spectra measured on the Fe for upwards pointing $B_{[110]}$ reveal, that the atom increases the asymmetry, i.e. it acts in the same way as the tip spin filter. In contrast, for $B_{[110]}$ pointing downwards, the atom decreases the asymmetry even reversing its sign between $B_{[110]} = -6$ T and $B_{[110]} = -7$ T, i.e. it counteracts the tip spin filter. The sign change is also visible in the plot of the extracted A_{LL0} from several atoms as a function of $B_{[110]}$ (Fig. 3.34 (b)). Qualitatively, these experimental findings can be understood considering the spin orientation of the majority electrons in the tip, in the Fe atom, and of the electrons in the two LLs as given in the inset of Fig. 3.33 (b).

To deduce how A_{LL0} is linked to the atom magnetization, we adapt the model utilized above to the description of the LL asymmetry. It can be analytically shown, that for an unpolarized tip A_{LL0} is proportional to the component of the atom-spin expectation value along the applied magnetic field, i.e. to the atom magnetization. To predict the measured A_{LL0}, the average values for D and E extracted from the inelastic tunneling spectra, and a constant tip spin-polarization measured by the substrate A_{LL0} for the polarized tip are taken into account. The calculated A_{LL0} for the three possible cases of Fig. 3.32 (c) is plotted in Fig. 3.34 (a) on top of the measured data. While the easy axis and the hard axis cases can be excluded a good quantitative agreement is found for the case with the [110] direction being an intermediate axis, i.e. the easy axis lies in the (110) plane. Within this case the model also correctly predicts the behavior for the series of the atom and tip spin-filters as shown in Fig. 3.34 (b). From the experimental values of D and E one can calculate that it costs 0.75 meV and 0.5 meV to rotate the spin from the easy axis into the hard axis and into the intermediate [110] direction, respectively. Using DFT, we calculate that the spin of the Fe atom is preferably oriented along $[1\bar{1}0]$ and the corresponding energies are 1.8 meV and 0.4 meV, in good agreement with the experimental values.

Finally, the system studied here is an example of a "magnetic" 2DES in which the magnetic dopants might be exchange coupled to the itinerant 2DES electrons. An indication for this coupling is given by the hump in the Fe magnetization curve (Fig. 3.34 (a)) between 6 T and 8 T. Here the Fe magnetization saturates ($A_{\mathrm{LL0}} = 50\%$) and then goes back to the value predicted within the isolated-spin model (straight blue line). In the same magnetic field range, the local 2DES magnetization oscillates, as proven by the consecutive E_{F} crossing of the $\downarrow$ and $\uparrow$ Landau levels (LL1) in Fig. 3.33 (a). This suggests that the Fe atom acts as atomic detector of the local magnetization of the 2DES. Future experiments with larger dopant density will probably show interesting effects of magnetism in this type of diluted magnetic semiconductor.

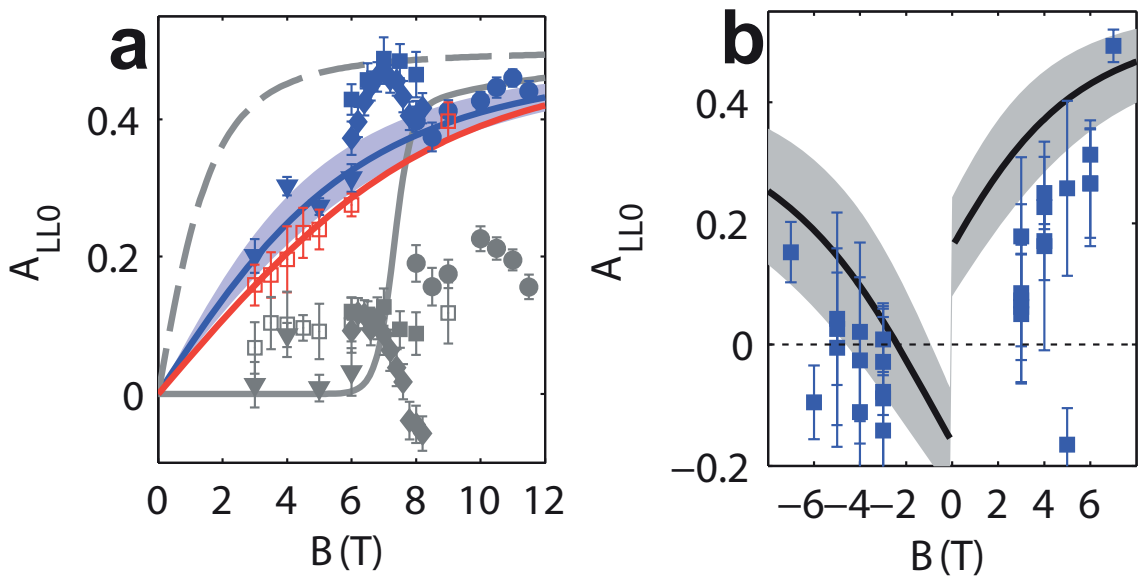

Figure 3.34: Landau level asymmetry as a function of the magnetic field. (**a**) The asymmetry A_{LL0} from the lowest Landau level LL0 measured with a nonmagnetic tip is plotted as a function of $B_{[110]}$. Blue (red) points are taken at $T = 0.3$ K ($T = 4$ K). Different data sets are indicated by different symbols and were measured with different tips on different samples. The corresponding A_{LL0} from the spectra measured with the same tip on the bare substrate is indicated in gray using the same corresponding symbols. The error bars are calculated from the error of the Lorentzian fit to the two LL peaks. The solid gray, the solid colored, and the dashed lines show A_{LL0} calculated from the model for the hard axis case, the intermediate, and the easy axis case, respectively, using D and E determined from the inelastic electron tunneling spectra (Fig. 3.32). The shaded area indicates the error of the calculated curve due to the variance in D and E. (**b**) Same as (a) but from the spectra measured with a magnetic tip. The solid line shows A_{LL0} calculated from the model for the intermediate case assuming a tip spin-polarization of 30%. The shaded area includes the error from the uncertainty in this polarization.

3.6.3 Energy gap of Si(111)-7 × 7

S. Modesti, H. Gutzmann, J. Wiebe, and R. Wiesendanger

The Si(111)-7×7 surface is metallic at room temperature, having an odd number of electrons per unit cell. At low temperature, a gap in the ground state can open when the electron correlation is strong enough to overbalance the electron kinetic energy. This drives the system into a Mott-Hubbard state. Another possible reason for a gap at E_{F} are structural distortions such as charge-density waves. Here, we use a method for the correction of the systematic errors caused by the transport of the carriers injected by the STM tip and evaluate the gap of the ground state of the Si(111)-7 × 7 surface at 0.3 K [15].

The corrected $(\mathrm{d}I/\mathrm{d}V_{\mathrm{tip-surf}})\,(I/V_{\mathrm{tip-surf}})$ and the $\mathrm{d}I/\mathrm{d}V_{\mathrm{tip-surf}}$ curves are shown in Figs. 3.35 (a) and (b) together with the linear fits of the near gap regions used to evaluate the gap. Our estimation of the energy gap is 70 ± 10 meV. The energies of the other features in the spectrum, corresponding to the rest atom (R, -0.8 eV) and adatom (A, -0.15 eV and 0.3 eV) contributions to the surface density of states (DOS), are in agreement with the energies measured at 295 K (Fig. 3.35 (c)), a temperature where the charge transport effects should be negligible. The zoom into the gap region shown in Fig. 3.35 (d) shows that the gap vanishes at room temperature.

The remaining question is whether the observed gap is primarily due to electron-electron interactions and thus resulting from a Mott-Hubbard mechanism or whether it is dominated by electron-phonon interaction and thus connected with lattice distortions, which have not yet been observed.

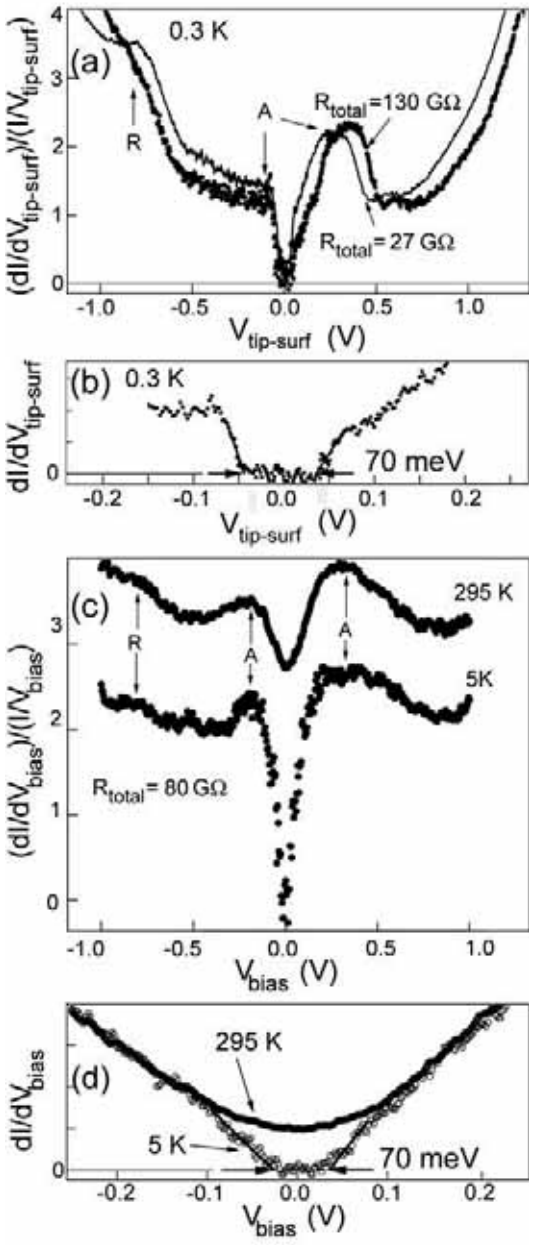

Figure 3.35: (a) Corrected normalized conductance $(\mathrm{d}I/\mathrm{d}V_{\mathrm{tip-surf}})\,(I/V_{\mathrm{tip-surf}})$ of the Si(111)-7 × 7 surface at 0.3 K for two different R_{total}. The arrows point to the DOS features of the rest atoms (R) and of the adatoms (A). (b) Corrected differential conductance near the gap region at 0.3 K for $R_{\mathrm{total}} = 130\,\mathrm{G\Omega}$. The straight lines are used to estimate the gap by a linear extrapolation of the near gap spectrum. (c) Normalized conductance $(\mathrm{d}I/\mathrm{d}V_{\mathrm{bias}})\,(I/V_{\mathrm{bias}})$ of Si samples with improved electric contacts to the sample holder measured at 295 and 5 K with a stabilization resistance of $R_{\mathrm{total}} = 80\,\mathrm{G\Omega}$ at a stabilization voltage of $V_{\mathrm{stab}} = -1.6\,\mathrm{V}$. The 295 K spectrum is vertically displaced by +1.5. (d) Differential conductance $\mathrm{d}I/\mathrm{d}V_{\mathrm{bias}}$ at 5 and 295 K and the linear fit used to estimate the gap at 5 K.

References

[1] D. Haude, M. Morgenstern, I. Meinel, and R. Wiesendanger, Phys. Rev. Lett. **86**, 1582 (2001).

[2] F. Marczinowski, J. Wiebe, J.-M. Tang, M. E. Flatte, F. Meier, M. Morgenstern, and R. Wiesendanger, Phys. Rev. Lett. **99**, 115318 (2007).

[3] F. Marczinowski, J. Wiebe, F. Meier, K. Hashimoto, and R. Wiesendanger, Phys. Rev. B **77**, 115318 (2008).

[4] M. Morgenstern, M. Getzlaff, D. Haude, R.L. Johnson, and R. Wiesendanger, Phys. Rev. B **61**, 13805 (2000).

[5] M. Morgenstern, J. Wiebe, A. Wachowiak, M. Getzlaff, J. Klijn, L. Plucinks, R. L. Johnson, and R. Wiesendanger, Phys. Rev. B **65**, 155325 (2002).

[6] J. Wiebe, Chr. Meyer, J. Klijn, M. Morgenstern, and R. Wiesendanger, Phys. Rev. B **68**, 041402 (2003).

[7] M. Getzlaff, M. Morgenstern, Chr. Meyer, R. Brochier, R.L. Johnson, and R. Wiesendanger, Phys. Rev. B **63**, 205305 (2001).

[8] M. Morgenstern, J. Klijn, Chr. Meyer, M. Getzlaff, R. Adelung, K. Roßnagel, L. Kipp, M. Skibowski, and R. Wiesendanger, Phys. Rev. Lett. **89**, 136806 (2002).

[9] M. Morgenstern, J. Klijn, Chr. Meyer, and R. Wiesendanger, Phys. Rev. Lett. **90**, 056804 (2003).

[10] Chr. Meyer, J. Klijn, M. Morgenstern, and R. Wiesendanger, Phys. Rev. Lett. **91**, 076803 (2003).

[11] R. Dombrowski, Chr. Steinebach, Chr. Wittneven, M. Morgenstern, and R. Wiesendanger, Phys. Rev. B **59**, 8043 (1999).

[12] K. Hashimoto,C. Sohrmann, J. Wiebe, T. Inaoka, F. Meier, Y. Hirayama, R. A. Römer, R. Wiesendanger, and M. Morgenstern, Phys. Rev. Lett. **101**, 256802 (2008).

[13] A. A. Khajetoorians, B. Chilian, J. Wiebe, S. Schuwalow, F. Lechermann, and R. Wiesendanger, Nature **467**, 1084 (2010).

[14] N. Lorente and J.-P. Gauyacq, Phys. Rev. Lett. **103**, 176601 (2009).

[15] S. Modesti, H. Gutzmann, J. Wiebe, and R. Wiesendanger, Phys. Rev. B **80**, 125326 (2009).

3.7 Magnetic molecules

While silicon remains the computer chip industry's material of choice, organic electronics emerges as a competitive rival for simpler and cheaper circuits. The original idea of using few, or even single molecules that are embedded between electrodes to perform the basic functions of electronics - rectification, amplification and storage - was put forward in the mid-1970s. Since then organics have come a long way and have (nearly) arrived in commercial applications, e.g. in organic light emitting diodes (OLEDs), organic photovoltaic cells (OPVCs), organic thin-film transistors (OTFTs), and, more recently, organic spin valves.

The fundamental challenge of increasing the efficiency of these novel organic and molecular applications is directly linked to the understanding of the processes at the interfaces of molecular devices. To gain insight into the interface properties the scanning tunneling microscope (STM) offers unique abilities. It allows not only to probe molecules in an atomically well defined environment, with submolecular resolution, it also enables the controlled manipulation of molecules with the probe tip.

We have studied various molecular model systems, including porphyrin derivatives (Sec. 3.7.1), corrole complexes (Sec. 3.7.2), Co-N,N'-ethylenebis (salicydeneiminato) complexes (Co-Salen) (Sec. 3.7.3), and phthalocyanine molecules (Sec. 3.7.4), on a multitude of metallic surfaces and gained unique insight into the molecule-molecule, molecule-tip as well as the molecule-substrate interaction. These interactions manifest in (absence of) molecular self-assembly, switchable molecular conformations, metastable adsorption sites, and tunable electronic properties. Our experimental observations are supported by state-of-the-art-theory as supplied by our collaborators. Furthermore, chemical tailoring of molecular properties - done by our partners in chemistry - allows for a higher degree of functionality of molecular - over conventional metal- and semiconductor systems.

A highlight of the ongoing research was the application of spin-polarized STM (SP-STM), toward the molecule-ferromagnet interface (Sec. 3.7.5). We were able to show, for the first time, the spin-polarization of such an interface at the single molecule level, with submolecular resolution. It turns out that even non-magnetic molecules can substantially modify the spin polarization of an underlying ferromagnetic film, due to the formation of molecule-metal hybrid states. These new states have the peculiar property to invert the spin polarization at the molecular site with respect to the surrounding ferromagnetic film. An effect which can explain the inverse giant magnetoresistance of organic spin valves which has been intensely discussed in the molecular thin film community [1–3].

3.7.1 Adsorption, conformation and molecular self-ordering of porphyrins on surfaces

J. Brede, M. Linares, S. Kuck, J. Schwöbel, A. Scarfato, S.-H. Chang, G. Hoffmann, R. Lensen, P. H. J. Kouwer, J. Hoogboom, A. E. Rowan, M. Bröring, M. Funk, S. Stafström, F. Zerbetto, R. Lazzaroni, and R. Wiesendanger

Introduction

An important goal in future nanoelectronics is the miniaturization of electronic circuits and other electronic elements to molecular sizes. Besides the reduction in size usage of single molecules as isolated functional entities gains potentially from a rational design by synthetic means [4]. It is hoped that this approach may lead to advanced opportunities in steering the growth behavior and other physical properties of molecular assemblies. To this end, however, a detailed understanding of the interaction of such molecules among each other and with their surroundings is of utter importance. This is particularly true for the influence of the substrate on the conformational and electronic properties of a given molecular system.

Due to their extended π-systems and flat architectures, polyenic and aromatic compounds have often been studied as molecular layers on metallic surfaces. Within this class, porphyrins and metalloporphyrins are preferentially investigated, as these compounds are very robust, polyfunctional, volatile, and readily available with a range of different electronic and steric properties. Specific questions of modern physics can therefore be addressed by investigating monolayers of tailor-made porphyrins deposited on a solid substrate. Evidence has been provided by local experiments such as scanning tunneling microscopy (STM) and volume averaging techniques such as near-edge X-ray absorption fine structure spectroscopy that indeed the molecular conformation of porphyrins on metallic substrates deviates from their known shapes in bulk systems [5–7].

The general chemical structure of tetra phenyl porphyrins (TPPs) is depicted in Fig. 3.36. The porphyrin macrocycle hosts two central hydrogen atoms or, when metalated, any metallic ion. The phenyl legs are connected to the porphyrin core via C-C bonds, which allow for a rotation and can result in a reduction of molecular symmetry. The crystalline structure of bulk TPP molecules has been known for decades [8]. Depending on the metallic center and the ligand sphere, different deformations of the porphyrin core are reported as ruffled or saddled structures [5, 9].

Here, we experimentally investigate the (cold) adsorption of isolated molecules on metallic substrates. Moreover, controlled manipulation experiments with single molecules have been performed.

Then, we especially address the role of the phenyl legs on the growth behavior and self-assembly of TPPs. Adsorption and formation of molecular aggregates are

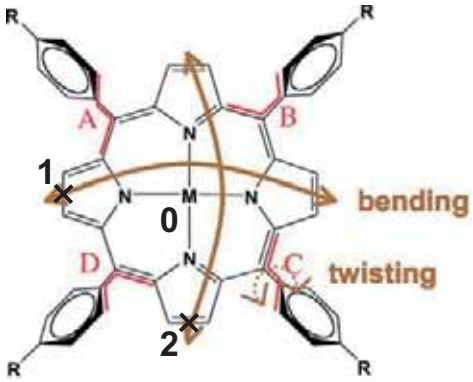

Figure 3.36: Chemical structure of TPP. The molecules have an inner porphyrin core which hosts a metallic center (M=Co, Cu) or two hydrogen atoms. The porphyrin core can be planar or bent in a saddle conformation. Attached to the core are phenyl rings, which are terminated by H or by an additional substituent R (R=MeS or Br). These phenyl rings are rotatable along their axes. '0','1', and '2' denote positions in the porphyrin core that are relevant for the discussion of the results of molecular modeling.

locally studied on Cu(111) and Au(111). In contrast to previous studies where self-assembling was observed [10, 11] here TPP molecules are systematically modified to control molecule-molecule interaction by the chemical synthesis and experimental results are combined with molecular modeling simulations, to address the underlying dynamic processes present at first stages of growth, in relation with the nature of the molecule-molecule and molecule-surface interactions [12, 13].

Experimental conditions

Sample preparation and local investigations were performed under ultra-high vacuum conditions ($< 2 \times 10^{-10}$ mbar). After preparation of Cu(111), Cu(100), and Au(111) surfaces by standard techniques (several consecutive cycles of argon ion etching and following annealing above 700 K) molecules were deposited on these surfaces. For the study of an isolated molecule, deposition took place with the sample kept at approximately 30 K. Self-assembly of molecular clusters was induced by heating these samples up to room temperature to enable thermally induced mobility. As reference, molecules were also deposited with the sample maintained at room temperature during deposition. After preparation, these samples were locally investigated in a home-built variable-temperature STM operated at approximately 25 K [14]. U is defined as the applied voltage between the STM probe and the sample. Positive voltages refer to tunneling into unoccupied sample states and negative voltages to tunneling out of occupied sample states, respectively. All images are processed with WSxM in terms of line and plane fitting procedures [15].

Modeling

Modeling TPP molecules is based on a two-step approach. First, a conformational study of an isolated molecule by density functional theory (DFT) was performed with

the B3LYP/6-31+G(d) formalism. The second step of the modeling study, aimed at investigating the adsorption of a single molecule and self-assembly on gold, is based on a force-field molecular mechanics and molecular dynamics approach [16,17]. In this method, the interactions between gold atoms are represented within the Glue model approximation [18]. The dynamics of molecule-molecule interactions are described by MM3 force-field calculations [19, 20]. For gold-molecule interactions, a charge equilibration procedure [21] in combination with a repulsive potential are used [22].

For modeling the adsorption of a single molecule on gold, the molecule was adsorbed on a surface made of 4 layers of gold; each layer consisting of 14 × 16 atoms. The atoms in the top two layers of the surface were allowed to relax while the atoms in the two bottom layers were kept frozen. To simulate an infinite surface, periodic boundary conditions were employed. Considering the size of the cell ($\sim$ 40.4 Å× 40 Å) and the cutoff used (9.5 Å), there is no interaction between a single molecule adsorbed on the gold surface and its image in the neighboring cell.

Then, starting with a molecule optimized on a surface with four-fold rotational symmetry and planar porphyrin core (see Fig. 3.36 which is distinctively different to the experimentally observed geometry (two-fold mirror symmetry and saddled porphyrin core) we performed Molecular Dynamics (MD) simulations. The simulations of the dynamic behavior were carried out within the canonical ensemble, i.e., at constant number of molecules, volume, and temperature (constant NVT). All simulations of the dynamic behavior were realized at 300 K. The temperature is maintained during the dynamics using the Groningen method of coupling to external baths [23]. During the MD simulation of the single molecule adsorbed on the surface, the evolution of the tilting of phenyl legs and bending of the core of the porphyrin were followed and recorded over a period of 100 ps. Based on the adsorption geometry obtained for a single molecule, the self-assembly of four porphyrin molecules deposited on a surface of 4 layers of 11 × 12 atoms of gold was modeled. After an equilibration time of 100 ps in the canonical ensemble, the lattice parameters were followed and recorded for 100 ps.

Adsorption, orientation and appearance of isolated TPPs

Figures 3.37 and 3.38 provide an overview of observable molecular conformations and their appearances in STM images for the different surfaces. Figure 3.37a-f shows molecules - Cu-TPP, Co-TPP, TMeSPP - in their predominant twofold C_{2v} symmetric appearance, with four pronounced lobes. Following [24], these lobes are interpreted as tilted phenyl legs whereas the reduced symmetry of the porphyrin core (in comparison with the structural model) originates from a bending into a saddle conformation. In direct comparison, Cu-TPP and Co-TPP can be distinguished at the given voltage by the characteristic appearance of the centers [26]. Cu-TPP shows a depression whereas Co-TPP a broad protrusion as originating from $3d$ states of the central ion [10, 25, 27].

Co-TPP and Co-TBrPP significantly vary in the extension of phenyl legs due to attached bromine atoms (compare Fig. 3.38). Similarly, $(MeS)_4$TPP which is for the

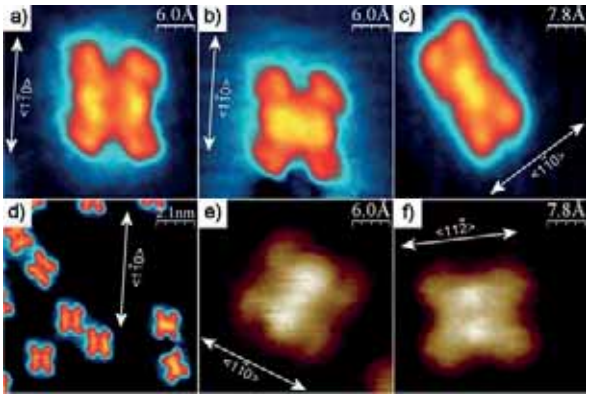

Figure 3.37: High resolution images of three different and isolated porphyrin molecules for negative voltages on Cu(111) (a-d) and on Au(111) (e-f). (a) shows Cu-TPP, (b) and (e) show Co-TPP and (c) and (f) TMeSPP. The characteristic contrast at the central position and of the four lobes enables a precise identification within mixed samples of Co-TPP and Cu-TPP on Cu(111) as presented in (d). For Cu-TPP and Co-TPP three well defined orientations are identified, which coincide with the atomic structure underneath. (a)-(d) $U = -1$ V ; (e) $U = -1.2$ V; (f) $U = -1.5$ V. (a),(b),(d) $I = 50$ pA; (c),(e),(f) $I = 100$ pA;

first time investigated by a local technique shows the same extension at its phenyl legs as bromine terminated TPPs whereas again the center shows a minimum.

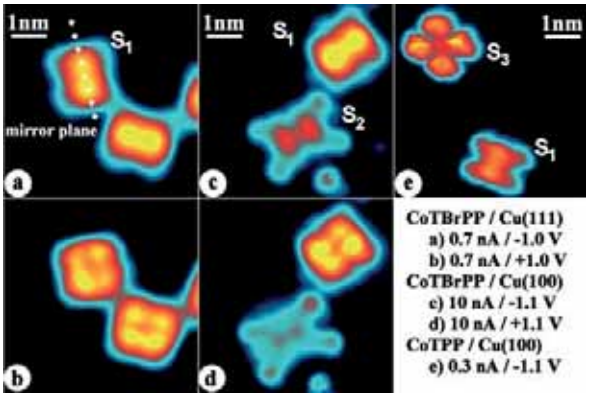

Figure 3.38: Observed conformations by STM: saddle conformation S_1, rectangular conformation S_2, square conformation S_3. Characteristically for the saddle conformation S_1, the two upward bent pyrrole units are accentuated when imaged at negative polarity and the methine bridges are highlighted when imaged at positive polarity. The 'mirror plane' denotes the plane perpendicular to the surface and along the accentuated backbone.

Upon close inspection one can identify three distinct conformations which are denoted in the following as S_1, S_2, and S_3 (Fig. 3.38). The exact molecular conformations of structures S_2 and S_3 are unknown. The structure S_2 has been previously reported along with a suggested conformation [28], the structure S_3 is so far only reported

for a densely packed and well ordered mixture of metalated TPP and phthalocyanine molecules [29, 30].

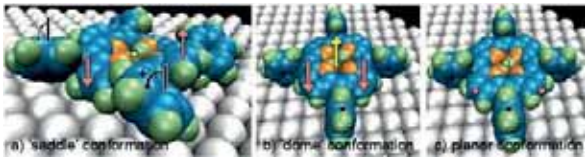

Figure 3.39: Adsorption conformations of TPP molecules. a) calculated 'saddle' conformation for TPP/Au(111). (b,c) proposed conformations for TPP/Cu(100) with C_4 symmetry; b) 'dome' and c) planar conformation. Colors and arrows/circles indicate deformations of the molecular structure - rotation of phenyl legs (black), bending of the pyrrole unit (red), and displacement of the core position (yellow).

For the structure denoted as S_2, the overall shape as well as the inner molecular contrast exhibit a clear C_{2v} symmetry. This is indicative for a saddle conformation of the porphyrin macrocycle whereas the elongated appearance of the full molecule has to be interpreted not only in terms of a rotation of phenyl legs but also in terms of a bending along the axially connecting C-C bond. Consistent with Ref. [28], our interpretation is as follows: The phenyl legs are fully planar to the surface and bent toward the mirror plane. As a consequence, the surface-molecule distance is reduced compared to S_1 as well as the apparent height in STM images (see Fig. 3.38c,d). Due to the bending of the phenyl legs and the resulting steric interaction between the phenyl legs and two of the pyrrole units, these pyrrole units are bent upwards. Comparable to images of molecules in the S_1 structure the upward bent pyrrolic units appear as two protrusions.

In the structure denoted as S_3, the symmetry reduction is lifted. The observed four-fold symmetry has to be attributed to a four-fold symmetric adsorption geometry of the porphyrin macrocyle and a saddle conformation can be excluded. Such structures are known from bulk materials and denoted as 'dome' and 'planar'. Both suggested structures are depicted in Fig. 3.39b,c and, as a consequence of steric interactions, phenyl legs are oriented perpendicular to the surface. This is experimentally manifested in a fully square like appearance of molecules without any additional fine structures within the images of the phenyl legs.

On Cu(111) and Au(111), independent of central ion, all TPP derivatives adsorb in the saddle conformation. Whereas some Co-TBrPP and all TMeSPPs adsorb with all phenyl legs parallel to the surface (S_2). This observation can be interpreted in terms of an increased interaction of the phenyl legs due to the attached end groups. Moreover, it reflects the increased reactivity of the sulfur containing end group over the bromine terminated molecules.

This is different for the adsorption on Cu(100) and a large variety of conformations and orientations (Fig. 3.38c,d) are identified. Whereas Co-TBrPPs preferentially adsorb in a saddle conformation, Co-TPPs are primarily found in the S_3 conformation,

which we interpret as a conformation with a perpendicular arrangement of phenyl legs. Since Co-TBrPP can also be found in a S_3 conformation, we can directly compare the orientations of molecules to each other. There is no difference in the molecular orientation of S_3 for H or Br terminated molecules. This supports the interpretation of a perpendicular arrangement of the S_3 conformation due to the inherent lifting of the bromine atom away from the surface minimizing the influence of the end group on the adsorption. Contrary, in the case of the S_1 conformation, a clear and distinct influence of the bromine atom is manifested in different orientations of molecules for Co-TPP and Co-TBrPP (see Table 3.1). This indicates a considerable interaction between the surface and the bromine atoms.

Cu(111)		0	$\pi/3$	$2\pi/3$	n.s.	irreg.		
Co-TBrPP (S_1)	cts	34	36	28		(8)		
Co-TBrPP (S_2)	cts				1			
TMeSPP (S_2)	cts	19	20	18		(7)		
Co-TPP (S_1)	cts	18	9	14		(1)		
Cu-TPP (S_1)	cts	36	30	43		(9)		
Cu(100)		0	$\pi/6$	$\pi/3$	$2\pi/3$	$5\pi/6$	n.s.	
Co-TBrPP (S_1)	cts		31	34	31	25	20	
Co-TBrPP (S_2)	cts						7	
Co-TBrPP (S_3)	cts	21						
Cu(100)		0	$\pi/12$	$\pi/4$	$5\pi/12$	$7\pi/12$	$3\pi/4$	$11\pi/12$
Co-TPP (S_1)	cts		6	4	10	7	6	14
Co-TPP (S_3)	cts	79						

Table 3.1: Observed frequencies of molecular orientations for different pairs of surfaces, TPP derivatives, and conformations following the classification introduced in Fig. 3.38, where 0 denotes the orientation of a principal symmetry axes of the surface. For Co-TBrPP on Cu(100), several molecules in other, statistically not significant (n.s.) directions are observed. Molecules with irregular shapes are found on Cu(111) surfaces as listed in brackets. The origin of these shapes (additional conformations, thermal decomposition during preparation, side products of the synthesis) remains unclear.

In STM images of TMeSPP (see Figure 3.37c and f) the aspect ratio of the short molecular side versus the long molecular side is approximately 1 : 1.8 on Cu(111) whereas on Au(111) the same ratio is approximately 1 : 1.1, in line with [28]. This indicates enhanced sensitivity of the sulphur terminated ends toward the surface compared to the case of hydrogen termination. Sulphur is known to undergo a strong binding to a gold surface [31]. Sulphur terminated molecules are established for the formation of self-assembled chemisorbed mono-layers from wet solutions [32]. Here, TMesPP molecules have been designed to clip the end of the phenyl group to the gold surface. The origin of the behavior on different substrates remains speculative as it will reflect a complex interplay of preferred adsorption site for sulphur and the whole molecule.

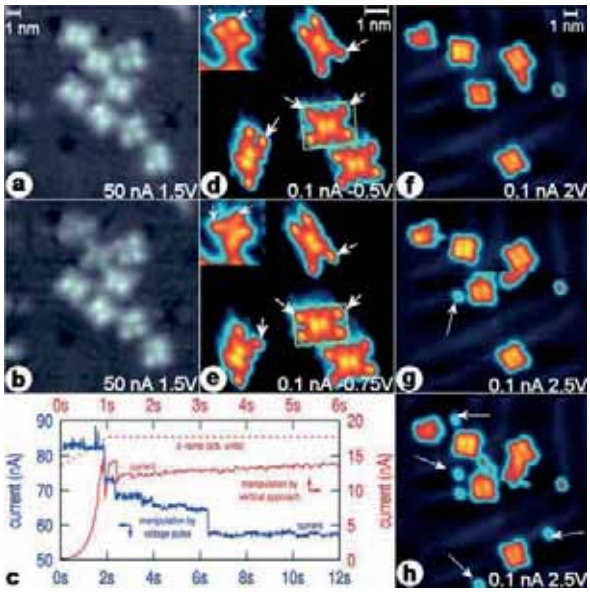

Figure 3.40: Examples of manipulation of TPP molecules: (a,b) Controlled switching of conformations for Co-TBrPP/Cu(100) and (c) the respective $I(t)$ curves as recorded during the manipulation process with characteristic jumps in the current due to reorganization of the molecules (red curve: by vertical approach of the tip toward the molecule - indicated by the dotted line -; blue curve: by a voltage pulse of +2.5V), (d,e) flipping of MeS terminated phenyl legs during scanning of TMeSPP adsorbed on Cu(111), and (f-h) dissociation of methyl-sulfur end groups at elevated bias settings for TMeSPP/Au(111).

Manipulation of molecular conformations

For illustration of molecular manipulation with the STM, Fig. 3.40a-h gives representative examples. In the first example, (a,b) Co-TBrPP molecules on Cu(100) are switched from a saddle conformation (S_1) into a rectangular conformation (S_2). Switching can be induced by applying a voltage pulse or an increase of tip-molecule interaction by reducing the tip-molecule distance. For both procedures, the variations of the tunneling current with time are recorded and plotted in Fig. 3.40c; the red curve shows the current variation during (1 s) and after tip approach (5 s). The jumps in the current in the first 0.5 s after approach reflect the reorganization of the molecular structure. Afterward the molecule is found in a new conformation, indicated by an arrow in Fig. 3.40a,b. The blue curve depicts the variation of the current directly after the bias voltage has been increased (from 1.5 V to 2.5 V at t=0). It is followed by a cascade of four individual current jumps, which are interpreted as tilting of each of the four phenyl legs [28]. Although no indication for a decomposition of Co-TBrPP during the manipulation process is found (as newly appearing adsorbates) such a decomposition cannot be fully excluded. Attempts to reverse the manipulation process as demonstrated for Zn(II) Etioporphyrin [33] were unsuccessful within a bias range of up to 2.5 V. It must be noted that larger voltages to induce such a reversal cannot be applied due to the dissociation of bromine atoms [34].

The second example addresses TMeSPP/Cu(111) (Fig. 3.40d,e). Four individual TMeSPP molecules can be identified. One of the molecules (lower left corner) - as it is rarely observed - was decomposed during thermal deposition with only three outer protrusions left. We attribute this to a missing methyl-sulfur or phenyl-methyl-sulfur group, which cannot be experimentally distinguished. Moreover, intact phenyl-sulfur groups show a high degree of flexibility when adsorbed on a Cu(111) surface. Already

in the imaging mode of the STM, phenyl legs are switching between two different conformations as marked by arrows (Fig. 3.40d,e). Flipping of phenyl legs is also observed for bromine terminated porphyrins and demonstrated in the inserts for Co-TBrPP/Cu(100).

The third example shows the dissociation of the methyl-sulfur group (Fig. 3.40f-h). By scanning at lower bias settings ($U \leq 2$ V), the molecules can be investigated without any modification. By scanning at elevated voltages ($U \geq 2.5$ V) a decomposition of TMeSPP molecules is observed. As a consequence, additional adsorbates appear afterward on the surface. We attribute this experimental observation to the dissociation of the methyl-sulfur group from the molecules. A similar effect is reported for Co-TBrPP, where under elevated bias settings bromine atoms were removed from the molecule [34].

Formation of long-range ordered molecular clusters

Deposition of molecules at room temperature or alternatively post-annealing of samples after low-temperature preparation lead to the formation of molecular islands. Several combinations of TPP molecules and substrates were studied with respect to their growth behavior. Among these, three representative examples are presented in Figure 3.41; Co-TBrPP/Cu(111) in Figure 3.41a, a mixture of Co-TPP and Cu-TPP on Au(111) in Figure 3.41b with the herring bone reconstruction of the substrate impinged into the organic layer, and Cu-TPP/Cu(111) in Figure 3.41c.

Cu-TPP, Co-TPP, and Co-TBrPP adsorbed on Cu(111) and Au(111) form regular networks. The structure of these networks is unaffected by an exchange of the metallic ion (see Fig. 3.41 b) and c)) whereas modification of the phenyl groups alters the unit cell sizes (see Fig. 3.41 a)). The unit cell consists of one molecule each with the molecule in a two-fold symmetric adsorption geometry. The observed symmetry indicates alternation of clock-wise and anti-clock-wise rotated phenyl groups. With the structure periodically reproduced it can be concluded that pairs of nearest neighbor phenyl groups are always perpendicularly rotated. Similar structures of self-assembled molecular clusters of TPP molecules and derivatives are reported but the underlying physics remained unresolved [11]. The case of pyridyl terminated porphyrins [10] which was also addressed by force field calculations is distinctively different as the numerical and experimental results suggest π-π stacking.

Modeling the dynamics and the assembly of porphyrin molecules

From the comparison of the molecular networks found for different porphyrin species it can be concluded that the adsorption of single molecules as well as the formation of molecular clusters are predominantly governed by the (substituted) phenyl legs, rather than the porphyrin core or the metallic center. Instead, the interaction of phenyl legs with atoms of the substrate system controls the adsorption of single molecules and formation of clusters. To better understand those issues, simulations on the (numeri-

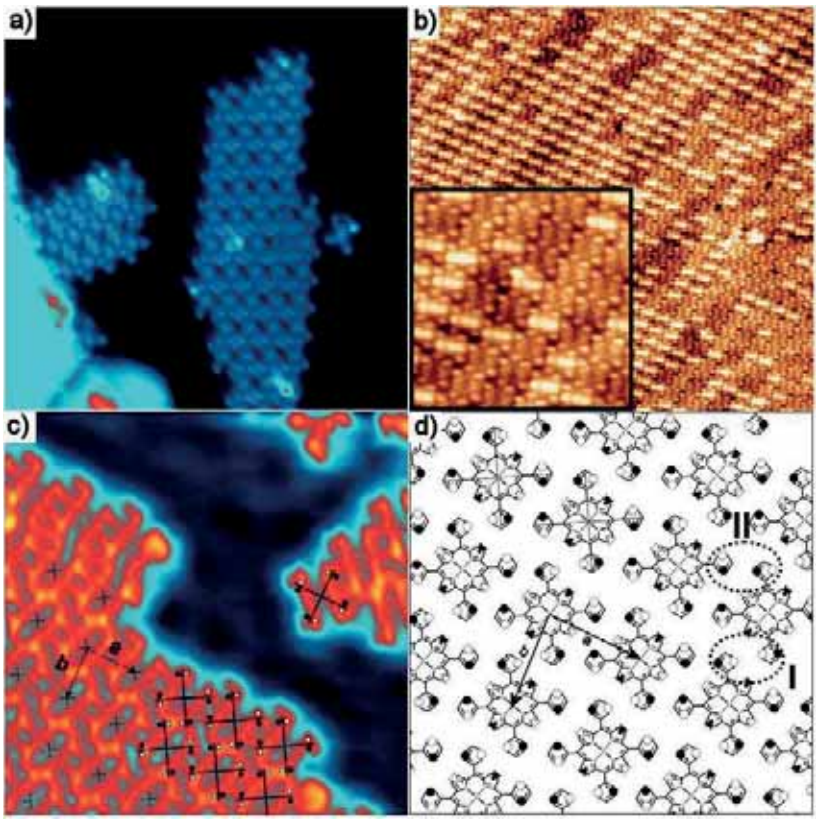

Figure 3.41: (a-c) Upon deposition or post annealing at room temperature hydrogen and bromine terminated metallic TPPs show strong tendency to form well ordered molecular islands on Cu(111) and Au(111) in STM images. (a) shows an aggregate of Co-TBrPP on Cu(111). In (b) a STM image after room temperature deposition of Co-TPP and Cu-TPP on a Au(111) surface is presented. The resulting structure is intermixed but well ordered with Co-TPP molecules showing the typical protrusion in the center. The herring-bone reconstruction of the Au(111) surface is transmitted through the organic layer. (c) shows a detailed view into the structure of a Cu-TPP island. For orientation, the center of each molecule is marked (x). Tilting of phenyl legs is indicated by ∘ and • as deduced from a molecule at the edge of a cluster with its internal structure well resolved. (d) depicts the proposed molecular alignment resulting from the analysis of the island. Phenyl legs next to each other are always perpendicularly arranged (indicated by circles I and II). The connecting lines between two opposing ends (△ and ▲, respectively) mark mirror axes of the porphyrin core (Co-TBrPP/Cu(111) : $a = 1.70 \pm 0.10$nm, $b = 1.50 \pm 0.10$nm, $\angle_{ab} = 83 \pm 5°$; Co-TPP & Cu-TPP / Au(111) : $a = 1.45 \pm 0.05$nm, $b = 1.40 \pm 0.05$nm, $\angle_{ab} = 87 \pm 3°$; Cu-TPP / Cu(111): $a = 1.29 \pm 0.05$nm, $b = 1.36 \pm 0.05$nm, $\angle_{ab} = 80 \pm 5°$). (a) $U = -0.37$ V, $I = 166$ pA; (b) $U = -1.2$ V, $I = 100$ pA; (c) $U = 0.14$ V, $I = 340$ pA;

cally) simplest case of a metal-free porphyrin (H_2-TPP) in interaction with a Au(111) surface have been performed.

First, a single isolated molecule in the gas phase, i.e., without interaction with any

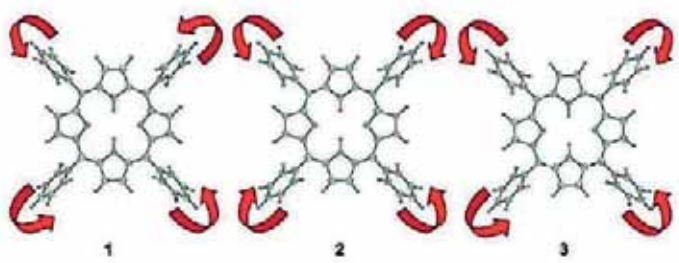

Figure 3.42: Three conformations of TPP in the gas phase related to minima in the potential energy surface. The tilting of phenyl legs is denoted by arrows. Conformation '1' is denoted as propeller shape within the text. Conformation '2' is the molecule in its global minimum.

other object - a surface or a neighboring molecule - was studied at the DFT B3LYP/6-31+G(d) level, in order to determine accurately the conformational behavior.

In the global energy minimum ('2' in Fig. 3.42) the phenyl groups are tilted by 65 degrees relative to the plane of the porphyrin core, in agreement with previous calculations [35]. The porphyrin core remains planar but the four-fold symmetry is broken due to a specific arrangement of the phenyl groups with opposite orientations of neighboring phenyl groups (structure '2' in Fig. 3.42). This results in a C_{2v} symmetry. Other, energetically less favored conformations are a propeller shape ('1' in Fig. 3.42) configuration (by about 0.5 kcal/mol) and configuration '3' (in Fig. 3.42) where three phenyl groups are parallel oriented and opposite to the fourth phenyl group (C_1 symmetry group, by 0.2 kcal/mol).

To pass from one structure to the other, the phenyl rings can pass through two possible transition states. The first transition state has a tilt angle of 90° with a low energy barrier to overcome (0.4 kcal/mol). Passing the other transition state, with a tilt angle of 0° (i.e., with the phenyl ring in the plane of the core), is rather unlikely due to a high transition barrier (16.3 kcal/mol). This high energy barrier of 16.3 kcal/mol reflects the repulsive interaction between hydrogen atoms in ortho positions of the phenyl ring and hydrogen atoms of the pyrrole ring.

A dynamic simulation of an isolated molecule with the MM3 force field (depicted in Figure 3.43) confirms the DFT results. Indeed the simulation reveals a continuous and uncorrelated rotation of all phenyl legs through 90° at 300 K. This free rotation is expected to be strongly reduced upon adsorption.

Next, modeling of the adsorption of a single molecule on a Au(111) surface was done. In the starting configuration, the TPP molecule is adsorbed in a propeller shape configuration on top of gold (see Figure 3.44A). The molecule as well as the first gold layers are free to relax in the time dependent simulation.

The time evolution of the tilting of phenyl groups and bending of the porphyrin core is depicted in Figure 3.43 (b) and (c). After a short time period of less than three ps, the porphyrin rearranges on the surface into a C_{2v} geometry and keeps it during the whole simulation period. This rearrangement favors the deformation of the core of the

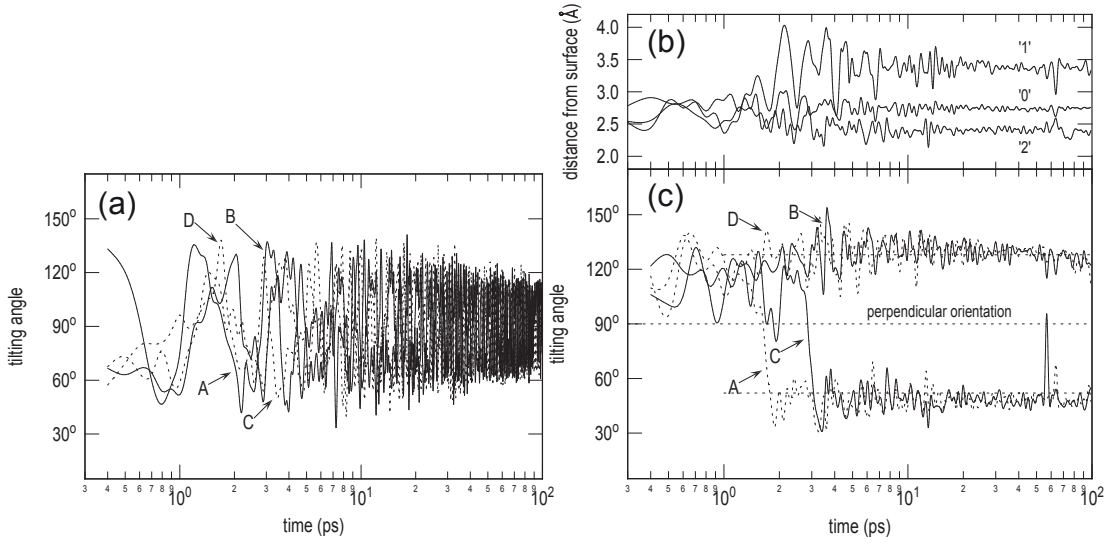

Figure 3.43: (a) Time evolution of tilting angles of the phenyl legs with respect to the plane of the core, at a simulation temperature of 300 K. At this temperature the phenyl legs continuously flip and the TPP porphyrin undergoes transitions between the global minimum (2 in Figure 3.42) and local minima (1 and 3) through 90°. Left panels: Time evolution of H_2-TPP adsorption on Au(111). The simulation starts with the molecule in the propeller shape geometry. (b): Within 3 ps the molecule rearranges into a mirror symmetric conformation with the porphyrin core undergoing a transition into a saddle conformation. This is reflected by the increase of the distance from location '1' and by the decrease of the distance from location '2' relative to center of mass denoted as '0'. Positions of '0','1', and '2' are defined in Fig. 3.36. (c): The phenyl legs (A-D) align in well defined orientations relative to the surface plane with the directions alternating relative to the surface normal (C_{2v} symmetry).

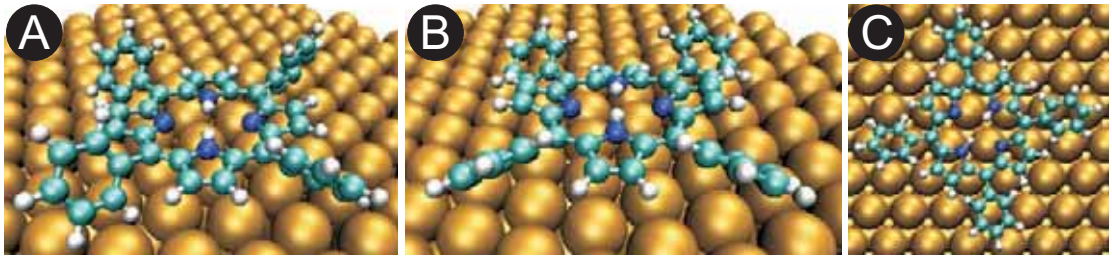

Figure 3.44: (A) shows the initial configuration of the simulation with a TPP molecule in the propeller shape conformation. During the course of simulations the porphyrin core bends into a saddle conformation and phenyl legs rearrange. (B) and (C) show the final configuration with the center of the porphyrin molecule located on top of a hollow site.

porphyrin to increase the adsorption energy on the gold surface. An adsorption energy of -77.2 ± 1.3 kcal/mol is computed (the adsorption energy is defined as the difference between the energy of the complex (molecule on surface) and the sum of the energies of the molecule and the surface). The final saddle conformation of the molecule after relaxation is illustrated in Figure 3.44B; in such conformation, the 'back' and 'front' pyrrole rings are tilted with their nitrogen atoms pointing upwards while the 'left' and 'right' pyrrole rings are tilted with their nitrogen atoms closer to the surface. The molecular axis is tilted by 10° relative to the crystallographic axis, with the central position located above a hollow site (see Figure 3.44C).

Comparison of experiment and simulation

Based on the adsorption geometry obtained for a single molecule, a self assembly of four porphyrin molecules is built as the elementary structure for a periodic simulation of a full layer and then optimized. The result of this simulation is depicted in Figure 3.45b. The following lattice parameters are obtained: $a = 1.47 \pm 0.03$nm, $b = 1.50 \pm 0.02$nm, and an opening angle of $89.0 \pm 1.6°$. Due to the C_{2v} geometry of adsorbed molecules, phenyl rings of adjacent molecules interact in a T-shape arrangement. It is well known that the most stable configuration for a benzene dimer is the T-shape conformation, in which the two molecules are perpendicular to each other, with one hydrogen atom of the first molecule pointing to the center of the π system of the second one [38]. The presence of a similar conformation here, between phenyl rings of adjacent molecules, indicates the existence of attractive intermolecular interactions which most probably play an important role in the supramolecular organization.

In order to confirm the importance of the orientation of the phenyl groups on the supramolecular organization, the growth of TMeSPP on Au(111) was compared to Co-TPP. As a consequence of the sulphur termination, the phenyl groups are forced into a (more) planar conformation and thereby suppressing the T-shape attractive interactions between the phenyl groups on adjacent molecules. This would impede the formation of self-assembled molecular structures. TMeSPP molecules were deposited

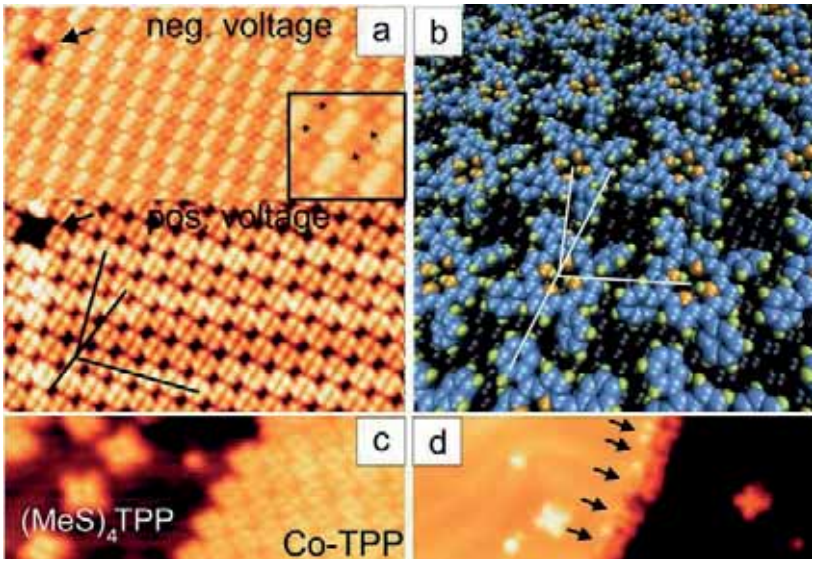

Figure 3.45: Comparison of experimental observations and results from numerical simulations: (a) shows two images of the same Co-TPP island on Au(111) for negative and positive voltage (a defect in the molecular island serves as a marker). The internal molecular structure is clearly resolved. For each molecule protrusions of its four phenyl legs can be identified (see inset) and the molecular axis is tilted relative to the unit cell of the molecular lattice. In agreement, the result of the numerical simulation (b) reflects the same tilting of the molecular axis, the same unit cell, as well as the same arrangement of molecules relative to each other. For orientation, the axes of the unit cell and the molecular axis are indicated. In contrast, (c) and (d) illustrate the role of the phenyl legs for a modified TPP. (c) Whereas Co-TPPs form islands TMeSPP molecules stay isolated when prepared on the same surface in parallel. However, under the given preparation parameters TMeSPP are sufficiently mobile and (d) step edges are fully decorated by TMeSPP.

on the surface at room temperature and studied at 25 K. STM images from this system reveal that self-assembly does not occur (see Figure 3.45c and d) although under the preparation conditions thermally induced mobility is sufficient for the formation of islands and therefore, Au(111) step edges are fully decorated (Figure 3.45d).

Then, on top of the same system Co-TPP was deposited at room temperature. Among the isolated TMeSPP molecules well ordered islands of Co-TPP are formed (Figure 3.45c). The unit cell of this island is determined to be a=1.45±0.05 nm, b=1.40±0.05 nm and has an opening angle of 87±3°. The same unit cell is observed for a mixture of Co-TPP and Cu-TPP / Au(111) (Fig. 3.41 b). Individual molecules show a C_{2v} symmetry with the molecular axis tilted by 22° relative to the unit cell. Within the error bar of experimental results we find excellent agreement with the results of the simulation of the self-assembly, as illustrated in Figure 3.45b.

Conclusions

The adsorption geometry, i.e., conformation and orientation of TPP molecules with respect to the underlying substrate is not influenced by the metallic center (Co ion vs. Cu ion) but is determined by attractive interaction of the phenyl legs with the substrate and steric, repulsive interaction with the pyrrolic units of the porphyrin macrocycle.

The interaction of the molecules with the substrate results in a characteristic deformation of the porphyrin core with three distinctively different resulting conformations identified. Whereas on Cu(111) for each molecular class only one preferred conformation was found after adsorption at ≈25K, the presence of molecules in different conformations when adsorbed on Cu(100) indicates quenching of metastable conformations. This interpretation is supported by previous experimental observations in terms of temperature effects and the impact of molecule-molecule interaction. When Co-TBrPP is prepared on Cu(111) at considerably higher temperatures (≈ 100K) two different conformations instead of only one are reported to occur, see Ref. [28]. Whereas Co-TPP, Ni-TPP, and Cu-TPP on Au(111) prepared at room temperature form highly ordered molecular islands with the metalated TPP molecules stabilized in the S_1 conformation with C_{2v} symmetry co-preparation of metalated TPP and metalated phthalocyanine molecules on Au(111) results in highly ordered molecular islands with the metalated TPP molecules stabilized in S_3 conformation with C_4 symmetry due to the altered molecule-molecule interaction [29, 30]. Both observations suggest that the energy differences between the different conformations are low and indicate a possible route to controllably steer the stabilization of TPP molecules in one or in the other conformation through temperature or the environment.

Switching between different conformations as well as manipulation and dissociation of methyl-sulphur terminated phenyl legs as induced by the probe tips are demonstrated.

A systematic study of the growth behavior of tailor made tetraphenyl porphyrins adsorbed on Cu(111) and Au(111) is presented and compared to results of DFT cal-

culations and, for the first time, to the numerical simulation of the dynamic behavior of tetraphenyl porphyrins in the gas phase, of individual molecules in contact to a metallic substrate, and of an assembly of molecules interacting with each other and in direct contact with a metallic surface. The comparison shows excellent qualitative and quantitative agreement. Within molecular clusters, relative orientations of molecules is T-stacking like. This maximizes the interacting molecular surface and explains similar observations for molecular crystals. Further experimental evidence is given by the intended suppression of self-assembling for the newly introduced TMeSPP due to an increased surface attraction via sulphur termination.

3.7.2 A novel molecule in scanning tunneling microscopy: The corrole.

S. Kuck, M. Prostak, G. Hoffmann, M. Bröring, M. Fechtel, M. Funk, and R. Wiesendanger

Introduction

Corroles are tetrapyrrolic macrocycles that are closely related to porphyrins, with one carbon atom less in the outer periphery and one NH proton more in the inner core. The first successful synthesis was done by Johnson and Kay in 1964, where they got corrole as an intermediate product of their initial synthesis of corrin [39]. Corrin is a part of vitamin B_{12} [40]. The contracted coordination of the core and the fact that they act as trisanionic ligands leads to a special feature of corroles relative to porphyrins, i.e., the stabilization of metal ions in high oxidation states [41]. The latter feature leads to more intense metal-ligand interactions in metal chelates and to interesting electronic structures. Corroles have been developed in the past decade to be a very accessible, easily tunable compound with many potential applications in material science and catalysis. The study on corrole molecules presented here was done with derivatives of the triphenylcorrole (TPC) with a central iron ion (FeTPC). Figure 3.46 gives an overview of FeTPC employed in our work and their appearance in STM images.

FeTPC appears without any symmetry. Each molecule has three dominant protrusions at its opposite ends which represent the phenyl legs and one unoccupied end which breaks mirror symmetry. For the corrole center, we find an accentuated backbone in cigar shape with one side highlighted. This side is located between two outer protrusions. The interpretation of the adsorption geometry follows in a natural way the observed symmetry. The corrole macrocycle is deformed into a saddle conformation and all three phenyl legs are twisted relative to the surface normal. The accentuated backbone reflects the upward bent pyrrolic units of the corrole macrocycle, whereas the other pyrrolic units show toward the surface plane. Additionally, the macrocycle

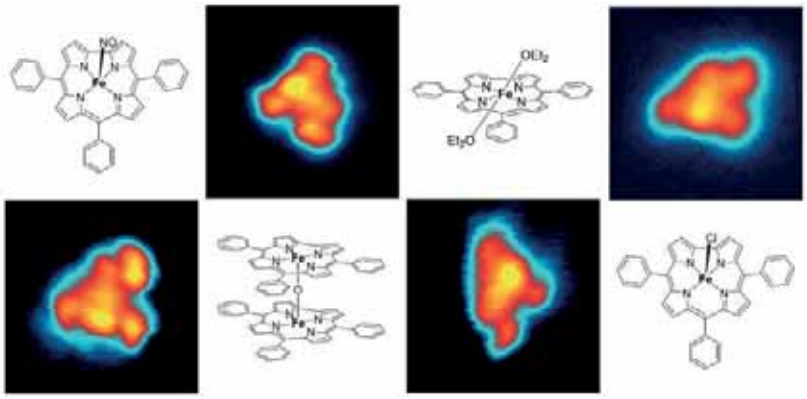

Figure 3.46: Iron(III)-triphenylcorroles with different axial ligands employed in this study. The corresponding STM image is shown above / below.

is slightly tilted relative to the plane of the substrate due to the asymmetry of phenyl legs with one side lifted by the supporting phenyl legs.

Disposition of the axial ligand during physical vapor deposition

When the disposition of an axial ligand is unresolved, this potentially hampers a correct interpretation of experimental data. Here, we systematically address the axial ligand (X) in the system of FeTPC-X with X = NO, 1/2 O, Cl, and $(Et_2O)_2$ adsorbed on Cu(111) in a scanning tunneling microscopy study. We discuss undesired side effects due to released axial ligands which are co-adsorbed on a surface. NO is identified as the most appropriate axial ligand for in-situ preparation of uncoordinated FeTPC whereas the adsorption of axially coordinated FeTPC was not observed.

Fig. 3.47a shows the result of a preparation of the FeTPC complex with NO as axial group. Entities of one to three individuals are recognized on the surface. The result of the preparation of the double-decker complex appears similar (Fig. 3.47b). In this case neither intact double-deckers nor two different FeTPCs are found. The presence of two different FeTPCs would be an indication of partially remaining oxygen in the axial position. This is not given. Entities of one and two individuals are in convenient agreement with the preparation of FeTPC-NO and are therefore attributed to intact FeTPCs without axial ligands.

For FeTPC-Et_2O and FeTPC-Cl (Fig. 3.47c,d) not only double and triple entities are identified, but in addition patches of stripe patterns are observed. These stripe patterns follow the crystallographic axes of the hexagonal substrate. Observed additional structures after preparation of these complexes indicate a significant amount of adsorbates evolving as side products of a continuous dissociation of axial ligands during sublimation (Fig. 3.47c,d). Based on numerical calculations in combination with magnetic experiments the release of Cl was also proposed for FeOEP-Cl [42]. Not further investigated, diethylether (Et_2O) can be assumed as co-adsorbates during the

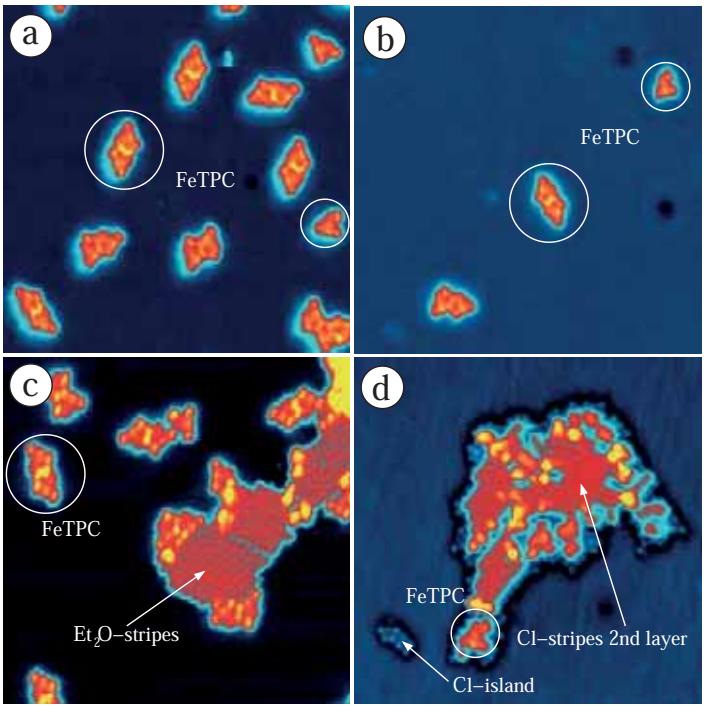

Figure 3.47: Topographic images of FeTPC molecules with (a) NO, (b) O, (c) Et_2O, and (d) Cl as axial groups deposited on a Cu(111) surface. (18×18 nm^2, $U = -1000$ mV).

preparation of the FeTPC-Et_2O complex. When thoroughly performed, such a system might be suitable for the investigation with scanning probe methods but certainly be not adequate for an approach by volume averaging techniques as FeTPCs are observed in direct electronic contact to Et_2O patches.

From the comparison of the STM images, we conclude that in all four cases a dissociation of the axial ligand already occurs during the sublimation and degassing process. Apart from a slight but not significant variation of molecular appearances which we attribute to the actual shape of the tip no indication for the adsorption of ligands in the axial position is identified.

Observation of chirality on a surface

A major consequence of the bending of the corrole macrocycle and twisting of phenyl legs is surface supported chirality. Exactly 12 different orientations and conformations are identified for the adsorption of FeTPC on Cu(111), Fig. 3.48. Six different orientations of the backbone and two mirror symmetric conformations of phenyl legs for each orientation are found. The backbones of the macrocycle are perpendicular to the closed packed rows of the underlying substrate (as previously determined by atomic resolution data) and the pyrrolic units which are bent toward the substrate, are parallel to one of the crystallographic axes of the substrate. Whereas the six orientations reflect the symmetry of the substrate the two different conformations reflect chirality.

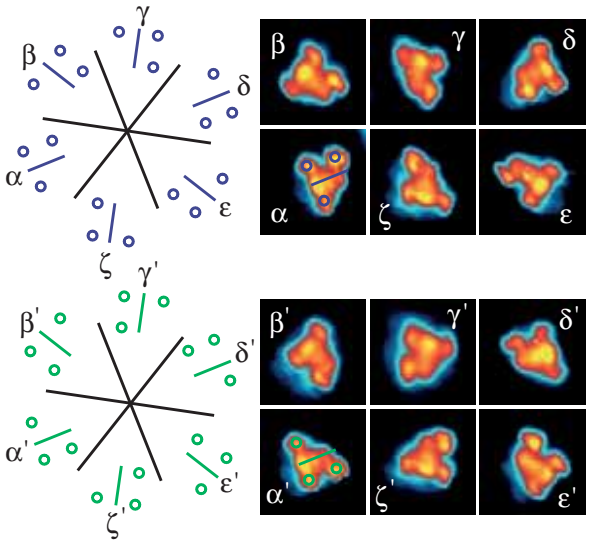

Figure 3.48: Representation of the different orientations and conformations of FeTPC on Cu(111) in STM images. For orientation, all 12 geometries (6 enantiomeric pairs shown in blue and green, respectively) are schematically indicated by the backbones (line) and phenyl legs (circles) along the crystalline axes of the Cu(111) substrate (black lines, all STM images 3×3 nm^2, $U = -1000$ mV).

Conclusions

In a pilot study we have now established the suitability of the simple iron complexes of 5,10,15-triphenylcorrole (FeTPC) for vapor deposition under ultra high vacuum conditions. The parent compound (FeTPC) arrives intact on the surface, while the axial ligands are dissociated during deposition. Furthermore, a surface supported chirality is found for the FeTPC adsorbed on Cu(111) [43, 44].

3.7.3 Controlled sequential dehydrogenation of single molecules by scanning tunneling microscopy

N. Baadji, S. Kuck, J. Brede, G. Hoffmann, S. Sanvito, and R. Wiesendanger

Introduction

The practice of inducing chemical reactions by passing a current through molecules deposited on surfaces is today well established in the STM community. The basic concept includes selectively exciting those particular vibrational modes driving the desired reaction. This strategy has been adopted to move, desorb or dissociate small molecules on surfaces [45–48], to fuse two molecules together [49], or to manipulate the bonding geometry between the molecule and the surface [50, 51]. In most of these situations it is easy to establish that a reaction has occurred from a clear change in the topographic STM images before and after the reaction. For instance, the fingerprint of a dissociation is the detection of isolated byproducts around the position of the original molecule [45]. In some cases one can associate different molecules to seemingly similar topographic images, differing only by their orientation with respect to a known

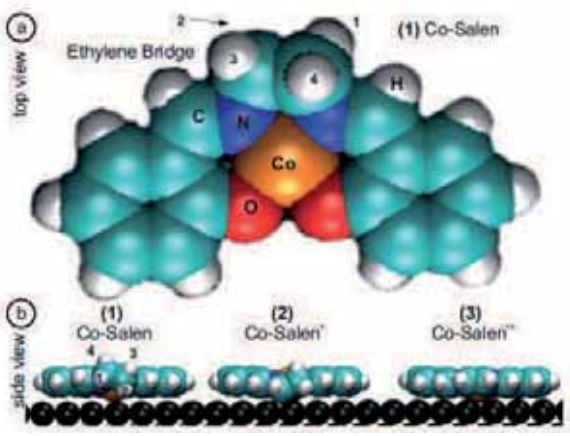

Figure 3.49: (The three Co-Salen molecules investigated in this work: **(1)** intact ($C_2H_4N_2$ apex), **(2)** single dehydrogenated ($C_2H_3N_2$ apex), and **(3)** double dehydrogenated ($C_2H_2N_2$ apex). Top and side views show the structures after numerical relaxation on the Cu(111) surface.

crystallographic direction of the substrate [50]. The identification of the reaction products then proceeds by chemical intuition and by comparing the topographic images with those of known molecules. Sometimes this is supported by a further comparison between the inelastic electron tunneling spectrum with available data on vibrational modes of the molecule [52].

A more complex situation is given when the system appears little "talkative", i.e. when the chemical reaction does not produce a major change in the geometry. An extreme case is represented by dehydrogenation of planar molecules. Here, one of the products of the reaction, the hydrogen, leaves the surface and therefore is not detectable. The other one, the molecule, changes only little its geometry. The study of such a reaction poses the ultimate challenge for STM.

The molecules of choice for this work are Co-N,N'-ethylenebis (salicydeneiminato) complexes (hereafter "Co-Salen"). Salens are versatile objects [53], which allow for the incorporation of a range of transition metals so that their electronic properties can be finely tuned. Due to their given planarity and robustness, Salens are also ideally suited to locally probe chemical and magnetic properties by scanning probe techniques [54]. In Co-Salen, the Co ion is bonded to two O and two N atoms. These form with the ethylene bridge (C_2H_4) a di-aminoethane ($C_2H_4N_2$) group [see figure 3.49] from which the hydrogen will be sequentially extracted in a STM-controlled dehydrogenation process [55].

Sample preparation and STM measurements

Tips and Cu(111) surfaces are prepared by standard procedures (alternating cycles of argon-ion etching and annealing) in an ultra-high vacuum (UHV) environment. In-situ, Co-salen molecules are dosed onto room-temperature Cu(111) surfaces by sublimation from homebuilt Knudsen cells. Due to repulsive interaction among adjacent molecules Co-salens stay isolated. Then after the temperature is decreased, surfaces are investigated at 25 K in a variable temperature STM [14], and spectroscopic results are reconfirmed with higher energy resolution in a bath cryostat system operated at

7 K [96].

STM images presented are obtained in the constant-current mode at the indicated current settings and bias voltages. Voltages refer to the potential of the tip relative to the sample, with positive voltages associated to tunneling into unoccupied sample states and negative voltages to tunneling out of the occupied ones.

For the acquisition of the differential conductivity, a modulation voltage (ΔU = 5 mV, f = 2.77 kHz) is added to the bias voltage and the modulation of the current due to contributions of the local density of states at the appropriate energy is recorded by a Lock-In amplifier (SR-830). Thereby, maps of the differential conductivity ($\mathrm{d}I/\mathrm{d}U$ maps) are obtained in parallel to constant-current images. Scanning tunneling spectroscopy data are obtained at selected positions, i.e. the feedback is disabled, the (x, y, z) coordinates of the tip are kept fixed and the bias voltage is ramped.

Simulated STM images

Simulated data are obtained from density functional theory (DFT) combined with the perturbative Bardeen's approach [56] for evaluating the STM current. DFT calculations are performed by using the localized pseudo-atomic orbital basis and pseudopotential code SIESTA [57].

The STM images, both in the topographic and spectroscopical mode, are calculated with a modified version of the Tersoff-Hamann scheme [60], which takes into account the electronic structure of the tip. Our scheme is conceptually similar to that of reference [61]. It is more insightful than the more standard Tersoff-Hamann approximation, which does not account for the electronic structure of the tip, but still computationally less demanding than fully self-consistent scattering theory [62].

Importantly, STS maps are also calculated in the constant-current mode, i.e. under the same conditions in which the experiments have been carried out. This eliminates any uncertainty about the interpretation of the $\mathrm{d}I/\mathrm{d}U$ maps in terms of the molecule's local density of state [63,64]. Practically we evaluate the tip-to-sample distance $z_0(x, y)$ yielding a given current along the molecule x-y plane and then evaluate the STS maps over such a surface.

Results and discussion

Figure 3.50(a) shows a representative image of six molecules directly after sample preparation as imaged at low bias (U = 1 V). Due to the out-of-plane tilted ethylene bridge, Co-Salen is chiral and adsorbs in two enantiomeric shapes in six orientations on the six-fold symmetric surface. The chirality is manifested by the asymmetric central position.

Since no data on dehydrogenated Co-Salens are available, we rely on theory for an unambiguous identification, namely on the atomistic details as calculated from density functional theory (DFT). The C_2H_4 bridge of the $C_2H_4N_2$ group of the intact

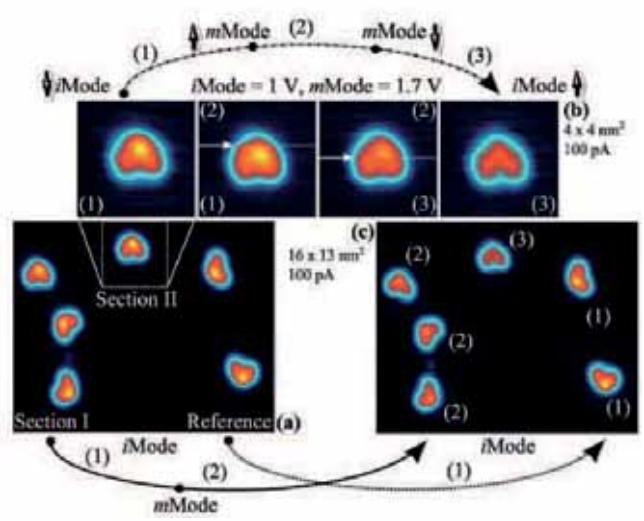

Figure 3.50: Manipulation of intact Co-Salen (**1**) by constant current imaging into its single- (**2**) and double- (**3**) dehydrogenated form at a bias voltage above the threshold for manipulation (*m*Mode). (a) An area with six (**1**) is selected. Two molecules serve as unaltered reference and are only imaged at low bias voltage (*i*Mode). Molecules in section I are imaged once, the molecule in section II twice in the *m*Mode. The top panel (b) shows the same molecule obtained during imaging in the *i*Mode and the *m*Mode. Whereas *i*Mode imaging does not affect the molecule, in each of the *m*Mode images a characteristic jump in the line scans is revealed (→). The first dehydrogenation is detected by a sudden reduction of the molecule apparent height (second panel). During the second dehydrogenation the molecule adopts a mirror symmetric shape (third panel). (c) shows the surface again in the *i*Mode. The reference molecules remained unmodified, whereas the molecules in section I and II transformed into (**2**) and (**3**). The top panel (b) shows the same molecule obtained during imaging in the *i*Mode and the *m*Mode (with the scan directions as indicated).

molecule (**1**) adsorbed on the Cu (111) is tilted by 20° with respect to the planar position. Thus, the C_2 symmetry is broken in correspondence of two enantiomeres in the experiment. One hydrogen is pointing toward the Cu surface [atom 2 of (**1**), Fig. 3.49(b)], one pointing out of it [atom 4 of (**1**), Fig. 3.49(b)] and the last two remaining approximately in the plane of the molecule. The central Co ion ends up at 2.7 Å above the Cu(111) hollow site.

The first dehydrogenation removes the most external H, thus leaving (**1**) with a $C_2H_3N_2$ apex [(**2**) of Fig. 3.49(b)]. In this rearrangement the double hydrogenated C becomes the most external atom of the molecule and is about 0.3 Å closer to the surface than the most external C in (**1**). The Co ion in (**2**) is displaced by 0.1 Å toward the surface, i.e. the molecule's apparent height has been reduced. Notably, also in this case the C_2 symmetry is broken. The second dehydrogenation [(**3**), Fig. 3.49(c)] transforms the Co-Salen apex into a cis-ethyl-diamino ($C_2H_2N_2$) group with a C double bond and yields a C_2 symmetry. The two peripheral hydrogens of $C_2H_2N_2$ lie in the

plane of the molecule, which is flat on the surface. This second dehydrogenation brings the entire molecule closer to the surface by 0.3 Å as compared to (**1**).

Next, we demonstrate our ability to produce the sequential dehydrogenation from (**1**) by STM manipulation. Imaging at low bias, i.e. $U \leq 1.5$ V, leaves the system undisturbed (*i*Mode) and is used to characterize molecules before and after each manipulation cycle. Whereas at elevated bias, i.e. $U > 1.5$ V, Co-Salens are modified (*m*Mode) and undergo a characteristic and irreversible transition. The transition reflects two dehydrogenations of the C_2H_4 bridge equally observed in point manipulation and *m*Mode imaging with identical intermediate **(2)** and final **(3)** products. Figure 3.50 demonstrates the dehydrogenation during scanning in the *m*Mode for six neighboring Co-Salens. During the manipulation cycle, two molecules serve as unaltered reference. Once switched (section I), Co-Salen remains chiral whereas the double dehydrogenated Co-Salen (section II) adopts a mirror symmetric appearance at reduced apparent height. Note that the height reduction and the symmetry of the images are already consistent with identifying the products with (**2**) and (**3**).

The signature of the dehydrogenation process is also given by two characteristic jumps in the recorded current during local STS experiments as presented in Fig. 3.51a. Up to the threshold voltage the current is stable (*i*Mode). Beyond that value, i.e. in the *m*Mode range, sudden current jumps occur regularly. Each change in the current reflects one irreversible dehydrogenation process, highly reproducible with a symmetric final product. The induced dehydrogenation preferentially occurs, when the electron source (tip) is located close to the C_2H_4 bridge. As the rate of transitions does not show any non-linear current dependence, the origin of the processes can be attributed to an energy exchange between a single tunneling electron ($E = eU > 1.5$ eV) and the ethylene group. Apart from the induced change of molecular appearance no other byproducts are observable in the STM images.

Figure 3.52(a) shows calculated and experimental topographic images side by side. As one can easily see in the case of both (**1**) and (**2**) the largest intensity is always in between the Co center and the $C_2H_4N_2$ apex and the mirror symmetry is broken. A broken symmetry persists for all the applied bias voltages. This is different from what happens for (**3**), whose topographic images remain always symmetric. A richer analysis can be obtained in the spectroscopical mode.

STS data taken from the sites of the Co ion [Fig. 3.51(b)] reveal a subtle but significant and characteristic change in the local density of molecular states before and after the double dehydrogenation. This can be explored in details by STS mapping of the molecular states, i.e. by spatially resolved maps of the differential conductivity at specific energies. The comparison between theory and experiments is presented in Fig. 3.52(b) where the three molecules are juxtaposed and data are shown for three representative voltages (small U=800 mV, moderate U=1000 mV and large U=1400 mV). The picture demonstrates a substantial quantitative agreement between the experimental and simulated STS maps and allow us to identify with certainty the three different molecules as (**1**), (**2**) and (**3**). Having identified with certainty the

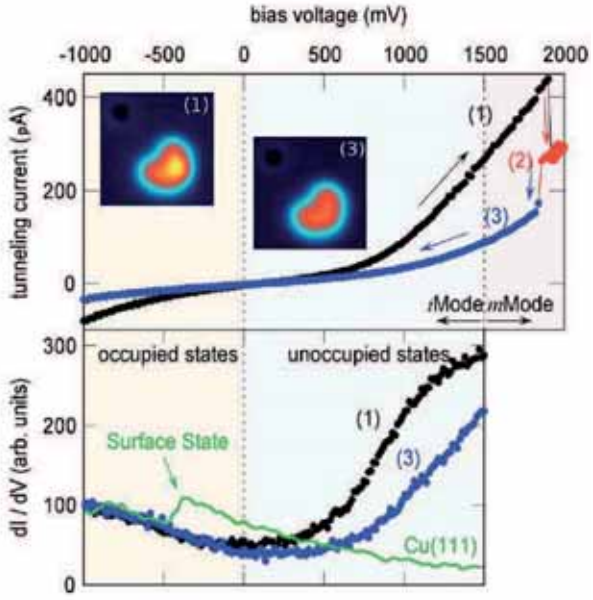

Figure 3.51: The transformation from (**1**) into (**2**) and (**3**) is efficiently achieved by voltage pulses above the C_2H_4 bridge at constant height. With the current monitored, characteristic jumps reveal the moment of dehydrogenation which is only observed above the threshold voltage of 1.5 V. In (a) the recorded current during such a manipulation is presented which shows two abrupt changes. This is indicative for the transition from (**1**) into (**2**) and finally (**3**). Respectively, the images before and after (see insets) show complex (**1**) and (**3**). With the voltage limited to 1.5 V (b), STS data on the differential conductivity manifest a quantitative change in the spectra. Whereas no significant change in the occupied states is found (U <0), unoccupied states (U >0) are shifted toward higher energies after dehydrogenation. The copper spectrum is recorded for the characterization of the tip status at a location nearby with the clear signature of the Cu(111) surface state.

reaction products we now turn to the energy needed for the dehydrogenation, i.e. the energy associated with the following two reactions

$$C_2H_4N_2 \rightarrow C_2H_3N_2 + \frac{1}{2}H_2\,, \tag{3.29}$$

$$C_2H_4N_2 \rightarrow C_2H_2N_2 + H_2\,. \tag{3.30}$$

These are evaluated from the difference in total energy between the intact molecule and the two products of reaction as calculated by DFT. The reference energy for hydrogen is that of the H_2 molecule in vacuum. We obtain 1.49 eV and 1.75 eV, respectively, for the single and double dehydrogenation. These calculated values are thus in rather good agreement with the voltages necessary for dehydrogenation, which are larger than 1.5 V.

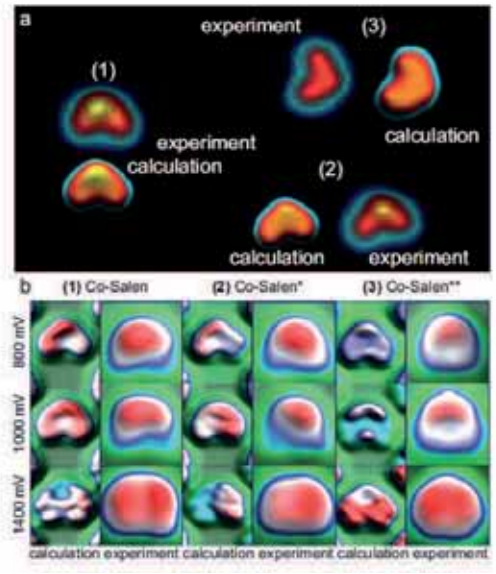

Figure 3.52: STM/STS maps for the three molecules investigated. In (a) we present the experimental and the simulated topography of Co-Salen adsorbed on Cu (111). The images were taken at a voltage of U=1.4 V. Note that the mirror symmetry is broken for (**1**) and (**2**) but not for (**3**). In panel (b) the experimentally measured STS maps are compared with the calculated ones at three representative voltages of 800 mV, 1000 mV and 1400 mV. The color scale is identical within each row and the very same tip is used for all the images. In the simulated images the periodic replica of the unit cell appear at the edge of the figure. In addition to a general increase of the molecule's lateral extension with bias, we remark three main features: 1) in (**1**) the largest intensity is on the left-hand side of the $C_2H_4N_2$ apex and shifts to give a more symmetric image at higher U; (**2**) is similar to (**1**) except that the asymmetry persists at higher U; (**3**) remains symmetric at all voltages with the maximum intensity at $C_2H_2N_2$ apex for small U and a shallow minimum at the same position for large U.

Conclusion

In conclusion we have investigated the ultimate limit offered by STM techniques for both imaging small molecules and manipulating their geometry. In particular we have demonstrated that sequential dehydrogenation of the planar Co-Salen is possible with both single point spectroscopy and slow scan at high voltage. In the process, we have been able to detect not only the final product of the dehydrogenation, but also an intermediate reaction product in which a single H atom is dissociated. This is a particularly delicate test for STM, since the reaction products do not show any specific change in bonding configuration and they are not known *a priori*. Thus the interpretation of the data is done by comparing the experimental data with state-of-the-art STM simulations based on density functional theory. This work demonstrates that STM combined with theory can be a fully quantitative tool for studying surface chemistry.

3.7.4 Symmetry effects of metal phthalocyanines on copper surfaces

S.-H. Chang, S. Kuck, J. Brede, L. Lichtenstein, G. Hoffmann, and R. Wiesendanger

Imaging of metal phthalocyanines (MPcs) and of their intramolecular structures by STM was first achieved by Gimzewski *et al.* [65] and Lippel *et al.* [66] under UHV condition. Until now, various MPcs (M = Cu [65, 66], Co [87], Fe [67], Ni [68], Pd [69], Zn [70], Mn [71]) have been studied on many surfaces: they adsorb in a planar configuration and exhibit four-lobed cross shapes in STM images. The central metal ion appears either as a dip or as a protrusion in STM images depending on the energetic position of the d_{z^2} orbital with respect to the Fermi level [68]. For the growth behavior on metallic surfaces Cu, Au, Ag, and graphite, no ordered structures are found at low coverages. With increasing coverage, ordered molecular domains start to appear and form a complete molecular monolayer before the formation of the second molecular layer begins [67–70]. Upon further increase of coverage, self-assembling in higher layers can be observed with the molecular plane parallel [86] or tilted [67] toward the surface plane.

In the low-coverage regime, the physical properties of isolated MPcs on metallic substrates are dominated by the molecule-substrate interaction. For instance, this manifests for some magnetic MPcs in a Kondo resonance [71]. The distance between magnetic centers of MPcs and substrate [87] as well as the exact adsorption site were found to strongly modify the Kondo temperature. For metallic substrates, three orientations of FePcs have been reported for the adsorption on Cu(111) [67] and Au(111) in the sub-monolayer regime, which reflect the substrate symmetry. Low-energy electron diffraction (LEED) observations exhibited two orientations for CuPcs and FePcs on Cu(100) of $\pm 22.5^\circ$ relative to the <001> direction [72]. Later, this was reconfirmed by STM experiments on CuPc on Cu(100) [66].

However, in the above experiments molecules were evaporated onto surfaces being held either at room temperature or above and therefore, MPcs adsorbed in stable configurations. It remains an open question whether there are more meta-stable configurations, which might have different properties than stable ones when adsorbed on surfaces at low temperatures. In addition, the adsorption of fourfold symmetric MPcs on substrates with commensurate and incommensurate symmetries, as Cu(100) and Cu(111), respectively, can provide a valuable contribution to the understanding of molecule-substrate interactions.

In this study three kinds of MPcs (M = Cu, Co, and Fe) were employed [73]. The molecular sources were thoroughly degassed and sublimated onto the sample at low temperatures (20-35 K).

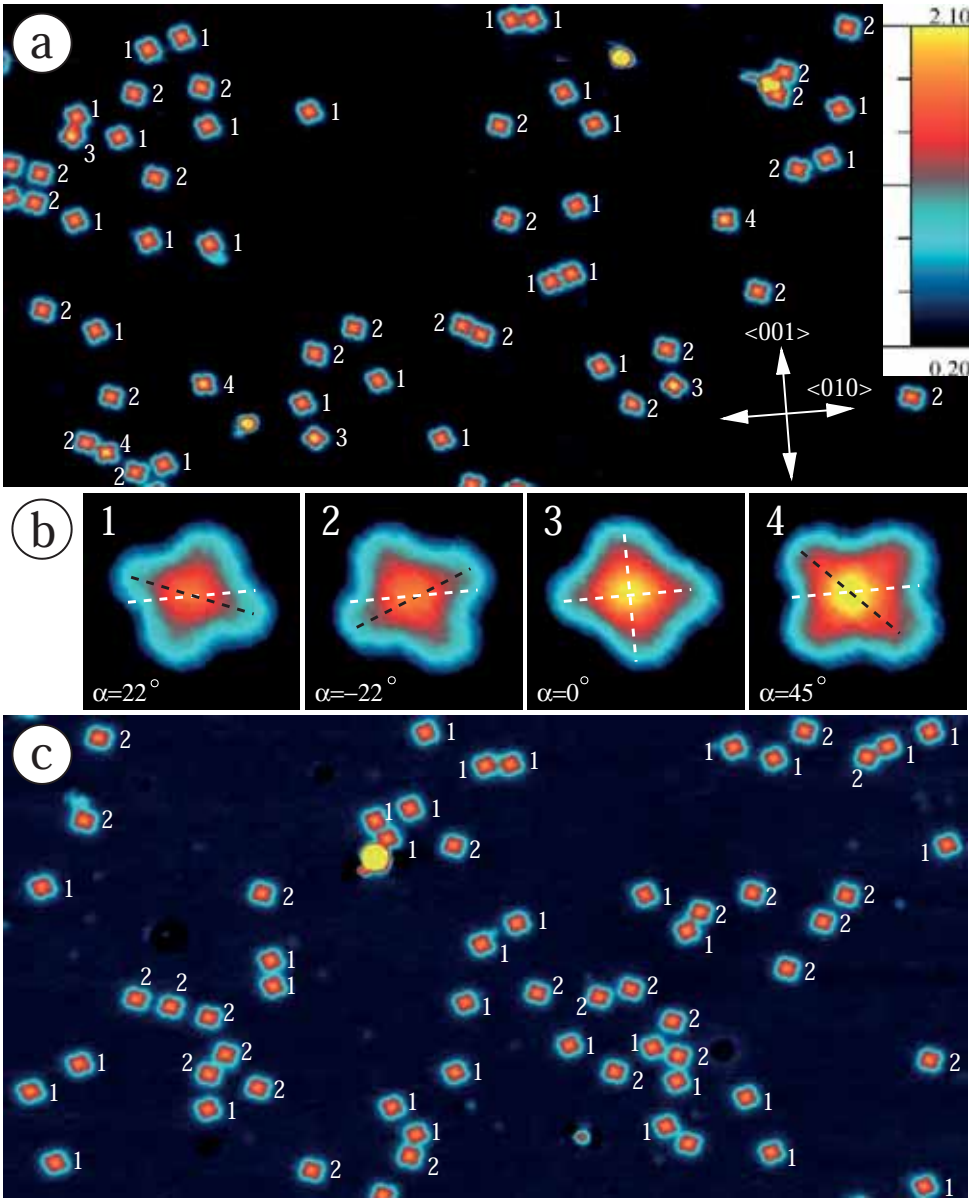

Figure 3.53: STM images of CoPc on Cu(100) prepared at 29 K (a) and after post annealing to room temperature (c) (60 × 30 nm^2, U= −1200 mV). (b) Magnifications of four different orientations as marked in (a) with 1–4 (3 × 3 nm^2). In (a), a set of arrows reflects the crystallographic axes of Cu(100) as determined from the clean surface. In (b) one crystallographic axis (white dotted line) and one molecular axis (black dotted line) are indicated.

Meta-stable configurations of metal phthalocyanines on Cu(100)

Figure 3.53a shows a STM image of a stepped Cu(100) surface with adsorbed CoPcs. CoPcs are arbitrarily distributed while copper steps remain uncovered. Four different adsorption orientations are identified. For each orientation, enlarged images of

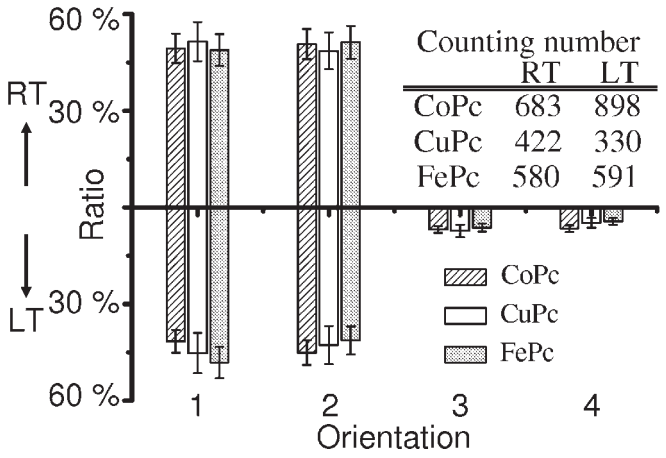

Figure 3.54: Relative frequencies of adsorption orientations for CoPcs, CuPcs, and FePcs on Cu(100) after preparation at room temperature (RT) and at low temperature (LT). The statistical error is indicated.

representative CoPcs are plotted in Fig. 3.53b. CoPcs appear in their characteristic four-lobe structure with a bright center similar to the appearance on other metals [87], suggesting a planar structure. Upon closer inspection, the molecular axes of configuration 3 are found to be parallel with the crystallographic axes of Cu(100). The molecular axes of configurations 1 and 2 are rotated by $\sim \pm 22°$ and of configuration 4 by $\sim \pm 45°$ with respect to configuration 3 and to the crystallographic axes, respectively. Relative frequencies of molecular configurations clearly manifest two groups of distributions as shown in Fig. 3.54: orientations 1 and 2 ($\sim$87%) significantly dominate over orientations 3 and 4 ($\sim$13%). Within each group different orientations have almost identical appearing rates. Within the limits of statistical significance, an identical distribution of molecular orientations can be found for FePc and CuPc on Cu(100) (see Fig. 3.54).

The observation of four different orientations of CuPc, CoPc, and FePc on Cu(100) is in apparent disagreement with previous findings for CuPc and FePc on Cu(100) [66, 72]. In previous findings, after room temperature preparation STM and LEED data reveal an alignment of MPcs in only two orientations ($\pm 22.5°$) corresponding to orientations 1 and 2 of this study. The disagreement suggests a decisive temperature effect. To test the influence of preparation temperature, samples were annealed to room temperature and the resulting surface structures were compared to those of samples after room temperature preparation. In both cases the observable orientations are reduced to the previously reported orientations. This is demonstrated in Figs. 3.53c and 3.54. Consequently, orientations 3 and 4 have to be assigned to meta-stable configurations.

Under the given scanning conditions (U$\leq$2000 mV, I$\leq$300 pA) the appearances of benzene groups of MPcs are identical as shown in the line profiles crossing MPcs in stable and meta-stable configurations (Fig. 3.55b). However, the apparent height at the metallic centers varies significantly with the configuration of MPcs. In Figs. 3.53 and 3.55b the molecular center of the meta-stable configurations of CoPc at $U = -1200$ mV appears significantly higher (Δz$\sim$0.25 Å) than the stable configuration. The effect is

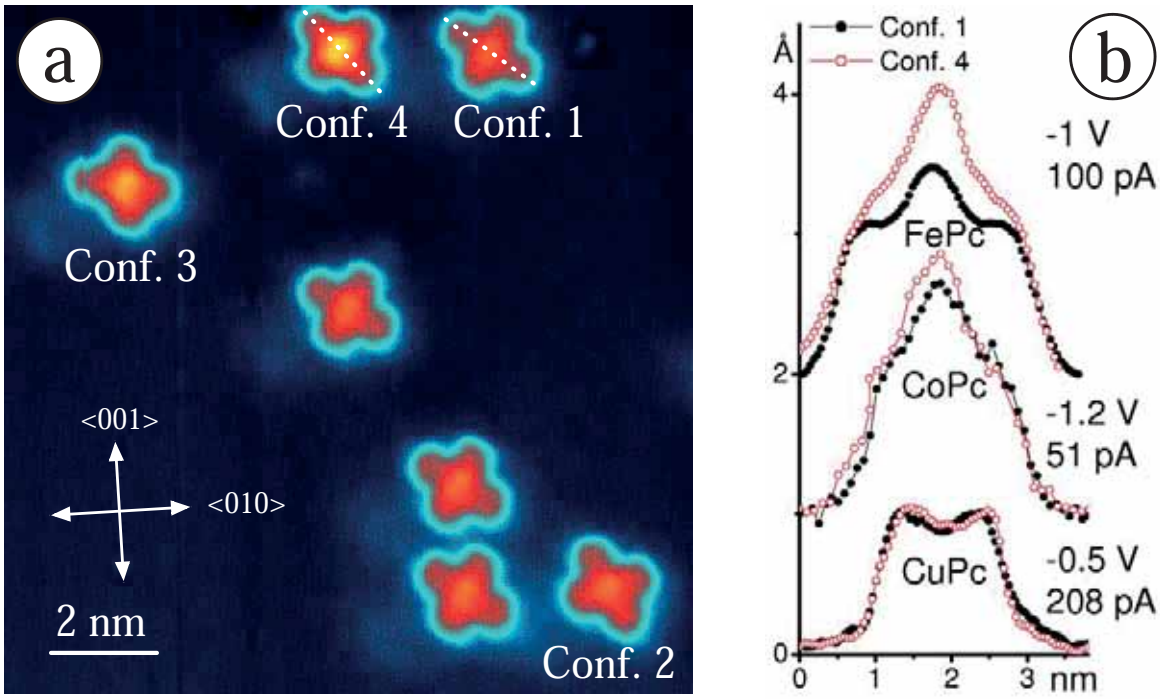

Figure 3.55: (a) STM image of FePcs on Cu(100) prepared at low temperature. (b) Line profiles crossing configurations 1 and 4 of FePc, CoPc, and CuPc. For each pair of line profiles identical tips were used.

more pronounced for FePcs (see Figs. 3.55a+b) but is not observed for CuPcs. This is further evidence that the d_{z^2} state is very sensitive to the local environment.

Symmetry reduction of metal phthalocyanines on Cu(111)

In another experiment, the growth of fourfold symmetric MPcs on the sixfold symmetric surface of Cu(111) was investigated in order to find the fingerprint of the incommensurate symmetries. To study intramolecular details, Fig. 3.56a gives an enlarged view of CoPcs adsorbed on Cu(111). At the given voltage, CoPcs evolve as parallelograms with one axis pronounced and a second perpendicular axis appearing at reduced apparent height. For all molecules, this second axis is perfectly aligned to one of the close-packed directions of the substrate, i.e., CoPcs in three different orientations are present, independent of the preparation temperature.

The appearance of PC molecules in STM images depends on the molecular states involved in the tunneling process, i.e., on the applied bias voltage as well as on the central transition metal ion. The evolution of molecular appearances is depicted in Figs. 3.56b-d for CoPc, CuPc, and FePc at representative bias voltages. Instead of sharp transitions with bias, a gradual change can be observed. This is indicative for a strong hybridization of molecular and substrate states [66]. For FePc and CoPc, the center appears as a protrusion in the topography for all bias voltages between

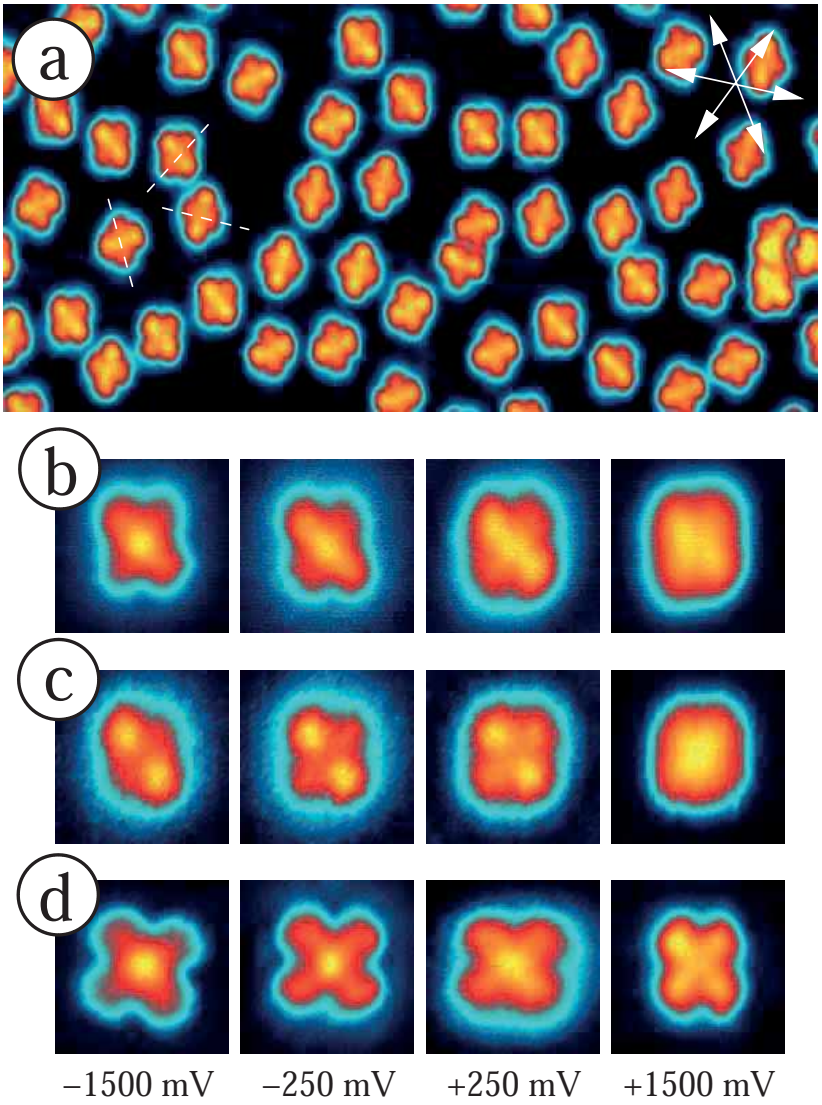

Figure 3.56: STM images of CoPc (a)+(b), CuPc (c), and FePc (d) on Cu(111). In (a), for each of the three orientations of CoPcs, the molecular axis of one molecule which appears at reduced apparent height is marked by a white dotted line. These axes are parallel to one of the three crystallographic axes determined from atomically resolved images of the bare Cu(111) substrate. (b-d): 3×3 nm^2.

$U = 1500$ mV and $U = +400$ mV. This effect is attributed to the half filled d_{z^2} state [68]. For MPcs with higher atomic numbers for the central ion, e.g., CuPc, this d_{z^2} state is filled with two electrons. As a consequence this state shifts at least 2 eV below the ligand HOMO, creating a large interval with no significant contribution from the d-orbital around the Fermi energy as calculated by Rosa *et al.* [74]. Within the studied energy range the only hint for the d_{z^2} state of CuPc was observed starting at $U = +1500$ mV (see Fig. 3.56c). Instead, for CuPc a strong symmetry-reduction

results in two pronounced protrusions at the sites of the benzene rings. This symmetry reduction is of similar intensity for CoPc as long as contributions of the d_{z^2} state to the tunneling process do not become dominant. For FePc the symmetry reduction is only faintly visible (see also Ref. [67]).

So far, the origin of the observed symmetry reduction of molecular structure (which is present for all MPcs studied) remains unclear. The incommensurability of molecular and surface symmetries results in a different atomic configuration underneath two perpendicular molecular axes. Therefore, electronic effects, due to the atomic structure underneath, and geometric effects, due to a structural deformation, have to be considered since STM does not distinguish between them. Indeed, indications for such a geometrically driven reduction of symmetry can be found. Although MPcs on Cu(100) can be found in four different orientations with three different molecule-substrate configurations (orientations 1 and 2 are mirror symmetric), indications for a substrate-induced effect are not found in STM images and the benzene groups appear identical for all molecular orientations within the experimental accuracy (Fig. 3.55b). We conclude that the driving contribution of the observed symmetry reduction is a vertical bending along one of the molecular axes. As a consequence of the reduced molecular symmetry the degeneracy of molecular states is partially lifted. This is manifested as a strongly bias-voltage-dependent symmetry of molecular appearances (Figs. 3.56b-d).

3.7.5 The magnetism of the molecule-ferromagnet interface

Introduction

Molecular based systems are fascinating, yet promising candidates for nanoscale spintronic devices and open viable routes toward quantum computing [75,76]. Previous experiments on the spin transport through break junctions [77] and spin valves [78] unveil exciting new frontiers of molecular magnetism. Much effort is dedicated to understand the properties of organic/magnetic interfaces [79]. To this end, spatially averaging techniques show substantial spin-injection into, as well as long spin-coherent transport throughout films of metal-phthalocyanines (MPc) [80–82]. However, detailed and quantitative access to different constituents of a single molecule is desirable, though challenging. Scanning tunneling microscopy (STM) is well established as a probe of a local spin [83–88] in an atomically well defined environment.

We demonstrate in the following how spin-polarized STM (SP-STM) and state-of-the-art density functional theory allow for unique insights into the organic/magnetic interfaces and predict new ways of favorably tailor such an interface to increase device efficiency. We reveal a significant spin-polarization for single phthalocyanine molecules - paramagnetic Cobalt-phthalocyanine (CoPc) and diamagnetic metal free phthalocyanine (H_2Pc)in contact with a ferromagnetic Fe thin film due to molecule-substrate hybridization even though the molecule does not carry a net spin [89]. Moreover, we present a concept to use non-magnetic molecules to design the spin properties of the

organic/magnetic interface.

Experimental and theoretical procedures

Simulations were carried out in the DFT [90] formalism with a plane wave implementation as provided by the VASP code [91]. Pseudopotentials used were generated with the projector augmented wave method [92] by using the PBE generalized-gradient exchange-correlation energy functional [93] (GGA). Optimized molecule-surface geometries were obtained by relaxing all molecular degrees of freedom and those of the Fe overlayers by including long-range vdW interactions in a semi-empirical way [94,95].

Experiments were performed in an ultra-high vacuum system with an STM operated at 6 K [96]. *In-situ* chromium coated tungsten tips with out-of-plane spin sensitivity [97] were utilized for all measurements. 1.8 ML Fe was *in-situ* deposited on a W(110) single crystal kept at 400K. Afterward, the magnetic sample was cooled down to measurement temperature and spin sensitivity was confirmed by imaging the alternating spin-up ($\odot$) and spin-down ($\otimes$) domains of the 2^{nd} layer portion of the Fe film [97]. Phthalocyanine molecules were *in-situ* thermally sublimated from a home-built crucible onto the pre-cooled substrate to ensure spatially well separated molecules.

All STM images were recorded in constant-current mode at the set current I and sample bias voltage U. The local spin-polarization of the atomic-scale tunnel junction can directly be determined from height variations Δs resulting from different magnetization directions of electronically identical areas as introduced by Wiesendanger *et al.* [98]:

$$P_\mathrm{t} P_\mathrm{s} \cos\theta = \frac{e^{a\sqrt{\phi}\Delta s} - 1}{e^{a\sqrt{\phi}\Delta s} + 1} = \tanh {}^{a}\!/_{2}\sqrt{\phi}\Delta s \overbrace{\approx {}^{a}\!/_{2}\sqrt{\phi}\Delta s}^{\Delta s<1\ \text{Å}}.$$

The polarization of tip (P_t) and sample (P_s) are defined as the normalized difference of the energy integrated spin-up and spin-down states ($P_\mathrm{t(s)} := \rho^{\odot}_\mathrm{t(s)} - \rho^{\otimes}_\mathrm{t(s)}; \rho^{\odot}_\mathrm{t(s)} + \rho^{\otimes}_\mathrm{t(s)} = 1$). θ is the angle between the respective magnetization directions, ϕ the mean local tunneling barrier height, and $a \cong 1\ \mathrm{eV}^{-\frac{1}{2}}\mathrm{\AA}^{-1}$.

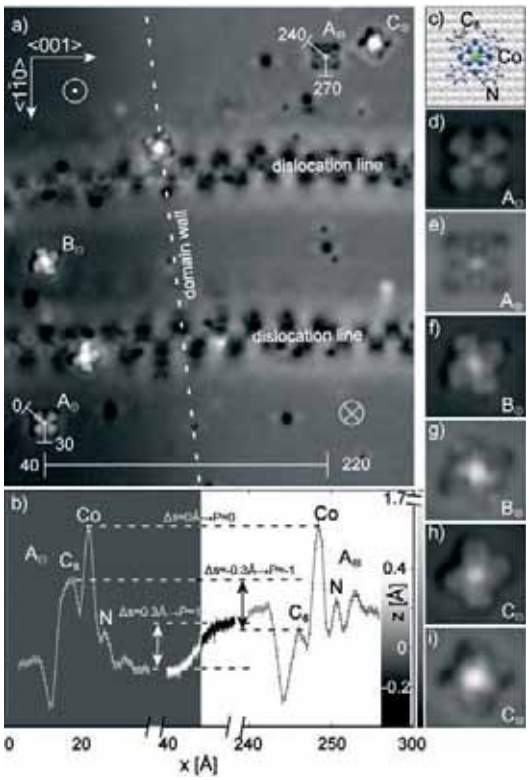

Figure 3.57: (a) SP-STM image of CoPcs on magnetic domains of iron ($\odot, \otimes$). (b) Line profile as indicated in (a). (d)-(i) High-resolution images of CoPcs in all three orientations (A, B, C) on oppositely magnetized domains. (c) Adsorption configuration of a CoPc in orientation A. (a) and (d)-(i) 0.05 V, 200 pA; a) 240 Å × 280 Å; (d)-(i) 25 Å × 25 Å. The colorscale for (a) is non-linear to illustrate the domain structure, while the colorscale for (d)-(i) is linear.

Spin- and energy-dependent tunneling through a single molecule with intramolecular spatial resolution

J. Brede, N. Atodiresei, S. Kuck, P. Lazić, V. Caciuc, Y. Morikawa, G. Hoffmann, S. Blügel, and R. Wiesendanger

Figure 3.57(a) shows a representative 2^{nd} ML area of Fe after deposition of CoPc molecules. The two dislocation lines indicate the crystallographic axes. Isolated CoPcs adsorb in three well-defined orientations (denoted as A, B, and C). The line profile (Fig. 3.57(b)) along the indicated positions in (a) quantitatively illustrates the height variation within the atomically flat Fe film ($\Delta s = 0.3$ Å) and the domain-dependent molecular appearance across a type A CoPc on an up- and down-domain. This variation is due to the relative alignment of tip and sample magnetization being either parallel or anti-parallel. While the center of the molecule (Co-site) has the same apparent height on both domains ($\Delta s = 0$ Å), we see a profound contrast at the ligand-site ($\Delta s = -0.3$ Å). For an up-domain the ligand exhibits an increased apparent height relative to the surrounding Fe film, which is in contrast to the apparent height for a molecule on the down-domain.

Thereby, orientation A represents a highly symmetric configuration (C_{2v}-symmetry) with one molecular axis oriented exactly along the <001> direction. While there are differences in intramolecular contrast amongst the three molecular orienta-

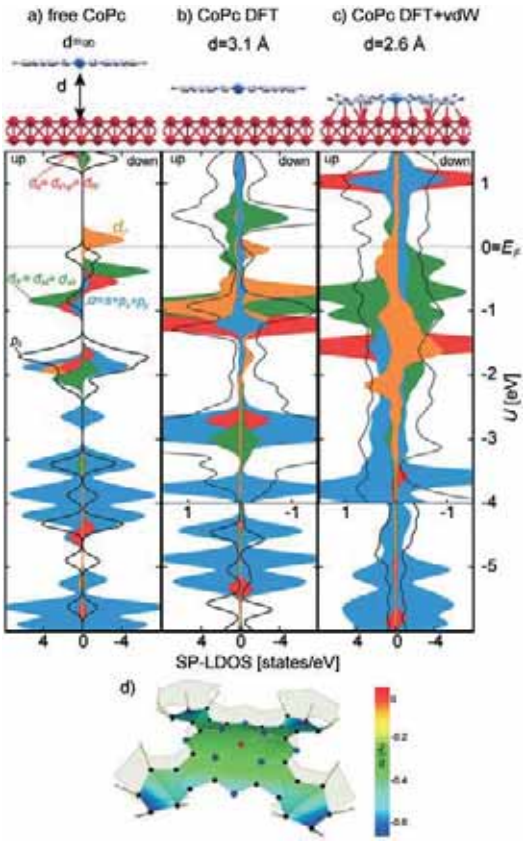

Figure 3.58: The geometry and electronic structure for a free CoPc (a) and adsorbed CoPc on an Fe surface (b) without and (c) with vdW forces included during the relaxation. (d) Molecular deformation due to vdW forces. The C_6 rings and two of the outer N are twisted by up to 0.3 Å toward the surface and away from the plane defined by the Co ion and four inner N. All H are pointing away from the surface.

tions (Fig. 3.57(d) to (i)), all three configurations show similar domain dependent contrast variations. In the following, we focus on molecules in configuration A which are not in the vicinity of dislocation lines or domain walls. As the molecular appearance controllably switches under an external magnetic field applied, the magnetic contrast can unambiguously be attributed to the spin-polarized local density of states (SP-LDOS) of the molecule-surface system.

First-principles calculations within DFT (GGA) clarify the origin of the observed spin-dependence. Calculations for the A geometry show the preferred top adsorption, i.e. the Co atom on top of a surface Fe atom. Furthermore, calculations cover both spin-orbit coupling (SOC) as well as the considerable role of vdW interactions. Results without SOC are discussed in terms of molecular orbitals (MOs) to clearly illustrate the effect of vdW interactions alone.

Figure 3.58 depicts the change in electronic structure of a CoPc with increasing molecule-substrate interaction. Figure 3.58(a) shows the SP-LDOS for the free molecule. In agreement with previous work [86, 87] the origin of spin-splitting is an unpaired electron in a MO with d_{z^2} contribution situated at the Co-site and the total molecular spin S is $1/2$. Figure 3.58(b) presents the effect of the surface, when vdW forces are neglected during the relaxation process. The molecule adsorbs 3.1 Å above the surface remaining flat. The SP-LDOS shows a hybridization of MOs and

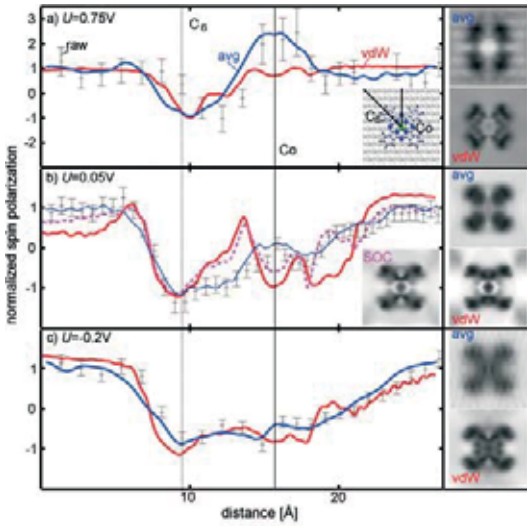

Figure 3.59: Local spin polarization at (a)-(c) three representative energies. Raw- and avg. experimental data are compared with DFT simulations incl. vdW and incl. spin-orbit-coupling. Line profiles follow high-symmetry directions as indicated in the sphere model inset in (a). Simulated data including SOC is only given in (b) as the SOC corrections for (a) and (c) are negligible. Insets: 22 Å×22 Å.

substrate 3d states. According to the spatial extension of the MOs perpendicular to the molecular plane (i.e., with π character), the hybridization of MOs containing the Co d_{z^2} atomic orbital is the strongest, followed by those including d_π and p_z atomic contributions. The d_σ and σ MOs are only slightly broadened, compared to the free molecule case, as they are localized in the molecular plane. The spin-splitting of the molecule-surface hybrid states is reduced due to a transfer of an electron from the substrate to the CoPc. As a result the formerly unoccupied d_{z^2} type MO becomes occupied and the total molecular spin is quenched (0 μ_b).

The role of vdW forces is crucial as it brings the molecule 0.5 Å closer to the surface (Fig. 3.58(b)) and distorts the molecular geometry (Fig. 3.58(d)). This new adsorption geometry has a drastically different electronic structure due to the overall changes of hybridization between molecule and substrate. The SP-LDOS (Fig. 3.58(c)) shows not only MOs with a π character which strongly hybridize with spin-polarized Fe 3d states of the same symmetry to form broad spin-split bands but also σ type MOs which are significantly affected by the interaction with the surface. Again, a transfer of one electron from the surface to the molecule annihilates the molecular spin, but spin-splitting is recovered due to the local molecule-surface bonding at different parts of the molecule. The newly formed molecule-surface hybrid states have, within a given energy interval $[E, E']$, an unbalanced, locally varying electronic charge in the up and down channels which is mapped in SP-STM ($E = E_F, E' = E_F + eU$).

Figure 3.59 illustrates quantitatively the local spin polarization. To compensate for the tip polarization, we normalized the experimental polarization above the molecule ($P^{\mathrm{exp}}_{\mathrm{CoPc}}$) relative to the spin polarization of the free surface ($P^{\mathrm{exp}}_{\mathrm{Fe}}$),

$$P = \frac{P^{\mathrm{exp}}_{CoPc}}{P^{\mathrm{exp}}_{Fe}} = \frac{P_{\mathrm{t}} P_{\mathrm{CoPc}} \cos\theta}{P_{\mathrm{t}} P_{\mathrm{Fe}} \cos\theta} = \frac{P^{sim}_{\mathrm{CoPc}}}{P^{sim}_{\mathrm{Fe}}}. \tag{3.31}$$

The normalized polarization (P) is therefore, to a first approximation, independent

of the tip polarization and can directly be compared to our simulated polarization (P^{sim}).

For comparison both experimental and theoretical spatial maps of the polarization at three characteristic energies are given in Fig. 3.59. We see an excellent agreement of experimental findings and DFT calculations, when the vdW relaxed adsorption geometry is used. Remarkably, not only reduction ($1 > P > 0$) but also inversion ($P < 0$) and amplification ($P > 1$) of spin polarization can equally be observed. The P above the C_6-ring shows an inversion for all energies, while the spin polarization near the Co-site ranges from inversion (at -0.2 V) to amplification (at 0.75 V).

In conclusion we investigated in this first part single CoPc molecules adsorbed on a ferromagnetic Fe surface and locally observed the energy-dependent spin transport with intramolecular spatial resolution. The tunneling current above the entire molecule - metal ion, as well as the organic ligand - shows a high, locally varying spin polarization ranging from inversion up to amplification with respect to the ferromagnetic Fe film. Optimized molecule-surface geometries for the first principles calculations were obtained by including long-range van-der-Waals interactions during the relaxation, leading to an excellent agreement of theoretical and experimental data. Therefore, the observed spin polarization is identified as a unique property of the molecule-substrate hybrid states, by our combined DFT and SP-STM approach.

Design of the Local Spin-Polarization at the Organic-Ferromagnetic Interface

N. Atodiresei, J. Brede, P. Lazić, V. Caciuc, G. Hoffmann, S. Blügel, and R. Wiesendanger

Here, we address how to tailor the electronic and magnetic structure of a ferromagnetic-organic interface based on a systematic study on prototypical conjugated organic molecules adsorbed on the ferromagnetic 2ML Fe/W(110) surface [99]. We selected molecules containing $\pi(p_z)$-electron systems like benzene (Bz), cyclopentadienyl radical (Cp) and cyclooctatetraene (Cot) because they are representative to classes of organic molecules with significantly different reactivities [100, 101].

The calculations show that the Bz molecule adsorbs with two C atoms on top of two neighboring Fe atoms along the [110] direction while the other four C atoms sit in bridge positions between Fe atoms of adjacent [110] rows. The Cp molecule adsorbs in a similar geometry. With one C less than the Bz, Cp binds to the surface with a C atom and a C-C bond on top two neighboring Fe atoms of the [110] row. The Cot molecule binds to the surface with two C atoms and a C-C bond on top of Fe atoms, while the other C atoms sit in bridge sites between Fe atoms of adjacent [110] rows. As a general characteristic of the adsorption geometry, we note that all adsorbed molecules have a nonplanar structure in which the H atoms are situated slightly above

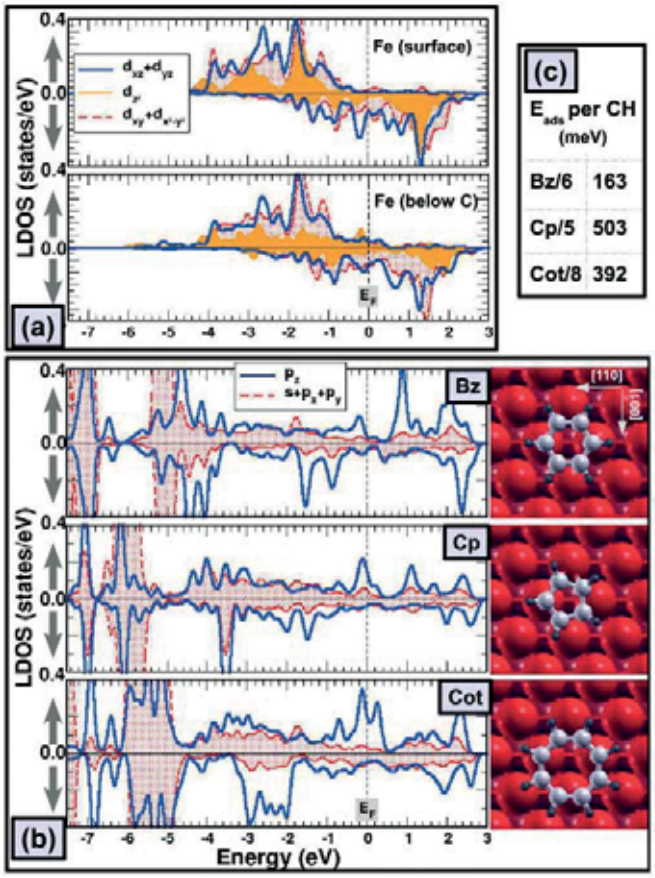

Figure 3.60: (a) Spin-resolved local density-of-states of an Fe atom of the clean surface (upper panel) and an Fe atom below a C atom of the Cot molecule (lower panel); (b) adsorption geometries and the spin-resolved local density-of-states of the Bz, Cp and Cot molecules adsorbed on the 2ML Fe/W(110); (c) the adsorption energies of the Bz (C_6H_6), Cp (C_5H_5) and Cot (C_8H_8) are given in meV per CH group of atoms. Compared to Bz, Cp and Cot molecules interact strongly with the surface due to an effective hybridization between out-of-plane orbitals (p_z of C and d_{z^2}, d_{xz}, d_{yz} of Fe), while the in-plane orbitals are weakly interacting (s, p_x, p_y of C and/or $d_{x^2+y^2}$, d_{xy} of Fe). All adsorbed molecules show a general characteristic: the *energy dependent spin-polarization*, i.e. in a given energy interval the number of spin-up and spin-down electrons is *unbalanced*. For this specific interval the molecule has a net *magnetic moment* delocalized over the molecular plane, although the total magnetic moment of the molecule is 0.0 μ_B. Note also the increased weight of the states crossing the Fermi level situated in the spin-down channel at metal site and in the spin-up channel at molecular site. Therefore, at the molecular site, an *inversion* of the spin-polarization occurs with respect to the ferromagnetic surface.

C atoms (0.35 up to 0.45 Å). The shortest C−Fe bond is about 2.1 Å and corresponds to the C atoms sitting directly on top of Fe while the C atoms situated in bridge positions are 2.3 up to 2.5 Å away from Fe atoms. Furthermore, each of the molecules is nonmagnetic upon adsorption on the ferromagnetic surface. A general picture of

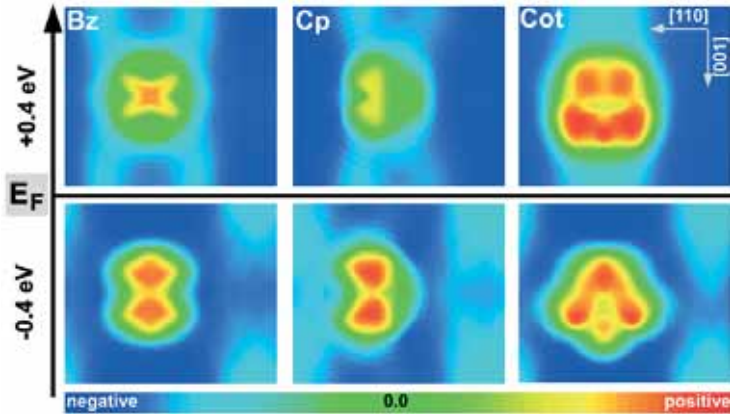

Figure 3.61: The spin-polarization at 2.5 Å above the Bz, Cp, and Cot molecules adsorbed on 2ML Fe/W(110) (15.85Å×13.45Å) surface plotted for occupied ($[-0.4, 0.0]$ eV) and unoccupied ($[0.0, +0.4]$ eV) energy intervals around the Fermi level. All the organic molecules show a high, locally varying spin-polarization ranging from attenuation to inversion with respect to the ferromagnetic Fe film. As compared to Bz, the strongly interacting Cp molecule shows an amplification of the inversion of the spin-polarization below the Fermi level, while the Cot molecule shows a strong amplification of the inversion of the spin-polarization for both occupied and unoccupied states around the Fermi level due to a higher number of p_z interacting electrons.

the binding mechanism between Bz, Cp, and Cot molecules and the ferromagnetic surface can be extracted from the analysis of the spin-resolved local density-of-states (LDOS) of the calculated molecule-surface systems shown in Fig. 3.60. In the spin-up channel, the p_z atomic type orbitals which originally form the π-molecular orbitals hybridize with the majority d-states of the Fe atoms forming molecule-metal hybrid states with bonding and antibonding character. The bonding states are situated at low energies while the antibonding states appear at much higher energies, more precisely in an energy window situated around the Fermi level. Due to the $p_z - d$ interaction in the spin-up channel, the spin-down p_z atomic type orbitals are lowered in energy and slightly hybridize with the minority d-states of Fe. As a consequence, the states with large weight around the Fermi level are in the spin-up channel at the molecule site and in the spin-down channel at clean metal sites. As a consequence, at the molecular site an *inversion* of the spin-polarization occurs with respect to the ferromagnetic surface. To be more specific, in Fig. 3.60 (a) we plot the LDOS of a clean surface Fe atom (upper panel) and an Fe below a C atom (lower panel). As compared to the clean surface Fe atom, for the Fe below C, the shape of the out-of-plane spin-up d-states (d_{z^2}, d_{xz}, d_{yz}) is strongly changed due to the hybridization with the out-of-plane spin-up p_z atomic orbitals of the C. However, the spin-down d-states of iron and p_z-orbitals

of carbon as well as the in-plane states in both spin channels $d_{x^2+y^2}$, d_{xy} of the metal and s, p_x, p_y of the molecule are less affected by the molecule-surface interaction. Characteristic for the strongly interacting molecules as Cp and Cot [Fig. 3.60 (b)] are the spin-up $p_z - d$ bonding states in the $[-5.0, -3.0]$ eV energy interval and the spin-up antibonding states around the Fermi level in the $[-1, +1]$ eV energy interval. In the spin-down channel the states having large weight at the molecular site are situated at low energies, i.e. $[-3.0, -2.0]$ eV energy interval for the Cot molecule and around $[-3.5, -1.5]$ eV energy interval for the Cp molecule. Since the Bz-surface interaction is weaker as compared to Cp and Cot molecules [see adsorption energies (E_{ads}) given in Fig. 3.60 (c)], the spin-up antibonding molecule-surface hybrid states have smaller weight around the Fermi level while the spin-down states at the molecule site are not shifted as low in energy (i.e. $[-2.0, -0.8]$ eV energy interval).

The mechanism explaining the hybridization occurring at the molecule-metal interface resembles the well known $p_z - d$ Zener exchange mechanism [102] present in diluted magnetic semiconductors. A magnetic impurity in a semiconductor host remains magnetic [103] where, due to the $p - d$ mixing, the p-band of the semiconductor is broadened and part of it is pushed above the Fermi level. In our specific case, the nonmagnetic molecule represents the impurity while the magnetism is carried by the ferromagnetic surface. This effect is clearly seen in Fig. 3.61 which illustrates the spin-polarization at 2.5 Å above the molecule in the energy intervals below $[-0.4, 0.0]$ eV and above $[0.0, +0.4]$ eV the Fermi level. A common characteristic for all the molecule-ferromagnetic surface systems is the high and locally varying spin-polarization ranging from *attenuation* to *inversion* with respect to the ferromagnetic surface. Since the carbon's p_z atomic orbitals of the Cp and Cot molecules are strongly interacting with the d-states of the iron atoms, as compared to Bz molecule, an *amplification* of the molecule's local spin-polarization below the Fermi level occurs. Besides this, the presence of a large number of p_z electrons in the Cot molecule causes an amplification also above the Fermi level because a larger number of antibonding p_z-d hybrid states are generated.

So far, our first-principles calculations suggest that the spin injection efficiency ranging from inversion to amplification can be tailored by an appropriate selection of organic molecules adsorbed. Even when the molecule is nonmagnetic, the spin-unbalanced electronic structure implies the presence of a voltage-driven and -dependent spin current generated at the interface accessible by any kind of experimental approach with energy selectivity.

To demonstrate the universal applicability of this concept, we probe the spin-polarization above a fully diamagnetic, metal free phthalocyanine molecule (H_2Pc), adsorbed on out-of-plane magnetized 2ML Fe/W(110). In a simplified view H_2Pc consists of four benzene rings and two hydrogens attached to a $(C\text{-}N)_9$ cycle forming a conjugated 40π-electron system. This is demonstrated in the overview image in Fig. 3.62 (a). The appearance of H_2Pc on the different domains varies significantly as demonstrated in Fig. 3.62 (b,c), which presents color encoded height maps at an

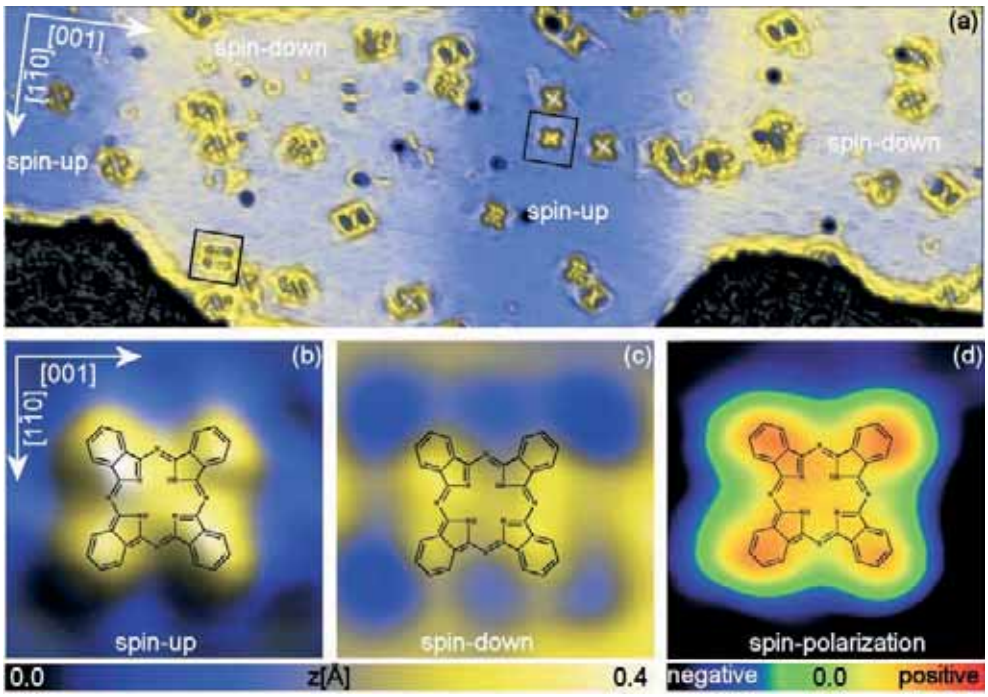

Figure 3.62: Overview SP-STM image of a multi-domain (blue / yellow) 2 ML Fe stripe on W(110) with intact and few metalized H_2Pc present in three distinct orientations. Experimental (22Å×22Å) SP-STM images for H_2Pc adsorbed on 2ML Fe/(W110) at $U = +0.05$ V for both spin channels [i.e. up (↑) and down (↓)] and local spin-polarization. H_2Pc molecules show a high, locally varying spin-polarization ranging from attenuation to inversion with respect to the ferromagnetic Fe film.

applied bias voltage of 0.05 V. Therefore, a positive bias voltage reflects probing of unoccupied interface states and, in the given case, only interface states in the energy interval $[0.0, 0.05]$ eV contribute to the observed spin-dependent contrast. From the spin-dependent height maps, we can directly deduce the spin-polarization above the investigated H_2Pc molecules with respect to the spin-polarization above the ferromagnetic Fe layer in the same energy interval. The experimentally determined local spin-polarization is depicted in Fig. 3.62 (d). Whereas at the sites of the hydrogens an insignificant spin-polarization remains, an *inversion* of the spin-polarization can be observed above all four benzene rings. With the tip-molecule distance certainly larger than 2.5 Å as calculated, we can deduce the presence of a significant and device-relevant spin-polarization even far above the interface localized at the benzene rings. The same behavior is observed for H_2Pc in all orientations.

To summarize, the spin-polarization of a ferromagnetic surface can be locally tailored by flat adsorbing organic molecules containing $\pi(p_z)$-electrons onto it. The complex energy dependent magnetic structure created at the organic molecule-surface interface resembles the $p_z - d$ exchange type mechanism. Although adsorbed molecules are nonmagnetic, due to an energy dependent spin-polarization, in a given energy in-

terval the molecules have a net magnetic moment delocalized over the molecular plane. Highly electronegative molecules as Cp and Cot strongly interact with the ferromagnetic surface which yields an amplification of the inversion of the spin-polarization as compared to less reactive molecules as Bz.

Our combined first-principles and experimental study demonstrates that electrons of different spin [i.e. up (↑) and down (↓)] can selectively be injected from the same ferromagnetic surface by locally controlling the inversion of the spin-polarization close to the Fermi level, an effect which can be exploited to increase the efficiency of future molecular spintronic devices.

References

[1] Z. H. Xiong, Di Wu, Z. Valy Vardeny and Jing Shi, Nature **427**, 821-824 (2004).

[2] J. S. Jiang, J. E. Pearson, and S. D. Bader, Phys. Rev. B **77**, 035303 (2008).

[3] C. Barraud, P. Seneor, R. Mattana, S. Fusil, K. Bouzehouane, C. Deranlot, P. Graziosi, L. Hueso, I. Bergenti, V. Dediu, F.c Petroff and A. Fert , Nat. Phys. **6**, 615-620 (2010).

[4] C. Joachim, J.K. Gimzweski and A. Aviram, Nature **408**, 541 (2000).

[5] E. B. Fleischer and C. K. Miller and L. E. Webb, J. Am. Chem. Soc. **86**, 2342 (1964).

[6] T. A. Jung and R. R. Schlittler and J. K. Gimzewski, Nature **386**, 696 (1997).

[7] E. Unger and M. Beck and R. J. Lipski and W. Dreybrodt and C. J. Medforth and K. M. Smith and R. Schweitzer-Stenner, J. Phys. Chem. B **103**, 10022 (1999).

[8] M. E. Kosal and K. S. Suslick, J. Sol. State. Chem. **152**, 87 (2000).

[9] M. E. Kosal and K. S. Suslick, J. Am. Chem. Soc. **89**, 3331 (1967).

[10] W. Auwärter and A. Weber-Bargioni and S. Brink and A. Riemann and A. Schiffrin and M. Ruben and J. V. Barth, ChemPhysChem **8**, 250 (2007).

[11] F. Buchner and V. Schwald and K. Comanici and H.-P. Steinrück and H. Marbach, ChemPhysChem **8**, 241 (2007).

[12] J. Brede, M. Linares, S. Kuck, J. Schwöbel, A. Scarfato, S.-H. Chang, G. Hoffmann, R. Lensen, P. H. J. Kouwer, J. Hoogboom, A. E. Rowan, M. Bröring, M. Funk, S. Stafström, F. Zerbetto, R. Lazzaroni, and R. Wiesendanger, Nanotechnology, **20**, (2009).

[13] J. Brede, M. Linares, S. Kuck, J. Schwöbel, A. Scarfato, S.-H. Chang, G. Hoffmann, R. Lensen, P. H. J. Kouwer, J. Hoogboom, A. E. Rowan, M. Bröring, M. Funk, S. Stafström, F. Zerbetto, R. Lazzaroni, and R. Wiesendanger, J. Vac. Sci. Technol. B, **27**, 799-804 (2009).

[14] S. Kuck, J. Wienhausen, G. Hoffmann, R. Wiesendanger, Rev. Sci. Instrum. **79**, 083903 (2008).

[15] I. Horcas, R. Fernandez, J. M. Gomez-Rodriguez, J. Colchero, J. Gomez-Herrero and A. M. Baro, Rev. Sci. Instrum. **78**, 013705 (2007).

[16] R. Baxter, G. Teobaldi and F. Zerbetto, Langmuir **19**, 7335 (2003).

[17] G. Teobaldi and F. Zerbetto, J. Phys. Chem. C **111**, 13879 (2007).

[18] F. Ercolessi, M. Parrinello and E. Tosatti, Philosop. Mag. A **58**, 213 (1988).

[19] N. L. Allinger, Y. H. Yuh and J.-H. Lii, J. Am. Chem. Soc. **111**, 8551 (1989).

[20] B. Ma and J.H. Lii and N. L. Allinger, J. Comput. Chem. **21**, 813 (2000).

[21] A. K. Rappe and W. A. Goddard, J. Phys. Chem. **95**, 3358 (1991).

[22] M. Von Born and J. E. Mayer, Z. Phys. **75**, 1 (1933).

[23] H. J. C. Berendsen, J. P. M Postma , W. F. van Gunsteren, A DiNola and J. R. Haak, J. Chem. Phys. **81**, 3684 (1984).

[24] W. Auwärter, F. Klappenberger, A. Weber-Bargioni, A. Schiffrin, T. Strunskus, Ch. Wöll, Y. Pennec, A. Riemann and J. V. Barth, J. Am. Chem. Soc. **129**, 11279 (2007).

[25] M.-S. Liao and S. Scheiner, J. Chem. Phys. **117**, 205 (2002).

[26] L. Scudiero, D. E. Barlow and K. W. Hipps, J. Phys. Chem. B **104**, 11899 (2000).

[27] A. Weber-Bargioni, J. Reichert, A. P. Seitsonen, W. Auwärter, A. Schiffrin and J. V. Barth, J. Phys. Chem. B **112**, 3453 (2008).

[28] V. Iancu, A. Deshpande and S.-W. Hla, Nano Lett. **6**, 820 (2006).

[29] D. E. Barlow, L. Scudiero and K. W. Hipps, Langmuir **20**, 4413 (2004).

[30] K. W. Hipps, L. Scudiero, D. E. Barlow and M. P. Cooke, J. Am. Chem. Soc. **124**, 2126 (2002).

[31] R. G. Nuzzo, B. R. Zegarski and L. H. Dubois, J. Am. Chem. Soc. **109**, 733 (1987).

[32] A. Ulman, Chem. Rev. **96**, 1533 (1996).

[33] X. H. Qiu, G. V. Nazin and W. Ho, Phys. Rev. Lett. **93**, 196806 (2004).

[34] L. Grill, M. Dyer, L. Lafferentz, M. Persson, M.V. Peters and S. Hecht, Nature Nanotechnology **2**, 687 (2007).

[35] T. Yokoyama, S. Yokoyama, T. Kamikado and S. Mashiko, J. of Chem. Phys. **115**, 3814 (2001).

[36] S. Grimme, Angew. Chem. Int. Ed. **47**, 3430 (2008).

[37] P. C. Jha, Z. Rinkevicius, H. Ågren, P. Sealb and S. Chakrabarti, Phys. Chem. Chem. Phys. **10**, 2715 (2008).

[38] J. G. Hill, J. A. Platts and H.-J. Werner, Phys. Chem. Chem. Phys **8**, 4072 (2006).

[39] A. W. Johnson and I. T. Kay, J. Chem. Soc. , 1620 (1965).

[40] D. Crowfoot Hodgkin, J. Pickworth, J. H. Robertson and K. N. Trueblood, R. J. Prosen, J. G. White, Nature **176**, 325 (1955).

[41] E. Vogel, S. Will, A. Schulze Tilling, L. Neumann, J. Lex, E. Bill, A. X. Trautwein, K. Wieghardt, Angew. Chem. Int. Ed. **33**, 731 (1994).

[42] H. Wende, M. Bernien, J. Luo, C. Sorg, N. Ponpandian, J. Kurde, J. Miguel, M. Piantek, X. Xu, P. Eckhold, *et al.*, Nat. Mater. **6**, 516 (2007).

[43] S. Kuck, M. Prostak, G. Hoffmann, M. Bröring, M. Fechtel, M. Funk, and R. Wiesendanger, Am. Chem. Soc., **130**, 14072-14073 (2008).

[44] S. Kuck, M. Prostak, G. Hoffmann, M. Bröring, M. Fechtel, M. Funk, and R. Wiesendanger, J. Vac. Sci. and Tech. A **28**, 795 (2010).

[45] B. C. Stipe, M. A. Rezaei, W. Ho, S. Gao, M. Persson, and B. I. Lundqvist, Phys. Rev. Lett. **78**, 4410 (1997).

[46] T. Komeda, Y. Kim, M. Kawai, B. N. J. Persson, and H. Ueba, Science **295**, 2055 (2002).

[47] J. I. Pascual, N. Lorente, Z. Song, H. Conrad, and H.-P. Rust, Nature (London) **423**, 525 (2003).

[48] P. A. Sloan and R. E. Palmer, Nature (London) **434**, 367 (2005).

[49] S.-W. Hla, L. Bartels, G. Meyer, and K.-H. Rieder, Phys. Rev. Lett. **85**, 2777 (2000).

[50] Y. Kim, T. Komeda, and M. Kawai, Phys. Rev. Lett. **89**, 126104 (2002).

[51] L. J. Lauhon and W. Ho, J. Phys. Chem. A **104**, 2463 (2000).

[52] H. Lesnard, M.-L. Bocquet, and N. Lorente, J. Am. Chem. Soc. **129**, 4298 (2007).

[53] P. G. Cozzi, Chem. Soc. Rev. **33**, 410 (2004).

[54] J. A. A. W. Elemans, S. J. Wezenberg, M. J. J. Coenen, E. C. Escudero-Adán, J. Benet-Buchholz, D. den Boer, S. Speller, A. W. Kleij, and S. De Feyter, Chem. Commun. **46**, 2548 (2010).

[55] N. Baadji, S. Kuck, J. Brede, G. Hoffmann, S. Sanvito, and R. Wiesendanger, Phys. Rev. B, **82**, 115447 (2010).

[56] J. Bardeen, Phys. Rev. Lett. **6**, 57 (1961).

[57] J. M. Soler, E. Artacho, J. D. Gale, A. Garcia, J. Junquera, P. Ordejon, and D. Sanchez-Portal, J. Phys.: Condens. Matter **14**, 2745 (2002).

[58] N. Troullier and J. L. Martins, Phys. Rev. B **43**, 8861 (1991).

[59] J. Zhu, X. W. Wang, and S. G. Louie, Phys. Rev. B **45**, 8887 (1992).

[60] J. Tersoff and D. R. Hamann, Phys. Rev. Lett. **50**, 1998 (1983).

[61] O. Paz and J. M. Soler, Phys. Status Solidi B **243**, 1080 (2006).

[62] C. Toher, I. Rungger, and S. Sanvito, Phys. Rev. B **79**, 205427 (2009).

[63] W.-H. Soe, C. Manzano, A. De Sarkar, N. Chandrasekhar, and C. Joachim,, Phys. Rev. Lett. **102**, 176102 (2009).

[64] M. Ziegler, N. Néel, A. Sperl, J. Kröger, and R. Berndt, Phys. Rev. B **80**, 125402 (2009).

[65] J. K. Gimzewski, E. Stoll and R. R. Schlittler, Surf. Sci. **181**, 267 (1987).

[66] P. H. Lippel, R. J. Wilson, M. D. Miller, Ch. Wöll and S. Chiang, Phys. Rev. Lett. **62**, 171 (1989).

[67] A. Scarfato, S.-H. Chang, S. Kuck, J. Brede, G. Hoffmann, and R. Wiesendanger, Surf. Sci. **602**, 677 (2008).

[68] X. Lu and K. W. Hipps, J. Phys. Chem. B **101**, 5391 (1997).

[69] T. G. Gopakumar, M. Lackinger, M. Hackert, F. Müller and M. Hietschold, J. Phys. Chem. B **108**,7839 (2004).

[70] M. Koudia, M. Abel, C. Maurel, A. Bliek, D. Catalin, M. Mossoyan, J.-C. Mossoyan and L. Porte, J. Phys. Chem. B **110**,10058 (2006).

[71] Y.-S. Fu, S.-H. Ji, X. Chen, X.-C. Ma, R. Wu, C.-C. Wang, W.-H. Duan, X.-H. Qiu, B. Sun, P. Zhang, J.-F. Jia and Q.-K. Xue, Phys. Rev. Lett. **99**, 256601 (2007).

[72] J. C. Buchholz and G. A. Somorjai, J. Chem. Phys. **66**,573 (1977).

[73] S.-H. Chang, S. Kuck, J. Brede, L. Lichtenstein, G. Hoffmann, and R. Wiesendanger, Phys. Rev. B **78**, 233409 (2008)

[74] A. Rosa and E. J. Baerends, Inorg. Chem. **33**, 584 (1994).

[75] L. Bogani and W. Wernsdorfer, Nature Mater. **7**, 179 (2008).

[76] M.N. Leuenberger and D. Loss, Nature (London) **410**, 789 (2001).

[77] J. Park, A. N. Pasupathy, J. I. Goldsmith, C. Chang, Y. Yaish, J. R. Petta, M. Rinkoski, J. P. Sethna, H. D. Abruna, P. L. McEuen, and D. C. Ralph, Nature (London) **417**, 722 (2002).

[78] A. J. Drew, J. Hoppler, L. Schulz, F. L. Pratt, P. Desai, P. Shakya, T. Kreouzis, W. P. Gillin, A. Suter, N. A. Morley, V. K. Malik, A. Dubroka, K. W. Kim, H. Bouyanfif, F. Bourqui, C. Bernhard, R. Scheuermann, G. J. Nieuwenhuys, T. Prokscha, and E. Morenzoni, Nature Mater. **8**, 109 (2009).

[79] C. Barraud, P. Seneor, R. Mattana, S. Fusil, K. Bouzehouane, C. Deranlot, P. Graziosi, L. Hueso, I. Bergenti, V. Dediu, F. Petroff, and A. Fert, Nature Phys. **6**, 615-620 (2010).

[80] T. Suzuki, M. Kurahashi, X. Ju, and Y. Yamauchi, J. Phys. Chem. B **106**, 11553 (2002).

[81] T. Suzuki, M. Kurahashi, and Y. Yamauchi, J. Phys. Chem. B **106**, 7643 (2002).

[82] M. Cinchetti, K. Heimer, J.-P. Wüstenberg, O. Andreyev, M. Bauer, S. Lach, C. Ziegler, Y. Gao, and M. Aeschlimann, Nature Mater. **8**, 115 (2009).

[83] F. Meier, L. Zhou, J. Wiebe, and R. Wiesendanger, Science **320**, 82 (2008).

[84] C. F. Hirjibehedin, C.-Y. Lin, A. F. Otte, M. Ternes, C. P. Lutz, B. A. Jones, and A. J. Heinrich, Science **317**, 1199 (2007).

[85] Y. Yayon, V. W. Brar, L. Senapati, S. C. Erwin, and M. F. Crommie, Phys. Rev. Lett. **99**, 067202 (2007).

[86] X. Chen, Y.-S. Fu, S.-H. Ji, T. Zhang, P. Cheng, X.-C. Ma, X.-L. Zou, W.-H. Duan, J.-F. Jia, and Q.-K. Xue, Phys. Rev. Lett. **101**, 197208 (2008).

[87] A. Zhao, Q. Li, L. Chen, H. Xiang, W. Wang, S. Pan, B. Wang, X. Xiao, J. Yang, J. G. Hou, and Q. Zhu, Science **309**, 1542 (2005).

[88] C. Iacovita, M. V. Rastei, B. W. Heinrich, T. Brumme, J. Kortus, L. Limot, and J. P. Bucher, Phys. Rev. Lett. **101**, 116602 (2009).

[89] J. Brede, N. Atodiresei, S. Kuck, Predrag Lazić, V. Caciuc, Y. Morikawa, G. Hoffmann, S. Blügel and R. Wiesendanger, Phys. Rev. Lett., **105**, 047204 (2010).

[90] P. Hohenberg and W. Kohn, Phys. Rev. **136**, B864 (1964).

[91] G. Kresse and J. Hafner, Phys. Rev. B **50**, 17953 (1994).

[92] P. E. Blöchl, Phys. Rev. B **50**, 17953 (1994).

[93] J. P. Perdew, K. Burke, and M. Ernzerhof, Phys. Rev. Lett. **77**, 3865 (1996).

[94] S. Grimme, J. Comput. Chem. **27**, 1787 (2006).

[95] N. Atodiresei, V. Caciuc, P. Lazić, and S. Blügel, Phys. Rev. Lett. **102**, 136809 (2009).

[96] C. Wittneven, R. Dombrowski, S. H. Pan, and R. Wiesendanger, Rev. Sci. Instrum. **68**, 3806 (1997).

[97] A. Kubetzka, M. Bode, O. Pietzsch, and R. Wiesendanger, Phys. Rev. Lett. **88**, 057201 (2002).

[98] R. Wiesendanger and H.-J. Güntherodt, Phys. Rev. Lett. **65**, 247 (1990).

[99] N. Atodiresei, J. Brede, P. Lazić, V. Caciuc, G. Hoffmann, S. Blügel, and R. Wiesendanger, Phys. Rev. Lett., **105**, 066601 (2010).

[100] I. Fleming, Frontier Orbitals and Organic Chemical Reactions (John Wiley & Sons, 1978).

[101] F. A. Carey, Organic Chemistry (McGraw-Hill, 2000).

[102] T. Dietl, Semicond. Sci. Technol. **17**, 377 (2002).

[103] J. Kanamori and K. Terakura, J. Phys. Soc. Jpn. **70**, 1433 (2002).

3.7.6 Magnetic molecules on bulk insulating surfaces

After having introduced magnetic exchange force microscopy (MExFM) as a new tool to map spin structures with atomic resolution on insulating [1] as well as conducting materials [2], our next goal is to study magnetic molecules adsorbed on bulk insulators. On such substrates strong coupling to the conduction electrons, commonly observed on metal surfaces, is absent. As a first step we investigated growth and adsorption of magnetic molecules to study the molecule-molecule as well as the molecule-substrate interaction. Magnetic sensitive experiments will follow in the future.

As magnetic molecule we selected Co-Salen ($Co(C_{16}H_{14}N_2O_2)$), which is synthesized in the group of M. Prosenc [3]. The central Co atom of this paramagnetic metal-organic Schiff-base complex possesses four coordinative covalent bonds to two O atoms and two N atoms (see Fig.3.63a and b). The aromatic rings to the left and right result in a characteristic banana-like shape. Its planar geometry provides direct access to the spin-carrying Co atom ($S = 1/2$) from the top with the tip. Note that the tilted C_2H_4-bridge is responsible for the chiral character of the molecule. Co-Salen is known for its oxygen affinity [4, 5] and its magnetic properties have already been studied with volume averaging techniques [6, 7].

As insulating substrates we chose the (001) surface of two binary ionic crystals with rock salt structure, i.e., rock salt itself, cf. Fig.3.63c, and the antiferromagnet nickel oxide, cf. Fig.3.63d. On such surfaces only atomic force microscopy (AFM) can acquire real space images with atomic resolution. As mode of operation we employed the frequency modulation technique (FM-AFM) in the non-contact regime (NC-AFM). For growth studies at room temperature a slightly modified Omicron Multiprobe SPM was used, while high resolution studies on individual molecules were performed with a homebuilt low temperature force microscope [8].

Both microscopes are located in the same multi-chamber ultrahigh vacuum (UHV) system with *in situ* preparation facilities. For the room temperature growth study we deposited Co-Salen by sublimation in a separate molecule preparation chamber [9]. To investigate individual well separated molecules (coverages <0.3 ML) with high resolution, aggregation has to be prevented by deposition onto a cold substrate and subsequent imaging at cryogenic temperatures using our low temperature force microscope. Since our experimental set-up does not possess a flange with direct line-of-sight to the sample holder, we developed a miniaturized crucible that can be inserted directly into the cantilever stage of the low temperature microscope [10].

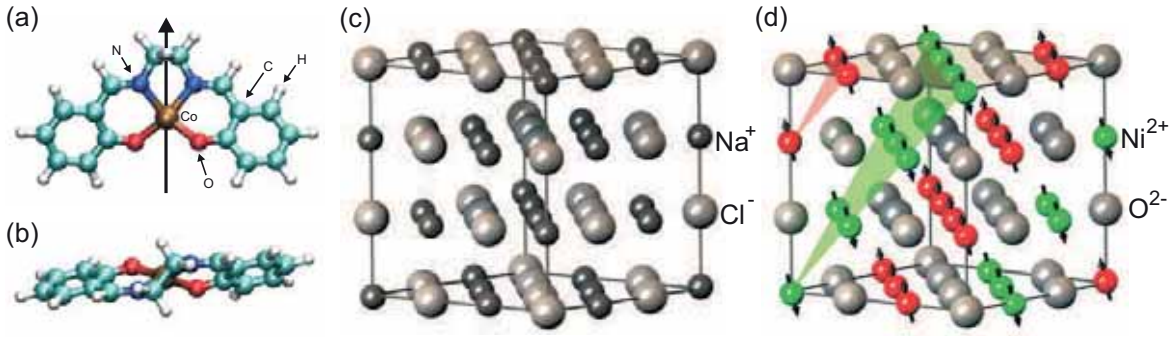

Figure 3.63: (a) Top-view and (b) side view of Co-Salen. (c) Crystal structure of NaCl, a large band gap binary ionic alkali halide insulator. (d) Crystal structure of NiO. It possesses the same crystal structure as NaCl, is also a binary ionic bulk insulator, but the cations (nickel) carry a magnetic moment and are antiferromagnetically coupled by superexchange via oxygen, which results in a row-wise antiferromagnetic spin structure at the (001) surface.

3.7.7 Co-Salen on NaCl(001)

K. Lämmle, S. Fremy, and A. Schwarz

NaCl is the prototype cubic alkali halide ($a = 562$ pm). Rod-shaped single crystals (3 mm $\times$ 3 mm $\times$ 16 mm) are cleaved and heated *in situ* to expose a clean and uncharged (001) plane; cf. Fig. 3.64a. The surface exhibits several atomically flat terraces separated by steps. Their heights correspond to integer multiples of $a/2$.

Growth and Morphology

In general, the growth of adsorbed species is governed by thermodynamic arguments, e.g., surface energies, as well as kinetic arguments, e.g., diffusion and nucleation. Compared to the adsorption and subsequent aggregation of atoms, the situation is more complex for molecules, because (i) they are extended entities, (ii) substrate-molecule interactions as well as intermolecular interactions are not isotropic and (iii) they possess more degrees of freedom.

After depositing a few monolayers of Co-Salen on NaCl(001) held at room temperature, we find a bimodal Volmer-Weber mode at room temperature [11], cf. Fig. 3.64. In the following the two morphologies are named nanowires (2 - 8 nm high elongated structures) and compact nanocrystallites (20-40 nm high rectangular-shaped structures).

Compact nanocrystallites grow with four-fold symmetry and are flat on top. Their edges are oriented along $\langle 110 \rangle$-directions of the substrate. Nanowires are curved on top and grow preferentially along the $\langle 110 \rangle$-directions. However, growth along $\langle 120 \rangle$-directions and along step edges can be frequently found as well. In between the bare

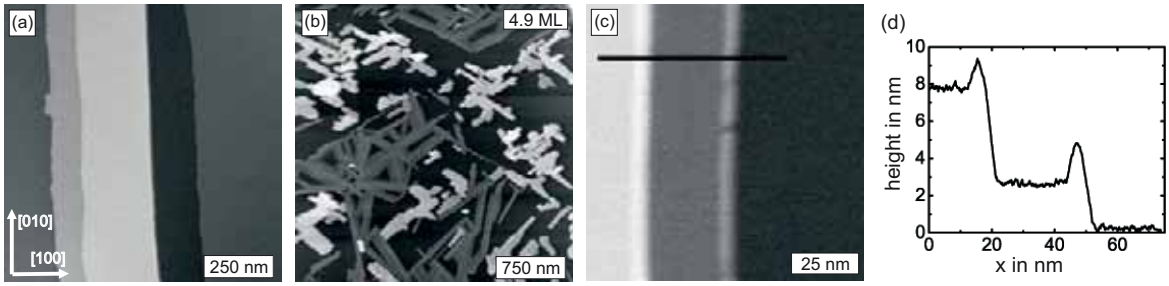

Figure 3.64: (a) NaCl(001) surface with atomically flat terraces separated by step edges. (b) Overview after depositing 4.9 ML of Co-Salen molecules onto NaCl(001). Two different morphologies with well defined shapes can be observed: relatively high compact crystallites (nanocrystallites) and relatively low wire-shaped crystallites (nanowires). (c) Image recorded on an area between the crystallites. Substrate step edges are decorated by molecules as visible in the line section displayed in (d).

NaCl substrate is exposed. Step edges are decorated by molecules, as evidenced by topographic elevations visible in Figs. 3.64c and d.

Coverage dependent studies show that the growth of nanowires is preferred initially. However, temperature and time dependent studies reveal that compact nanocrystallites are the thermodynamically stable variant. The latter is demonstrated in Fig. 3.65: Keeping the substrate at $T_S = 30°C$ as in Fig. 3.65a results in much less nanowires compared to images with T_S held at temperatures around $T_S = 20°C$, cf. Fig. 3.64b. At $T_S = 40°C$, see Fig. 3.65b, only compact nanocrystallites are visible on the surface. The same behavior was found in post annealing experiments. In addition, similar results were obtained from long-term experiments: Scanning the sample surface continuously for a day at room temperature revealed a substantial material transport from nanowires to compact nanocrystallites. Figure 3.65d was recorded 21.5 hours after 3.65c. Clearly, the fork-like compact nanocrystallite in the center (marked by circle) grew in size while the number of nanowires became smaller.

Crystalline Structure

After having established the growth mode, it is interesting to know the crystalline order within both morphologies. For bulk samples an analysis of X-ray diffraction data reports a monoclinic unit cell consisting of eight Co-Salen molecules with every two Co-Salen molecules forming a dimer (see Fig. 3.66f) [12]. In these Co-Salen dimers the Co atom of each molecule exhibits an additional coordinative covalent bond to one O atom of the opposite molecule. Another X-ray study reports an orthorhombic unit cell consisting of eight Co-Salen monomers (see Fig. 3.66e) [13]. Since Volmer-Weber growth indicates a rather weak interaction between molecules and surface, it is likely that molecular packing in the ordered structures is bulk-like.

High resolution NC-AFM images displayed in Fig. 3.66 indicate that both morphologies exhibit a monoclinic packing of Co-Salen monomers with the *c*-axis either

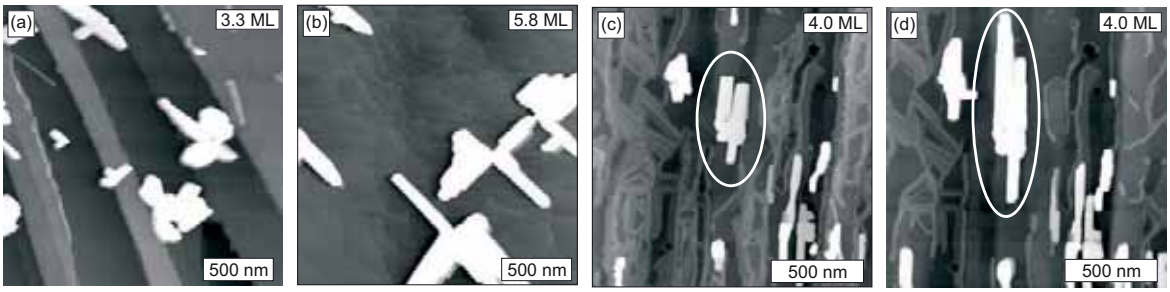

Figure 3.65: Temperature and time dependent behavior of both morphologies. Deposition on a substrate at $T_S = 30\,°C$ (a) and $T_S = 40\,°C$ (b) shows that compact crystallites are thermodynamically more stable. (c) and (d) illustrate the material transfer from nanowires to compact nanocrystallites at room temperature in a time span of 21.5 h.

parallel (nanowires) or perpendicular (compact nanocrystallites) to the substrate: Figure 3.66a shows an image with molecular resolution recorded on top of a compact nanocrystallite. Regularly ordered banana-shaped maxima are visible. Their apices all point into the same direction. Shape and dimensions of the maxima indicate that they represent flat lying molecules. Fig. 3.66b and c display the orientation of flat lying molecules for the orthorhombic (*bc*-plane parallel to the (001) surface) and monoclinic (*ab*-plane parallel to the (001) surface) unit cell, respectively. Only the arrangement of molecules in the monoclinic unit cell complies with the image contrast, because all apices point into the same direction. If this assignment is correct, *a*- and *b*-axis of the compact crystallites are parallel to the ⟨110⟩-directions of the substrate and the *c*-axis is nearly normal to the (001) plane. Figure 3.66d was recorded on top of a nanowire aligned along the $[\bar{1}10]$ direction of the substrate. Two parallel stripes, about 1.6 nm apart, run diagonally across the image along the axis of the imaged nanowire. They exhibit regularly spaced maxima separated by ≈ 0.65 nm. In contrast to Fig. 3.66a, the maxima are not banana-shaped. Hence, we infer that the molecules do not lie flat, but are in a more upright standing position. The measured distances fit better to the monoclinic dimer bulk unit cell as for the compact nanocrystallites, but with the *c*-axis parallel to the surface.

Single Molecule Adsorption Geometry

Although the island growth indicates that the molecule-substrate interaction is relatively weak on NaCl(001), the alignment of the crystallites along principal axes of the substrate evidence that a significant influence of the substrate on the orientation of the molecule on the surface exists. Moreover, the molecular resolution images suggest dimers as building blocks for the compact nanocrystallites as well as for the nanowires. Hence, it is interesting to know whether thermally evaporated Co-Salen adsorbs as monomer or as dimer and how the substrate influences the orientation of single molecules initially.

To study the adsorption geometry of Co-Salen with respect to the underlying

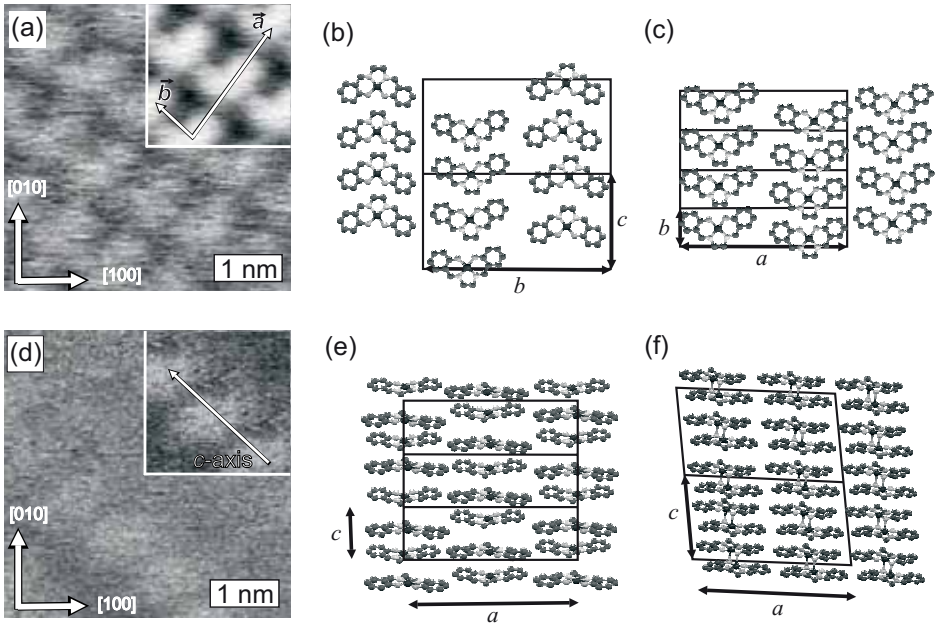

Figure 3.66: (a) Molecular resolution recorded on a compact nanocrystallite (inset: unit-cell averaged representation). (b), (c) Configuration of planar-lying molecules in the orthorhombic and monoclinic unit cell, respectively. (c) Molecular resolution recorded on a nanowire (inset: unit-cell averaged representation). Configuration of upright-standing molecules in the orthorhombic (e) and monoclinic (f) unit cell. The images suggest that both morphologies are formed by Co-Salen dimers in the monoclinic bulk unit-cell with the *c*-axis either perpendicular (a) or parallel (d) to the surface.

NaCl(001) surface, individual, well separated molecules have to be studied. At the same time atomic resolution has to be achieved on the substrate. Since Co-Salen is quite mobile on NaCl(001) at room temperature, imaging as well as deposition has to take place onto a sufficiently cold substrate to freeze out thermally activated translations.

At cryogenic temperatures electrostatic forces due to localized trapped charges at the tip apex (we use highly-doped Si cantilevers, which are oxidized) can hamper data acquisition dramatically. Therefore, we used metalized (Cr coated) tips for the low temperature experiments. High resolution data acquisition at small tip-sample separation was performed with great care to prevent tip-induced jumps of the weakly bonded molecule. Our experimental data were compared with density functional theory (DFT) calculations performed in the group of A. Shluger [15].

Figure 3.67(a) depicts a typical overview image of the NaCl(001) surface after molecule deposition. The banana-shaped objects can be identified as flat lying Co-Salen molecules. They can be straightforwardly distinguished from contaminations by their characteristic shape and their much larger apparent height. The orientations of the molecules appear to be random, but a systematic analysis of the images revealed 16 clearly distinguishable orientations relative to the underlying lattice. Using atomically

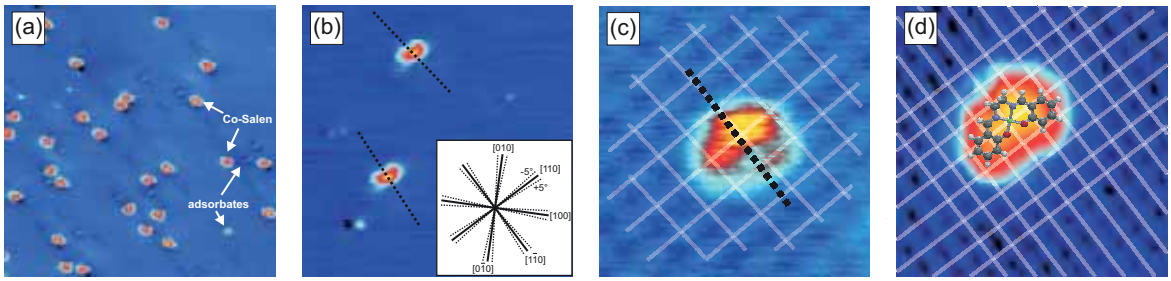

Figure 3.67: (a) Overview NC-AFM image after deposition of Co-Salen molecules on NaCl(001). (b) Two individual Co-Salen molecules. The angle between their axes is approximately $\pm 5°$ away from the [1$\bar{1}$0]-direction. The inset displays the 16 different observed orientations of the molecule with respect to the principal crystallographic axes of the substrate. (c) and (d) represent two high resolution NC-AFM images with the center of the Co-Salen molecule above a maximum.

resolved NC-AFM data on the bare substrate as a reference, we found that the primary axes of all the molecules are rotated either clockwise or anticlockwise by about $(5 \pm 2)°$ away from the <100>- and <110>-directions of the substrate; see Fig. 3.67(b). From $N = 87$ evaluated molecules, 62 (71%) were oriented approximately along <110>-directions, while only 25 (29%) were oriented approximately along <100>-directions. Moreover, we found that 38 (44%) molecules were rotated clockwise and 49 (56%) anticlockwise with respect to the two principal crystallographic axes of the substrate.

In Fig. 3.67(c) and (d) two images with an isolated Co-Salen molecule on the atomically resolved NaCl(001) substrate recorded with two different Cr coated tips are displayed. Atomic corrugation, apparent height and length of the molecule are 8 pm, 60 pm and 1.2 nm in (c) and 25 pm, 330 pm and 1.6 nm in (d). The larger atomic corrugation and apparent height in (d) indicates that the tip was approached closer to the surface than in (c). Furthermore, the larger apparent lateral dimensions of the molecule in (d) and its less well expressed banana shape suggests a larger mesoscopic tip radius. As reported in several other publications, only one sublattice is imaged as maxima on binary ionic surfaces [17–20]. To accurately identify the adsorption site, the lattice periodicity is superimposed over the image. Clearly, the center of the molecule is directly over a surface site corresponding to a maximum in the surface corrugation. Note that in both images the largest contrast is not observed above the center, but somewhat shifted away from it, a feature, which we observed quite often.

On binary ionic surfaces like NaCl(001) the ion type that interacts more strongly with the tip, and hence is imaged as maxima in images, directly depends on the atomic species present at the tip apex [21]. Characterizing tips is therefore crucial for our understanding of the images. The tips of the Si cantilevers used are covered by an oxide layer. After *in-situ* evaporation of Cr onto the cantilever and before and after taking the data shown in Fig. 3.67(c), we recorded $\Delta f(U_{\mathrm{bias}})$ curves to check whether the tip is indeed metallic and hence Cr-terminated at its apex. For the two different tips used to record Fig. 3.67(c) and (d) the curves were smooth without jumps and

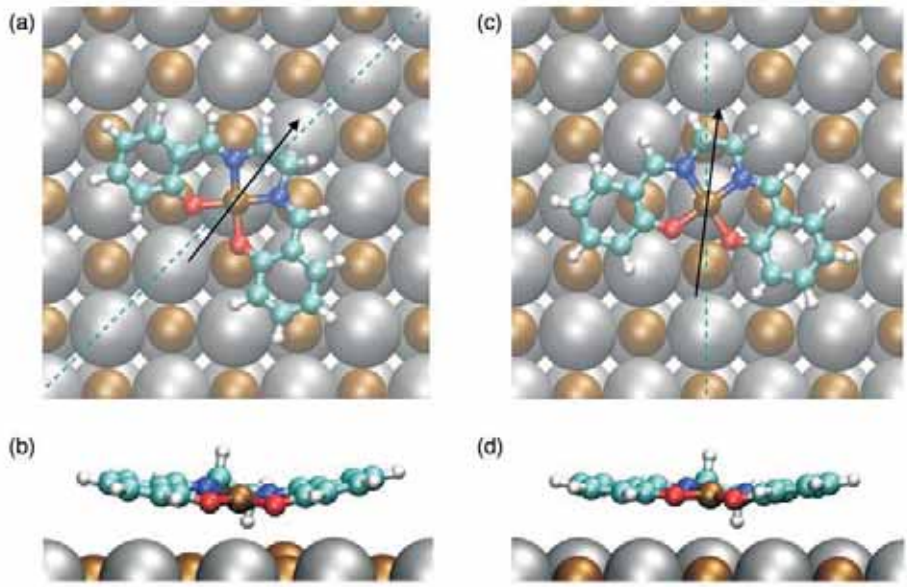

Figure 3.68: (a) Top view of the configuration of the molecule adsorbed in its lowest energy configuration with the primary molecular axis (black line) and [110] surface axis (dashed line) shown. (b) Side view of the molecule viewed along the [110] direction. (c) Top view of the configuration of the molecule adsorbed in a local energy minimum with the primary molecular axis (black line) and [100] surface axis (dashed line) shown. (d) Side view of the molecule viewed along the [010] direction.

look identical independent of the sweeping direction (no hysteretic behavior). Jumps would indicate charge reconfigurations due to tunneling processes at the tip apex, while hysteresis can be attributed to slow charge relaxation processes. Both effects occur on tip apices, which are either not metallic at all or on which the metallic film is not continuous. Hence, we can infer that the tip apex is most likely Cr-terminated.

In order to determine the origin of the atomic scale contrast on the bare substrate, we performed periodic DFT simulations to investigate the interaction of a Cr tip with the NaCl(001) surface. Force-distance curves calculated for the tip apex atom located directly above Na and Cl lattice positions clearly show that the attractive tip-surface interaction above Cl ions in the surface is significantly stronger than the interaction above Na ions. Hence, maxima in experimental images recorded on NaCl(001) with a Cr tip represent the Cl sublattice. By implication, the center of the molecule, i.e., the central Co atom, as imaged in 3.67 (c) and (d) is above the surface Cl ion.

To validate this conclusion and to further confirm the adsorption site, we investigated the interaction of a single molecule with the surface and possible stable configurations of the molecule on the surface. We performed a series of embedded cluster density functional theory calculations, employing the B3LYP hybrid functional [22,23]. The optimized structure of the free molecule in the $S = 1/2$ state is shown in 3.63(a)

and (b). Here, all of the spin density is localized on the Co atom. The $S = 3/2$ state of the molecule is 0.28 eV higher in energy than the $S = 1/2$ state. The NaCl surface is treated using an embedding scheme. To include the effect of the van der Waals interaction between the molecule and the surface, which is not accounted for effectively within standard DFT methods and can be a significant contributor to surface binding in systems such as this, we included damped pair-wise London terms between the atoms of the molecule and the surface, based on the scheme described in detail in Ref. [24].

The Co-Salen molecule is initially placed above the NaCl(001) surface with the plane of the molecular board parallel to the surface plane, separated by 0.4 nm. This configuration is suggested by the shape of the molecule when imaged with NC-AFM (see Fig. 3.67). To find all stable configurations of the molecule on the surface we then tried several initial guesses with the axis of the molecule parallel to the [100]-direction and at 5° intervals from here until the axis of the molecule was aligned along the [010]-direction. The molecule was located with the Co atom directly above a Cl ion in the surface, directly above a Na ion, and in the bridge position between two neighboring Cl atoms. For each of these initial configurations the structure was optimized by minimizing the system's total energy. All atoms in the NaCl quantum cluster as well as several hundred classical NaCl ions were allowed to relax. The lowest energy configuration was found for the molecule orientated laterally 5° from the [110] direction with the Co atom directly above a Cl ion in the surface. The relaxed structure is shown in Fig. 3.68(a) and (b), where the orientation of the molecule due to the interaction with the surface has slightly changed ($< 2°$). The adsorption energy of the molecule in this configuration is 0.82 eV. The molecular structure is distorted due to adsorption: the separation of the Co complex from the surface plane is approximately 0.34 nm, and the separation of the aromatic part of the molecule from the surface plane is approximately 0.39 nm. A local minimum exists for a lateral molecular orientation 5° from the [001] direction with an adsorption energy of 0.76 eV. This configuration is shown in Fig. 3.68 (c) and (d). The adsorption energies at other sites are significantly lower. In every adsorption position of the molecule no transfer of charge between the molecule and the surface occurs, and the interaction is purely electrostatic. The total charge on the molecule is zero to within 0.005 e ($e = 1.6 \cdot 10^{-19}$ C is the elementary charge). In addition, the atomic charges, atomic spin densities, and HOMO and LUMO energy levels are not significantly affected by the interaction with the surface.

The physical origin of the existence of the two low energy states is primarily due to the electrostatic interaction between the positively charged Co atom and a Cl ion in the surface and the negatively charged O and N atoms neighboring the Co atom interacting with the four Na ions surrounding the Cl ion. In addition, the asymmetric -C_2H_4- bridge, which is distorted towards the surface, strongly affects the stability of the low energy configurations, with the lowermost H atom interacting strongly with a Cl atom in the surface. The two aromatic rings on the molecule are only weakly attracted to the surface and are repelled from it at separations much less than 0.40

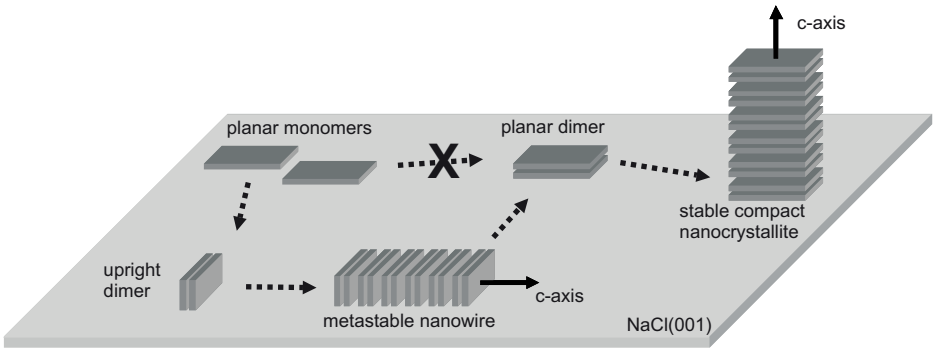

Figure 3.69: Growth model for Co-Salen on NaCl(001). Co-Salen adsorbs in a planar configuration as a monomer and forms dimers on the surface. The thermodynamically stable morphology, i.e., the compact nanocrystallites, is reached via the growth of metastable nanowires. The molecular packing of Co-Salen dimers is identical in both morphologies, only the c-axis is oriented differently.

nm.

Both, experiment and theory show that the adsorption geometry with the lowest energy is rotated by approximately 5° away from the <110> directions. Hence, 8 adsorption orientations corresponding to this geometry exist, i.e., four due to the fourfold symmetry of the surface and two per direction, because of the chiral C_2 symmetry of the molecule, which remains unaltered upon physisorption on NaCl(001). In addition, a local energy minimum configuration exists approximately ±5° away from the <100> directions. The calculated energy difference between these two low energy configurations is 0.06 eV.

Growth Model and Monomer-To-Dimer Transition

Finally, we can deduce a conclusive growth model by summarizing the experimental results evaluated in the previous sections (see Fig. 3.69): At room temperature Co-Salen molecules deposited by sublimation on NaCl(001) diffuse on the atomically flat terraces. Step edges serve as diffusion barriers and as preferred adsorption sites, i.e., molecules decorate them and nucleation starts there. At room temperature a bimodal growth of compact nanocrystallites and nanowires is observed. The Volmer-Weber growth mode indicates a weak molecule-substrate interaction (compared to the intermolecular interaction) as expected for molecules physisorbed on insulators. Nanowires transmutate into compact nanocrystallites at elevated temperatures or, much slower, after some time elapsed. Thus, compact nanocrystallites can be identified as the thermodynamically stable morphology. However, the formation of metastable nanowires is preferred initially.

Both morphologies are formed by Co-Salen dimers in the same monoclinic packing as found in macroscopic single crystals. Only the orientation of the *c*-axis with respect to the surface is different. For nanowires the *c*-axis is aligned along ⟨110⟩-directions of

the substrate and, less often, along ⟨120⟩-directions. For compact nanocrystallites *a*- and *b*-axis are oriented along ⟨110⟩-directions and the *c*-axis is nearly normal to the surface.

One interesting question remains: Why is the metastable nanowire morphology initially preferred? Images of individual Co-Salen molecules deposited by sublimation onto a cold NaCl(001) substrate clearly show that they adsorb as monomers. This finding is consistent with scanning tunneling microscopy images of individual Co-Salen molecules sublimated onto a cold Cu(111) substrate [26]. Thus, at some point a transition from monomers to dimers must take place. Note that such a transition involves a coordinative bond formation, i.e., a chemical reaction.

3.7.8 Co-Salen on NiO(001)

J. Hattendorf, K. Lämmle, and A. Schwarz

NiO exhibits the same crystal structure as NaCl, but with a smaller lattice constant ($a_{\mathrm{NiO}} = 417$ pm). It is also a binary insulating ionic crystal (charge is transferred from

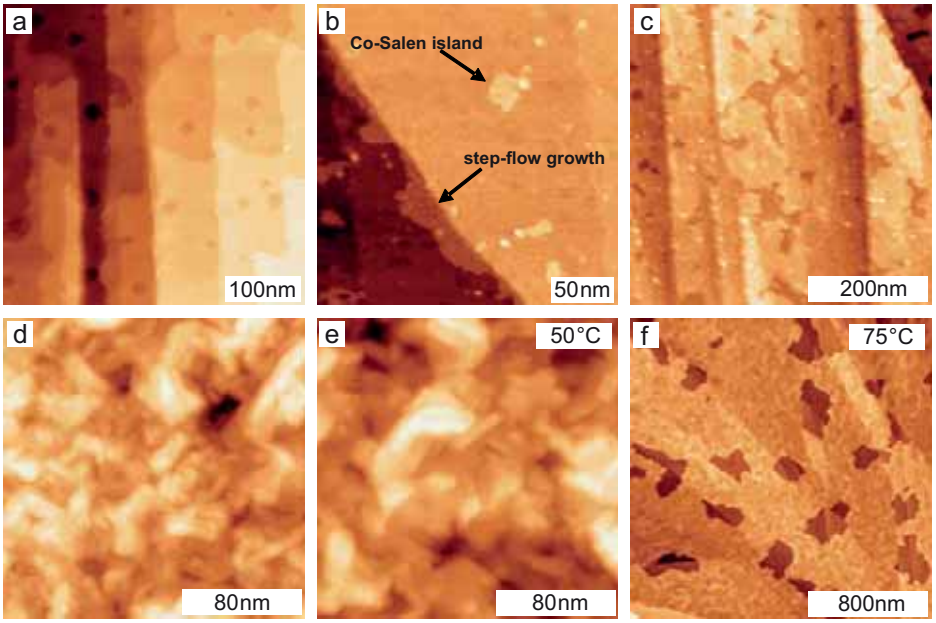

Figure 3.70: (a) Bare NiO(001) with steps and vacancy islands after annealing to 450°C. (b) Island and step flow growth of Co-Salen on NiO(001) for submonolayer coverage. The island heights correspond roughly to the height of a flat-lying dimer (about 0.7 nm). (c) Layer-by-layer step flow growth of Co-Salen on NiO(001) for few monolayer coverages. (d) For higher coverages a rough morphology evolves. (e) Post annealing to 50°C leads to a more regular morphology showing fourfold symmetric structures. (d) After post annealing to 75°C holes appear in the film.

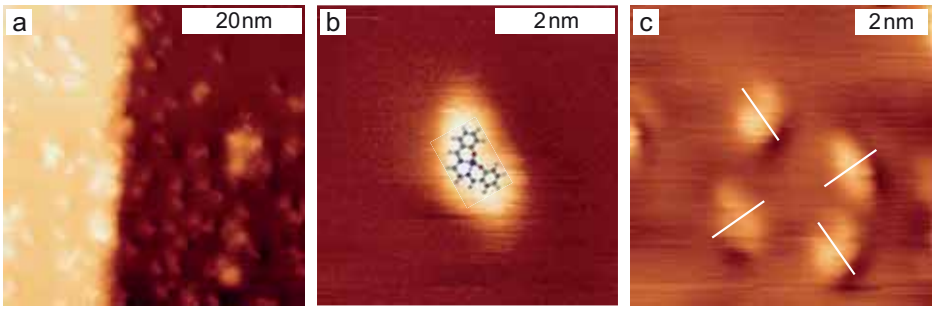

Figure 3.71: Images of individual Co-Salen molecules recorded at about 8 K after Co-Salen deposition onto a 30 K cold NiO(001) substrate. (a) Overview image recorded around a step edge. (b) An isolated single banana-shaped Co-Salen molecule. (c) Four molecules with their axes oriented along the four equivalent ⟨110⟩-directions.

Ni to O), but with a significant covalent contribution. In addition, the Ni sublattice exhibits a antiferromagnetic spin structure. Coupling takes place by superexchange via the oxygen atoms. On the (001) surface Ni spins exhibit a row-wise antiferromagnetic order along <110>-directions. Preparation is similar to NaCl. However, terraces are not as wide as on NaCl(001) and charge problems are more severe. To reduce charge effects heating temperatures up to 450°C were used. At this temperature some material transport takes place, which manifests itself as square-shaped vacancy islands on bare NiO(001)terraces as visible in Fig. 3.70a.

Evaporation of Co-Salen shows initially a layer-by-layer step-flow growth, cf. Fig. 3.70b and c. The layer heights of about 0.7 nm and multiples indicate flat-lying dimers as building blocks. At larger coverages the film becomes quite rough, cf. Fig. 3.70d. Post annealing at 50°C increases ordering; cf. Fig. 3.70e. At 75°C large area scans reveal extended holes within the film;, cf. Fig. 3.70f. At 100°C no surface structures related to molecules are visible anymore (not shown).

Since we do not observe an island growth like on NaCl(001), but a layer-by-layer step flow growth, we can infer that the molecule-substrate interaction is significantly larger on NiO(001) than on NaCl(001). This conclusion is supported by experiments performed on single molecules evaporated onto a cold substrate. We find that tip-induced translations are less frequent than on NaCl(001), even if the tip is approached very close.

Figure 3.71a shows an overview image recorded at about 8 K after deposition of molecules onto a 30 K cold substrate. As demonstrated in Fig. 3.71b, individual Co-Salen molecules adsorbed on NiO(001) exhibit the same banana-like shape than on NaCl(001). They also adsorb in preferred orientations, cf. Fig. 3.71c. We evaluated such images in a similar way than for the NaCl(001) substrate and find that the molecule axes are oriented along ⟨110⟩-directions of the substrate. High resolution data indicate a small rotation by about ±2° away from the main axis. However, the number of evaluated molecules is small up to now. Unlike for NaCl(001), ⟨100⟩-directions are not observed. An accurate assignment of the adsorption site was not

possible up to now, neither from experimental images nor from theoretical calculations. In analogy to NaCl(001) one could speculate that the Co center sits on top of the surface oxygen, a likely scenario, because Co-Salen is known for its strong oxygen affinity. Moreover, this could explain why Co-Salen interacts stronger with NiO(001) than with NaCl(001). From an experimental point of view it is much easier to record high resolution data at small tip-sample separations on molecules that are strongly attached to a surface. Regarding magnetic interactions, the Co center might interact via superexchange across surface oxygen with the nickel atom in the first subsurface layer. The originally paramagnetic Co-Salen might than possess a spin fixed in space, which can be probed with magnetic exchange force microscopy.

References

[1] U. Kaiser, A. Schwarz, and R. Wiesendanger, Nature **446**, 522 (2007).

[2] R. Schmidt, C. Lazo, H. Hölscher, U. H. Pi, V. Caciuc, A. Schwarz, R. Wiesendanger, and S. Heinze, Nano Lett. **9**, 200 (2009).

[3] J.-P. Klöckner and A. Frank, and M. Prosenc, Institute of Anorganic and Applied Chemistry, University of Hamburg.

[4] W. P. Schaefer and R. E. Marsh, Acta Cryst. B **25**, 1675 (1969).

[5] R. Fiammengo, C. M. Bruinink, M. Crego-Calama, and D.-N. Reinhoudt, J. Org. Chem. **67**, 8552 (2002).

[6] G. O. Carlisle, G. D. Simpson, W. E. Hatfield, V. H. Crawford, and R. F. Drake, Inorg. Chem. **14**, 217 (1975).

[7] K. S. Min, J. Arthur, W. W. Shum, M. Bharathy, H.-C. zur Loye, and J. S. Miller, Inorg. Chem. **48**, 4593 (2009).

[8] M. Liebmann, A. Schwarz, S. M. Langkat, and R. Wiesendanger, Rev. Sci. Instrum. **73**, 03508 (2002).

[9] K. Lämmle, Diploma Thesis, Hamburg (2006).

[10] K. Lämmle, A. Schwarz, and R. Wiesendanger, Rev. Sci. Instrum. **81**, 053902 (2010).

[11] S. Fremy, A. Schwarz, K. Lämmle, M. Prosenc, and R. Wiesendanger, Nanotechnology **20**, 405608 (2009).

[12] R. DeIasi, S. L. Hol and B. Post, Inorganic Chemistry **10**, 1498 (1971).

[13] W. B. Yuan, H.-Y. Wang, J.-F. Du, S.-W. Chen, and Q. Zhang, Acta Cryst. **E62**, 3504 (2006).

[14] M. Ashino, A. Schwarz, T. Behnke, and R. Wiesendanger, Phys. Rev. Let. **93**, 136101 (2004).

[15] T. Trevethan, M. Watkins, and A. Shluger, University College London.

[16] K. Lämmle, T. Trevethan, A. Schwarz, M. Watkins, A. Shluger, and R. Wiesendanger, Nano Lett. **10**, 200 (2010).

[17] M. Bammerlin, R. Lüthi, E. Meyer, A. Baratoff, J. Lü, M. Guggisberg, C. Gerber, L. Howald, and H.-J. Güntherodt, Probe Microsc. **1**, 3 (1997).

[18] R. Bennewitz, O. Pfeiffer, S. Schär, V. Barwich, E. Meyer, and L. N. Kantorovich, Appl. Surf. Sci. **188**, 232 (2002).

[19] T. Trevethan and L. Kantorovich, Nanotechnology **16** S79 (2005).

[20] R. Hoffmann, D. Weiner, A. Schirmeisen, and A. S. Foster, Phys. Rev. B **80**, 115426 (2009).

[21] A. S. Foster and A. L. Shluger, Surf. Sci. **490**, 211 (2001).

[22] A. D. Becke, J. Chem. Phys. **98**, 5648 (1993).

[23] C. Lee, W. Yang, R. G. Parr, Phys. Rev. B **37**, 785 (1988).

[24] F. Ortmann, F. Bechstedt, W. G. Schmidt, Phys. Rev. B **73**, 205101 (2006).

[25] S. F. Boys and F. Bernardi, Mol. Phys. **19**, 553 (1970).

[26] S. Kuck, PhD Thesis, Hamburg (2009).

3.8 Superconductors

Vortex configurations of superconductors in real space can be studied very well utilizing magnetic force microscopy (MFM) [1–6]. For highly anisotropic type-II superconductors like $Bi_2Sr_2CaCu_2O_{8+\delta}$, such studies are of particular interest, because they possess a rather complex B-T phase diagram showing various solid and liquid phases. In many respects it resembles p-T phase diagrams of conventional matter with various solid and liquid phases present. Hence, the phrase *vortex matter* has been coined to describe this area of research. However, the analogy has its limits, because the so-called *pancake vortices* in highly anisotropic type-II superconductors, which form flux-lines at sufficiently low temperatures, are rather elastic and can be easily deformed, e.g., by the presence of pinning sites or due to thermal fluctuations. These effects can be visualized with MFM and a thorough data evaluation provides detailed information about magnitude and temperature dependence of such elastic deformation of the flux lines [7].

Real space visualization of thermal fluctuations in a triangular flux line lattice

A. Schwarz, U. H. Pi, and M. Liebmann

In their mixed state magnetic fields can penetrate type-II superconductors in the form of vortices. Their cores of radius ξ (the coherence length of the Cooper pairs) are normal conducting. A magnetic field, corresponding to one quantum flux $\Phi_0 = 2 \times 10^{-15}$ Tm^2, threads the vortex core and is screened from the surrounding superconducting phase by circular supercurrents, which decay on the length scale of the London penetration depth λ. In the highly anisotropic superconductor $Bi_2Sr_2CaCu_2O_8$ (BSCCO) the Cooper pairs, and therefore the vortices as well, are confined to the copper oxide double planes, which are separated along the crystal c-axis by a distance $s > \xi$ (BSCCO: $s = 1.54$ nm and $\xi \approx 1$ nm). If located in neighboring planes, these so called pancake vortices (PVs) attract each other magnetostatically and via Josephson tunneling of Cooper pairs. Hence, they align along the c-axis to build up flux lines (FLs). On the other hand, PVs within the same plane repel each other. Consequently, FLs as a whole also repel each other and arrange themselves in a triangular flux line lattice (FLL). Its lattice constant $a_\triangle$ depends on the flux density B ($a_\triangle = \sqrt[4]{4/3} \cdot \sqrt{\Phi_0/B}$).

It has been realized that the discrete nature of FLs results in a strong susceptibility to thermal fluctuations leading to a rich variety of vortex phases in the B-T-phase diagram of BSCCO and similar high temperature superconductors (see, e.g., Refs. [8, 9] for reviews). Indirect volume averaging transport and magnetization measurements revealed regularly ordered or glassy solid-like phases as well as liquid-like phases in BSCCO. In the following it is demonstrated that by means of temperature dependent MFM experiments it is possible to visualize the impact of thermal fluctuation on the

alignment of PVs in individual FLs and on the regularity of the whole FLL. Particularly, a thorough evaluation of MFM images allows to analyze the regularity of a FLL in the *ab*-plane and to infer the degree of ordering along the *c*-axis. Moreover, it is also possible to detect a MFM signal, if PVs in adjacent layers are decoupled and hence do not form FLs.

Magnetic Force Microscopy Applied to Superconductors

MFM has proven its ability to detect [1–4] and manipulate [10,11] individual FLs. This *in-situ* real space imaging technique utilizes a cantilever of spring constant c_z with a ferromagnetic tip at its free end to sense the magnetostatic interaction between tip and sample at a fixed height h above the surface. For our experiments data acquisition was performed using the frequency modulation technique. In this mode of operation the amplitude A of the oscillating cantilever is kept constant and the frequency shift Δf, i.e., the deviation from the resonance frequency f_0 of the free cantilever, is a measure of the interaction strength. Details of the instrumentation (*Hamburg design*) and the MFM imaging mode can be found in Ref. [12].

For the following it is important to know that MFM senses the force gradient $\partial F/\partial z = 2c_z\Delta f/f_0$ of the magnetostatic interaction between a ferromagnetic tip and the stray field emanating from FLs. Hence, for intervortex distances larger than λ, FLs in MFM images appear as circular objects with radii on the order of λ (BSCCO: $\lambda \approx 200$ nm). If the magnetic polarization of the tip and the FL polarity are parallel, the magnetostatic interaction is attractive and FLs are displayed bright in images. Clem [13] could show that the magnetic field of an isolated PV in an anisotropic layered superconductor decays exponentially perpendicular to the surface with a decay length of λ. Therefore, the information depth of MFM is on the order of λ. Hence, in BSCCO more than 100 near surface PVs contribute to the signal stemming from one FL. As a consequence of the long range of the magnetostatic interaction, MFM data also contain information about the alignment of PVs within a FL.

Platelet $Bi_2Sr_2CaCu_2O_{8+\delta}$ single crystals ($T_c \approx 88$ K), grown by the floating zone method, were investigated using iron coated commercially available standard silicon sensors ($f_0 \approx 200$ kHz, $c_z \approx 40$ nm). To achieve out-of-plane magnetic sensitivity and to obtain a localized magnetic stray field, only one side face of the pyramidal tip was coated with about 5 nm of iron. Iron thickness and imaging parameters ($A \approx 30$ nm and $h \approx 30$ nm) were chosen to obtain a detectable MFM signal without disturbing the genuine arrangement of FLs.

Experimental Results

Figure 3.72 compares the arrangement of FLs in an irradiated (a) and an as grown (b) sample, respectively. The as grown sample only contains intrinsic point defects, i.e. oxygen vacancies [14]. For reference, an as grown sample was irradiated with heavy uranium ions parallel to the crystal *c*-axis to produce randomly distributed columnar

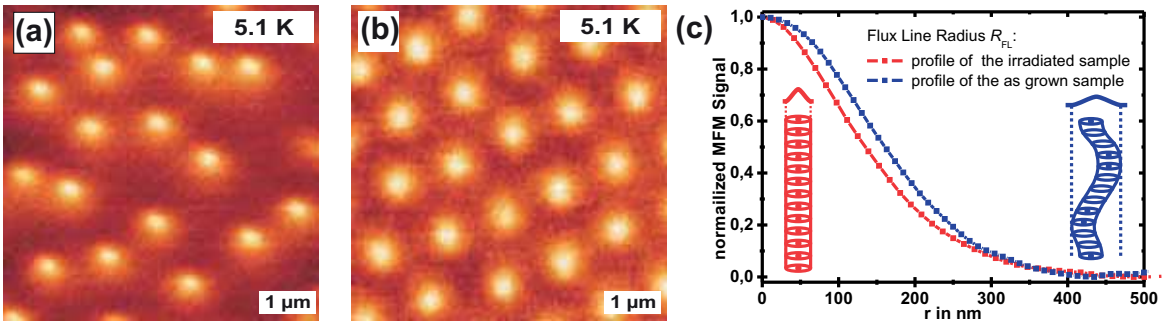

Figure 3.72: (a) MFM image of randomly distributed FLs in the irradiated sample after field cooling, which are strongly pinned at columnar defects. (b) MFM image of a regular triangular FLL obtained after field cooling in the as grown sample. Intrinsic randomly distributed pinning sites result in curved FLs and the absence of perfect long-range order. (c) Red and blue lines correspond to circular line sections [15] across a FL in (a) and (b), respectively. As depicted by the two sketches, the imaged flux line radius R_{FL} is larger for curved FLs.

defects. FLs were introduced into both samples by slow field cooling from above T_{c} down to $T =$ 5.1 K. The field cooling flux density B_{FC} was chosen so that the mean distance between FLs was much larger than λ (low flux density regime). Hence, both images in Fig. 3.72 exhibit well separated FLs. However, in (a), the irradiated sample, FLs are randomly distributed, while they form a triangular FLL in (b), the as grown sample. The two circular line sections [15] displayed in Fig. 3.72(c) reveal that the imaged FL size is smaller for the irradiated sample (red curve).

To investigate the impact of thermal fluctuations on the FLs in the FLL, the same area of the as grown sample was imaged at different temperatures. The starting condition after initial field cooling is shown in Fig. 3.73(a). Thereafter, the temperature was increased stepwise towards T_{c}. After each step, the FLL was imaged; cf. Fig. 3.73(b)-(f). The FLL remains intact (all FLL are surrounded by six neighbors) until the FLL contrast disappears at 54.1 K. To analyze our image data, we determined at every temperature the imaged FL radius R_{FL} (half width at half maximum of profiles across the FLs), the lattice parameter $a_{\triangle}$ using Delaunay triangulation and its standard deviation $\sigma_{a_{\triangle}}$.

Upon increasing the temperature, R_{FL} increases monotonically; cf. Fig. 3.74(a). Initially, R_{FL} increases only slightly from 183 nm (5.1 K) to 207 nm (23.2 K). Thereafter, a much steeper increase to 271 nm at 34.5 K can be observed until R_{FL} has nearly doubled to about 352 nm at 49.7 K. At 54.1 K the typical FLL contrast is absent. However, horizontally, i.e., along the fast scan direction, small contrast modulations are still visible. Note that the disappearance of the contrast happens far below T_{c} and also far below typically reported melting temperatures T_{m} for such a low flux density [16–18].

Expectedly, $a_{\triangle}$ remains constant as long as the FLL is visible. However, its standard deviation $\sigma_{a_{\triangle}}$, displayed in Fig. 3.74(b), exhibits a peculiar temperature depen-

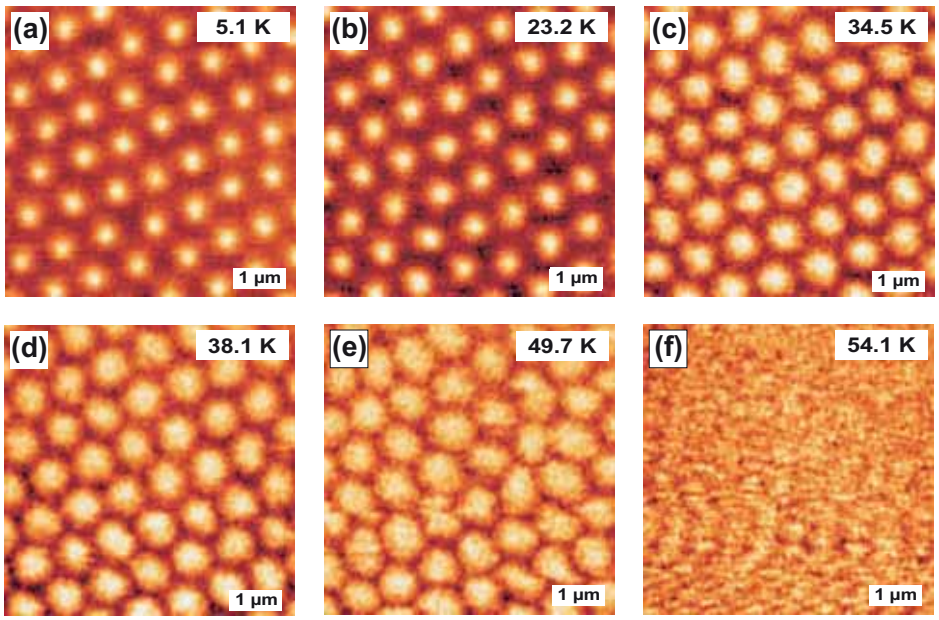

Figure 3.73: (a)-(e) MFM images of a triangular FFL at different temperatures. In (f) the previously observed FL contrast is absent. Only small contrast modulations along the fast scan direction are visible.

dence. As sketched in the inset this quantity is a measure of the lattice regularity, because the spread of the FL-separation $a_\triangle$ becomes larger, if translational and orientational disorder within the *ab*-plane of the FLL increases. Below $T \approx 30$ K, $\sigma_{a_\triangle}$ decreases only slightly (from 66 nm at 5.1 K to 65 nm at 23.2 K), but above $T \approx 30$ K the decrease is significantly stronger (from 63 nm at 34.5 K to 59 nm at 38.1 K), which indicates that the regularity of the FLL becomes better with increasing temperatures. Interestingly, the stronger decrease of $\sigma_{a_\triangle}$ happens in the same temperature regime where R_{FL} exhibits a much stronger increase with temperature than before. If the temperature is increased further towards T_{c} the decrease of $\sigma_{a_\triangle}$ turns into a sudden steep increase to about 92 nm at 49.7 K before the FLL contrast finally disappears at 54.1 K.

Data Evaluation and Discussion

We first analyze the FLs in Fig. 3.72(a). Since the straight columnar defects provide strong pinning sites, all FL are formed by coherently aligned PVs. Therefore, FLs are straight and their arrangement reflects the random distribution of ion trajectories during irradiation, which generated the columnar defects. This situation is known as the Bose-Glass state.

In the as grown sample, cf. Fig. 3.72(b), only intrinsic defects are present. For pinning of PVs in BSCCO the most relevant defects are believed to be randomly distributed oxygen vacancies in the CuO-layers [14]. They are randomly distributed

in all three dimensions and act as weak pinning sites. In the low flux density regime the interaction between FLs is very small, because for separations larger than λ the repulsion between FLs decays exponentially with distance. In this situation even weak pinning sites introduce significant disorder into the system, because they attract PVs. Of course, PVs still tend to form FLs. However, to accommodate the pinning sites the rather elastic FLs are not straight anymore, but curved [9, 19].

Since MFM is sensitive to many layers with PVs, the envelope of all laterally shifted PVs contributes to the imaged FL radius. Therefore, curved FLs will appear broader than straight ones as sketched in the insets of Fig. 3.72(c). Indeed, the circular line section [15] in Fig. 3.72(c) shows that the FL radius in the Bose glass state with straight FLs is smaller than for curved FL in the as grown sample. The difference measured at half width at half maximum between red and blue curve is about 30 nm. It should be noted that without any pinning FLs are perfectly straight as well. Therefore, our finding that R_{FL} in the as grown sample is larger than in the irradiated sample strongly indicates that pinning at intrinsic defects occurs and is indeed relevant in our case.

The presence of randomly distributed point like pinning sites show up in the lattice regularity as well. A standard deviation $\sigma_{a_\triangle}$ of 66 nm, which corresponds to about 7.5% of $a_\triangle$ demonstrates that the FLL does not exhibit perfect long-range order in the *ab*-plane. How randomly distributed pinning sites lead to positional disorder is sketched in the inset of Fig. 3.74(b). PVs (and hence FLs) are slightly displaced from the equilibrium positions, if pinning sites are nearby. As a result $a_\triangle$ exhibits a Gaussian distribution of width $\sigma_{a_\triangle}$. A larger $\sigma_{a_\triangle}$ indicates more disorder. The observed absence of perfect long-range order is characteristic for a Bragg glass [20].

Figure 3.74(a) clearly shows that $R_{\mathrm{FL}}(T)$ behaves distinctively different below and above the temperature regime around 30 K, i.e., from 5.1 K to 23.2 K the increase is only 13% while it increases by 31% between 23.2 K and 34.5 K. Interestingly, Dewhurst and Doyle reported magnetization measurements on BSCCO samples, which revealed a clear feature in the derivative of the magnetic moment as function of temperature at about 32 K [21]. They interpreted this feature as a sign for a depinning transition. We performed such magnetization measurements as well and found the same feature in the as-grown sample at a slightly lower temperature of about 30 K. Around the same temperature the positional order expressed by $\sigma_{a_\triangle}$ increases significantly. At first sight this finding is counterintuitive, because higher temperatures, i.e., increased thermal fluctuations, usually lead to more disorder in a system. However, as explained in the following. a depinning transition can explain the significant reduction of $\sigma_{a_\triangle}(T)$ above 30 K as well as the peculiar different temperature dependence of $R_{\mathrm{FL}}(T)$ in the same temperature regime.

To understand the broader appearance of FLs after depinning one has to consider the potential landscape for a PV surrounded by other PVs near a point-like weak pinning site. Due to the mutual repulsion between PVs within the same CuO-layer, each PV is caged in a potential minimum formed by the six surrounding PVs. A

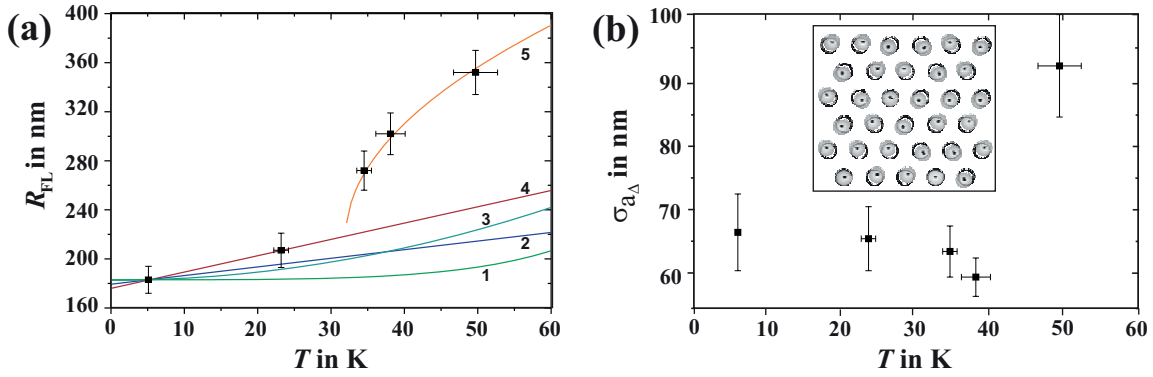

Figure 3.74: (a) Temperature dependence of the imaged FL radius $R_{\mathrm{FL}}(T)$ extracted from Fig. 3.73. Curves 1 to 5 represent different models for the observed T-dependence. Below depinning at $T_{\mathrm{D}} \approx 30$ K the small broadening is due to the temperature dependence of $\lambda = \lambda(T)$. After depinning, thermal fluctuations are much stronger resulting in a $\sqrt{T - T_{\mathrm{D}}}$-dependence. (b) Temperature dependence of the standard deviation $\sigma_{a_\triangle}$ of the mean FL distance $a_\triangle$ extracted from Fig. 3.73. It is a measure of the lattice regularity, as sketched in the inset. After depinning the lattice becomes significantly better ordered. At 49.7 K, just before the typical FLL contrast disappears, the FLL becomes strongly disordered.

simplified one-dimensional potential landscape of a PV in such an environment is displayed in Fig. 3.75. The cage potential is parabolic with a curvature $k_{\mathrm{c,PV}}$ and centered at r_0, i.e., $E_{\mathrm{c,PV}} = \frac{1}{2}k_{\mathrm{c,PV}}(r - r_0)^2$. The width of the cage potential $E_{\mathrm{c,PV}}$, given by $k_{\mathrm{c,PV}}$, depends on the flux density. In addition, pinning sites are present, which alter the cage potential locally. The pinning potential E_{p}, which stems from a localized point defect, is characterized by its depth $E_{\mathrm{p,0}}$ below the minimum of the cage potential. As for the cage potential, it can be approximated by a parabola, but with a different curvature k_{p}. For atomic scale defects like oxygen-vacancies its range u is on the order of 1 nm. Since vortex cores in BSCCO are of similar size ($\xi \approx 1$ nm), such defects can act as pinning sites. Beyond this range the pinning strength decays quickly to zero, i.e., $E_{\mathrm{p}} = \frac{1}{2}k_{\mathrm{p}}(r - r_{\mathrm{p}})^2 - E_{\mathrm{p,0}}$ for $r \leq u$ and $E_{\mathrm{p}} \approx 0$ for $r > u$. In the low flux density (as in our case) $E_{\mathrm{c,PV}}$ is certainly much wider than E_{pin}, i.e., $k_{\mathrm{c,PV}} << k_{\mathrm{p}}$. The superposition of $E_{\mathrm{c,PV}}$ and E_{p} is sketched in Fig. 3.75.

The energy E_{D} needed for depinning depends not only on $E_{\mathrm{p,0}}$, but also on the distance between r_0 and the location of the pinning site r_{p}, i.e., $E_{\mathrm{D}} = \frac{1}{2}k_{\mathrm{c,PV}}(r_{\mathrm{p}} - r_0)^2 + E_{\mathrm{p,0}}$. Therefore, even if one type of pinning sites with a well defined pinning strength $E_{\mathrm{p,0}}$ dominates, e.g., oxygen vacancies, a certain distribution of depinning energies exists. Such a distribution of depinning energies explains the steady decrease of $\sigma_{a_\triangle}$ with increasing temperature. However, the distribution is not very wide, because in the low flux density regime much more pinning sites than PVs are present. Hence, the actual pinning positions r_{p} after slow field cooling are mostly relatively close to the equilibrium position r_0. Consequently, the depinning transition is relatively sharp as indicated by the distinctive feature found in volume averaging magnetization data.

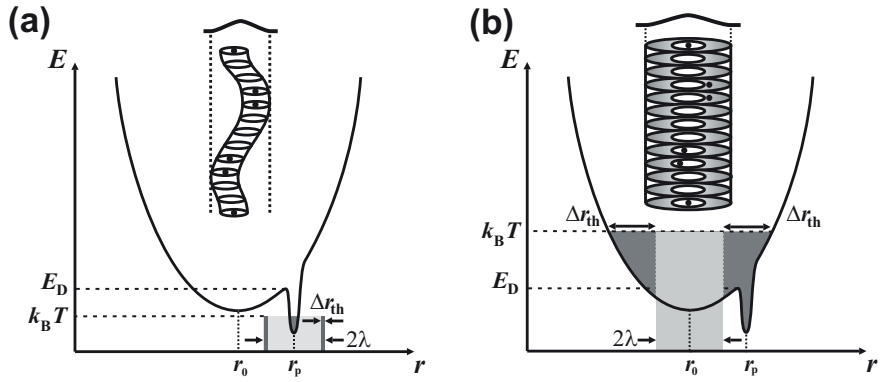

Figure 3.75: Simplified energy landscape of a single PV. It consists of a wide cage potential at r_0 and a localized narrow pinning potential at r_p. Bright and dark gray shaded areas indicate the magnitude of λ and the broadening Δr_th due to thermal fluctuations, respectively. The MFM signal from one PV stems from a region with radius $r_\mathrm{PV} = \lambda + \Delta r_\mathrm{th}$. (a) Below the depinning temperature T_D the PV is located at r_p, thermal broadening is negligible and FLs are curved. (b) Above T_D FLs become straighter and thermal broadening is significant.

Although the MFM signal of one FL contains contributions from all PVs in the FL up to distance on the order of λ below the surface, it is sufficient for the time being to restrict the discussion regarding contrast formation to the behavior of a single PV. As explained above, the MFM signal of one PV stems from a region with radius $r_\mathrm{PV} = \lambda$. However, this is only exact for an immobile PV, i.e., at $T = 0$ K. For $T > 0$ K the position fluctuates around its equilibrium position. The time scale of such thermal fluctuations is much faster than the data acquisition time (typically a few ms per image point for MFM). Therefore, the MFM signal is averaged over a region of radius $r_\mathrm{PV} = \lambda + \Delta r_\mathrm{th}$, where Δr_th is the range of the thermal fluctuations around the equilibrium position.

At a given temperature T the available thermal energy E_th is on the order of $\frac{1}{2}k_\mathrm{B}T$ (k_B is Boltzmann's constant). The magnitude of Δr_th depends on the width of the potential, in which the PV is trapped. As long as E_th is smaller than E_D, the movement of the PV is confined by the narrow pinning potential. Thus $\Delta r_\mathrm{th} << \lambda$, and the MFM signal stems to a very good approximation from a region with radius λ; cf. Fig. 3.75(a). If the pinning potential is very narrow, Δr_th does not increase significantly for higher temperatures. However, above the depinning temperature T_D, i.e., if $E_\mathrm{th} > E_\mathrm{D} = \frac{1}{2}k_\mathrm{B}T_\mathrm{D}$, the PV can move freely across the localized pinning site. Now the thermal fluctuations are limited by the much wider cage potential; cf. Fig. 3.75(b). As a result, Δr_th is not negligible and $r_\mathrm{PV} = \lambda + \Delta r_\mathrm{th}$ is significantly thermally broadened.

Depinning of individual PVs also shows up in appearance of individual FLs and the FLL. With increasing temperature more and more PVs within a FL are located at their equilibrium position r_0. Hence, the FLs become straight and the FLL becomes better ordered. We cannot directly detect this straightening in the $R_\mathrm{FL}(T)$-plot, be-

cause the resulting decrease of R_{FL} is masked by the thermal broadening. However, the increased long-range positional order results in the significant decrease of $\sigma_{a_\triangle}$ at elevated temperatures.

Next, we check the qualitative picture given above in a more quantitative manner by analyzing the $R_{\mathrm{FL}}(T)$-plot in Fig. 3.74(a). Below T_{D}, the imaged FL size R_{FL} is determined by λ. Since λ is temperature dependent, R_{FL} should exhibit the same temperature dependence, because $R_{\mathrm{FL}}(T) \propto \lambda(T)$. For conventional isotropic type-II superconductors the temperature dependence according to the two-fluid model is given by $\lambda(T) = \lambda_0/\sqrt{1-(T/T_{\mathrm{c}})^{1/4}}$, where λ_0 is the London penetration depth at 0 K. However, for d-wave superconductors like BSCCO different temperature dependencies have been proposed for temperatures sufficiently below T_{c}, i.e., $\lambda(T) = \lambda_0(1+\alpha T^{\beta})$ with $\beta = 1$ or 2. Assuming $R_{\mathrm{FL}}(T) \propto \lambda(T)$ and $\lambda_0 \propto R_0$ corresponding fits are included in Fig. 3.75(a) as curves 1 to 3: (1) two-fluid model; (2) $\alpha = 3.92 \times 10^{-3}$ K^{-1}, $\beta = 1$; (3) $\alpha = 9.03 \times 10^{-5}$ K^{-2}, $\beta = 2$. The values for curve (2) and (3) are taken from torque magnetometry measurements by Waldmann et al. [22] for materials with a T_{c} close to its optimal T_{c} of about 90 K ($\beta = 1$) and for materials with a significantly reduced T_{c} ($\beta = 2$), respectively.

None of the models describe the experimental data correctly over the whole temperature range. Below T_{D} curve 2 ($\beta = 1$, for an optimal T_{c}) fits best, which is in agreement with our relatively high T_{c}. If we use the two data points below T_{D} to determine α from a linear fit ($\beta = 1$; see curve 4), its value of 7.5×10^{-3} K^{-1} is very close to the one found by Waldmann et al. [22]. Since only two data points are below T_{D}, the other models cannot be excluded. However, the temperature dependent behavior of R_{FL} below T_{D} can be satisfactorily explained by the temperature dependence of λ.

Above T_{D} all models for $\lambda(T)$ fail to explain the MFM data, because additional broadening by thermal fluctuations is not considered in these models. If we assume a parabolic cage potential, the additional thermal broadening ΔR_{th} should exhibit a $\sqrt{T}$-dependence, i.e., $\Delta R_{\mathrm{th}} = \sqrt{k_{\mathrm{B}}(T-T_{\mathrm{D}})/k_{\mathrm{c,FL}}}$. Note that $k_{\mathrm{c,FL}}$ cannot be identified with $k_{\mathrm{c,PV}}$, which was introduced for a single PV, because the MFM signal stems from a FL segment with a length on the order of λ. Similarly, ΔR_{th} denotes the thermal broadening of the FL-segment of length λ sensed by MFM, which, in general, will be different from Δr_{th}, the thermal broadening of a single PV.

After depinning the PVs of each FL probe their potential landscape stemming from the PVs in the surrounding FLs. This can be utilized to determine the effective stiffness $k_{\mathrm{c,FL}}$ of the cage potential for a FL segment of length λ. To fit the $R_{\mathrm{FL}}(T)$ data above T_{D}, we take a linear temperature dependence of λ into account as well as thermal fluctuations within the cage potential for one FL, i.e., $R_{\mathrm{FL}}(T) = R_0(1+\alpha T) + \sqrt{k_{\mathrm{B}}(T-T_{\mathrm{D}})/k_{\mathrm{c,FL}}}$. For α we use the value from the best fit in the regime below T_{D}, i.e., $\alpha = 7.5 \times 10^{-3}$ K^{-1} (curve 4), and $R_0 = R_{\mathrm{FL}}$ at $T = 5.1$ K. Thus, $k_{\mathrm{c,FL}}$ is the only free parameter. The fit with $k_{\mathrm{c,FL}} = 1.8 \times 10^{-8}$ N/m clearly shows that the temperature dependence of the imaged FL size $R_{\mathrm{FL}}(T)$ can be directly related to thermal fluctuations, which become significant after depinning. As mentioned before,

the magnitude of the thermal broadening depends on the width of the cage potential, i.e., on the flux density B. For higher flux densities the interaction between FLs starts to dominate over thermal effects, because the cage potential becomes narrower, i.e., $k_{\mathrm{c,FL}}$ gets larger. Note also that below T_{D} a similar formula applies, i.e., $\Delta r_{\mathrm{th}} = \sqrt{k_{\mathrm{B}}T/k_{\mathrm{p}}}$. However, since $k_{\mathrm{p}} >> k_{\mathrm{c,PV}}$, Δr_{th} is negligibly small compared to the effect due to the temperature dependence of λ itself, these tiny thermal fluctuations do not show up in our data.

Decoupling of Pancake Vortices

If the temperature is further increased, the thermal energy will surpass the coupling energy between PVs in neighboring layers. Hence, the disappearance of the typical FLL contrast at 54.1 K could be interpreted in terms of a melting transition. Randomly relative positions of mobile PVs in adjacent CuO-layers are consistent with the observed smeared out contrast in MFM images visible in Fig. 3.73(f). Moreover, we found a point-like feature shown in Fig. 3.76(a) at this temperature, which could be a still pinned FL segment. The ring-like structures around it, clearly visible in the circular line section [15] of Fig. 3.76(b), can be interpreted as decoupled PVs, which locally form a standing wave pattern.

Data recorded with other techniques in the low flux density regime for BSCCO suggest a melting temperature T_{m} much closer to T_c ($\approx 88\ K$ for our sample) than 54.1 K [16–18]. Therefore, the features in Fig. 3.74(f) and Fig. 3.76(a) cannot be simply identified with the vortex liquid phase observed with other experimental techniques. More likely the decoupling of PVs is not exclusively a consequence of large thermal fluctuations. Additionally, dragging due to the magnetostatic attraction between PVs and tip could play a significant role as well. It has been pointed out by Wadas et al. [24] that lateral magnetostatic forces during MFM imaging could also lead to a depinning of FLs. We reported that FLs can be moved along antiphase boundaries due to the stray field of a magnetic tip [10]. Moreover, we determined experimentally the magnitude of the lateral force between an MFM tip and a FL by analyzing force spectroscopy data [23]. Recently, MFM tips were deliberately utilized to bend a FLs away from their equilibrium positions without actually depinning them [11]. Therefore, it is likely that shearing forces exerted by the horizontally scanned tip on the FLL together with thermal fluctuations can decouple the PVs near the surface resulting in the observed horizontal contrast modulations. This happens even at temperatures far below the thermodynamic melting transition, but only in the vicinity of the tip. PVs outside the scanned area and PVs in the bulk are not affected.

The onset of the proposed shearing can already be observed at 49.7 K in Fig. 3.73(e). For this temperature $\sigma_{a_\triangle}$ behaves against the trend, i.e., it becomes very large (about 92 nm) instead of becoming smaller (cf. discussion in the previous section). Although the FLL is still clearly visible, individual FLs appear less well defined than before, e.g., some look squeezed others are elongated. This is a clear sign that lateral forces start to distort the genuine FLL structure.

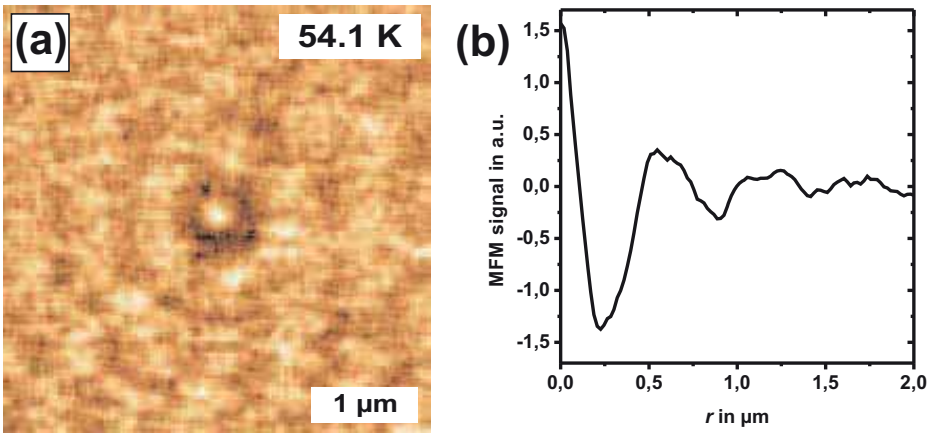

Figure 3.76: Liquid-like behavior of decoupled PVs. (a) MFM image of a point-like feature, probably a still pinned FL segment. (b) Circular line section [15] around the point-like feature. The contrast pattern resembles a standing wave pattern.

References

[1] A. Moser, H. J. Hug, I. Parashikov, B. Stiefel, O. Fritz, H. Thomas, A. Baratoff, H. J. Güntherodt, and P. Chaudhari, Phys. Rev. Lett. **74**, 1847 (1995).

[2] A. Volodin, K. Temst, C. Van Haesendonck, and Y. Bruynseraede, Appl. Phys. Lett. **73**, 1134 (1998).

[3] M. Rosemann and P. Grütter, New J. Phys. **3**, 24 (2001).

[4] U. H. Pi, Z. G. Khim, D. H. Kim, U. Kaiser, A. Schwarz, M. Liebmann, and R. Wiesendanger, J. Low Temp. Phys. **131**, 993 (2003).

[5] U. H. Pi, Z. G. Khim, D. H. Kim, A. Schwarz, M. Liebmann, and R. Wiesendanger, Phys. Rev. B **69**, 094518 (2004).

[6] A. Schwarz, U. H. Pi, M. Liebmann, R. Wiesendanger, Z. G. Khim, and D. H. Kim, Appl. Phys. Lett. **88**, 012507 (2006).

[7] A. Schwarz, M. Liebmann, U. H. Pi, and R. Wiesendanger, New J. Phys. **12**, 033022 (2010).

[8] D. S. Fisher, M. P. A. Fisher and D. A. Huse, Phys. Rev. B **43**, 130 (1991).

[9] G. Blatter, M. V. Feigel'man, V. B. Geshkenbein, A. I. Larkin, and V. M. Vinokur, Rev. Mod. Phys. **66**, 1125 (1994).

[10] U. H. Pi, Z. G. Khim, D. H. Kim, A. Schwarz, M. Liebmann, and R. Wiesendanger, Phys. Rev. B **69**, 094518 (2004).

[11] O. M. Auslaender, L. Luan, E. W. J. Straver, J. E. Hofmann, N. C. Koshnick, E. Zeldov, D. A. Bonn, R. Liang, W. N. Hardy, and K. A. Moler, Nature Phys. **5**, 35 (2009).

[12] M. Liebmann, A. Schwarz, S. M. Langkat, and R. Wiesendanger, Rev. Sci. Instr. **73**, 3508 (2002).

[13] J. R. Clem, Phys. Rev. B **43**, 7837 (1991).

[14] E. M. Chudnovsky, Phys. Rev. Lett. **65**, 3060 (1990).

[15] From the center of a circular object all line sections of length r on the circumference are radially averaged. The result is the *circular line section*.

[16] R. Cubitt, E. M. Forgan, G. Yang, S. L. Lee, D. McK. Paul, H. A. Mook, M. Yethiraj, P. H. Kes, T. W. Li, A. A. Menovsky, Z. Tarnawski, and K. Mortensen, Nature **365**, 407 (1993).

[17] B. Khaykovich, E. Zeldov, D. Majer, T. W. Li, P. H. Kes, and M. Konczykowski, Phys. Rev. Lett. **76**, 2555 (1996).

[18] A. Oral, J. C. Barnard, S. J. Bending, I. I. Kaya, S. Ooi, T. Tamegai, and M. Henini, Phys. Rev. Lett. **80**, 3610 (1998).

[19] D. R. Nelson and V. M. Vinokur, Phys. Rev. Lett. **68**, 2312 (1992).

[20] T. Giamarchi and P. Le Doussal, Phys. Rev. B **55**, 6577 (1997).

[21] C. D. Dewhurst and R. A. Doyle, Phys. Rev. B **56**, 10832 (1997).

[22] O. Waldmann, F. Steinmeyer, P. Müller, J. J. Neumeier, F. X. Regi, H. Savary, and J. Schneck, Phys. Rev. B **53**, 11825 (1996).

[23] U. H. Pi, Z. G. Khim, D. H. Kim, A. Schwarz, M. Liebmann, and R. Wiesendanger, Appl. Phys. Lett. **85**, 5307 (2004).

[24] A. Wadas, O. Fritz, H. J. Hug, and H.-J. Günterodt, Z. Phys. B **88**, 317 (1992).

[25] L. Luan, O. M. Auslaender, D. A. Bonn, R. Liang, W. N. Hardy, and K. A. Moler, Phys. Rev. B **79**, 214530 (2009).

[26] M. Willemin, C. Rossel, J. Hofer and H. Keller, A. Erb, and E. Walker, Phys. Rev. B **58**, R5940 (1998).

3.9 Instrumental developments

In the study of magnetic phenomena it is of fundamental importance to observe a sample's response to the action of an applied external field. Basic magnetic properties like susceptibility, hysteresis, or anisotropy can only be scrutinized under these conditions. With the routine establishment of spin-polarized STM investigations of magnetic nanostructures it was but a natural step to equip the experimental setups with means to supply external magnetic fields. With the probing tips being magnetic themselves, yet another objective became desirable: to control the magnetization direction of the STM tip.

So far, in our group measurements could be performed in low temperature UHV systems equipped with superconducting magnets capable to apply magnetic fields of up to 2.5 T (STM, 10 K) [1], 5 T (AFM/MFM, 5.2 K) [2], and 12 T (STM, 300 mK) [3]; in all these cases, the field is applied perpendicular to the sample plane, that is, along the tip axis. Yet another 4.2 K system has a 7 T magnet perpendicular with an additional 2 T magnet in-plane, suitable to rotate the field vector within a plane [4]. In the following, a new system is described [5], uniquely equipped with a three axes vector magnet. For the first time, this system provides the freedom to orient the magnetic field vector into any desired spatial direction.

3.9.1 SP-STM in a superconducting triple-axes magnet system

S. Meckler, M. Gyamfi, O. Pietzsch, and R. Wiesendanger.

The new scanning tunneling microscope (STM) for spin-polarized experiments is operated at 4.7 K in a superconducting three axes vector magnet providing the possibility for measurements depending on the direction of the external magnetic field. In single axis mode the maximum field is 5 T perpendicular to the sample plane and 1.3 T in the sample plane, respectively. In cooperative mode fields are limited to 3.5 T perpendicular and 1 T in-plane. The microscope is operated in an ultra-high vacuum system providing optimized conditions for the self-assembled growth of magnetic structures at the atomic scale. The available temperature during growth ranges from 10 K up to 1100 K. The performance of the new instrument is illustrated by spin-polarized measurements on 1.6 atomic layers Fe/W(110). It is demonstrated that the magnetization direction of ferromagnetic Fe- and Gd-tips can be adjusted using the external magnetic field. Atomic resolution is demonstrated by imaging an Fe monolayer on Ru(0001).

Motivation and design concept

Despite their differences, all methods to achieve spin contrast in scanning tunneling experiments [6,8,9] rely on the idea that spin contrast depends on the relative orientation of the magnetizations of sample and tip [10]. For a collinear configuration the contrast is maximized whereas for an orthogonal configuration the spin contrast vanishes. However, the magnetization direction of the tip is in general not known exactly, thus detailed conclusions about the magnetization directions in magnetic nanostructures have remained a fundamental problem of SP-STM since its beginnings.

A successful and relatively simple way to overcome this problem has been to apply an external magnetic field to a ferromagnetic tip, resulting in a canting or full alignment [11] of the tip magnetization along the direction of the external field. On the other hand, by using antiferromagnetic chromium tips the tip magnetization can be kept stable in external magnetic fields [12, 13] thus allowing to investigate the behaviour of a sample system in an external field without any superimposed tip effects [11, 13–15]. However, up to now the direction of the external field was in general restricted to one specific axis. We are aware of two setups where the external field is restricted to a specific plane only. This has been achieved by using two magnets in a perpendicular configuration [4, 16]. Only recently, another new system with a 3D-vector magnet was reported in the literature [17].

In this article we present an STM for spin-polarized measurements which is rigidly mounted inside the center of a superconducting three axes magnet. The design allows easy access to the microscope from two sides which guarantees a fast and easy exchange of samples and tips in the STM as well as the option to deposit single adsorbate atoms directly onto the cryogenic sample surface inside the microscope. It is important to note that due to the requirement of a direct access to the microscope the magnet design is based on three pairs of split coils instead of a configuration with a solenoid as the central coil.

The design focus of the sample and tip preparation facilities outside the microscope has been put on a maximum of flexibility for the self-assembled growth of atomic scale magnetic structures. To increase the throughput of the system, we developed a LabView based software package for monitoring and control of the complete setup as well as for the automation of substrate cleaning processes and measurements.

The UHV system was realized in a fully customized design and consists of three chambers plus loadlock interconnected by gate valves to allow sample transfer (Fig. 3.77). The complete design was done in close collaboration with Omicron Nanotechnology GmbH [18] who manufactured the system according to our technical drawings. In the laboratory the whole setup is installed on a huge block of concrete which is vibrationally decoupled from the building. Additionally, the UHV chambers are supported by a bench resting on pneumatic damping legs. All vacuum chambers are pumped by ion getter and titanium sublimation pumps (TSP). In the cryostat chamber the cold surfaces of the cryostat act as an additional cryopump. To counterbalance the desorption of hydrogen during cryostat warm-up the cryostat chamber is

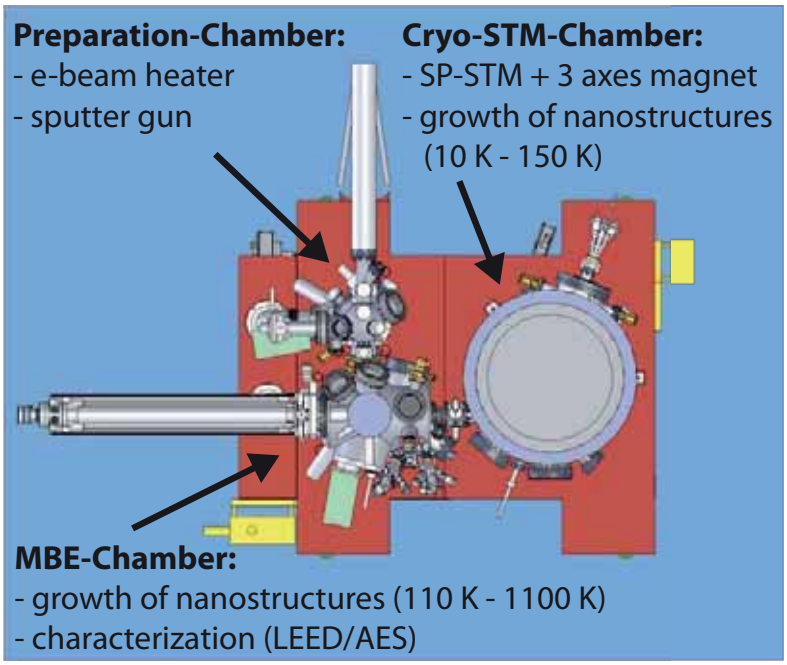

Figure 3.77: Top view of the three chamber UHV system schematics. The system bench rests on a solid foundation of concrete decoupled from the building. Additional air damping legs are installed under the bench.

equipped with a non evaporating getter (NEG) pump. The base pressures are below 1×10^{-10} mbar for all vacuum chambers.

Substrate cleaning and MBE growth facilities

Preparation chamber For the investigation of magnetic nanostructures at the atomic scale the cleanliness of the underlying substrate is essential. Since all cleaning procedures inevitably lead to high gas loads they are accomplished in the preparation chamber which is separated from the other chambers by a gate valve. The preparation chamber is connected to a load lock chamber where up to four substrates or STM tips can be transfered into the system in a single step.

There are two cleaning procedures of major importance, depending on the material of the single crystals in use. An ion source in conjunction with a manipulator equipped with a resistive heating stage providing temperatures up to 1100 K can be used for repeated cycles of Ar^+ ion sputtering and subsequent annealing. For the Ar gas inlet a piezo motor controlled leak valve is used which can be addressed by an appropriate control electronics. Thus, the desired gas pressure can be accurately adjusted and is stabilized by a feedback loop. This feature allows to run unattended automated sputter and annealing cycles.

In the second cleaning procedure a home-built electron bombardment heating stage is applied to achieve temperatures as high as 2000° C and more. This facility is de-

Figure 3.78: An empty sample tray being heated by electron bombardment. Grooves in two tungsten rods receive the sample tray or the tip transporter. The electron-emitting filament is positioned right underneath the tray. With the tungsten rods held at high positive voltage, the electrons get accelerated and release their kinetic energy upon impingement on the tray's back side.

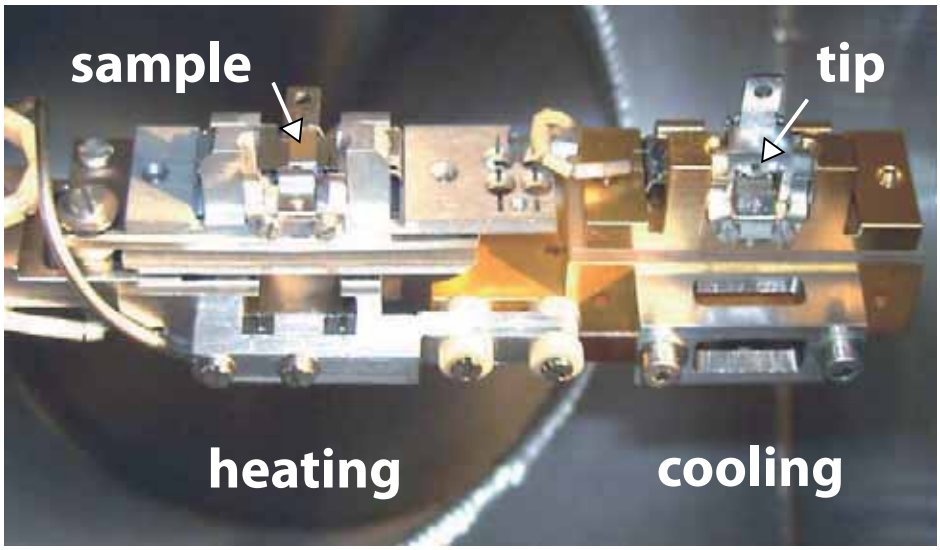

Figure 3.79: The two stages of the manipulator head used for heating or cooling the sample or the tip during evaporation. For illustration purposes both a sample and a tip transporter have been put on the manipulator head at the same time. The overall achievable temperature range is 110 K to 1100 K.

signed to enable not only a treatment of samples, but also of STM tips (Fig. 3.78). An advanced cleaning procedure for tungsten single crystals involving high temperatures has been described previously [19]. In short, the tungsten substrate is repeatedly kept at elevated temperatures in an oxygen atmosphere for a certain time, followed by a short flash to high temperature after a recovery of the base pressure to the low 10^{-10} mbar range. Similar procedures can be applied for other materials. Again, by making use of a piezo-driven leak valve and a suitable home-built control software the time consuming cleaning cycles have been automated.

MBE chamber The main purpose of the MBE chamber is the growth of magnetic nanostructures on the clean substrates using self-assembly. A process of equal importance is the deposition of thin magnetic films on the pre-cleaned STM-tips. For controlling the process of self-assembly there are three major parameters on which the growth result depends crucially: (i) the choice of material combination of the adsorbate/substrate system with a particular surface crystallographic orientation, (ii) the substrate temperature during growth, and (iii) the deposition rate.

The chamber is equipped with five Focus EFM3 e-beam evaporators [20] for submonolayer growth of various magnetic transition metals. They contain flux meters enabling the growth to be controlled by well defined deposition rates. One of the evaporators is of the EFM3i type [21]. As a special feature, this evaporator can generate ions during evaporation. This can be useful to deliberately create nucleation centers at the sample surface. By virtue of this process, smooth heteroepitaxial films can be grown on surfaces where otherwise Vollmer-Weber [22] growth would be present [21]. In the context of the investigation of atomic scale nanostructures this ion assisted deposition technique may be useful to nucleate atomic scale clusters at high areal densities on a substrate surface.

During evaporation sample or tip are held in an Omicron manipulator head which is mounted to a VG Scienta Omniax manipulator. Essentially, the manipulator head is the standard Omicron design but with a few important modifications to meet the geometry of our custom sample trays and tip transporters (Fig. 3.79). Instead of just one receptacle for the sample there is another one for the tip transporter at an angle of 90°. Furthermore, this manipulator head consists of two stages, one for heating and another one for cooling the sample. Both stages are thermally decoupled at elevated temperature by a sapphire plate. The heater stage is equipped with a PBN-heater enabling us to heat both sample or tip to about 1100 K. At the cooling stage a temperature of 110 K is achieved using cold nitrogen gas that can be circulated through tubes thereby cooling a copper block at the cooling stage. At both stages the temperature is measured by a thermocouple. At the heater stage the temperature can be adjusted with a precision below 1 K. For low temperatures a precise temperature control is not possible. However, the temperature can be adjusted with some precision by adjusting the nitrogen flux and heating with the PBN-heater. The travel of the manipulator was chosen long enough to allow the transfer of the sample all the way

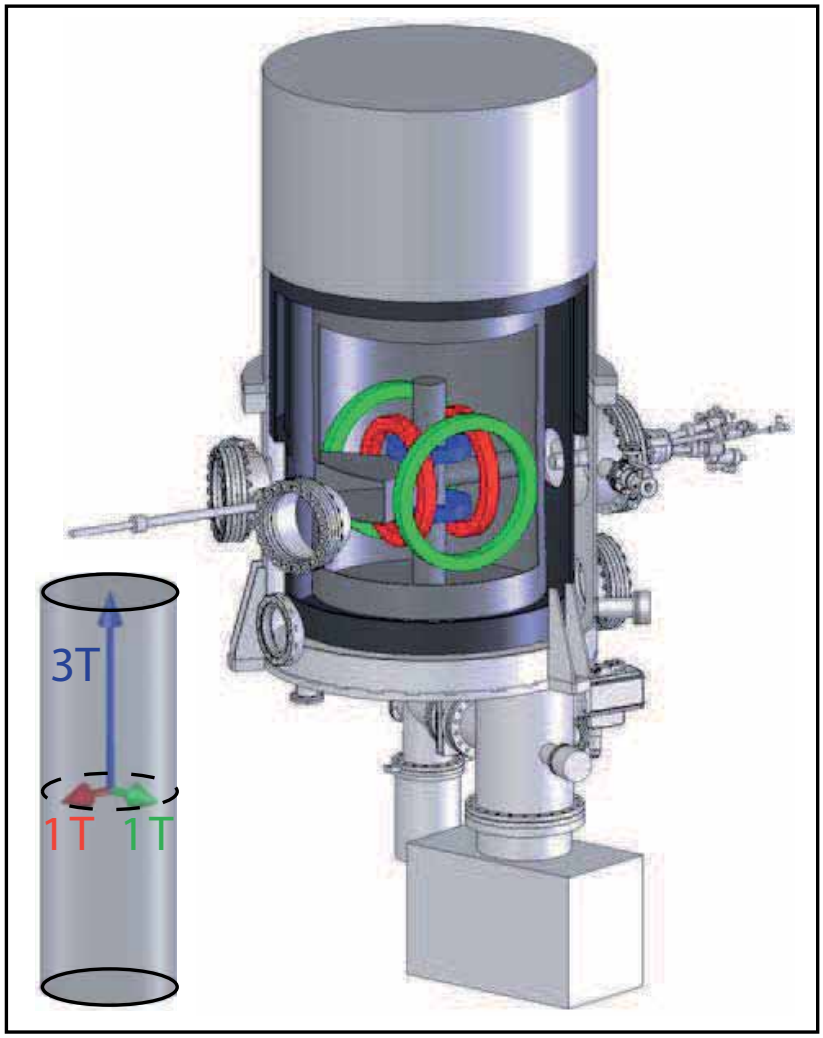

Figure 3.80: Cutaway view of the cryostat chamber hosting the superconducting three axes magnet with the STM. The split coils of the magnet are shown in red, green and blue, respectively. The sample is inserted into the microscope using the wobble stick to the left. An evaporator for single adsorbate deposition at very low temperatures is mounted opposite to the wobble stick. Inset: Schematic drawing of the accessible magnetic field range.

into the cryostat while being cooled. Since the wobble stick for the sample transfer into the microscope can be precooled by direct thermal contact to the nitrogen reservoir the sample can be inserted into the STM without warming up significantly after evaporation.

In addition to the evaporation facilities, standard surface analysis instruments for low energy electron diffraction (LEED) and Auger electron spectroscopy (AES) are available in the MBE chamber.

3D magnet cryostat

At the heart of the UHV system described here is a large vacuum chamber hosting a cryostat system [23] with a superconducting three axes magnet [24] and a home-built scanning tunneling microscope. The inner diameter of the vacuum chamber amounts to 700 mm and the UHV tight connection between the chamber and the cryostat system is accomplished by a COF700 flange. A three dimensional cutaway view of the setup

is given in Fig. 3.80. The vector magnet system consists of three pairs of split coils allowing to apply magnetic fields of 1.3 T along the x- and y-axis and 5 T along the z-axis, respectively. These values can only be achieved when any one of the three split coils is operated in single axis mode. When operated in cooperative mode the magnetic field vector is restricted to values inside a cylinder of radius 1 T and height ± 3.5 T, as illustrated in Fig. 3.80. The maximum sweep rates for the x-, y- and z-coils are limited to 1.2 mT/s, 1.3 mT/s and 5 mT/s, respectively.

There were three major constraints for the design of this vector magnet. First of all, the inner bore of the z-coils was demanded to be large enough to mount the microscope. In addition an opening of 60° was desired to allow an easy access to the microscope for sample and tip exchange which has proven to be highly beneficial in terms of sample throughput [1]. The third requirement was another, smaller direct access to the microscope from the backside. Since the STM is equipped with a mechanism for sample rotation (Fig. 3.81), this second direct access allows to deposit single adsorbates directly onto the cold sample without removing it from the microscope.

A major task in building a superconducting three axes magnet is to construct a solid mechanical structure preventing the coils from moving due to their pairwise dipolar interaction. Movements on the order of micrometers can already cause the superconducting magnet to quench. To accomplish the two openings mentioned above a design with a solenoid as the central coil is not appropriate and three pairs of split coils must be used. All split coils must be larger and therefore stronger than in a solenoid geometry resulting in a tendency towards reduced static stability. Thus, building a magnet with the given constraints poses a great challenge to the magnet design. The key issue to meet all the required specifications is a firm steel frame. In combination with the large diameters of the split coils this results in the big overall size of the magnet.

The magnet is mounted inside a ^{4}He bath cryostat which is shielded by a liquid nitrogen (LN_2) reservoir against thermal radiation. In order to prevent an excessive heat load through the large openings two double-walled shutters are employed, to be operated by vertical linear feedthroughs. The two walls of each shutter are thermally decoupled, with the outer one anchored to LN_2, the inner one to the He bath, by means of copper braids. This shutter system, in conjunction with the efficient cooling of the microscope itself as discussed below results in a base temperature of the microscope of 4.7 K. The magnet can only be energized when totally covered by liquid helium, thus the active volume of the He reservoir above the magnet plays a key role in terms of hold time. With an active volume of 80 l of liquid helium a hold time of 36 hours is achieved. The cryostat remains at base temperature for another 20 hours. However, during that time the magnet cannot be operated.

To obtain proper UHV conditions the magnet is designed to safely endure bakeout at 90° C. During bakeout we heat the surrounding chamber and the nitrogen reservoir up to 130° C for 60 hours. Due to its large thermal mass the magnet's temperature follows slowly with a delay of about 24 hours. As a concequence, the temperature

of the magnet never exceeds 75° C. The magnet temperature is measured by two temperature sensors close to the central bore and one on top of the magnet. The microscope's temperature is measured by a CERNOX [25] temperature sensor mounted to the sample receptacle as shown in Fig. 3.81. The signal of either of these sensors can be fed into a control unit that supplies a flow of cold nitrogen gas across the magnet if the temperature is about to surpass a critical value due to some unforeseen event. Thus, a safe bakeout operation is guaranteed. After bakeout and with the cryostat cooled down, a base pressure below 1×10^{-10} mbar is achieved.

To avoid vibrations due to boiling nitrogen the LN_2 reservoir is pumped to below 5 mbar. As a consequence the nitrogen undergoes a transition to its solid phase. We use a rotary vane pump with a nominal pumping speed of 65 m^3/h which is necessary to cope with the very high initial gas load. The pump is located in an adjacent room which is acoustically isolated from the STM laboratory. Once the gas flow through the pumping line is sufficiently low we observe no acoustic coupling of the cryostat system to the pump. Besides the significant reduction of vibrations a positive side effect is the reduced temperature of the solid nitrogen compared to the liquid phase. The temperature drops from 77 K down to 63 K which is of considerable advantage in terms of helium boil-off.

Due to the large area of the cold surfaces exposed to UHV the cryostat itself acts as a very efficient cryo-pump. While this is very advantageous in terms of improving the vacuum, it can be quite problematic during warm-up. In this situation, without any precautions, a pressure rise to the 10^{-3} mbar range may be observed which is mainly due to hydrogen desorbing from the cryo-surfaces. To avoid this extreme pressure rise an additional NEG pump, which is very efficient in pumping hydrogen, has been mounted to the chamber. As a result the described pressure rise is limited to the 10^{-8} mbar range.

STM design

Figure 3.81 shows a sketch of the STM which is operated in the center of the three axes magnet as illustrated in Fig. 3.80. While the overall design follows the general ideas described previously [1], we focus here on some significant modifications.

Instead of the ceramics MACOR, phosphorous bronze ($CuSn_8P$) was chosen for the microscope body. This material is easy to machine, it is UHV compatible and non-magnetic. The body is gold plated to reduce the emissivity of the surface. Compared to MACOR, the metallic body has a much higher thermal conductivity. Thus, after a sample exchange at low temperatures, the microscope reaches thermal equilibrium within a few minutes, while a typical waiting time with a MACOR body amounts to about 45 minutes. The microscope is rigidly mounted on top of an oxygen-free highly conductive (OFHC) copper column which rests on a flange of the same material. This allows to mount the microscope inside the magnet by inserting it from the bottom where the microscope's flange is firmly screwed to the LHe reservoir. All wirings necessary to operate the STM are also fed from the bottom side. The leads

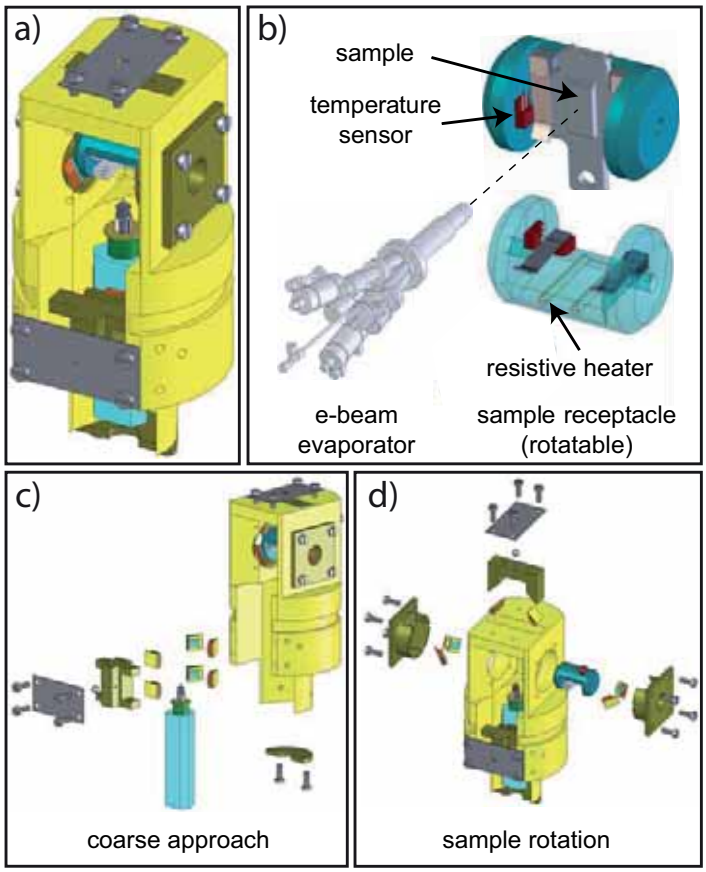

Figure 3.81: a) Microscope body with the tip approaching from the bottom. b) Adsorbate deposition inside the microscope using the sample rotation mechanism. c) Exploded drawing of the approach mechanism. d) Exploded drawing of the mechanism for sample rotation

are custom made twisted pairs of 0.1 mm stainless steel inside a braided shield, with Kapton insulation [26]. The overall diameter of these very rugged cables is 1 mm. We refrained from thermally anchoring the wires to the LN_2 reservoir. Instead, following Ref. [27], the wires couple thermally to the LHe bath. They run inside straight grooves in the copper column, firmly pressed by screwed-on plates, on a length of 130 mm. As a result, the temperature difference between the wire and the copper column is reduced to less than 1 mK at the wire ends close to the microscope. For comparison, a similar wire made of Cu, would require a length of 670 mm for the same result. The cold wire ends are fixed to a Teflon ring where plug and socket connections allow to proceed using copper wires to finally contact the microscope. In conjunction with the earlier mentioned double-walled radiation shields shutting the access openings to the microscope, the heat load on the microscope is effectively reduced. The equilibrium temperature as measured by a calibrated Cernox [25] sensor mounted directly to the sample receptacle is below 4.7 K. For the coarse approach a stepper motor based on the slip-stick principle is used, similar to the one described in Ref. [1], with six shear piezo stacks clamping a sapphire prism which carries the tube scanner with the tip as shown in Fig. 3.81. In contrast to the previously described microscope the sample surface is facing downward, the tip points upward. For the scanner a 1/4' EBL #4 piezo tube [28] with 0.02' wall thickness and an effective length of 19.5 mm is used. For a maximum applied voltage of $\pm$ 150 V the scan range amounts to 4.3 μm at room temperature and 2.5 μm at 4.7 K, respectively.

A key requirement for SP-STM experiments is a reliable tip exchange mechanism, allowing an *in situ* preparation of tips with magnetic sensitivity. The scanner houses a tip exchange mechanism as described in Ref. [1]. Taking this additional load into account, the lowest resonance frequency of the tube scanner has been calculated to 4.44 kHz following Ref. [29], well above typical cutoff frequencies occurring during scanning.

A special feature of the microscope is its rotatable sample stage made of sapphire (Fig. 3.81b)). Such a stage was already described in Ref. [1]. By virtue of this device the sample surface can be reoriented by 90° towards an evaporator which is mounted on the back side of the cryo-chamber. The radiation shield is equipped with a shutter which gives access to a bore in the magnet structure providing line-of-sight between the sample surface and the evaporator. With the shutter open, one can supply an atom beam directly onto the cold sample surface while the temperature does not rise above 10 K. On the cold surface, the impinging atoms have no mobility which is a prerequisite for the preparation of individual magnetic adatoms. To increase the versatility of the STM, a resistive heating was integrated into the sample stage (Fig. 3.81b). The key to do this was to drill two holes 1 mm in diameter through the sapphire stage right underneath the sample receptacle. A tungsten filament of 0.1 mm diameter and about 40 mm length, guided by appropriate alumina tubings, is fixed into the bores. A local temperature of 150 K is easily achieved, allowing to induce a controlled surface diffusion of the adsorbates if desired. Summarizing, together with the variable temperature

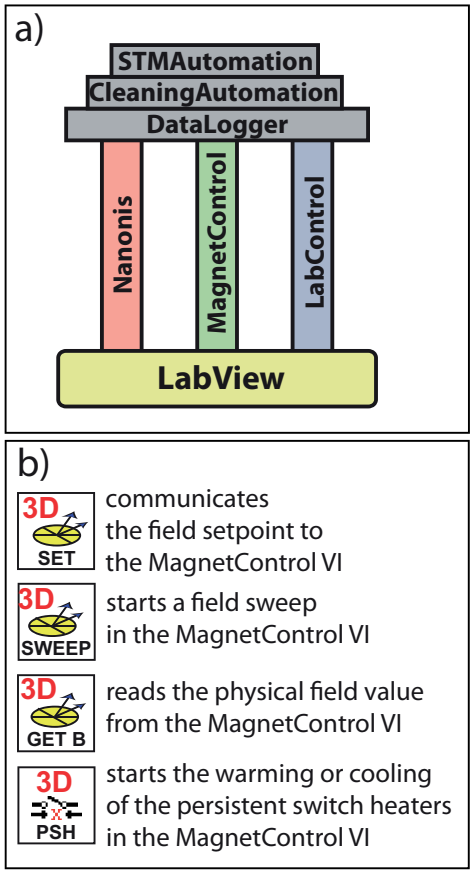

Figure 3.82: a) Schematics of the software concept. All applications are based on three pillars with LabView as the programming language. b) Overview of the subVIs contained in the programming interface of the Magnet Control VI. The programming interfaces for the other software modules follow the same concept.

equipment of the manipulator in the MBE chamber the temperature range available for sample preparation extends from about 1100 K down to 10 K.

Software control and automation

The low-temperature STM described above has been installed in a laboratory in the basement of the building. The refill of cryogenic liquids and the operation of the STM and magnet sytem is done from a second laboratory room one floor above. Therefore it is essential to have an appropriate software to remotely monitor and control the microscope, the three axes magnet, the cryostat and some important UHV-related devices. In addition, it is desirable to have an automation software to control routine processes such as substrate cleaning. To meet these requirements a monitoring and control software package has been developed which is based on three software components each realized as a LabView [30] virtual instrument (VI) as illustrated by the pillars in Fig. 3.82a):

- LabControl software for control and monitoring of the UHV system and the cryostat.
- MagnetControl software for control and monitoring of the three axes magnet.

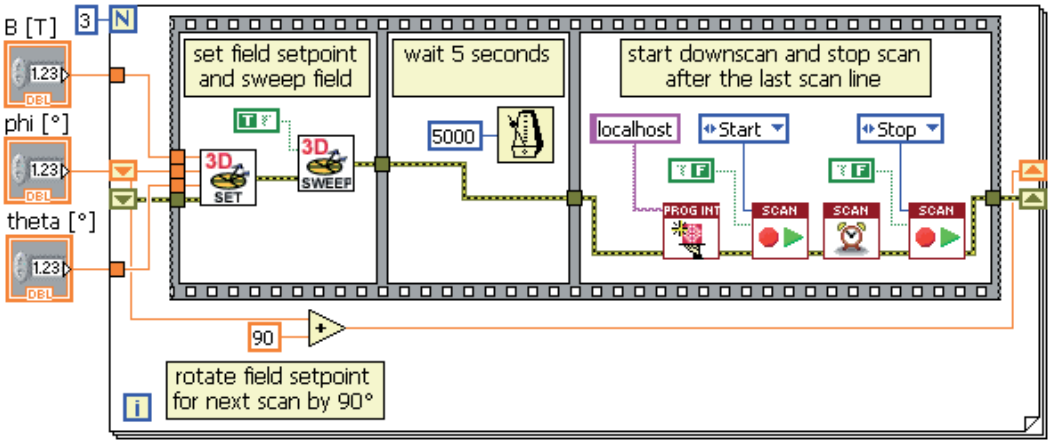

Figure 3.83: Block diagram of a LabView VI controlling an automated cycle of STM measurements. Four images are taken at four different orientations of the external magnetic field. Between two image scans the field is rotated in-plane by 90° using the programming interface of the magnet control VI.

- Nanonis data acquisition software for the control and monitoring of the STM [31].

Each software component provides a programming interface for the communication with other VIs. In that sense the home-built VIs are formally equivalent to the LabView based commercial Nanonis software. A programming interface consists of a set of subVIs as exemplified in Fig. 3.82b) for the case of the MagnetControl VI. They can be used in LabView block diagrams just as any other subVI. Every subVI in a programming interface establishes a well defined communication access to set, modify, or read a specific parameter or set of parameters in the respective VI.

Based on these subVIs, customized VIs for various purposes can be developed. Applications that have been accomplished already are shown in grey colors in Fig. 3.82a).

Software control and automation

Using the Nanonis programming interface one can easily customize STM measurement series and run them in a computer controlled way. In combination with the MagnetControl and LabControl software and their programming interfaces this offers numerous new options for measurements that would not be possible with standard software alone. As a first application our new software package is used as a tool to conduct automated field dependent STM measurement series. This is illustrated in the block diagram shown in Fig. 3.83. A sequence of four STM images is taken using the Nanonis programming interface. Prior to each individual scan the magnetic field is ramped to a new value, i.e. by performing an in-plane rotation of the field vector by 90°. This is accomplished by using the MagnetControl programming interface. After pausing 5 seconds scanning is started. This type of measurement is particularly interesting as it offers a tool to save all relevant parameters of the experiment, i.e.

magnetic field values, temperatures, etc. in a single file together with the image data.

Automated Substrate Cleaning To be able to operate the experimental setup at maximum efficiency it is valuable to run routine processes such as substrate cleaning at night or over the weekend. To increase efficiency we automized the substrate cleaning processes in the preparation chamber as a second application of the software package described above. The CleaningAutomation software is capable of ramping the power of the home-built e-beam heater power supply and thereby stabilizing the substrate temperature at elevated values as shown in Fig. 3.78. In addition, it contains a PID control loop which is used to stabilize the oxygen pressure in the preparation chamber at a desired value. This is achieved by applying an appropriate voltage to a piezo controlled leak valve [32] using the EVC 300 power supply of the Focus evaporators [20]. The software allows to define complete cycles of substrate cleaning, as described previously [19] and run them in an automated fashion. During these cleaning cycles the input data necessary for the pressure control as well as for the operation of TSP and ion getter pump is provided by the programming interface based communication with the LabControl software as described above.

Data Logging Due to the MagnetControl and LabControl software all important status parameters of the laboratory are available on the computer at any time. Thus, it was straightforward to implement the option to log the data continuously to a file. The log files acquired so far turned out to be very useful for the analysis of unexpected events and problems. By saving the log file directly to a network drive we are in the position to remotely check the status of our laboratory from any computer with web access. This is a very convenient feature in particular during system bakeout at night and over the weekend.

Demonstration of functionality

Atomic Resolution Figure 3.84 shows an STM image of an Fe monolayer on Ru(0001) with atomic resolution as it was recorded on the island marked by the green arrow in the inset. The measured lattice constant corresponds to the lattice constant of the underlying Ru(0001) surface confirming pseudomorphic growth in agreement with Ref. [33]. The inset shows an overview of the sample where the ruthenium substrate (Ru), Fe monolayer (ML) and Fe doublelayer regions (DL) can be identified. Image processing has beeen done using the WSxM software [34].

Tip magnetization direction control using the three axes magnet Figure 3.85 shows a series of SP-STM measurements recorded on 1.6 atomic layers of Fe on W(110) using an in-plane sensitive Fe coated W-tip. The results could be reproduced using a Gd coated W-tip (not shown). ML and DL regions can be identified (a). The doublelayer has an out-of-plane anisotropy whereas the magnetic easy axis in the ML

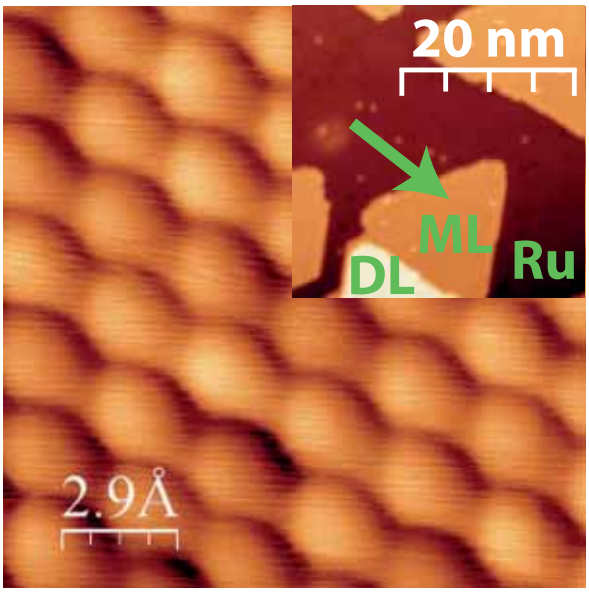

Figure 3.84: STM image of the Fe monolayer on Ru(0001) demonstrating the atomic resolution capability of the microscope. $U = 10\,\mathrm{mV}$, $I = 7\,\mathrm{nA}$. The inset shows an overview of the sample with ruthenium (Ru), Fe monolayer (ML), and Fe doublelayer (DL) areas. The atomically resolved image was taken on the monolayer area marked by the arrow.

is in-plane pointing along $[1\bar{1}0]$. [35] Thus, with an in-plane sensitive STM tip the domain walls (A) in the DL and the domains (B) in the ML can be imaged (a,b).

In zero field only the domain wall contrast in the DL is observed (a), indicating an in-plane magnetic sensitivity of the tip perpendicular to the easy axis of the ML. Upon applying the magnetic field along $[1\bar{1}0]$ the domain wall contrast in the DL disappears whereas the domain contrast in the ML becomes visible (b). This can be attributed to the alignement of the tip magnetization along the easy axis of the ML in the external field. In addition, the tip magnetization is slightly canted out-of-plane resulting in a weak domain contrast in the DL. Upon field reversal the domain contrast in the ML is inverted since the tip magnetization remains aligned parallel to the field (d). In zero field the tip magnetization switches back to its initial easy axis (c) resulting in the same spin contrast as observed before applying the field (a).

Summary

The design of a new low-temperature spin-polarized STM operated in the center of a superconducting three axes magnet was described. It was shown that this setup permits for the first time to control the direction of the tip magnetization in all three spatial directions. The capability of the microscope to achieve atomic resolution on a hexagonal close packed metal surface was demonstrated. Finally, the facilities for substrate cleaning and the MBE growth of magnetic nanostructures were described. The focus was put on the versatility of the growth conditions and the automation of substrate cleaning and measurement processes.

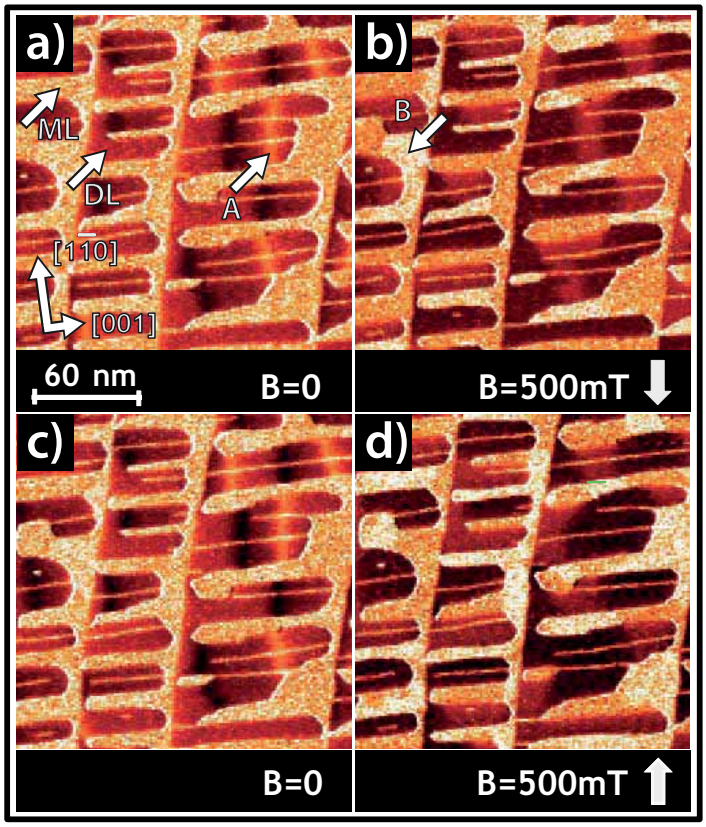

Figure 3.85: Spin-polarized dI/dU maps of 1.6 atomic layers of Fe on W(110) using an in-plane sensitive Fe coated W-tip. Monolayer and doublelayer regions can be identified (a). In zero field the domain walls (A) in the Fe doublelayer can be identified. Upon applying an external field along [1$\bar{1}$0] the domain wall contrast in the doublelayer disappears. Instead the domains (B) in the monolayer with the easy magnetic axis along [1$\bar{1}$0] become visible due to the rotation of the tip magnetization in the external field (c). The contrast of this pattern is inverted upon reversal of the tip magnetization in the external magnetic field (d). In zero field the tip magnetization switches back to its initial easy axis (c). Tunnel parameters: $U = 550\,\mathrm{mV}$, $I = 500\,\mathrm{pA}$.

References

[1] O. Pietzsch, A. Kubetzka, D. Haude, M. Bode, and R. Wiesendanger, Rev. Sci. Instrum. **80**, 023708 (2009).

[2] M. Liebmann, A. Schwarz, S. M. Langkat, and R. Wiesendanger, Rev. Sci. Instrum. **73**, 3508 (2002).

[3] J. Wiebe, A. Wachowiak, F. Meier, D. Haude, T. Foster, M. Morgenstern, and R. Wiesendanger, Rev. Sci. Instrum. **75**, 4871 (2004).

[4] Ch. Wittneven, R. Dombrowski, S. H. Pan, and R. Wiesendanger, Rev. Sci. Instr. **68**, 3806 (1997).

[5] S. Meckler, M. Gyamfi, O. Pietzsch, and R. Wiesendanger, Rev. Sci. Instrum. **80**, 023708 (2009).

[6] R. Wiesendanger, H.-J. Güntherodt, G. Güntherodt, R. J. Gambino, and R. Ruf, Phys. Rev. Lett. **65**, 247 (1990).

[7] R. Wiesendanger, I. V. Shvets, D. Bürgler, G. Tarrach, H.-J. Güntherodt, J. M. D. Coey, S. Gräser, Science **255**, 583 (1992).

[8] S. F. Alvarado and P. Renaud, Phys. Rev. Lett. **68**, 1387 (1992).

[9] W. Wulfhekel and J. Kirschner, Appl. Phys. Lett. **75**, 1944 (1999).

[10] J. C. Slonczewski, Phys. Rev. B **39**, 6995 (1989).

[11] A. Kubetzka, O. Pietzsch, M. Bode, and R. Wiesendanger, Phys. Rev. B **67**, 020401(R) (2003).

[12] A. Kubetzka, M. Bode, O. Pietzsch, and R. Wiesendanger, Phys. Rev. Lett. **88**, 057201 (2002).

[13] O. Pietzsch, A. Kubetzka, M. Bode, and R. Wiesendanger, Phys. Rev. Lett. **92**, 057202 (2004).

[14] O. Pietzsch, A. Kubetzka, M. Bode, and R. Wiesendanger, Science **292**, 2053 (2001).

[15] F. Meier, L. Zhou, J. Wiebe, and R. Wiesendanger, Science **320**, 82 (2008).

[16] Y. Kondo, E. T. Foley, T. Amakusa, N. Shibata, S. Chiba, M. Iwatsuki, and H. Tokumoto, Rev. Sci. Instrum. **72**, 2977 (2001).

[17] T. Mashoff, M. Pratzer, and M. Morgenstern, Rev. Sci. Instrum. **80**, 053702 (2009).

[18] Omicron Nanotechnology GmbH, Taunusstein, Germany.

[19] M. Bode, S. Krause, L. Berbil-Bautista, S. Heinze, and R. Wiesendanger, Surf. Sci. **601**, 3308 (2007).

[20] Distributed by Omicron Nanotechnology GmbH, Taunusstein, Germany.

[21] J. Kirschner, H. Engelhard, and D. Hartung, Rev. Sci. Instrum. **73**, 3853 (2002).

[22] M. Volmer and A. Weber, Z. Phys. Chem. **119**, 277 (1926).

[23] Cryovac GmbH, Troisdorf, Germany.

[24] Scientific Magnetics, Abingdon, UK.

[25] Lake Shore Cryotronics Inc., Westerville, OH, USA.

[26] Isotec Kabel GmbH, Norderstedt, Germany.

[27] J. G. Hust, Rev. Sci. Instrum. **41**, 622 (1970).

[28] EBL Products Inc., East Hartford, CT, USA.

[29] M. E. Taylor, Rev. Sci. Instrum. **64**, 154 (1993).

[30] National Instruments, Austin, TX, USA.

[31] Specs Zurich GmbH, Zurich, Switzerland.

[32] Specs GmbH, Berlin, Germany.

[33] C. Liu and S. D. Bader, Phys. Rev. B **41**, 553 (1990).

[34] I. Horcas, R. Fernández, J. M. Gómez-Rodríguez, and J. Colchero, Rev. Sci. Instrum. **78**, 013705 (2007).

[35] H. J. Elmers, J. Hauschild, H. Höche, U. Gradman, H. Bethge, D. Heuer, and U. Köhler, Phys. Rev. Lett. **73**, 898 (1994).

3.9.2 Magnetic exchange force microscopy (MExFM)

U. Kaiser, U. H. Pi, R. Schmidt, A. Schwarz, and R. Wiesendanger

It is the magnetic exchange interaction between magnetic moments of atoms that is central to our understanding of magnetic phenomena in nanostructures formed by individual atoms. Magnetic exchange interactions between atomic magnetic moments are mediated by the electron spin and can be described in the Heisenberg model with the Hamiltonian $H = -\sum J_{ij}(\vec{S}_i \cdot \vec{S}_j)$. In this relation, $\vec{S}_i$ and $\vec{S}_j$ are the interacting spins and J_{ij} is the exchange coupling between them. A novel experimental approach to directly probe this interaction is magnetic exchange force microscopy (MExFM). Unlike magnetic force microscopy it does not detect long-range dipolar magnetostatic forces, but short-range electron mediated magnetic exchange forces [1]. This method, which requires an atomically sharp force microscopy tip and subnanometer tip-sample distances, has been proposed by Wiesendanger *et al.* [2] in 1991. However, the feasibility of this approach has been only demonstrated by us in 2007 [3]. Now it is crucial to understand the contrast formation and particularly the influence of the tip state.

To understand the role of the tip we evaluated several data sets recorded with different tips [4] and tip materials [5] on the same surface, i.e., NiO(001), with a well known row-wise antiferromagnetic magnetic structure of the Ni sublattice with canted spins. We find sudden contrast reversals, which indicate that the magnetic exchange interaction can be strong enough to alter the magnetic configuration at the tip apex. Furthermore, we also find magnetic double tips - the magnetic equivalent of frequently observed structural double tips. In addition, we studied a well known itinerant metallic system, i.e., Fe pseudomorphically grown on W(001) [7]. On this surface a checkerboard antiferromagnetic structure with out-of-plane anisotropy evolves in the Fe monolayer due to strong spin-orbit coupling with the substrate. Our experimental results are compared with theoretical calculations using realistic tips from the group of S. Heinze [8]. They show a peculiar interplay between chemical and magnetic exchange interactions that finally determines the observed contrast pattern.

Both sample systems have been studied using a homebuilt low temperature force microscope (base temperature 8.1 K) operated in an ultrahigh vacuum compatible cryostat equipped with a 5 T superconducting magnet [6]. Tip and sample preparations were performed *in-situ*. For imaging, the frequency modulation (FM-AFM) technique in the non-contact (NC-AFM) regime was employed. In this mode of operation the frequency shift Δf of the cantilever's resonance frequency f_0 is kept constant to record the surface topography, while a second feedback loop keeps the oscillation amplitude A constant. Height variations in constant Δf images on the atomic scale correspond to local variations of the short-ranged chemical and magnetic exchange forces.

Evaluating Magnetic Tip States on NiO(001) with MExFM

To elucidate the influence of the tip on the imaging process in MExFM we compare experimental results taken with different tips on NiO(001). The surface is prepared by *in-situ* cleavage and subsequent heating. Chemical, structural and magnetic properties of this surface are well known: Nickel oxide is an antiferromagnetic insulator with the crystal structure of rock salt. The surface is nearly bulk-terminated (except a tiny rumpling [9]) and exhibits a (1×1) chemical surface unit cell. The magnetic moments of the nickel atoms show a ferromagnetic ordering within (111) planes and an antiferromagnetic one between neighboring (111) planes. Therefore, a row-wise arrangement of the magnetic moments is found at the (001) surface resulting in a (2×1) magnetic surface unit cell. Magnetic ordering is due to superexchange between the nickel atoms, mediated by the 2*p*-electrons of the bridging oxygen atoms. The magnetic moments of the nickel atoms in the bulk as well as at the (001) surface are canted and point in one of twelve possible ⟨211⟩ directions [10]. For eight of these configurations the polar angle on the (001) surface is about 29.2°, while it is about 60.8° for the other four directions.

From a practical point of view NiO(001) is well suited to evaluate properties of magnetic tips, because this system was previously investigated with MExFM [3], and density functional calculations exist for this distinct surface [11]. The tips analyzed in the following were made from silicon and coated *in-situ* with Fe, Ni, or Gd. A magnetic flux density B of 5 T, which is larger than the bulk saturation magnetic polarization of these materials, was applied perpendicular to the sample surface to achieve out-of-plane sensitivity.

First, the contrast, which corresponds to the genuine configuration of the sample, i.e., NiO(001), has to be identified. Atomic resolution on NiO(001), typically obtained by AFM using a tip without magnetic sensitivity, reveals the (1×1) chemical surface unit cell as shown in Fig. 3.86(a). The image contrast agrees well with previously published data [12–14]. In such experiments, an atomically sharp tip is approached to distances of only a few hundred picometers above the surface while the oscillating cantilever is at its lower turnaround point. At these distances the electronic states of the foremost tip atom and the underlying surface atom begin to overlap resulting in a strong electron mediated chemical interaction. If a metallic tip is used, the interaction between tip and sample is expected to be strongest above the oxygen sites, because the valence charge density is largest at these positions. Therefore, maxima in constant Δf images of NiO(001) represent oxygen atoms, as indicated by spheres in Fig. 3.86. In (b) a magnetically sensitive tip is used resulting in an additional row-wise atomic scale contrast on the minima, i.e., the nickel atoms. This additional modulation on structurally and chemically identical rows of nickel atoms in MExFM images reflects the genuine antiferromagnetic structure of NiO(001). Since this contrast agrees well with theoretical calculations presented in Ref. [11], where the tip was modeled by a single iron atom, we can infer that Fig. 3.86(b) represents the contrast expected on NiO(001), if imaged with an iron tip apex, for which the foremost tip atom dominates

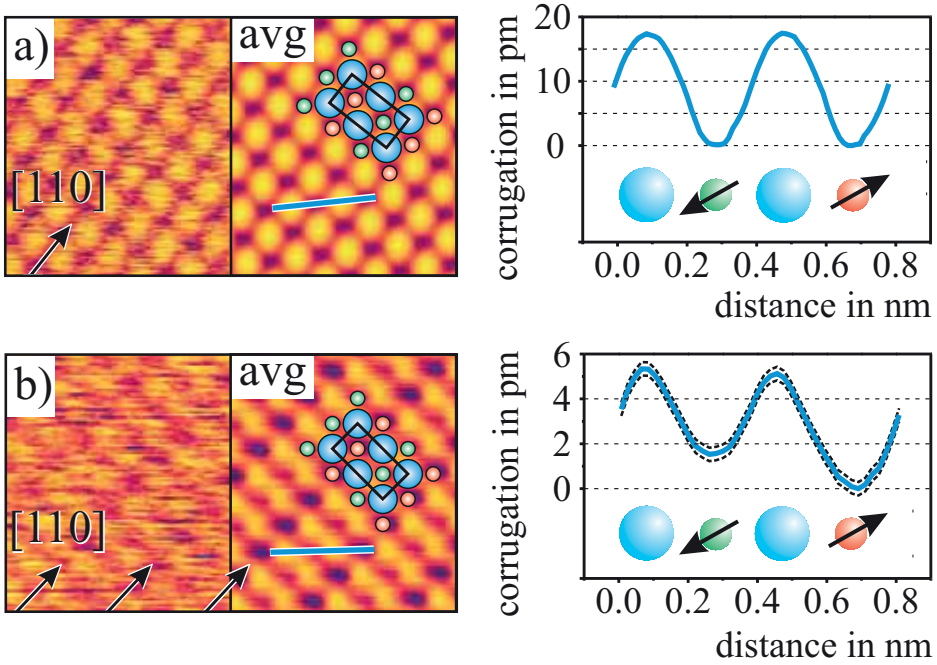

Figure 3.86: (a) AFM and (b) MExFM image of NiO(001), respectively. Maxima and minima represent oxygen (blue shaded spheres) and nickel (red and green shaded spheres) atoms, respectively. The MExFM image reveals the row-wise antiferromagnetic arrangement of the nickel atoms and the (2×1) magnetic surface unit cell. In the right part of the images averaged representations of the raw data are shown and line sections thereof. Only in the MExFM data a clear difference between chemically and structurally equivalent rows of nickel atoms is visible, which represents the genuine antiferromagnetic structure of NiO(001).

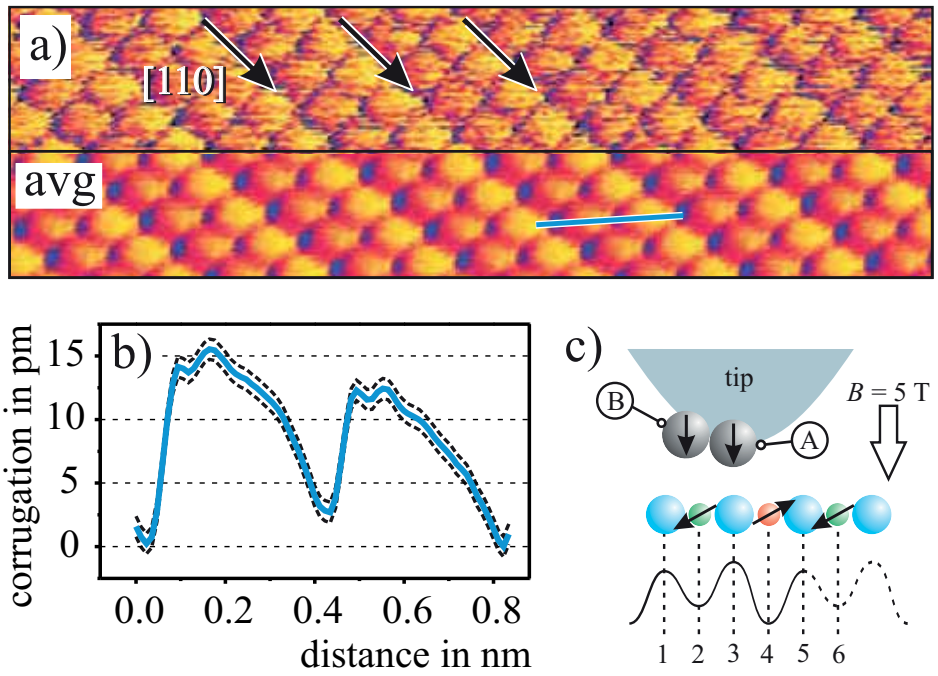

Figure 3.87: (a) MExFM image of NiO(001) recorded with an iron coated tip showing a magnetic exchange contrast on neighboring rows of nickel atoms and neighboring rows of oxygen atoms (top: raw data, bottom: averaged data. (b) Line section obtained from the averaged data. Maxima appear wider than minima and the slopes are asymmetric. (c) Sketch of a magnetic double tip, which can explain the experimentally observed contrast qualitatively.

the tip-sample interaction.

Using Fig. 3.86(b) as starting point, we can now analyze qualitatively different image contrasts obtained with other tips. For example, in Fig. 3.87(a) we find a modulation between neighboring rows of nickel atoms and between neighboring rows of oxygen atoms, as clearly visible in the line section (b). The modulation on neighboring rows of oxygen atoms has to be of magnetic origin as well, because they are structurally and chemically equivalent. However, such a modulation does not reflect the genuine antiferromagnetic structure of NiO(001), which is related to the nickel atoms, cf., Fig. 3.86(b). Hence, the contrast seen in Fig. 3.87(a) has to be related to the magnetic configuration at the tip apex. It should be mentioned that in Ref. [11] a magnetic moment of 0.07 μ_B was determined for surface oxygen atoms. Thus, a small magnetic exchange interaction would also be expected on oxygen atoms. However, the moment for nickel atoms is on the order of 1.16 μ_B. As visible in the line section Fig. 3.87(b), the contrast between oxygen atoms is on the same order of magnitude like on nickel atoms, while the predicted magnetic moments differ by a factor of about 16. Another mechanism to explain the height modulation on the neighboring rows of oxygen atoms would be a superexchange interaction between the foremost tip atom and the second

layer nickel atoms, which are located below surface oxygen rows. If such a mechanism would also be relevant, we would expect to always see a modulation on neighboring rows of oxygen atoms, which is not the case, e.g., not in 3.86(b).

The most likely cause, which explains all features observed in Fig. 3.87(a) and (b) qualitatively, is a *magnetic* double tip as sketched in (c). Here, two magnetic atoms (A and B) at the tip apex contribute to the magnetic signal. If the foremost tip atom A is for example above the oxygen atom at position 3, the magnetic moment of tip atom B interacts with the magnetic moment at the neighboring nickel site (position 2). As a result, the magnetic signal above the oxygen atom stems from atom B at the tip apex, which is actually located above the nickel atom as indicated in the line section. This effect is analogous to a *structural* double tip. However, it should be emphasized that a pure structural double tip could not result in the observed contrast. The described wedge-like two atom tip apex model is also strongly supported by the shape of the line section in Fig. 3.87(b), which reveals maxima that are wider than the minima and have asymmetric slopes. In contrast, a single atom tip apex exhibits symmetric slopes, cf., line section in Fig. 3.86(b). Note that an iron double tip still allows atomic resolution on NiO(001), because two maxima at this surface (the oxygen atoms) are 417 pm apart, while the iron-iron distance is only about 286 pm (value for bulk α-Fe).

Surprisingly, the magnetic contrast on neighboring rows of oxygen atoms (3.1±0.9 pm) is on the same order of magnitude like on neighboring rows of nickel atoms (2.6±0.9 pm). Intuitively, one would expect that the magnetic contrast on nickel atoms is larger than on oxygen atoms, since the mean tip-sample distance above the nickel atoms in this constant Δf image is approximately 12.5±0.9 pm smaller than above the oxygen atoms, cf., Fig. 3.87(b). However, this is possible if the magnetic moment of atom B is farther away but better aligned relative to the canted magnetic moments of the nickel surface atoms than that of atom A. This would indicate that 5 T are not sufficient to fully align the magnetic moments at the tip apex along the direction of B. Note that the Zeeman energy per atom related to 5 T is on the order of 1 meV, whereas the magnetic exchange energy between closely spaced iron atoms is one order of magnitude larger.

To achieve a large magnetic signal, the relative orientation between the magnetic moments of the foremost tip atom and the surface atoms is crucial. If antiferromagnetic samples are investigated, an obvious way to control the direction of the magnetic moments of the tip is to apply a sufficiently large external magnetic field that does not alter the sample. However, we found a direct proof that even for $B > J_{\mathrm{sat}}$ the magnetic moment at the foremost tip apex atom is not necessarily collinear to B. Fig. 3.88(a) and (b) show the same location of the sample imaged by MExFM in 5 T with atomic scale magnetic resolution. The structural defect in the lower left corners, marked by dashed circles, acts as a marker to check the registry of the atomic positions. Between recording images (a) and (b) the tip apex changed its configuration spontaneously. Close inspection reveals a reversal of the magnetic contrast, i.e., rows of nickel atoms with deeper minima in (a) appear as rows of nickel atoms with shallower minima in

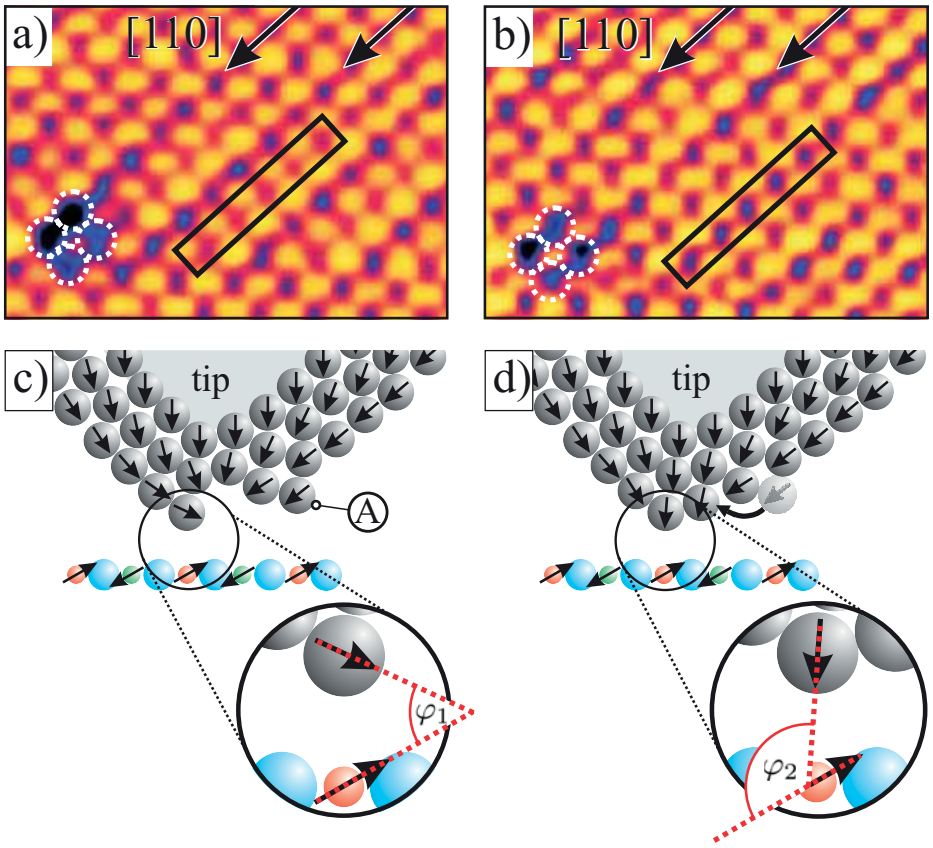

Figure 3.88: MExFM images (low pass filtered) of the same location in NiO(001) recorded before (a) and after (b) a spontaneous tip change, which resulted in a contrast reversal (see contrast within the rectangles relative to the marker defect). In (c) and (d) a simplified tip model is shown that can explain the contrast reversal. Here, the angle between the magnetic moments of tip and sample atom changes from $\varphi_1 \approx 55°$ to $\varphi_1 \approx 125°$.

(b) and vice versa.

How a spontaneous tip change can alter the direction of the magnetic moment at the foremost tip atom is explained by employing a simplified two-dimensional tip model sketched in Fig. 3.88(c) and (d). Due to local magnetocrystalline anisotropies, which are related via spin-orbit coupling to the structural configuration of the atoms at the tip end, the magnetic moment at the tip apex atom can point in any direction. Note that this anisotropy energy can easily exceed the Zeeman energy of 5 T. Let us assume that the initial angle φ_1 between the magnetic moments of the foremost tip atom and the canted magnetic moment of the nickel atom is about 55° as sketched in Fig. 3.88(c). Spontaneous jumps of an atom near the tip apex, like it was described for a non-magnetic system in Ref. [15], can now change the local magnetic coupling of the foremost tip apex atom to its environment and hence its relative angle to the fixed surface magnetic moments. Figure 3.88(d) shows a possible result of such a tip change with $\varphi_1 \approx 125°$, which would then lead to an inverted magnetic contrast.

Finally, it is worth to mention that we tried Ni and Gd coated tips as well. In both cases atomic resolution was routinely obtained, but without magnetic contrast on NiO(001) [5]. Ni has a smaller magnetic moment than Fe. In this case the magnetic exchange interaction might be so weak that the magnetic signal is below the detection limit of our instrument. For the rare earth element Gd the magnetic moment is larger than for Fe. However, the spin is carried by f-orbitals, which are strongly localized (within Gd the magnetic exchange is mediated via polarization of the conduction band electrons). Therefore, a detectable direct magnetic exchange interaction might only occur at such small distances, where tip-sample instabilities are inevitable and stable imaging becomes impossible.

Investigating Fe on W(001) with MExFM

Although structure and magnetism of nickel oxide is well known, it is a quite complex system. Firstly, it contains two elements and using Fe coated tips introduces a third element. Secondly, the observed magnetic contrast is quite small (only about 1.5 pm in constant Δf images), because the spin carrying d-electrons are localized. Therefore, at tip-sample distances, where tip-sample instabilities are absent, the magnetic signal is small. Thirdly, it is a strongly correlated system, which is difficult to treat using density functional theory (DFT). As a consequence, calculations performed by Momida and Oguchi [11] were done with single Fe atoms as tips. Such tips are unrealistic and it is impossible to include relaxation effects.

Having these issues in mind, we performed MExFM experiments and first-principles calculations based on density functional theory (DFT) of the antiferromagnetic Fe monolayer (ML) on the W(001) surface using an Fe tip. This system is not as complex as the strongly correlated NiO(001) and hence better suited for DFT. Moreover, only one species, i.e., chemically and structurally equivalent Fe atoms, is present in the surface layer and the same element is used as tip material as well. Since the Fe ML, as an itinerant two-dimensional antiferromagnetic metal with delocalized d-electrons, is

magnetically quite different from the insulating NiO, where the *d*-electron are strongly localized at the Ni atoms and coupled via superexchange, our investigation will also help to clarify the issue of the general applicability of MExFM.

The MExFM experiment clearly shows the antiferromagnetic structure of the Fe ML with atomic resolution. Compared to NiO(001), the magnetic signal is much larger and also qualitatively different. DFT calculations of site dependent force-distance curves using a Fe nanocluster as tip reveals that the magnetic exchange force changes qualitatively and quantitatively, if relaxation effects are accounted for and that the relaxation depends on the relative orientation between magnetic moments in tip and sample. They also disclose an interesting interplay between the short-ranged magnetic and chemical forces, which is responsible for the experimentally observed peculiar contrast pattern. Compared to previous calculations performed on NiO(001) [11] our results demonstrate that an accurate treatment requires a more realistic multi-atom tip and the implementation of relaxation effects. Finally, simulations using the *ab initio* data plus additional long-range van der Waals forces between tip and sample as input, reproduced very well the experimentally obtained image contrast.

As force sensors Si cantilevers were coated with Fe (typically about 15 nm) to obtain a magnetically sensitive tip. The W(001) substrate (lattice constant $a = 3.165$ Å) was coated with about 1.3 atomic layers Fe deposited on it at about 570 K. The resulting topography is displayed in Fig. 3.89(a). As visible in line section (b), the whole substrate is covered by an antiferromagnetic ML of Fe, which grows pseudomorphically and exhibits out-of-plane anisotropy [16]. Excess Fe forms ferromagnetic second layer islands and stripes along substrate steps with four-fold in-plane anisotropy [17].

Atomically resolved data on the Fe ML obtained with the same Fe coated cantilever using the same imaging parameters revealed two different contrast patterns, indicating the existence of two different tip configurations, cf. Fig. 3.89(c) and (d), respectively. In (c) protrusions are arranged in a p(1×1) array with respect to the W(001) substrate. Thus, every Fe atom is imaged as protrusion. On the other hand, protrusions in (d) are arranged in a c(2 × 2) array with respect to the W(001) substrate. For this tip state only every second Fe atom is imaged as protrusion. Since the contrast patterns in (c) and (d) reflect the symmetry of the chemical and antiferromagnetic surface unit cell, respectively, we can unambiguously infer that the tip state in (d) exhibits magnetic sensitivity, while the tip state in (c) does not. Hence, it is possible to unambiguously distinguish between magnetically insensitive and magnetically sensitive tip configurations.

As visible in the line section of Fig. 3.89(d), the magnetic corrugation amplitude is about 10 pm. Compared to results on the previously studied NiO(001) [3] the magnetic signal is seven times larger. From a practical point of view the much better signal-to-noise ratio is very promising regarding the general applicability of MExFM to other systems. There is also a very puzzling qualitative difference with respect to the MExFM data on NiO(001). There, the magnetic contrast was visible as modulation on top of the chemical contrast; cf. Fig. 3.86(b) [3]. Accordingly, one would

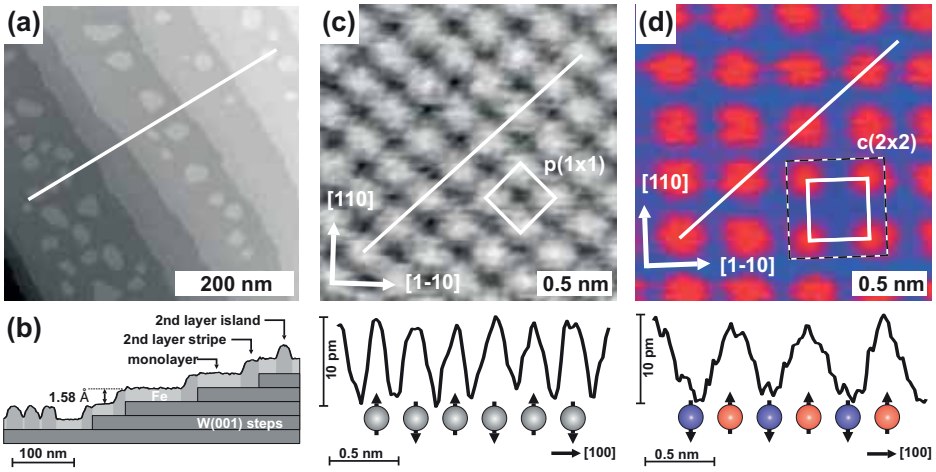

Figure 3.89: (a) Atomic force microscopy topography image of about 1.3 atomic layers of Fe deposited on W(001). (b) Line section showing substrate steps and areas covered by one and two atomic layers of Fe. (c) Atomic resolution on the Fe monolayer displaying the p(1 × 1) structural and chemical surface unit cell. Protrusions represent the positions of Fe atoms; cf. line section. (d) Magnetic exchange force microscopy image of the c(2 × 2) antiferromagnetic surface unit cell on the Fe ML. Only every second Fe atom appears as protrusion; cf. line section.

expect protrusions at the position of every Fe atom due to the chemical interaction, cf. Fig. 3.89(c), and a modulation of the magnitude on every second protrusion reflecting the c(2 × 2) magnetic unit cell. However, the line section along the [100]-direction in Fig. 3.89(d) exhibit minima at the position of Fe atoms instead of local maxima with reduced amplitude. This contrast is very surprising, because the magnetic exchange as well as the chemical interaction is electron mediated and thus both should be present simultaneously at small tip-sample separations.

In order to gain insight into the magnetic interactions and to interpret the image contrast in Fig. 3.89(d), particularly regarding the apparent absence of the chemical interaction, we have performed DFT based first-principles calculations within the generalized gradient approximation (GGA) [18] to the exchange-correlation potential. We apply the full-potential linearized augmented plane wave method as implemented in the WIEN2K [19] code.

The geometry of the coupled system of tip and sample is sketched in Fig. 3.90(a) and (b). The tip was modeled by a square-based pyramid of 5 ferromagnetically coupled Fe atoms. Tip and surface were initially relaxed independently before considering the coupled system. The separation z in the coupled system is defined as the distance between the tip apex atom and the Fe surface atom underneath before considering relaxations.

Upon approaching the tip to the surface along the z-direction indicated by a dotted line in Fig. 3.90(b), we allow all Fe atoms of the ML, the first layer of W atoms, and the Fe apex atom to relax at every tip-sample distance z. The remaining z-components of

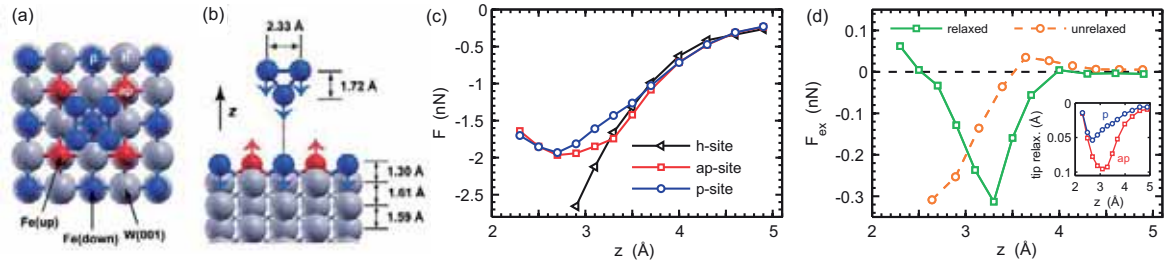

Figure 3.90: Top (a) and side (b) view of the tip and Fe/W(001) model used to calculate forces. High symmetry sites, i.e., h-, p- and ap-sites, are marked. Arrows indicate tip and surface Fe magnetic moments. z is defined as tip-sample distance along the approach trajectory (dotted line) before considering relaxations effects.(c) Calculated force curves $F_{\mathrm{ap}}(z)$, $F_{\mathrm{p}}(z)$ and $F_{\mathrm{h}}(z)$ including relaxations. (d) Distance dependence of the magnetic exchange force $F_{\mathrm{ex}}(z) = F_{\mathrm{ap}}(z) - F_{\mathrm{p}}(z)$ for the unrelaxed and the relaxed system. The inset shows the distance dependence of the tip apex atom relaxation towards the surface on the p- and ap-site, respectively.

the forces acting on the base atoms constitute the total force on the tip. Force curves are calculated on the three high symmetry points of the surface, which are magnetically different with respect to the magnetization direction of the Fe tip pyramid: on-top of an Fe atom with parallel magnetic moment, $F_{\mathrm{p}}(z)$ (p-site), on top of an Fe atom with antiparallel magnetic moment, $F_{\mathrm{ap}}(z)$ (ap-site), and on a hollow site between Fe atoms, $F_{\mathrm{h}}(z)$ (h-site).

The calculated forces acting on the tip, Fig. 3.90(c), display an attractive interaction for the ap- and p-site up to a maximum force of -2 nN at about 2.7 Å. On the h-site, the tip can approach the surface much closer before the repulsive regime is reached and the forces become much larger. The splitting of the force curves on the p- and ap-site, clearly visible in Fig. 3.90(c), is the magnetic exchange force, i.e., $F_{\mathrm{ex}}(z) = F_{\mathrm{ap}}(z) - F_{\mathrm{p}}(z)$, which is plotted in Fig. 3.90(d). Note that due to symmetry exchange forces cancel on the h-site. To emphasize the importance of relaxation effects, $F_{\mathrm{ex}}(z)$ is displayed in the same graph for the unrelaxed system. Both curves exhibit a significantly different distance dependence. Upon including relaxations, the onset of large magnetic exchange forces shifts towards larger tip-sample distances, which facilitates their experimental detection. In addition, $F_{\mathrm{ex}}(z)$ for the relaxed case does not display a change of sign at large tip-sample distances. These differences are caused by the relaxation of the tip apex atom which depends on its local magnetic configuration with respect to the approached surface atom, c.f. inset of Fig. 3.90(d). On the ap-site, the tip apex atom relaxes about 0.05 Å closer towards the surface atom than on the p-site which enhances the exchange interaction.

Since it is not possible to deduce tip-sample forces from experimental images, a comparison with theoretical calculations is required. For this procedure it is essential to consider the long-range tip-sample interaction caused by the van der Waals forces acting between the macroscopic tip and the sample. As in other studies [20–22] we

model the macroscopic part of the tip by a sphere with radius R. The corresponding long-range force is given by $F_{\mathrm{vdW}}(z) = -(A_{\mathrm{H}}R)/(6z^2)$ where A_H is the Hamaker constant [20]. We obtain the total tip-sample force $F_{\mathrm{ts}} = F_{\mathrm{sr}} + F_{\mathrm{vdW}}$, with $F_{\mathrm{sr}} = F_{\mathrm{p}}, F_{\mathrm{ap}}$, or F_{h} at the three distinct lattice sites. Δf can be calculated from the numerical solution of the integral [23]

$$\Delta f(D) = \frac{1}{\sqrt{2}\pi} \frac{f_0}{c_z A^{3/2}} \int_D^\infty \frac{F_{\mathrm{ts}}(z)}{\sqrt{z-D}} dz. \tag{3.32}$$

For simplicity we use reduced units, i.e., the normalized frequency shift $\gamma = c_z A^{3/2} \Delta f / f_0$. This quantity is independent of the actual experimental parameters A, c_z and f_0 [20, 21]. In order to simulate constant γ images we choose a suitable value γ_{c} and determine the corresponding nearest tip-sample distance at the lower turnaround point of the cantilever oscillation, D, numerically by solving $\gamma(D) = \gamma_{\mathrm{c}}$. As a result we obtain the corrugation amplitudes at the three distinctive lattice sites as a function of γ and hence D. In Fig. 3.91(a) the heights at the ap- and h-site are plotted with respect to the p-site. Based on these curves we have simulated complete MExFM images, Figs. 3.91(b-d), using the first two non-constant terms of a two-dimensional Fourier expansion [24].

The magnetic contrast depends sensitively on the actual normalized frequency shift, i.e. the nearest tip-sample distance D. At large D, Fig. 3.91(d), the chemical contrast dominates and the ap- and p-site appear as local maxima of only slightly different height due to a small exchange force of about 0.06 nN, c.f. Fig. 3.90(d). At very small D, Fig. 3.91(b), the magnetic forces dominate and Fe atoms with opposite magnetic moments appear as minima and maxima. At intermediate D, p- and h-site exhibit nearly the same height level and become indistinguishable. At the crossing point in Fig. 3.91(a) they are exactly equal and only the ap-sites appear as maxima, c.f. Fig. 3.91(c). Note that chemical and magnetic forces are both present and of considerable magnitude, but the total forces at p- and h-site are equal. The contrast in Fig. 3.91(c) fits best to the experimental image in Fig. 3.89(d) (see the zoom from Fig. 3.89(d) below the simulated image) indicating that we typically image in the intermediate distance regime. The calculated corrugation amplitude of about 4 pm is in reasonable agreement with the experimental value of 10 pm. It is significantly larger than the 1.5 pm observed on NiO(001) [3], because the spin-carrying d-electrons in NiO are very localized, while they extent much farther into the vacuum for the Fe ML. In a different experiment we also observed a contrast pattern similar to Fig. 3.91(d), which is expected to appear at relatively large separations. Since the corrugation amplitudes are much smaller at larger separations ($\approx$ 3 pm between large maxima and hollow sites and $\approx$ 1 pm between small maxima and hollow sites), an unit cell averaged representation of the experimental data is displayed Fig. 3.91(f). Up to now experimental data never exhibited a contrast pattern as shown in the simulated image Fig. 3.91(b), probably because stable imaging is difficult at such close distances.

Surprisingly, we find from our calculations that the ap-site of the Fe ML is energetically favorable for distances around 3 Å, e.g., by about 10 to 62 meV for distances

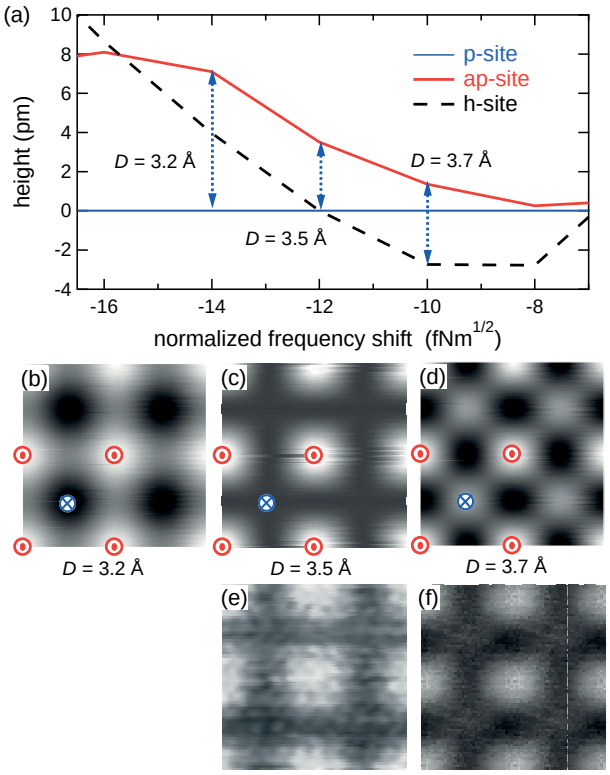

Figure 3.91: (a) Calculated height difference between p-, ap- and h-site, respectively, depending on γ_c and hence D. Long-range van der Waals forces were added assuming $R = 8\,\mathrm{nm}$ and $A_H = 0.1\,\mathrm{aJ}$ [25]. The p-site defines the zero line. (b-d) Simulated MExFM images at γ_c of $-14, -12$, and $-10\,\mathrm{fNm}^{1/2}$ corresponding to $D = 3.2, 3.5$, and $3.7\,\mathrm{Å}$, respectively. (e) Zoom taken from Fig. 3.89(d). The contrast agrees well with (c). (f) A different MExFM experiment, where a contrast pattern as in (d) was found. Note that up to now we never observed the contrast pattern displayed in (b).

between 3.3 and 2.9 Å. This antiferromagnetic coupling is due to the interaction of the foremost tip atom not only with the Fe atom directly underneath, but also with the four neighboring Fe surface atoms with opposite magnetic moments, which can dominate the total exchange coupling. To ensure that neither effect depends qualitatively on the tip size, we employed a larger Fe tip pyramid with an additional plane of 9 Fe atoms [26] and confirmed that both sign and distance-dependence of the magnetic exchange interaction are unchanged.

On the other hand, if we use only a single Fe atom as a tip, the magnetic exchange interaction is qualitatively and quantitatively different from those with multi-atom tips. In particular, the magnetic exchange force is artificially enhanced at large tip-sample separations, but decreases in magnitude already at much larger distances than for multi-atom tips. We attribute these differences to the unrealistic large and rigid

magnetic moment of a single Fe atom due to the missing hybridization with base atoms. In addition, magnetic exchange interactions with base atoms of the tip contribute to the total exchange force on the tip [26]. Therefore, it is crucial to use multi-atom tips and to include relaxation effects in order to obtain the correct sign and distance-dependence of the exchange interactions.

References

[1] A. Schwarz and R. Wiesendanger, Nano Today **3**, 28 (2008).

[2] R. Wiesendanger, D. Bürgler, G. Tarrach, A. Wadas, D. Brodbeck, H. J. Güntherodt, G. Güntherodt, R. J. Gambino and R. Ruf, J. Vac. Sci. Technol. B **9**, 519 (1990).

[3] U. Kaiser, A. Schwarz, and R. Wiesendanger, Nature **446**, 522 (2007).

[4] U. Kaiser, A. Schwarz and R. Wiesendanger, Phys. Rev. B **78**, 104418 (2008).

[5] A. Schwarz, U. Kaiser, and R. Wiesendanger, Nanotechnology **20**, 264017 (2009).

[6] M. Liebmann, A. Schwarz, S. M. Langkat, and R. Wiesendanger, Rev. Sci. Instr. **73**, 3508 (2002).

[7] R. Schmidt, C. Lazo, H. Hölscher, U. H. Pi, V. Caciuc, A. Schwarz, R. Wiesendanger, and S. Heinze Nano Lett. **9**, 200 (2009)

[8] S. Heinze and C. Lazo, University of Hamburg, now Christian-Albrecht Univesität zu Kiel.

[9] T. Okazawa, Y. Yagi, and Y. Kido, Phys. Rev. B **67**, 195406 (2003).

[10] 1F. U. Hillebrecht, H. Ohldag, N. B. Weber, C. Bethke, U. Mick, M. Weiss, and J. Bahrdt, Phys. Rev. Lett. **86**, 3419 (2001).

[11] H. Momida and T. Oguchi, Surf. Sci. **590**, 42 (2005).

[12] H. Hosoi, K. Sueoka, K. Hayakawa, and K. Mukasa, Appl. Surf. Sci. **157**, 218 (2000).

[13] H. Hosoi, K. Sueoka, and K. Mukasa, Nanotechnology **15**, 505 (2004).

[14] W. Allers, S. Langkat, and R. Wiesendanger, Appl. Phys. A: Mater. Sci. Process. **72**, S27 (2001).

[15] R. Hoffmann, A. Baratoff, H. J. Hug, H. R. Hidber, H. v. Löhneysen, and H.-J. Güntherodt, Nanotechnology **18**, 395503 (2007).

[16] A. Kubetzka, P. Ferriani, M. Bode, S. Heinze, G. Bihlmayer, K. von Bergmann, O. Pietzsch, S. Blügel, and R. Wiesendanger, Phys. Rev. Lett. **94**, 087204 (2005).

[17] K. v. Bergmann, M. Bode, and R. Wiesendanger, Phys. Rev. B **70** 174455 (2004).

[18] J. P. Perdew, K. Burke and M. Ernzerhof, Phys. Rev. Lett. **77**, 3865 (1996).

[19] K. Schwarz, P. Blaha, and G. K. H. Madsen, Comput. Phys. Commun. **147**, 71 (2002).

[20] F.-J. Giessibl, Phys. Rev. B **56**, 16010 (1997).

[21] H. Hölscher, A. Schwarz, W. Allers, U. D. Schwarz, and R. Wiesendanger, Phys. Rev. B **61**, 12678 (2000).

[22] V. Caciuc, H. Hölscher, and S. Blg̈el, Phys. Rev. B **72**, 035432 (2005).

[23] U. Dürig, Appl. Phys. Lett. **75**, 433 (1999).

[24] N. Sasaki, H. Aizawa, and M. Tsukada, Appl. Surf. Sci. **157**, 367 (2000).

[25] Since we are not aware of a better value for Fe we used 0.1 aJ, a typical value for A_{H}. However, the overall result does not change for reasonable values of R and A_{H}.

[26] C. Lazo, V. Caciuc, H. Hölscher and S. Heinze, Phys. Rev. B **78**, 214416 (2008).

Chapter 4

Collaborations

4.1 Research Partners

- Institute of Applied Physics and MARCH, University of Hamburg:
  Prof. Dr. W. Hansen, Prof. Dr. U. Merkt, Prof. Dr. H. P. Oepen
- I. Institute of Theoretical Physics, University of Hamburg:
  Prof. Dr. A. Lichtenstein, Prof. Dr. M. Potthoff,
  Jun.-Prof. Dr. F. Lechermann
- Institute for Laser Physics, University of Hamburg:
  Prof. Dr. K. Sengstock
- Institute for Physical Chemistry, University of Hamburg:
  Prof. Dr. H. Weller
- Institute for Inorganic and Applied Chemistry, University of Hamburg:
  Prof. Dr. J. Heck, Jun.-Prof. Dr. M. H. Prosenc
- Department of Computer Science, University of Hamburg:
  Prof. Dr. J. Zhang
- University of Kiel:
  Prof. Dr. R. Berndt, Prof. Dr. S. Heinze, Dr. P. Ferriani
- HGF-Forschungszentrum Jülich:
  Prof. Dr. S. Blügel, Prof. Dr. P. H. Dederichs, Dr. N. Atodiresei,
  Dr. G. Bihlmayer
- MPI for Solid State Research, Stuttgart:
  Dr. S. Roth, Dr. J. Smet, Dr. U. Starke
- University of Karlsruhe:
  Prof. Dr. M. Ruben, Dr. H. Hölscher

- University of Marburg:
  Prof. Dr. M. Bröring
- RWTH Aachen:
  Prof. Dr. M. Morgenstern
- University of Konstanz:
  Prof. Dr. P. Leiderer
- Center for Computational Nanoscience, Vienna, Austria:
  Prof. Dr. P. Weinberger
- University of Bialystok, Poland:
  Prof. Dr. A. Maziewski
- University of Trieste, Italy:
  Prof. Dr. S. Modesti
- National Nanotechnology Laboratory, Lecce, Italy:
  Dr. G. Maruccio
- University of Zaragoza, Spain:
  Prof. Dr. J. I. Arnaudas, Dr. D. Serrate
- University of Madrid, Spain:
  Dr. N. Mikuszeit
- University College London, GB:
  Prof. Dr. A. Shluger
- Trinity College Dublin, Ireland:
  Prof. Dr. S. Sanvito
- University of Iowa, USA:
  Prof. Dr. M. E. Flatté
- University of Ohio, Athens, USA:
  Prof. Dr. S.-W. Hla, Prof. Dr. A. R. Smith
- University of Michigan, East Lansing, USA:
  Prof. Dr. D. Tománek, Dr. S. Berber
- University of California, Irvine, USA:
  Prof. Dr. D. L. Mills, Dr. S. Lounis
- Columbia University, New York, USA:
  Prof. Dr. C. J. Chen

- Los Alamos National Laboratory, USA:
  Dr. A. V. Balatsky
- National Institute for Materials Science (NIMS), Tsukuba, Japan:
  Dr. M. Aono
- Tohoku University, Sendai, Japan:
  Dr. K. Hashimoto
- Samsung, South-Korea:
  Dr. U. H. Pi

Chapter 5

Theses

5.1 Diploma Theses

1. Matthias Nohme (2008):
   Aufbau und Erweiterung eines 300mK 17T UHV Rastertunnel-mikroskops für die Untersuchung magnetischer Moleküle auf Oberflächen

2. Matthias Prostak (2008):
   Entwicklung neuer Komponenten zur Molekülpräparation und Rastertunnelmikroskopie-Messung an organischen Molekülsystemen

3. Thimo Christian Göllnitz (2008):
   Photolytische OMCVD-Abscheidung von Wolfram auf Glas-Entwicklung, Realisation und erste Testmessungen

4. Henning von Allwörden (2008):
   Entwicklung neuartiger Sensoren für höchstauflösende Rasterkraftmikroskopie

5. Henning Gutzmann (2008):
   Scanning tunneling spectroscopy on a 2D Mott-Hubbard insulator and preparations for STM measurements on MBE grown GaMnAs

6. Anika Emmenegger (2008):
   Untersuchung spinabhängiger Bildladungszustände hoher Ordnung mittels spinpolarisierter Rastertunnelspektroskopie

7. Thomas Eelbo (2008):
   Construction of a new Ultra-High Vacuum Variable-Temperature Scanning Tunneling Microscope

8. Rolf Würdemann (2008):
   Berechnung von Bildladungszuständen der (110) Oberfläche von Eisen

9. Thim Stapelfeldt (2008):
   Superparamagnetic Switching of Two-dimensional Magnetic Islands Studied by Monte Carlo Simulation

10. Sweetlana Fremy (2009):
    Rasterkraftmikroskopie an Co-Salen

11. Anett Preßler (2009):
    Spinpolarisierte Rastertunnelmikroskopie an der Eisenmonolage auf Ruthenium(0001)

12. Oliver Ferdinand (2009):
    Herstellung und Charakterisierung von Tunnelspitzen für die inelastische Rastertunnelspektroskopie

13. Boris Wolter (2009):
    Semi-autonome laterale Manipulation einzelner Atome innerhalb einer simulierten Rastertunnelmikroskopumgebung

14. Leonid Lichtenstein (2009):
    Untersuchung eisenhaltiger metallorganischer Komplexe mittels Rastertunnelmikroskopie

15. Jan Samuelsen (2009):
    Untersuchung magnetischer metallorganischer Komplexe mittels Rastertunnelmikroskopie

16. Johannes Hattendorff (2010):
    Rasterkraftmikroskopie an Co-Salen auf NiO(001)

5.2 Ph. D. Theses

1. Stefan Krause (2008):
   Thermal and Current-Induced Magnetization Switching of Fe/W(110) Nanoislands Investigated by Spin-Polarized Scanning Tunneling Microscopy

2. Stefan Kuck (2009):
   Scanning Tunneling Microscopy and Spectroscopy of Magnetic Molecules on Surfaces

3. Felix Marczinowski (2010):
   Manganese in Indium Arsenide: Charge Switching and Electronic Structure on the Atomic Scale

4. Stefan Meckler (2010):
   Non-Collinear Magnetism in Fe on W(110)

5. Lihui Zhou (2010):
   Single-Atom Magnetism Mapped by Spin-Polarized Scanning Tunneling Microscopy

Chapter 6

Scientific Publications

6.1 Books

1. S. Morita, F. J. Giessibl, and R. Wiesendanger (eds.), *Non-Contact Atomic Force Microscopy Vol. 2*, Springer Berlin, Heidelberg 2009.

6.2 Book Contributions and Review Articles

1. K. von Bergmann, M. Bode, and R. Wiesendanger, Physik in unserer Zeit **2**/2008, p. 93 (2008): *"Magnetismus mit Dreh"*.

2. A. Schwarz and R. Wiesendanger, Nano Today **3**, p. 28 (2008): *"Magnetic sensitive force microscopy: MFM and MExFM"*.

3. R. Wiesendanger, Rev. Mod. Phys. **81**, p. 1495 (2009): *"Spin mapping at the nanoscale and atomic scale"*.

4. H. Fuchs and R. Wiesendanger, nanoTECHNOLOGIE aktuell **2**, p. 10 (2009): *Magnetismus im Nanokosmos*

5. A. Schwarz, U. Kaiser, R. Schmidt, and R. Wiesendanger, in: Non-Contact Atomic Force Microscopy II, eds. S. Morita, F. J. Giessibl, and R. Wiesendanger, Springer (2009), p. 275: *"Magnetic Exchange Force Microscopy"*.

6. G. Maruccio and R. Wiesendanger, in: Quantum Materials, ed. D. Heitmann, Springer (2010), p. 183: *"Scanning tunneling spectroscopy of semiconductor quantum dots and nanocrystals"*.

7. M. Morgenstern, J. Wiebe, F. Marczinowski, and R. Wiesendanger, in: Quantum Materials, ed. D. Heitmann, Springer (2010), p. 217: *"Scanning tunneling spectroscopy on III-V materials: Effects of dimensionaltiy, magnetic field, and magnetic impurities"*.

6.3 Original Articles

1. S.-H. Chang, S. Kuck, J. Brede, L. Lichtenstein, G. Hoffmann, and R. Wiesendanger, Phys. Rev. B **78**, 233409 (2008): *Symmetry reduction of metal phthalocyanines on metals*

2. K. Hashimoto, C. Sohrmann, J. Wiebe, T. Inaoka, F. Meier, Y. Hirayama, R. A. Römer, R. Wiesendanger, and M. Morgenstern, Phys. Rev. Lett. **101**, 256802 (2008): *Quantum Hall Transition in Real Space: From Localized to Extended States*

3. R. Wieser, E. Y. Vedmedenko, and R. Wiesendanger, Phys. Rev. Lett. **101**, 177202 (2008): *Quantized Spin Waves in Antiferromagnetic Heisenberg Chains*

4. S. Kuck, G. Hoffmann, M. Bröring, M. Fechtel, M. Funk, and R. Wiesendanger, J. Am. Chem. Soc. **130**, 14072 (2008): *"Naked" Iron-5,10,15-triphenylcorrole on Cu(111): Observation of Chirality on a Surface and Manipulation of Multiple Conformational States by STM*

5. U. Kaiser, A. Schwarz, and R. Wiesendanger, Phys. Rev. B **78**, 104418 (2008): *Evaluating local properties of magnetic tips utilizing an antiferromagnetic surface*

6. L. Sacharow, R. Wiesendanger, G. Bihlmayer, S. Blügel and M. Morgenstern, Surf. Sci. **602**, 3297 (2008): *Anisotropic superexchange in one-dimensional Fe-chains on InAs(110)*

7. S. Kuck, J. Wienhausen, G. Hoffmann, and R. Wiesendanger, Rev. Sci. Instr. **79**, 083903 (2008): *A versatile variable-temperature scanning tunneling microscope for molecular growth*

8. P. Ferriani, K. von Bergmann, E. Y. Vedmedenko, S. Heinze, M. Bode, M. Heide, G. Bihlmayer, S. Blügel, and R. Wiesendanger, Phys. Rev. Lett. **101**, 027201 (2008): *Atomic-Scale Spin Spiral with a Unique Rotational Sense: Mn Monolayer on W(001)*

9. E.Y. Vedmedenko, N. Mikuszeit, ChemPhysChem **9**, 1222 (2008): *Multipolar Ordering in Electro- and Magnetostatic Coupled Nanosystems*

10. E. Y. Vedmedenko, S. Even-Dar Mandel, R. Lifshitz, Phil. Mag. **88**, 2197 (2008): *In search of multipolar order on the Penrose tiling*

11. K. von Bergmann, M. Bode, A. Kubetzka, O. Pietzsch, E. Y. Vedmedenko, R. Wiesendanger, Phil. Mag. **88**, 2627 (2008): *Complex magnetic order on the atomic scale revealed by spin-polarized scanning tunnelling microscopy*

12. M. Ashino, D. Obergfell, M. Haluška, S. Yang, A. N. Khlobystov, S. Roth, and R. Wiesendanger, Nature Nanotechnology **3**, 337 (2008): *Atomically resolved mechanical response of individual metallofullerene molecules confined inside carbon nanotubes*

13. C. Etz, J. Zabloudil, P. Weinberger, E. Y. Vedmedenko, Phys. Rev. B **77**, 184425 (2008): *Magnetic properties of single atoms of Fe and Co on Ir(111) and Pt(111)*

14. A. Westphalen, A. Schumann, A. Remhof, H. Zabel, M. Karolak, B. Baxevanis, E. Y. Vedmedenko, T. Last, U. Kunze, T. Eimüller, Phys. Rev. B **77**, 174407 (2008): *Magnetization reversal of microstructured kagome lattices*

15. E. Y. Vedmedenko, R. Wiesendanger, Phil. Mag. **88**, 2683 (2008): *Modulated multipolar structures in magnetic arrays*

16. F. Meier, L. Zhou, J. Wiebe, and R. Wiesendanger, Science **320**, 82 (2008): *Revealing Magnetic Interactions from Single-Atom Magnetization Curves*

17. A. Remhof, A. Schumann, A. Westphalen, H. Zabel, N. Mikuszeit, E. Y. Vedmedenko, T. Last, and U. Kunze, Phys. Rev. B **77**, 134409 (2008): *Magnetostatic interactions on a square lattice*

18. F. Marczinowski, J. Wiebe, F. Meier, K. Hashimoto, and R. Wiesendanger, Phys. Rev. B **77**, 115318 (2008): *Effect of charge manipulation on scanning tunneling spectra of single Mn acceptors in InAs*

19. R. Wieser, E. Y. Vedmedenko, and R. Wiesendanger, Phys. Rev. B **77**, 064410 (2008): *Entropy driven phase transition in itinerant antiferromagnetic monolayers*

20. E. V. Konenkova, D. Grundler, M. Morgenstern, and R. Wiesendanger, Techn. Phys. Lett. **34**, 30 (2008): *Metal Insulator Transition in Graphite: A Comparison to Heterostructures with High Carrier Mobility*

21. A. Scarfato, S.-H. Chang, S. Kuck, J. Brede, G. Hoffmann, and R. Wiesendanger, Surf. Sci. **602**, 677 (2008): *Scanning tunneling microscope study of iron(II) phthalocyanine growth on metal and insulating surfaces*

22. B. Santos, J. M. Puerta, J. I. Cerda, R. Stumpf, K. von Bergmann, R. Wiesendanger, M. Bode, K. F. McCarty, and J. de la Figuera, New J. Phys. **10**, 13005 (2008): *Structure and magnetism of ultra-thin chromium layers on W(110)*

23. M. Bode, O. Pietzsch, A. Kubetzka, W. Wulfhekel, D. McGrouther, S. McVitie, and J. N. Chapman, Phys. Rev. Lett. **100**, 029703 (2008): *Comment on "Three-Dimensional, Spin-Resolved Structure of Magnetic Vortex and Antivortex States in Patterned Co Films Using Scanning Ion Microscopy with Polarization Analysis"*

24. L. Berbil-Bautista, S. Krause, M. Bode, A. Badía-Majós, C. de la Fuente, R. Wiesendanger, and J. I. Arnaudas, Phys. Rev. B **80**, 241408(R) (2009): *Nanoscale spin structures dominated by magnetoelastic interactions around dislocation cores as seen via spin-polarized STM*

25. S. Meckler, N. Mikuszeit, A. Preßler, E. Y. Vedmedenko, O. Pietzsch, and R. Wiesendanger, Phys. Rev. Lett. **103**, 157201 (2009): *Real-Space Observation of a Right-Rotating Inhomogeneous Cycloidal Spin Spiral by Spin-Polarized Scanning Tunneling Microscopy in a Triple Axes Vector Magnet*

26. S. Hankemeier, R. Frömter, N. Mikuszeit, D. Stickler, H. Stillrich, S. Pütter, E. Y. Vedmedenko, and H. P. Oepen, Phys. Rev. Lett. **103**, 147204 (2009): *Magnetic Ground State of Single and Coupled Permalloy Rectangles*

27. A. Stupakiewicz, E.Y. Vedmedenko, A. Fleurence, T. Maroutian, P. Beauvillain, A. Maziewski, and R. Wiesendanger, Phys. Rev. Lett. **103**, 137202 (2009): *Atomic-Level Control of the DomainWall Velocity in Ultrathin Magnets by Tuning of Exchange Interactions*

28. S. Modesti, H. Gutzmann, J. Wiebe, and R. Wiesendanger, Phys. Rev. B **80**, 125326 (2009): *Correction of systematic errors in scanning tunneling spectra on semiconductor surfaces: The energy gap of Si(111)-7x7 at 0.3 K*

29. S. Krause, G. Herzog, T. Stapelfeldt, L. Berbil-Bautista, M. Bode, E. Y. Vedmedenko, and R. Wiesendanger, Phys. Rev. Lett. **103**, 127202 (2009): *Magnetization Reversal of Nanoscale Islands: How Size and Shape Affect the Arrhenius Prefactor*

30. S. Fremy, A. Schwarz, K. Lämmle, M. Prosenc, and R. Wiesendanger, Nanotechnology **20**, 405608 (2009): *The monomer-to-dimer transition and bimodal growth of Co-Salen on NaCl(001): a high resolution atomic force microscopy study*

31. S. Pütter, N. Mikuszeit, E. Y. Vedmedenko, and H. P. Oepen, J. Appl. Phys. **106**, 043916 (2009): *The effect of tilted edges on the shape anisotropy and stray field coupling of uniformly magnetized rectangular elements*

32. N. Mikuszeit, L. Baraban, E. Y. Vedmedenko, A. Erbe, P. Leiderer, and R. Wiesendanger, Phys. Rev. B **80**, (2009): *Quasiantiferromagnetic* 120° *Néel state in two-dimensional clusters of dipole-quadrupole-interacting particles on a hexagonal lattice*

33. S. Kuck, S.-H. Chang, J.-P. Klöckner, M. H. Prosenc, G. Hoffmann, and R. Wiesendanger, ChemPhysChem **10**, 2008 (2009): *Steering two dimensional molecular growth via dipolar interaction*

34. J. Brede, S. Kuck, J. Schwöbel, S.-H. Chang, M. Linares, G. Hoffmann, R. Wiesendanger, A. Scarfato, R. Lensen, P. Kouwer, J. Hoogboom, A. Rowan, M. Bröring, M. Funk, S. Stafström, F. Zerbetto, and R. Lazzaroni, Nanotechnology **20**, 275602 (2009): *Dynamics of molecular self-ordering in tetraphenyl porphyrin monolayers on metallic substrates*

35. R. Schmidt, A. Schwarz, and R. Wiesendanger, Nanotechnology **20**, 264007 (2009): *Hydrogen-related contrast in atomic force microscopy*

36. M. Ashino, D. Obergfell, M. Haluska, S. Yang, A. N. Khlobystov, S. Roth, and R. Wiesendanger, Nanotechnology **20**, 264001 (2009): *Atomic-resolution three-dimensional force and damping maps of carbon nanotube peapods*

37. A. Schwarz, U. Kaiser, and R. Wiesendanger, Nanotechnology **20**, 264017 (2009): *Towards an understanding of the atomic scale magnetic contrast formation in NC-AFM: a tip material dependent MExFM study on Ni*

38. M. Ashino, R. Wiesendanger, A. N. Khlobystov, S. Berber, and D. Tománek, Phys. Rev. Lett. **102**, 195503 (2009): *Revealing Subsurface Vibrational Modes by Atom-Resolved Damping Force Spectroscopy*

39. R. Wieser, E. Y. Vedmedenko, and R. Wiesendanger, Phys. Rev. B **79**, 144412 (2009): *Quantized spin waves in ferromagnetic and antiferromagnetic structures with domain walls*

40. J. Brede, M. Linares, R. Lensen, A. E. Rowan, M. Funk, M. Bröring, G. Hoffmann, and R. Wiesendanger, J. Vac. Sci. Tech. B **27(2)**, 799 (2009): *Adsorption and Conformation of Porphyrins on Metallic Surfaces*

41. S. Meckler, M. Gyamfi, O. Pietzsch, R. Wiesendanger, Rev. Sci. Instr. **80**, 023708 (2009): *A low-temperature spin-polarized scanning tunneling microscope operating in a fully rotatable magnetic field*

42. G. Maruccio, Chr. Meyer, T. Matsui, D. V. Talapin, S. G. Hickey, H. Weller, and R. Wiesendanger, Small **5**, 808 (2009): *Wavefunction Mapping of Immobilized InP Semiconductor Nanocrystals*

43. R. Schmidt, C. Lazo, H. Hölscher, U. H. Pi, V. Caciuc, A. Schwarz, R. Wiesendanger, and S. Heinze, Nano Letters **9**, 200 (2009): *Probing the Magnetic Exchange Forces of Iron on the Atomic Scale*

44. A. A. Khajetoorians, B. Chilian, J. Wiebe, S. Schuwalow, F. Lechermann, and R. Wiesendanger, Nature **467**, 1084 (2010): *Detecting excitation and magnetization of individual dopants in a semiconductor*

45. R. Wieser, E. Y. Vedmedenko, P. Weinberger, and R. Wiesendanger, Phys. Rev. B **82**, 144430 (2010): *Current driven domain wall motion in cylindrical nanowires*

46. N. Baadji, S. Kuck, J. Brede, G. Hoffmann, R. Wiesendanger, and S. Sanvito, Phys. Rev. B **82**, 115447 (2010): *Controlled sequential dehydrogenation of single molecules by scanning tunneling microscopy*

47. A. Schlenhoff, S. Krause, G. Herzog, and R. Wiesendanger, Appl. Phys. Lett. **97**, 083104 (2010): *Bulk Cr tips with full spatial magnetic sensitivity for spin-polarized scanning tunneling microscopy*

48. N. Atodiresei, J. Brede, P. Lazic, V. Caciuc, G. Hoffmann, R. Wiesendanger, and S. Blügel, Phys. Rev. Lett. **105**, 066601 (2010): *Design of the Local Spin-polarization at the Organic-Ferromagnetic Interface*

49. L. Zhou, F. Meier, J. Wiebe, and R. Wiesendanger, Phys. Rev. B **82**, 012409 (2010): *Inversion of spin polarization above individual magnetic adatoms*

50. J. Brede, N. Atodiresei, G. Hoffmann, S. Kuck, P. Lazic, V. Caciuc, Y. Morikawa, S. Blügel, and R. Wiesendanger, Phys. Rev. Lett. **105**, 047204 (2010): *Spin- and Energy-Dependent Tunneling through a Single Molecule with Intramolecular Spatial Resolution*

51. K. Lämmle, T. Trevethan, A. Schwarz, M. Watkins, A. Shluger, and R. Wiesendanger, Nano Letters **10**, 2965 (2010): *Unambiguous Determination of the Adsorption Geometry of a Metal-Organic Complex on a Bulk Insulator*

52. K. Lämmle, A. Schwarz, and R. Wiesendanger, Rev. Sci. Instr. **81**, 053902 (2010): *Miniaturized transportable evaporator for molecule deposition inside cryogenic scanning probe microscopes*

53. C. J. Chen, A. Schwarz, R. Wiesendanger, O. Horn, and J. Müller, Rev. Sci. Instr. **81**, 053702 (2010): *Three-electrode self-actuating self-sensing quartz cantilever: design, analysis, and experimental verification*

54. S.-H. Chang, A. Scarfato, C. Kleeberg, M. Bröring, G. Hoffmann, and R. Wiesendanger, Langmuir **26**, 10868 (2010): *Adsorption behavior of asymmetric Pd pincer complexes on a Cu(111) surface*

55. D. Serrate, P. Ferriani, Y. Yoshida, S.-W. Hla, M. Menzel, K. von Bergmann, S. Heinze, A. Kubetzka and R. Wiesendanger, Nature Nanotechnology **5**, 350 (2010): *Imaging and Manipulating the Spin Direction of Individual Atoms*

56. A. Schwarz, M. Liebmann, U. H. Pi, and R. Wiesendanger, New J. Phys. **12**, 033022 (2010): *Real space visualization of thermal fluctuations in a triangular flux line lattice*

57. S. Kuck, M. Prostak, M. Funk, M. Bröring, G. Hoffmann, and R. Wiesendanger, J. Vac. Sci. Tech. A **28**, 795 (2010): *The disposition of the axial ligand in the physical vapor deposition of organometallic complexes*

58. G. Herzog, S. Krause, and R. Wiesendanger, Appl. Phys. Lett. **96**, 102505 (2010): *Heat assisted spin torque switching of quasistable nanomagnets across a vacuum gap*

59. L. Zhou, J. Wiebe, S. Lounis, E. Vedmedenko, F. Meier, S. Blügel, P. H. Dederichs, and R. Wiesendanger, Nature Physics **6**, 187 (2010): *Strength and directionality of surface Ruderman–Kittel–Kasuya–Yosida interaction mapped on the atomic scale*

60. R. Wieser, E. Y. Vedmedenko, and R. Wiesendanger, Phys. Rev. B **81**, 024405 (2010): *Domain wall motion damped by the emission of spin waves*

61. A. A. Khajetoorians and A. Kubetzka, Nature Nanotechnology **5**, 830–831 (2010): *Scanning probe microscopy: STM hits the fast lane*

62. R. Wiesendanger, Current Opinion in Solid State and Materials Science (in press): *Single-atom magnetometry*

63. J. I. Arnaudas, A. Badia-Majós, L. Berbil-Bautista, M. Bode, F. J. Castano, M. Ciria, C. de la Fuente, J. L. Diez-Ferrer, S. Krause, B. G. Ng, R. C. O'Handley, C. A. Ross, and R. Wiesendanger, The Physics of Metals and Metallography (in press): *Magnetoelastic effects in nanostructures*

64. H. Bistry, B. Wolter, B. Schütz, R. Wiesendanger, and J. Zhang, Proc. IEEE Nano 2010 (in press): *An approach for automated scale invariant STM-scan matching using SIFT*

65. K. Hashimoto, J. Wiebe, T. Inaoka, Y. Hirayama, R. Wiesendanger, and M. Morgenstern, J. Phys.: Conf. Series (in press): *Real-space mapping of a two-dimensional disordered system in the quantum Hall regime*

66. F. Meier, S. Lounis, J. Wiebe, L. Zhou, S. Heers, P. Mavropoulos, P. H. Dederichs, S. Blügel, and R. Wiesendanger, Phys. Rev. B (in press): *Spin-polarization of platinum (111) induced by the proximity to cobalt nanostripes*

67. A. A. Khajetoorians, S. Lounis, B. Chilian, A. T. Costa, L. Zhou, D. L. Mills, J. Wiebe, and R. Wiesendanger, Phys. Rev. Lett. (in press): *Itinerant nature of atom-magnetization excitation by tunneling electrons*

68. P. Weinberger, E. Y. Vedmedenko, R. Wieser, and R. Wiesendanger, Phil. Mag. (in press): *A multi-scale model of domain wall velocities based on ab initio parameters*

69. R. Wieser, E. Y. Vedmedenko, and R. Wiesendanger, Phys. Rev. Lett. (in press): *Indirect control of antiferromagnetic domain walls with spin currents*

Chapter 7

Talks and Posters

7.1 Invited Talks

5.2.2008: R. Wiesendanger, Int. Conf. on Computational Materials Science, Morelos (Mexico): *Spin mapping and spin manipulation on the atomic scale*

5.2.2008: K. von Bergmann, Winter Conference on Condensed Matter 2008, Aspen (2008): *Magnetism at the atomic scale by Scanning Probe Techniques*

18.2.2008: R. Wiesendanger, Russian-German Workshop, Kurchatov Institute, Moscow (Russia): *Nanoscience studies based on scanning probe microscopy*

26.2.2008: R. Wiesendanger, Int. Conf. on Nanoscience and Nanotechnology 2008, Melbourne (Australia): *New horizons in nanoscale magnetism: Fundamentals and applications*

5.3.2008: R. Wiesendanger, 16. Jahrestagung der Deutschen Gesellschaft für Kristallographie DGK 2008, Erlangen (Germany): *Atom-resolved spin mapping at surfaces of single crystals and thin films*

10.3.2008: J. Wiebe, 2008 APS March Meeting, New Orleans, Louisiana (USA): *Subkelvin spin polarized STM: measuring magnetization curves of individual adatoms*

10.3.2008: R. Wiesendanger, 2008 APS March Meeting, New Orleans, Louisiana (USA): *Scanning Probe Microscopy for spin mapping and spin manipulation on the atomic scale*

11.3.2008: S. Krause, 2008 APS March Meeting, New Orleans, Louisiana (USA): *Current-Induced Magnetization Switching with a Spin-Polarized Scanning Tunneling Microscope*

23.4.2008: R. Wiesendanger, 1st Nordic Workshop on Spintronics and Nanomagnetism, Gimo Herrgård (Sweden): *Oscillatory magnetic exchange coupling at the atomic level: a direct real space study by a sub-Kelvin spin-polarized STM*

6.5.2008: R. Wiesendanger, Intermag '08, Madrid (Spain): *Mapping atomic-scale spin structures on insulators by magnetic exchange force microscopy*

7.5.2008: A. Kubetzka, National Conference on Condensed Matter Physics, Aguas de Lindoia (Brazil): *Magnetism investigated by spin-polarized scanning tunneling microscopy*

14.5.2008: K. von Bergmann, Summer School on Creating and Analyzing Surfaces and Nanoscale Materials, Sant Feliu de Guixols (Spain): *Magnetism at the atomic scale by Scanning Probe Techniques*

5.6.2008: A. Schwarz, M. Liebmann, and R. Wiesendanger, NES Workshop "Probing Superconductivity at the nanoscale", Alicante (Spain): *How a Flux Line Lattice Melts: A Real Space Visualization by Magnetic Force Microscopy on Bi2212*

30.6.2008: R. Wiesendanger, Workshop on "High temporal and spatial resolution studies of magnetic nanostructures", Augustów (Poland): *Spin mapping and spin manipulation on the atomic scale*

2.7.2008: K. von Bergmann, XI$^{\text{th}}$ Symposium on Surface Physics, Prague (Czech Republic): *Complex magnetic order on the atomic scale revealed by spin-polarized STM*

13.7.2008: K. von Bergmann, Spin helicity and chirality in superconductor and semiconductor nanostructures, Karlsruhe (Germany): *Complex magnetic structures on the atomic scale revealed by spin-polarized STM*

16.7.2008: S. Krause, NSS5/SP-STM2, Athens, Ohio (USA): *Current-Induced Magnetization Switching with a Spin-Polarized Scanning Tunneling Microscope*

17.7.2008: R. Wiesendanger, NSS5/SP-STM2, Athens, Ohio (USA): *Oscillatory magnetic exchange coupling at the atomic level: a direct real-space study by a sub-Kelvin spin-polarized STM*

21.7.2008: J. Wiebe, F. Meier, L. Zhou, and R. Wiesendanger, International Conference on Nanoscience and Technology, Keystone, Colorado (USA): *Probing Single-Atom Magnetization Curves by Subkelvin Spin-Polarized STS*

21.7.2008: A. Schwarz, International Conference on Nanoscience and Technology, Keystone, Colorado (USA): *Magnetic Exchange Force Microscopy*

31.7.2008: S. Krause, European Conference on Surface Science (ECOSS 2008), Liverpool (UK): *Current-Induced Magnetization Switching with a Spin-Polarized Scanning Tunneling Microscope*

5.8.2008: A. Schwarz and R. Wiesendanger, 9$^{\text{th}}$ International Conference on the Structure of Surfaces (ICSOS-9), Salvador (Brazil): *Mapping Atomic-Scale Spin Structures on Insulators by Magnetic Exchnage Force Microscopy*

12.8.2008: L. Zhou, F. Meier, J. Wiebe, and R. Wiesendanger, 25$^{\text{th}}$ International Conference on Low Temperature Physics, Amsterdam (The Netherlands): *Oscillatory Magnetic Exchange Coupling at the Atomic Level Revealed from Single-Atom Magnetization Curves*

1.9.2008: K. von Bergmann, Gordon Research Conference on Magnetic Nanostructures, Aussois (France): *Complex magnetic order on the atomic scale revealed by spin-polarized STM*

4.9.2008: R. Wiesendanger, 14$^{\text{th}}$ European Microscopy Congress, Aachen (Germany): *Spin mapping on the atomic scale*

25.9.2008: R. Wiesendanger, ÖPG-Jahrestagung, Leoben (Austria): *Spin mapping on the atomic scale*

20.10.2008: K. von Bergmann, 55$^{\text{th}}$ Intl. Symposium of the American Vacuum Society, Boston (USA): *Complex magnetic order on the atomic scale revealed by spin-polarized STM*

11.11.2008: L. Zhou, F. Meier, J. Wiebe, and R. Wiesendanger, 53$^{\text{rd}}$ Annual Conference on Magnetism and Magnetic Materials, Austin, Texas (USA): *Oscillatory magnetic exchange coupling at the atomic level: a direct real-space study by a subkelvin spin-polarized STM*

27.11.2008: G. Hoffmann, Quantum Simulations for Atomically Controlled Fabrication Technology, Osaka (Japan): *STM investigation of Phthalocyanines*

3.12.2008: R. Wiesendanger, Rusnanotech ´08, Moscow (Russia): *Perspectives of Nano-Spintronics*

21.1.2009: A. Schwarz, 1$^{\text{th}}$ Global COE International Symposium "Electronic Devices Innovation" , Osaka (Japan): *Advances in Magnetic Sensitive Force Microscopy*

17.2.2009: R. Wiesendanger, 1$^{\text{st}}$ Russian-German Workshop on the Development and Use of Accelerator-Driven Photon Sources, Berlin (Germany): *Infrastructure for Nanoscience*

19.2.2009: R. Wiesendanger, DESY - VIII. Research Course on New X-ray Sciences, Hamburg (Germany): *Static and dynamic investigations of nanoscale magnets at the ultimate spatial resolution limit*

6.3.2009: R. Wiesendanger, EMPA - Symposium "Headways in Material Science", Zürich (Switzerland): *New horizons in nanomagnetism by spin-sensitive scanning probe methods*

27.3.2009: R. Wiesendanger, 73rd Spring Conference, Deutsche Physikalische Gesellschaft, Dresden (Germany): *Spin mapping and spin manipulation on the atomic scale*

21.4.2009: R. Wiesendanger, Public Lecture to "The Academic City – Poznan", Poznan (Poland): *Nanotechnology – gateway to a better world?*

20.7.2009: J. Wiebe, L. Zhou, S. Lounis, E. Y. Vedmedenko, F. Meier, P. H. Dederichs, S. Blügel, and R. Wiesendanger, 5th International Symposium on Scanning Probe Spectroscopy and Related Methods (SPS 09), Wasowo (Poland): *Using Single-Atom Magnetization Curves to Study Interactions on the Atomic Scale*

21.7.2009: A. Schwarz, 5th International Symposium on Scanning Probe Spectroscopy and Related Methods (SPS 09), Wasowo (Poland): *New Developments in the Field of Magnetic Exchange Force Microscopy*

23.7.2009: J. Wiebe, L. Zhou, S. Lounis, E. Y. Vedmedenko, F. Meier, P. H. Dederichs, S. Blügel and R. Wiesendanger, 20th International Colloquium on Magnetic Films and Surfaces (ICMFS 2009), Berlin (germany): *Atomic Scale Mapping of Magnetism in Adatom Nanostructures*

20.8.2009: R. Wiesendanger, 3rd International Workshop on "Smart Materials and Structures", Kiel (Germany): *Artificially structured nanomagnets: Perspectives of nano-spintronics*

30.8.2009: S. Modesti, H. Gutzmann, J. Wiebe, and R. Wiesendanger, European Conference on Surface Science (ECOSS-26), Parma (Italy): *Two-dimensional Mott-Hubbard insulators on semiconductor surfaces*

15.9.2009: R. Wiesendanger, 16th International Summer School "Spin Transport and Dynamics in Nanostructures", Madrid (Spain): *Magnetic exchange force microscopy: A novel approach towards atomic-scale magnetism of insulators*

16.9.2009: R. Wiesendanger, 16th International Summer School "Spin Transport and Dynamics in Nanostructures", Madrid (Spain): *Atomic and molecular spintronics based on spin-polarized STM*

20.9.2009: R. Wiesendanger, International Conference "Nanostructures at Surfaces", Ascona (Switzerland): *Artificially structured nanomagnets: Perspectives of nano-spintronics*

24.9.2009: J. Wiebe, 10$^{\text{th}}$ International Conference on Atomically Controlled Surfaces, Interfaces and Nanostructures (ACSIN 10), Granada (Spain): *Atomic scale mapping of magnetic interactions in adatom nanostructures*

15.10.2009: A. Schwarz, International Workshop "Simultaneous STM/AFM measurements using tuning fork based sensors" , Prague (Czech Republic): *Magnetic Sensitive Magnetic Force Microscopy*

7.11.2009: R. Wiesendanger, CNR School on "Spin Physics in Materials", Chiavari (Italy): *Spin Physics of Metallic Nanostructures revealed by Spin-Polarized Scanning Tunneling Microscopy*

8.11.2009: R. Wiesendanger, CNR School on "Spin Physics in Materials", Chiavari (Italy): *Spin Physics of Insulators revealed by Magnetic Exchange Force Microscopy*

30.11.2009: J. Wiebe, 3$^{\text{rd}}$ International Symposium on Vortex Dynamics, Hamburg (Germany): *Ultimate Spatial Resolution of Spin Structures: From Magnetic Vortex Cores to Individual Atoms.*

30.11.2009: R. Wiesendanger, MRS'09 Fall Meeting, Boston (USA): *Perspectives of Magnetic Exchange Force Microscopy*

7.1.2010: K. von Bergmann, 449. WE-Heraeus-Seminar, Bad Honnef (Germany): *Probing complex spinstructures at surfaces*

22.2.2010: R. Wiesendanger, Winter-School on New Developments in Solid State Physics, Mauterndorf (Austria): *Spin mapping and magnetometry down to the atomic level*

1.3.2010: A. Schwarz, Advenced Atomic Force Microscopy Techniques, Karlsruhe (Germany): *Recent Developments in the Field of Magnetic Exchange Force Microscopy*

25.3.2010: R. Wiesendanger, 74$^{\text{th}}$ Spring Conference, Deutsche Physikalische Gesellschaft, Regensburg (Germany): *Spin-dependent tunneling through a single molecule with intramolecular resolution*

15.4.2010: A. Schwarz, COST Workshop "Imaging of molecules, defects and oxide surfaces", Graz (Austria): *Oxides, molecules and magnetism: What can be achieved with atomic force microscopy?*

27.4.2010: R. Wiesendanger, International Conference on Superconductivity and Magnetism ICSM 2010, Antalya (Turkey): *Spin mapping and magnetometry on the atomic scale*

7.5.2010: R. Wiesendanger, 2nd Nordic Workshop on Spintronics and Nanomagnetism, Gimo Herrgård (Sweden): *Spin mapping, spin manipulation, and magnetometry at the atomic level*

27.5.2010: R. Wiesendanger, International Conference on Trends in Spintronics and Nanomagnetism, Lecce (Italy): *Spin mapping, spin manipulation, and magnetometry on the atomic scale*

10.6.2010: R. Wiesendanger, 12th International Ceramics Congress, Montecatini Terme (Italy): *SPM-based nanofabrication and analysis of atomic-scale magnetic systems*

17.6.2010: J. Wiebe, European Symposium on Nanospintronics , Hamburg (Germany): *Imaging magnetic interactions in nanostructures built from individual adatoms*

17.6.2010: A. Khajetoorians, European Symposium on Nanospintronics, Hamburg (Germany): *Single atom spin detection of quantum magnets embedded in a semiconductor*

17.6.2010: A. Schwarz, European Symposium on Nanospintronics, Hamburg (Germany): *Probing Magnetic Exchange Interactions with Atomic Resolution*

18.6.2010: J. Brede, European Symposium on Nanospintronics, Hamburg (Germany): *Spin- and energy-dependent tunneling through single Phthalocyanine molecules with intramolecular spatial resolution*

29.6.2010: R. Wiesendanger, 4th National Nanotechnology Conference NANO 2010, Poznan (Poland): *Exploring the spin in the nanoworld*

8.7.2010: R. Wiesendanger, World Wide Magnetic Resonance Conference 2010, Florence (Italy): *Atomic-resolution spin mapping and magnetometry at the atomic level*

9.7.2010: R. Wiesendanger, Laserion 2010, Schloß Ringberg, Tegernsee (Germany): *Probing magnetic exchange forces on the atomic scale*

19.8.2010: R. Wiesendanger, SPSTM-3, Seoul (South-Korea): *Spin-Polarized Scanning Tunneling Microscopy and Spectroscopy at the Atomic Scale*

27.8.2010: R. Wiesendanger, IVC-18 and ICN+T 2010, Beijing (China): *Spin Mapping, Spin Manipulation, and Magnetometry at the Atomic Level*

31.8.2010: R. Wiesendanger, EPS-CMD23, Warsaw (Poland): *Spin Mapping, Spin Manipulation, and Magnetometry at the Atomic Level*

1.9.2010: K. Hashimoto, J. Wiebe, T. Inaoka, Y. Hirayama, R. A. Römer, R. Wiesendanger, and M. Morgenstern, The Horiba-19$^{\text{th}}$ International Conference on "The Application of High Magnetic Fields in Semiconductor Physics and Nanotechnology" HMF-19, Fukuoka (Japan): *Real-Space Observation of Quantum Hall Transition*

13.9.2010: R. Wiesendanger, E-MRS 2010 Fall Meeting, Warsaw (Poland): *Multidimensional Characterization at the Nanometer Scale by Scanning Probe Methods*

14.9.2010: R. Wiesendanger, 10$^{\text{th}}$ Int. Conference on Nanostructured Materials NANO 2010, Rome (Italy): *Spin Mapping, Spin Manipulation, and Magnetometry at the Atomic Level*

20.9.2010: K. Hashimoto, C. Sohrmann, J. Wiebe, T. Inaoka, F. Meier, Y. Hirayama, R. A. Römer, R. Wiesendanger, and M. Morgenstern, 7$^{\text{th}}$ International Workshop on Disordered Systems, Puebla (Mexico): *Real-Space mapping of Landau quantization in a two-dimensional disordered system*

22.9.2010: J. Wiebe, 3$^{\text{rd}}$ Nordforsk Nanospintronics Workshop, Norköping (Sweden): *Magnetic Imaging and Excitation of Nanostructures Built from Individual Atoms*

30.9.2010: R. Wiesendanger, International Conference on Nanoscale Magnetism, ICNM 2010, Gebze (Turkey): *Spin Mapping, Spin Manipulation, and Magnetometry at the Atomic Level*

9.10.2010: J. Wiebe, 15$^{\text{th}}$ International Conference on Solid Films and Surfaces (ICSFS-15), Beijing (China): *Detecting excitation and magnetization of individual dopants in a semiconductor*

10.10.2010: R. Wiesendanger, 12$^{\text{th}}$ International Conference on Molecule-Based Magnets ICMM 2010, Beijing (China): *Spin-Dependent Tunneling through a Single Molecule with Intramolecular Resolution*

15.10.2010: R. Wiesendanger, Oak Ridge National Laboratory (Discovery Lecture), Oak Ridge (USA): *Atomic Spin Logic Devices*

20.10.2010: R. Wiesendanger, AVS 2010, Albuquerque (USA): *Atomic-Resolution Spin Mapping by Exploiting Magnetic Exchange Forces*

11.11.2010: R. Wiesendanger, Workshop on "Understanding Materials Using In-Situ Microscopy", Göttingen (Germany): *In-situ Scanning Probe Microscopy, Spectroscopy, and Manipulation with Atomic Resolution and Sensitivity at Variable Temperatures and Magnetic Fields*

18.11.2010: J. Wiebe, A.A. Khajetoorians, F. Meier, L. Zhou, B. Chilian, S. Lounis, S. Schuwalow, E.Y. Vedmedenko, S. Blügel, P.H. Dederichs, F. Lechermann and R.Wiesendanger, 55$^{\text{th}}$ Annual Conference on Magnetism and Magnetic Materials, Atlanta, Georgia (USA): *Imaging magnetic interactions in nanostructures built from individual adatoms.*

15.12.2010: O. Pietzsch, R. Wiesendanger, International Conference on Nano Materials and Nano Technology, Tiruchengode (India): *Non-Collinear Magnetic Order in Nanostructures Investigated by Spin-Polarized Scanning Tunneling Microscopy*

7.2 Conference Contributions and Talks at Other Institutes

7.2.1 Talks

15.1.2008: H. Fuchs, Ringvorlesung, Hamburg (Germany): *Nanotechnologie im Alltag mit Demonstrationen*

23.1.2008: R. Wiesendanger, Seminar MPI Physik komplexer Systeme, Dresden (Germany): *Dynamical processes in magnetic nanostructures studied by time- and spin-resolved scanning tunneling spectroscopy*

23.1.2008: A. Schwarz, Seminar Talk Kyoto University (H. Yamada Group), Kyoto (Japan): *Magnetic Exchange Force Microscopy*

7.2.2008: J. Wiebe, Seminar in the Photonics and Semiconductor Nanophysics group at the Eindhoven University of Technology, Eindhoven (The Netherlands): *Subkelvin spin polarized STM: measuring magnetization curves of individual adatoms*

8.2.2008: J. Wiebe, Seminar in the Photonics and Semiconductor Nanophysics group at the Eindhoven University of Technology, Eindhoven (The Netherlands): *Low-temperature scanning tunneling spectroscopy on individual Mn acceptors in InAs*

18.2.2008: S. Kuck, G. Hoffmann, and R. Wiesendanger, 72$^{\text{nd}}$ Spring Conference, Deutsche Physikalische Gesellschaft, Berlin (Germany): *Conformational study of FeTPC molecules on Cu(111) with STM*

22.2.2008: R. Wiesendanger, Seminar University of New South Wales, Sydney (Australia): *Spin mapping on the atomic scale*

25.2.2008: A. Kobs, D. Stickler, M. Scholz, G. Hoffmann, and H. P. Oepen, 72$^{\text{nd}}$ Spring Conference, Deutsche Physikalische Gesellschaft, Berlin (Germany): *Effects of Ga^+ irradiation on the magnetotransport in NiFe*

25.2.2008: G. Herzog, S. Krause, M. Bode, and R. Wiesendanger, 72$^{\text{nd}}$ Spring Conference, Deutsche Physikalische Gesellschaft, Berlin (Germany): *The Effect of Step Atoms on the Switching Behavior of Superparamagnetic Nanoislands*

25.2.2008: L. Zhou, F. Meier, J. Wiebe, and R. Wiesendanger, 72$^{\text{nd}}$ Spring Conference, Deutsche Physikalische Gesellschaft, Berlin (Germany): *Spin-polarized scanning tunneling spectroscopy on individual magnetic adatoms*

25.2.2008: U. Kaiser, A. Schwarz, and R. Wiesendanger, 72$^{\text{nd}}$ Spring Conference, Deutsche Physikalische Gesellschaft, Berlin (Germany): *Tip Effects in Magnetic Exchange Force Microscopy*

25.2.2008: M. Schult, N. Mikuszeit, E. Y. Vedmedenko, and R. Wiesendanger, 72nd Spring Conference, Deutsche Physikalische Gesellschaft, Berlin (Germany): *Magnetic ordering in 2 dimensional arrays of polarized particles with higher order multipole moments*

25.2.2008: A. Schumann, A. Remhof, A. Westphalen, H. Zabel, T. Last, U. Kunze, E. Y. Vedmedenko, and N. Mikuszeit, 72nd Spring Conference, Deutsche Physikalische Gesellschaft, Berlin (Germany): *Dipolar interactions on lateral structured square lattices*

25.2.2008: R. Wieser, E. Y. Vedmedenko, and R. Wiesendanger, 72nd Spring Conference, Deutsche Physikalische Gesellschaft, Berlin (Germany): *Computer experiments on standing spin wave resonances using Landau-Lifshitz-Gilbert dynamics*

25.2.2008: L. Zhou, F. Meier, J. Wiebe, and R. Wiesendanger, 72nd Spring Conference, Deutsche Physikalische Gesellschaft, Berlin (Germany): *Spin-polarized scanning tunneling spectroscopy on individual magnetic adatoms*

26.2.2008: A. Schwarz, U. Kaiser, R. Schmidt, R. Wiesendanger , 72nd Spring Conference, Deutsche Physikalische Gesellschaft, Berlin (Germany): *Advances in Magnetic Exchange Force Microscopy*

27.2.2008: S. Hankemeier, K. Sachse, Y. Stark, M. Scholz, G. Hoffmann, R. Frömter, and H. P. Oepen, 72nd Spring Conference, Deutsche Physikalische Gesellschaft, Berlin (Germany): *Nanowires for high DC current applications*

27.2.2008: A. Scarfato, S.-H. Chang, G. Hoffmann, and R. Wiesendanger, 72nd Spring Conference, Deutsche Physikalische Gesellschaft, Berlin (Germany): *Scanning Tunneling Microscopy Study of Iron(II) Phthalocyanine Growth on Metal and Insulating Surfaces*

27.2.2008: S. Krause, G. Herzog, M. Bode, and R. Wiesendanger, 72nd Spring Conference, Deutsche Physikalische Gesellschaft, Berlin (Germany): *Current-induced magnetization switching of thermally stable nanoislands*

28.2.2008: J. Brede, G. Hoffmann, and R. Wiesendanger, 72nd Spring Conference, Deutsche Physikalische Gesellschaft, Berlin (Germany): *A structural study of porphyrins interacting with a metallic surface*

28.2.2008: R. Schmidt, U. H. Pi, A. Schwarz, and R. Wiesendanger, 72nd Spring Conference, Deutsche Physikalische Gesellschaft, Berlin (Germany): *Fe/W(001) - a structurally, electronically and magnetically inhomogeneous system studied by force microscopy*

7.3.2008: J. Wiebe, Nanotechnology Seminar, Center for Nanoscale Science and Technology, National Institute of Standards and Technology, Gaithersburg (USA): *Revealing Magnetic Interactions From Single-Atom Magnetization Curves*

28.3.2008: K. von Bergmann, Seminar of Prof. M. Crommie, Department of Physics, University of California at Berkeley, USA, Berkeley (USA): *Complex magnetic structures on the atomic scale revealed by spin-polarized STM*

3.4.2008: K. von Bergmann, Condensed Matter Physics Seminar, Department of Physics, Stanford University, USA, Palo Alto (USA): *Complex magnetic structures on the atomic scale revealed by spin-polarized STM*

11.4.2008: K. von Bergmann, Condensed Matter Physics Seminar, Physics Department, Princeton University, USA, Princeton (USA): *Complex magnetic structures on the atomic scale revealed by spin-polarized STM*

12.4.2008: R. Wiesendanger, Bürgerdialog: Sichere Herstellung von Nanomaterialien, Hamburg (Germany): *Nanotechnologie in der Region Hamburg*

28.4.2008: R. Wiesendanger, University of Jena (Colloquium), Jena (Germany): *Neue Horizonte in der Festkörperforschung durch lokale Sondenmethoden*

2.5.2008: R. Wiesendanger, Ohio University (Colloquium), Athens, Ohio (USA): *New horizons in condensed matter physics by local probe techniques*

16.6.2008: R. Wiesendanger, RWTH Aachen (Colloquium), Aachen (Germany): *New horizons in condensed matter physics by local probe techniques*

25.6.2008: J. Wiebe, Nanoscale Science Department Seminar Max-Planck-Institute for Solid State Research, Stuttgart (Germany): *Probing single-atom magnetization curves: A method to detect magnetic interactions in nanostructures*

16.7.2008: M. Gyamfi, S. Meckler, O. Pietzsch, and R. Wiesendanger, NSS5/SP-STM2, Athens, Ohio (USA): *A new scanning tunneling microscope for spin-sensitive measurements in a fully rotatable magnetic field*

17.7.2008: S. Meckler, A. Preßler, M. Gyamfi, O. Pietzsch and R. Wiesendanger, NSS5/SP-STM2, Athens, Ohio (USA): *Bloch- or Néel-like walls in Fe double-layer nanowires*

17.7.2008: A. Schwarz, R. Schmidt, C. Lazo, V. Caciuc, H. Hölscher, S. Heinze, R. Wiesendanger, NSS5/SP-STM2, Athens, Ohio (USA): *Magnetic Exchange Force Microscopy: A force based spin sensitive method*

22.7.2008: F. Marczinowski, J. Wiebe, F. Meier, K. Hashimoto, R. Wiesendanger, International Conference on Nanoscience and Technology, Keystone, Colorado (USA): *Switching the charge of a single Mn-acceptor below InAs(110): STS study and simple model*

23.7.2008: R. Wiesendanger, International Conference on Nanoscience and Technology, Keystone, Colorado (USA): *Spin spiral states in low-dimensional magnets studied by low-temperature spin-polarized scanning tunneling spectroscopy*

23.7.2008: J. Brede, M. Linares, G. Hoffmann, and R. Wiesendanger, International Conference on Nanoscience and Technology, Keystone, Colorado (USA): *Molecular self-ordering on metallic substrates*

23.7.2008: S. Krause, G. Herzog, M. Bode, R. Wiesendanger, International Conference on Nanoscience and Technology, Keystone, Colorado (USA): *Current-induced Magnetization Switching of Thermally Stable Nanoislands Using SP-STM*

23.7.2008: S. Meckler, A. Preßler, M. Gyamfi, O. Pietzsch and R. Wiesendanger, International Conference on Nanoscience and Technology, Keystone, Colorado (USA): *Bloch- or Néel-like walls in Fe double-layer nanowires*

30.7.2008: R. Schmidt, C. Lazo, U. H. Pi, V. Caciuc, H. Hölscher, A. Schwarz, R. Wiesendanger and S. Heinze, European Conference on Surface Science (ECOSS 2008), Liverpool (UK): *Probing Fe/W(001) with magnetic exchange force microscopy*

12.9.2008: R. Wiesendanger, University of Basel (Colloquium), Basel (Switzerland): *New horizons in condensed matter physics by scanning probe techniques*

15.9.2008: R. Wiesendanger, 2nd Int. Summer School "Physics of Functional Micro- and Nanostructures", Hamburg (Germany): *Scanning Tunneling Microscopy and Spectroscopy*

16.9.2008: R. Wiesendanger, 2nd Int. Summer School "Physics of Functional Micro- and Nanostructures", Hamburg (Germany): *Scanning Force Microscopy and Spectroscopy*

16.9.2008: M. Ashino, D. Obergfell, S. Roth, S. Berber, D. Tomanek, R. Wiesendanger, 11th International Conference on Non-Contact Atomic Force Microscopy, Madrid (Spain): *Atomic-Resolution 3D Force and Damping Maps on Nanotube Peapods*

17.9.2008: R. Wieser, E. Y. Vedmedenko, and R. Wiesendanger, Joint European Magnetic Symposia (JEMS), Dublin (Ireland): *Standin spin waves in AFM spin systems*

18.9.2008: U. Kaiser, A. Schwarz, and R. Wiesendanger, Joint European Magnetic Symposia (JEMS), Dublin (Ireland): *Magnetic Exchange Force Microscopy with Atomic Resolution*

18.9.2008: L. Zhou, F. Meier, J. Wiebe, R. Wiesendanger, Joint European Magnetic Symposia (JEMS), Dublin (Ireland): *Revealing Magnetic Interactions from Single-Atom Magnetization Curves*

17.10.2008: R. Schmidt, GrK 611 "Design and Characterisation of Functional Materials" - Bonding 2008, Weissenhäuser Strand (Germany): *Magnetic Exchange Force Microscopy*

17.10.2008: J. Schwöbel, GrK 611 Workshop, Weißenhäuser Strand (Germany): *Approach towards molecular magnetism*

20.10.2008: K. Hashimoto, C. Sohrmann, J. Wiebe, T. Inaoka, Y. Hirayama, R. A. Roemer, R. Wiesendanger, and M. Morgenstern, The IEEE Nanotechnology Materials and Devices Conference, Kyoto (Japan): *Spatial Observation of Spin-Resolved Landau Levels on an Adsorbate-Induced Two-Dimensional Electron System*

25.10.2008: J. Wiebe, Symposium der Forschergruppe "Coherence and relaxation properties of electron spins", Dresden (Germany): *Probing single-atom magnetization curves: A method to detect low-energy magnetic interaction in nanostructures*

27.10.2008: R. Wiesendanger, TU Wien (Colloquium), Wien (Austria): *New horizons in condensed matter physics by scanning probe techniques*

30.10.2008: L. Zhou, 2nd Graduate-Class Workshop of the Graduietenkolleg 1286, Husum (Germany): *Revealing Magnetic Interactions from Single-Atom Magnetization Curves*

4.11.2008: R. Wiesendanger, MPI für Festkörperforschung (Colloquium), Stuttgart (Germany): *New horizons in condensed matter physics by scanning probe techniques*

12.11.2008: L. Zhou, F. Meier, J. Wiebe, and R. Wiesendanger, Seminar at the Nano Electronic Materials Research Group, the University of Texas at Austin, Austin, Texas (USA): *Oscillatory magnetic exchange coupling at the atomic level: a direct real-space study by a subkelvin spin-polarized STM*

25.11.2008: G. Hoffmann, Weekly Seminar, Osaka (Japan): *metal-organic complexes on metallic and insulating surfaces*

25.11.2008: A. Schwarz, Seminar Talk at UCL (Group of A. Shluger) , London (Great Britain): *From Single Molecules to Nanocrystalline Structures*

26.11.2008: R. Wiesendanger, Hanseatische Universitätsgespräche, Hamburg (Germany): *Nanotechnologie: Kleine Teile mit großer Wirkung*

7.12.2008: K. Hashimoto, C. Sohrmann, J. Wiebe, T. Inaoka, Y. Hirayama, R. A. Roemer, R. Wiesendanger, and M. Morgenstern, 13th Advanced Heterostructures and Nanostructures Workshop, Hawaii (USA): *Real space imaging of the quantum Hall transition*

9.12.2008: G. Hoffmann, Gemeinsames Kolloquium SFB 445, 491 und 616, Duisburg (Germany): *Metal-Organic Complexes in interaction with a surface*

10.12.2008: G. Hoffmann, internes Seminar, AG Wende, Duisburg (Germany): *STM investigation of Phthalocyanines: adsorption, electronic, and magnetic properties*

30.12.2008: G. Herzog, Graduate-Class Workshop GK1268, Husum (Germany): *Investigations of Superparamagnetic Nanoislands - Current Status*

6.1.2009: S.-H. Chang, Seminar, Division of Physics and Applied Physics, Nanyang Technological University, Singapore (Singapore): *Molecules on metals: A STM approach*

20.1.2009: K. Hashimoto, C. Sohrmann, J. Wiebe, T. Inaoka, F. Meier, Y. Hirayama, R. A. Römer, R. Wiesendanger, and M. Morgenstern, International Symposium on Nanoscale Transport and Technology, Atsugi (Japan): *Real-space imaging of quantum Hall transition*

22.1.2009: M. Ashino, Seminar at Departamento de Fisica Teorica de la Materia Condesada, Universidad Autonoma de Madrid , Madrid (Spain): *Unusual elastic and inelastic behaviors of carbon nanotubes due to molecular encapsulations: Dynamic force microscopy and spectroscopy studies.*

4.2.2009: R. Schmidt, GrK 611 "Design and Characterisation of Functional Materials" - Seminar, Hamburg (Germany): *Probing the Magnetic Exchange Forces of Iron on the Atomic Scale*

19.2.2009: J. Brede, S. Kuck, G. Hoffmann, R. Wiesendanger, Seminar FZ Jülich, Jülich (Germany): *The Physics of Molecule-Based TMR Spin Valves*

25.2.2009: R. Wiesendanger, 2nd MANA International Symposium, Tsukuba (Japan): *Perspectives of Nano-Spintronics*

26.2.2009: S.-H. Chang, Seminar, Research Center for Applied Sciences, Academia Sinica, Taipeh (Taiwan): *What we can learn from molecules? A STM approach*

23.3.2009: K. von Bergmann, S. Loth, M. Ternes, A. F. Otte, C. F. Hirjibehedin, C. P. Lutz, and A. J. Heinrich, 73rd Spring Conference, Deutsche Physikalische Gesellschaft, Dresden (Germany): *Spin-resolved excitations of single atoms with STM*

23.3.2009: E. Vedmedenko, J. Wiebe, and R. Wiesendanger, 73rd Spring Conference, Deutsche Physikalische Gesellschaft, Dresden (Germany): *Monte-Carlo study of hysteretic properties of atomic pairs and triplets*

23.3.2009: S. Meckler, A. Preßler, M. Gyamfi, O. Pietzsch and R. Wiesendanger, 73rd Spring Conference, Deutsche Physikalische Gesellschaft, Dresden (Germany): *Right rotating Néel type domain walls in the Fe double-layer on W(110)*

23.3.2009: J. Wiebe, L. Zhou, S. Lounis, E. Y. Vedmedenko, F. Meier, P. H. Dederichs, S. Blügel, and R. Wiesendanger, 73rd Spring Conference, Deutsche Physikalische Gesellschaft, Dresden (Germany): *Oscillatory indirect exchange in adatom pairs and triplets*

23.3.2009: S. Kuck, L. Lichtenstein, G. Hoffmann, R. Wiesendanger, 73rd Spring Conference, Deutsche Physikalische Gesellschaft, Dresden (Germany): *Electronic structure of FeTPC on Cu(111) vs Cu(100) investigated with STM and STS*

23.3.2009: M. Menzel, K. von Bergmann, A. Kubetzka, and R. Wiesendanger, 73rd Spring Conference, Deutsche Physikalische Gesellschaft, Dresden (Germany): *Periodic LDOS modulations in self-organized bi-atomic chains*

23.3.2009: A. Kubetzka, P. Ferriani, D. Serrate, Y. Yoshida, S.-W. Hla, M. Menzel, O. Ferdinand, K. von Bergmann, S. Heinze, and R. Wiesendanger, 73rd Spring Conference, Deutsche Physikalische Gesellschaft, Dresden (Germany): *Imaging single atom spins on a magnetic template*

23.3.2009: Y. Yoshida, D. Serrate, A. Kubetzka, M. Menzel, K. von Bergmann, and R. Wiesendanger, 73rd Spring Conference, Deutsche Physikalische Gesellschaft, Dresden (Germany): *Observation of spin-spiral magnetic order in 2 ML Mn/W(110)*

24.3.2009: E. Vedmedenko, T. Stapelfeldt, and R. Wiesendanger, 73rd Spring Conference, Deutsche Physikalische Gesellschaft, Dresden (Germany): *Splitting of the Curie temperature for two-dimensional anisotropic nanoparticles*

24.3.2009: S. Fremy, A. Schwarz, K. Lämmle, and R. Wiesendanger, 73rd Spring Conference, Deutsche Physikalische Gesellschaft, Dresden (Germany): *Formation of nanostructures by bimodal growth of a low symmetry magnetic molecule on a weakly interacting substrate*

25.3.2009: D. Serrate, Y. Yoshida, P. Ferriani, S.-W. Hla, M. Menzel, O. Ferdinand, K. von Bergmann, S. Heinze, A. Kubetzka, and R. Wiesendanger, 73rd Spring Conference, Deutsche Physikalische Gesellschaft, Dresden (Germany): *Spin polarized STM on an artificially engineered atomic structure*

25.3.2009: R. Schmidt, C. Lazo, U. Kaiser, A. Schwarz, S. Heinze, and R. Wiesendanger, 73rd Spring Conference, Deutsche Physikalische Gesellschaft, Dresden (Germany): *High Resolution 3D-Force-Field-Spectroscopy on Fe/W(001)*

25.3.2009: N. Mikuszeit, L. Baraban, E. Y. Vedmedenko, A. Erbe, P. Leiderer, and R. Wiesendanger, 73rd Spring Conference, Deutsche Physikalische Gesellschaft, Dresden (Germany): *Quasi-Antiferromagnetic* 120° *Néel-State in 2D Clusters of Dipole-Quadrupole-Interacting Particles Arranged on a Hexagonal Lattice*

25.3.2009: R. Wieser, E. Y. Vedmedenko, and R. Wiesendanger, 73rd Spring Conference, Deutsche Physikalische Gesellschaft, Dresden (Germany): *Quantized spin waves in ferromagnetic and antiferromagnetic systems with domain wall*

25.3.2009: K. Lämmle, A.Schwarz, M. Prosenc, and R. Wiesendanger, 73rd Spring Conference, Deutsche Physikalische Gesellschaft, Dresden (Germany): *Investigation of isolated single molecules on an insulating substrate*

26.3.2009: S. Krause, G. Herzog, L. Berbil-Bautista, M. Bode, and R. Wiesendanger, 73rd Spring Conference, Deutsche Physikalische Gesellschaft, Dresden (Germany): *Thermally Induced Magnetization Reversal of Fe/W(110) Nanoislands Investigated by SP-STM*

1.4.2009: R. Wiesendanger, nanoDE'09, Ulm (Germany): *Perspektiven der Nano-Spintronik*

6.4.2009: J. Brede, SpiDME Meeting 1/2009, Nijmegen (The Netherlands): *Real Space Observation of Molecular Frontier Orbitals*

7.4.2009: G. Hoffmann, Seminar IMM, Nijmegen (The Netherlands): *How innocent is an adsorbed molecule?*

20.4.2009: R. Wiesendanger, Seminar, Poznan (Poland): *New horizons in condensed matter physics by scanning probe techniques*

22.4.2009: R. Wiesendanger, Colloquium, Poznan (Poland): *Perspectives of Nano-Spintronics*

4.6.2009: J. Wiebe, International Symposium on Quantum Materials, Hamburg (Germany): *Low-Temperature Scanning Tunneling Spectroscopy on Individual Magnetic Dopants in III/V Semiconductors*

13.6.2009: R. Wiesendanger, Open Uni, Hamburg (Germany): *Magnetismus im Nanokosmos*

19.7.2009: J. Brede, S. Kuck, G. Hoffmann, P. Lazic, S. Blügel, R. Wiesendanger, and N. Atodiresei, 5th International Symposium on Scanning Probe Spectroscopy and Related Methods (SPS 09), Wasowo (Poland): *Resolving the interface magnetism of a molecule-based spin filter*

21.7.2009: M. Wasniowska, S. Schroeder, P. Ferriani, S. Heinze, 5$^{\text{th}}$ International Symposium on Scanning Probe Spectroscopy and Related Methods, Wasowo (Poland): *Observation of spin frustration in Cr on a triangular lattice*

24.7.2009: K. von Bergmann, S. Loth, M. Ternes, A. F. Otte, C. F. Hirjibehedin, C. P. Lutz, and A. J. Heinrich, 20$^{\text{th}}$ International Colloquium on Magnetic Films and Surfaces (ICMFS), Berlin (Germany): *Spin-resolved excitations of single atoms with scanning tunneling microscopy*

27.7.2009: Y. Yoshida, D. Serrate, A. Kubetzka, M. Menzel, K. von Bergmann, R. Wiesendanger, International Conference on Magnetism (ICM), Karlsruhe (Germany): *Observation of spin-spiral magnetic order and spin-orbit contrast in the 2nd monolayer Mn/W(110)*

29.7.2009: K. von Bergmann, Seminar talk in the group of K. Kern MPI Stuttgart, Stuttgart (Germany): *Complex magnetic structures on the atomic scale revealed by spin-polarized STM*

30.7.2009: S. Krause, G. Herzog and R. Wiesendanger, International Conference on Magnetism (ICM), Karlsruhe (Germany): *Current-Induced Magnetization Switching of Thermally Quasistable Nanoislands Using SP-STM*

6.8.2009: A. Schwarz, Seminar Talk at Princeton University (Group of A. Yazdani), Princeton, NJ (USA): *New Developments in the Field of Magnetic Exchange Force Microscopy*

12.8.2009: S. Fremy, A. Schwarz, K. Lämmle, R. Wiesendanger, and M. Prosenc, 12$^{\text{th}}$ International Conference on Non-Contact Atomic Force Microscopy, New Haven, CT (USA): *Steering the formation of molecular nanowires and compact nanocrystallites on NaCl(001)*

12.8.2009: M. Ashino, R. Wiesendanger, A. N. Khlobystov, S. Berber, and D. Tománek, 12$^{\text{th}}$ International Conference on Non-Contact Atomic Force Microscopy, New Haven (CT) (USA): *Atomic-Resolution Damping Force Spectroscopy on Nanotube Peapods with Different Tube Diameters*

14.9.2009: G. Hoffmann, Seminar AG Bauer, University of Kiel, Kiel (Germany): *From molecular magnetism to the tailoring of substrates*

18.9.2009: A. Schwarz, 3$^{\text{rd}}$ International Summer School on Physics of Functional Micro- and Nanostructures , Hamburg (Germany): *Scanning Force Microscopy and Spectroscopy*

14.10.2009: G. Hoffmann, GrK 611 Workshop, Weißenhäuser Strand (Lübeck): *Understanding and Designing Molecular Magnetism*

26.10.2009: F. Meier, Seminar at Max-Planck Institute, Halle (Germany): *Mapping of Magnetism in Adatom Nanostructures by Spin-Polarized STM*

30.10.2009: L. Zhou, 3rd Graduate-Class Workshop of the Graduiertenkolleg 1286, Schwerin (Germany): *Strength and Directionality of Surface RKKY-Interaction Mapped on the Atomic Scale*

5.11.2009: G. Hoffmann, Colloquium Ohio University, Athens (USA): *The Quest For Molecular Magnetism*

9.11.2009: S.-H. Chang, K. Clark, A. Dilullo, S. Kuck, S.-W. Hla, G. Hoffmann, R. Wiesendanger, AVS 2009, San Jose (USA): *Surface Supported Chain Formation of Magnetic Molecules*

9.11.2009: J. Brede, S. Kuck, G. Hoffmann, P. Lazic, S. Blügel, R. Wiesendanger, N. Atodiresei, AVS 2009, San Jose (USA): *Resolving the Interface Magnetism of a Molecule-Based Spin Filter*

13.11.2009: R. Wiesendanger, SFB602-Seminar, Göttingen (Germany): *Spin mapping and spin manipulation on the atomic scale*

20.11.2009: H. Fuchs, Lehrerweiterbildung, Hamburg (Germany): *Außerschulische Lernpartner und Schulen im Dialog*

23.11.2009: G. Hoffmann and R. Wiesendanger, EU Spidme Meeting, Dublin (Ireland): *Status of SPSTM applied to molecular systems*

23.11.2009: R. Wiesendanger, DESY Science Corridor Symposium, Hamburg (Germany): *Nanoscience research facilities at the University of Hamburg*

2.12.2009: R. Wiesendanger, MIT (Seminar), Cambridge (USA): *Spin mapping and magnetometry at the atomic level*

6.1.2010: M. Wasniowska, Seminar in Solid State Physics,AGH University of Science and Technology, Krakow (Poland): *Real space observation of spin frustration in Cr on a triangular lattice*

14.1.2010: R. Wiesendanger, Magnus-Haus (Colloquium), Berlin (Germany): *Faszinierende magnetische Phänomene im Nanokosmos*

15.1.2010: G. Hoffmann, Sonderseminar des SFB 767, Konstanz (Germany): *The Quest for Molecular Magnetism*

18.1.2010: R. Wiesendanger, Workshop on Nanoelectronics, Bad Honnef (Germany): *Spin-resolved electron transport through magnetic nanostructures studied by a low-temperature multiprobe-STM*

12.2.2010: H. Fuchs, Naturwissenschaftliche Fachtagung für Lehrer, Hamburg (Germany): *Nanotechnik als Anwendungsgebiet für die Profiloberstufe*

3.3.2010: B. Chilian, A. Khajetoorians, J. Wiebe, S. Schuwalow, F. Lechermann, and R. Wiesendanger, LEXI–Workshop "NANOSPINTRONICS", Hamburg (Germany): *Determining the magnetism of single atoms on a semiconductor surface*

3.3.2010: R. Schmidt, LEXI–Workshop "NANOSPINTRONICS", Hamburg (Germany): *Magnetic Exchange Force Microscopy*

4.3.2010: L. Zhou, LEXI–Workshop "NANOSPINTRONICS", Hamburg (Germany): *Using single-atom magnetization curves to study magnetic interaction*

4.3.2010: B. Wolter, LEXI–Workshop "NANOSPINTRONICS", Hamburg (Germany): *Study on Automated Atom Manipulation*

8.3.2010: J. Wiebe, Seminar "Kondensierte Materie", Gruppe Prof. M. Morgenstern, II. Physikalisches Institut B, RWTH Aachen, Aachen (Germany): *Probing the spin-state of individual quantum magnets embedded in a semiconductor*

9.3.2010: A.A. Khajetoorians, B. Chilian, J. Wiebe, S. Schuwalow, F. Lechermann, R. Wiesendanger, UCI Seminar, Wilson Ho Group, Irvine (USA): *Probing the spin-state of individual quantum magnets embedded in a semiconductor*

9.3.2010: K. Hashimoto, C. Sohrmann, J. Wiebe, T. Inaoka, F. Meier, Y. Hirayama, R. A. Römer, R. Wiesendanger, and M. Morgenstern, International Symposium on Quantum Nanostructures and Spin-related Phenomena, Tokyo (Japan): *Scanning tunneling Spectroscopy of wave functions in the integer quantum Hall regime*

14.3.2010: A.A. Khajetoorians, B. Chilian, J. Wiebe, S. Schuwalow, F. Lechermann, R. Wiesendanger, APS March Meeting 2010, Portland (USA): *Probing the spin-state of individual quantum magnets embedded in a semiconductor*

18.3.2010: A. DiLullo, K. Clark, S.-W. Hla, S.-H. Chang, S. Kuck, G. Hoffman, R. Wiesendanger, 2010 APS March Meeting, Portland, Oregon (USA): *Surface Supported Formation of Magnetic Molecular Chains*

20.3.2010: Y, Yoshida, D. Serrate, P. Ferriani, S. H. Hla, M. Menzel, K. v. Bergmann, S. Heize, A. Kubetzka, R. Wiesendanger, 65$^{\text{th}}$ Annual meeting, The physical society of Japan, Okayama (Japan): *Imaging and Manipulating the Spin Direction of Individual Atoms*

22.3.2010: R. Schmidt, U. Kaiser, A. Schwarz, and R. Wiesendanger , 74$^{\text{th}}$ Spring Conference, Deutsche Physikalische Gesellschaft, Regensburg (Germany): *Measuring the distance dependence of the magnetic exchange interaction across a vacuum gap*

23.3.2010: F. Meier, L. Zhou, J. Wiebe, and R. Wiesendanger, 74$^{\text{th}}$ Spring Conference, Deutsche Physikalische Gesellschaft, Regensburg (Germany): *Range of spin-polarization on the (111) surface of platinum induced by the proximity of cobalt stripes*

23.3.2010: M. Gyamfi, T. Eelbo, M. Wasniowska, O. Pietzsch, R. Wiesendanger, 74$^{\text{th}}$ Spring Conference, Deutsche Physikalische Gesellschaft, Regensburg (Germany): *Electronic structure of graphene on Ru(0001) studied with STS*

24.3.2010: R. Wieser, E. Y. Vedmedeko, and R. Wiesendanger, 74$^{\text{th}}$ Spring Conference, Deutsche Physikalische Gesellschaft, Regensburg (Germany): *Domain wall motion damped by the emission of spin waves*

25.3.2010: S. Krause, G. Herzog, A. Emmenegger, R. Wiesendanger, 74$^{\text{th}}$ Spring Conference, Deutsche Physikalische Gesellschaft, Regensburg (Germany): *Critical Current for Switching the Magnetization of Quasistable Nano-Islands Using SP-STM*

25.3.2010: L. Zhou, F. Meier, J. Wiebe, and R. Wiesendanger, 74$^{\text{th}}$ Spring Conference, Deutsche Physikalische Gesellschaft, Regensburg (Germany): *Inversion of Spin Polarization above Magnetic Adatoms*

25.3.2010: S. Pütter, M. R. R. Azad, N. Mikuszeit, M. Bubek, G. Hoffmann, and H. P. Oepen, 74$^{\text{th}}$ Spring Conference, Deutsche Physikalische Gesellschaft, Regensburg (Germany): *Anisotropies of permalloy elements in multidomain states*

25.3.2010: J. Brede, N. Atodiresei, S. Kuck, P. Lasic, S. Blügel, G. Hoffmann, R. Wiesendanger, 74$^{\text{th}}$ Spring Conference, Deutsche Physikalische Gesellschaft, Regensburg (Germany): *Resolving the interface magnetism of a molecule-based spin filter*

25.3.2010: B. Chilian, A. Khajetoorians, J. Wiebe, S. Schuwalow, F. Lechermann, and R. Wiesendanger, 74$^{\text{th}}$ Spring Conference, Deutsche Physikalische Gesellschaft, Regensburg (Germany): *Determining the Magnetism of Single Atoms on a Semiconductor Surface*

25.3.2010: M. Menzel, S. Heinze, K. von Bergmann, G. Bihlmayer, A. Kubetzka, S. Blügel, and R. Wiesendanger, 74$^{\text{th}}$ Spring Conference, Deutsche Physikalische Gesellschaft, Regensburg (Germany): *Two-dimensional non-collinear magnetic ground state in the Fe monolayer on Ir(111)*

25.3.2010: A. Emmenegger, G. Herzog, S. Krause, and R. Wiesendanger, 74$^{\text{th}}$ Spring Conference, Deutsche Physikalische Gesellschaft, Regensburg (Germany): *Cr Bulk Tips for Spin Polarized Scanning Tunneling Microscopy with both In-plane and Out-of-plane Sensitivity*

25.3.2010: G. Herzog, S. Krause, A. Schlenhoff, and R. Wiesendanger, 74$^{\text{th}}$ Spring Conference, Deutsche Physikalische Gesellschaft, Regensburg (Germany): *Heat assisted Spin Torque Switching of Nanomagnets by SP-STM*

25.3.2010: Y. Yoshida, Applied quantum physics seminar (Kyushu University), Fukuoka (Japan): *Imaging and Manipulating the Spin Direction of Individual Atoms*

9.4.2010: L. Zhou, Seminar talk at State Key Laboratory of Functional Materials for Informatics, Shanghai Institute of Microsystem and Information Technology, Chinese Academy of Sciences, Shanghai (China): *Mapping Single-Atom Magnetism by Spin-Polarized STM*

12.4.2010: L. Zhou, Seminar talk at Magnetic Ultrathin Film Group, Physics Department, Fudan University, Shanghai (China): *Mapping Single-Atom Magnetism by Spin-Polarized STM*

5.5.2010: R. Wiesendanger, TU Chemnitz (Colloquium), Chemnitz (Germany): *Faszinierende magnetische Phänomene im Nanokosmos*

10.5.2010: R. Wiesendanger, University of Marburg (Colloquium), Marburg (Germany): *Spinabbildung, Spinmanipulation und Magnetometrie auf atomarer Skala*

18.5.2010: R. Wieser, Hitachi GST Seminar, San Jose (USA): *Thermodynamic behavior of domain wall configurations, nanoparticles and spin waves.*

20.5.2010: R. Wiesendanger, University of Hamburg (Bioinformatics Seminar), Hamburg (Germany): *Molecules on surfaces: A challenging hybrid system*

25.5.2010: J. Brede, N. Atodiresei, S. Kuck, P. Lasic, S. Blügel, G. Hoffmann, and R. Wiesendanger, TSN2010, Lecce (Italy): *Resolving the interface magnetism of a molecule based spin filter*

27.5.2010: A. Dilullo, K. Clark, S.-H. Chang, G. Hoffmann, R. Wiesendanger, and S.-W. Hla, TSN 2010, Lecce (Italy): *Surface Supported Formation of Magnetic Molecular Chains*

31.5.2010: K. Hashimoto, C. Sohrmann, J. Wiebe, T. Inaoka, F. Meier, Y. Hirayama, R. A. Römer, R. Wiesendanger, and M. Morgenstern, The 37$^{\text{th}}$ International Symposium on Compound Semiconductors, Takamatsu (Japan): *Scanning Tunneling Spectroscopy of a Surface Two-Dimensional Electron System in High Magnetic Field*

10.6.2010: F. Meier, Seminar FOR1162, Würzburg University, Würzburg (Germany): *Magnetic interactions on the (111) surface of platinum probed by SP-STM*

11.6.2010: R. Wiesendanger, Nanodays of the University of Hamburg, Hamburg (Germany): *Magnetismus im Nanokosmos*

15.6.2010: A. Schwarz, Physikalisches Kolloquium der Universität Regensburg, Regensburg (Germany): *Magnetic Sensitive Force Microscopy: Mapping Magnetic Domains, Flux Line Lattices and Atomic-Scale Spin Structures*

30.6.2010: R. Wiesendanger, University of Duisburg (Colloquium), Duisburg (Germany): *Spinabhängiges Tunneln durch Einzelatome und Moleküle*

9.7.2010: A. A. Khajetoorians, CIN2 Seminar (Campus UAB, Barcelona), Barcelona (Spain): *Single atom spin detection of quantum magnets embedded in a semiconductor*

14.7.2010: M. Menzel, Y. Mokrousov, R. Wieser, A. Kubetzka, S. Heinze, E. Vedmedenko, K. von Bergmann, and R. Wiesendanger, Theorie I Seminar, Institut für Festkörperforschung Forschungszentrum Jülich, Jülich (Germany): *Complex magnetism in bi-atomic Fe chains on (5×1)-reconstructed Ir(001)*

25.7.2010: A.A. Khajetoorians, B. Chilian, J. Wiebe, S. Schuwalow, F. Lechermann, and R. Wiesendanger, ICPS-30, Seoul (Korea): *Probing the spin-state of individual quantum magnets embedded in a semiconductor*

1.8.2010: A.A. Khajetoorians, B. Chilian, J. Wiebe, S. Schuwalow, F. Lechermann, and R. Wiesendanger, PASPS-VI, Tokyo (Japan): *Probing the spin-state of individual quantum magnets embedded in a semiconductor*

2.8.2010: K. Lämmle, A. Schwarz, and R. Wiesendanger, 13th International Conference on Non-Contact Atomic Force Microscopy, Kanazawa (Japan): *Determination of the Adsorption Geometry of Co-Salen on Bulk NaCl(001) with Atomic Resolution*

3.8.2010: A. Schwarz, R. Schmidt, C. Lazo, U. Kaiser, S. Heinze, and R. Wiesendanger, 13$^{\text{th}}$ International Conference on Non-Contact Atomic Force Microscopy, Kanazawa (Japan): *Magnetic Exchange Force Spectroscopy with Atomic Resolution*

18.8.2010: M. Menzel, S. Heinze, K. von Bergmann, G. Bihlmayer, A. Kubetzka, S. Blügel, and R. Wiesendanger, SP-STM3, Seoul (Republic of Korea): *Atomic-scale magnetic skyrmion lattice observed in real space*

19.8.2010: S. Krause, G. Herzog, A. Schlenhoff, and R. Wiesendanger, SP-STM3, Seoul (Republic of Korea): *Critical current for switching the magnetization of quasistable nano-islands using SP-STM*

19.8.2010: A. Schlenhoff, S. Krause, G. Herzog, and R. Wiesendanger, SP-STM3, Seoul (Republic of Korea): *Bulk Cr tips with full spatial magnetic sensitivity for spin-polarized scanning tunneling microscopy*

20.8.2010: G. Herzog, S. Krause, A. Schlenhoff, and R. Wiesendanger, SP-STM3, Seoul (Republic of Korea): *Spin Torque Switching of Nanomagnets by SP-STM*

23.8.2010: F. Meier, L. Zhou, J. Wiebe, and R. Wiesendanger, International Conference on Nanoscience and Technology, Beijing (China): *Interplay between spin polarization and RKKY interaction on the (111) surface of platinum near cobalt nanostripes*

24.8.2010: S. Krause, G. Herzog, A. Schlenhoff, and R. Wiesendanger, International Conference on Nanoscience and Technology, Beijing (China): *Critical current for switching the magnetization of quasistable nano-islands using SP-STM*

24.8.2010: A. Schlenhoff, S. Krause, G. Herzog, and R. Wiesendanger, International Conference on Nanoscience and Technology, Beijing (China): *Cr bulk tips for SP-STM with both in-plane and out-of-plane sensitivity*

24.8.2010: G. Herzog, S. Krause, A. Schlenhoff, and R. Wiesendanger, International Conference on Nanoscience and Technology, Beijing (China): *Spin Torque Switching of Nanomagnets by SP-STM*

25.8.2010: B. Chilian, A. A. Khajetoorians, J. Wiebe, S. Schuwalow, F. Lechermann, and R. Wiesendanger, International Conference on Nanoscience and Technology, Beijing (China): *Spin resolved detection of tunneling electrons scattered off a quantum magnet in a semiconductor*

25.8.2010: J. Brede, N. Atodiresei, S. Kuck, P. Lazic, V. Caciuc, S. Blügel, G. Hoffmann and R. Wiesendanger, International Conference on Nanoscience and Technology, Beijing (China): *Spin-dependent tunneling through a single molecule with intramolecular resolution*

26.8.2010: S. Heinze, K. von Bergmann, M. Menzel, A. Kubetzka, R. Wiesendanger, G. Bihlmayer, and S. Blügel, International Conference on Nanoscience and Technology, Beijing (China): *Microscopic origin of the atomic-scale magnetic skyrmion lattice of Fe/Ir(111)*

26.8.2010: A. Kubetzka, D. Serrate, P. Ferriani, Y. Yoshida, S.-W. Hla, M. Menzel, K. von Bergmann, S. Heinze, and R. Wiesendanger, International Conference on Nanoscience and Technology, Beijing (China): *Spin-direction and orbital symmetry of magnetic adatoms on a magnetic surface investigated by SP-STM*

26.8.2010: M. Menzel, S. Heinze, K. von Bergmann, G. Bihlmayer, A. Kubetzka, S. Blügel, and R. Wiesendanger, International Conference on Nanoscience and

Technology, Beijing (China): *Atomic-scale magnetic skyrmion lattice observed in real space*

26.8.2010: A. Schwarz, R. Schmidt, U. Kaiser, and R. Wiesendanger , International Conference on Nanoscience and Technology, Beijing (China): *Magnetic Exchange Force Spectroscopy with Atomic Resolution*

30.8.2010: K. Hashimoto, International Symposium "Advanced functionality with three-dimensionally controlled quantum structures", Potsdam (Germany): *Imaging of wave functions in high Landau levels*

31.8.2010: S. Modesti, H. Gutzmann, J. Wiebe, R. Wiesendanger, G. Profeta, and E. Tosatti, 27$^{\text{th}}$ European Conference on Surface Science (ECOSS 27), Groningen (Netherlands): *Intrinsic low temperature insulating state of Si(111)-7x7*

31.8.2010: S. Modesti, H. Gutzmann, J. Wiebe, R. Wiesendanger, G. Profeta, and E. Tosatti, 27$^{\text{th}}$ European Conference on Surface Science (ECOSS 27), Groningen (Netherlands): *Searching for spin correlations in the low temperature insulating state of the Sn/Si(111)-$\sqrt{3} \times \sqrt{3}$ R30°*

2.9.2010: A. A. Khajetoorians, Condensed Matter Seminar (UC Berkeley), Berkeley, CA (USA): *Single atom spin detection of quantum magnets embedded in a semiconductor*

15.9.2010: J. Wiebe, 4$^{\text{th}}$ Int. Summer School "Physics of Functional Micro- and Nanostructures", Hamburg (Germany): *Scanning Tunneling Microscopy (STM) and Spectroscopy (STS) on III-V semiconductors*

16.9.2010: R. Wiesendanger, 4$^{\text{th}}$ Int. Summer School "Physics of Functional Micro- and Nanostructures", Hamburg (Germany): *Scanning Force Microscopy and Spectroscopy*

17.9.2010: J. Wiebe, 4$^{\text{th}}$ Int. Summer School "Physics of Functional Micro- and Nanostructures", Hamburg (Germany): *Spin-Resolved Scanning Tunneling Spectroscopy (SPSTS): from thin ferromagnetic films to atomic scale devices*

21.9.2010: K. von Bergmann, General Physics Colloquium, University of Aarhus, Aarhus (Denmark): *Complex magnetic order on the atomic scale revealed by spin-polarized STM*

13.10.2010: J. Schwöbel, Seminar AG Blügel, FZ Jülich, Jülich (Germany): *Spin-sensitive tunneling through individual Terbium-Pc2 Molecules by Spin-polarized STM*

14.10.2010: G. Herzog, S. Krause, A. Schlenhoff, and R. Wiesendanger, Graduate-Class 1286 Workshop, Jever (Germany): *Heat Assisted Spin Torque Switching of Nanomagnets by SP-STM*

15.10.2010: Y. Yoshida, Nanoscience seminar (ISSP, University of Tokyo), Kashiwa (Japan): *Imaging and Manipulating the Spin Direction of Individual Atoms*

18.10.2010: R. Wiesendanger, Los Alamos National Laboratory (Seminar), Los Alamos (USA): *Atomic Spin Logic Devices*

19.10.2010: A.A. Khajetoorians, Workshop on Quantum Spintronics, Maratea (Italy): *Detecting excitation and magnetization of individual dopants in a semiconductor*

16.11.2010: R. Wiesendanger, Ilmenau University (Colloquium), Ilmenau (Germany): *Von der Nanophysik zu atomaren Bauelementen*

16.11.2010: A. Schwarz, Seminar Talk at the Johannes Gutenberg Universität Mainz (AG A. Kühnle), Mainz (Germany): *Magnetic Molecules on Bulk Insulators*

24.11.2010: J. Wiebe, Seminar in Solid State Physics, Physik Institut, Universität Zürich, Zürich (Germany): *Magnetic Imaging and Excitation of Nanostructures Built from Individual Atoms*

16.12.2010: S. Krause, Verständliche Wissenschaft 2010, Helmholtz Zentrum Geesthacht, Geesthacht (Germany): *Wie schreibt man die Weltliteratur auf eine Briefmarke? Von tunnelnden Spins und magnetischen Inseln zur neuartigen Festplatte.*

7.2.2 Posters

7.1.2008: R. Wieser, E. Y. Vedmedenko and R. Wiesendanger, Dreikönigstreffen Magnetismus ´08 New Concepts in Spin Dynamics, Bad Honnef (Germany): *Computer experiments on standing spin wave resonances using Landau-Lifshitz-Gilbert dynamics*

25.2.2008: F. Marczinowski, F. Meier, J. Wiebe, and R. Wiesendanger, 72$^{\text{nd}}$ Spring Conference, Deutsche Physikalische Gesellschaft, Berlin (Germany): *Switching the Charge of a Single Mn-Dopant in InAs with the STM in Experiment and Model*

26.2.2008: M. Prostak, G. Hoffmann, and R. Wiesendanger, 72$^{\text{nd}}$ Spring Conference, Deutsche Physikalische Gesellschaft, Berlin (Germany): *Design of a vacuum system for the local study of molecules*

26.2.2008: A. Emmenegger, S. Krause, G. Herzog, A. Kubetzka, D. Haude, and R. Wiesendanger, 72$^{\text{nd}}$ Spring Conference, Deutsche Physikalische Gesellschaft, Berlin (Germany): *Spin-dependent Image Potential States Studied By SP-STS*

26.2.2008: T. Eelbo, M. Gyamfi, S. Meckler, O. Pietzsch, and R. Wiesendanger, 72nd Spring Conference, Deutsche Physikalische Gesellschaft, Berlin (Germany): *Development of an UHV Variable Temperature STM*

26.2.2008: M. Menzel, D. Haude, K. von Bergmann, M. Bode, and R. Wiesendanger, 72nd Spring Conference, Deutsche Physikalische Gesellschaft, Berlin (Germany): *Design of an UHV-STM for applications at low temperatures and high magnetic fields*

26.2.2008: H. von Allwörden, A. Schwarz, C.Julian Chen, and R. Wiesendanger, 72nd Spring Conference, Deutsche Physikalische Gesellschaft, Berlin (Germany): *Self-actuating self-sensing cantilever for dynamic AFM*

26.2.2008: H. Gutzmann, A. Stemmann, F. Adler, J. Wiebe, F. Marczinowski, C. Heyn, W. Hansen, and R. Wiesendanger, 72nd Spring Conference, Deutsche Physikalische Gesellschaft, Berlin (Germany): *STM investigation of MBE-grown GaMnAs*

26.2.2008: N. Mikuszeit, M. Schult, E. Y. Vedmedenko, and R. Wiesendanger, 72nd Spring Conference, Deutsche Physikalische Gesellschaft, Berlin (Germany): *Analytic formulae for multipole moments of general ellipsoids, elliptic cylinders and prisms*

26.2.2008: O. Ferdinand, K. von Bergmann, A. Kubetzka, R. Wiesendanger, 72nd Spring Conference, Deutsche Physikalische Gesellschaft, Berlin (Germany): *Einfluss der elektronischen Struktur der Tunnelspitze auf spektroskopische Messungen*

26.2.2008: M. Gyamfi, S. Meckler, O. Pietzsch and R. Wiesendanger, 72nd Spring Conference, Deutsche Physikalische Gesellschaft, Berlin (Germany): *A New Scanning Tunneling Microscope for Spin-Sensitive Measurements in Ultrahigh Vacuum, at Low Temperatures, and in High Magnetic Fields*

26.2.2008: K. von Bergmann, P. Ferriani, E.Y. Vedmedenko, A. Kubetzka, S. Heinze, and R. Wiesendanger , 72nd Spring Conference, Deutsche Physikalische Gesellschaft, Berlin (Germany): *Observation of a spin spiral state in the Mn monolayer on W(001)*

27.2.2008: S.-H. Chang, A. Scarfato, G. Hoffmann, and R. Wiesendanger, 72nd Spring Conference, Deutsche Physikalische Gesellschaft, Berlin (Germany): *Scanning tunneling microscope study of Fe, Co, and Cu- Phthalocyanine growth on metal surfaces*

27.2.2008: J. Schwöbel, M. Nohme, R. Ravlic, J. Wienhausen, G. Hoffmann, and R. Wiesendanger, 72nd Spring Conference, Deutsche Physikalische Gesellschaft,

Berlin (Germany): *Design and construction of a 300 mKelvin / 17 Tesla ultra-high vacuum scanning tunneling microscope for molecular studies*

27.2.2008: G. Hoffmann, S. Kuck, J. Brede, and R. Wiesendanger, 72nd Spring Conference, Deutsche Physikalische Gesellschaft, Berlin (Germany): *STM / STS investigation of porphyrin and corrole molecules on surfaces*

27.2.2008: J. Wochnowski, T. Göllnitz, G. Hoffmann, R. Wiesendanger, and J. Heck, 72nd Spring Conference, Deutsche Physikalische Gesellschaft, Berlin (Germany): *Metal coatings prepared by organometallic chemical vapour deposition (OMCVD)*

16.7.2008: G. Herzog, S. Krause, L. Berbil-Bautista, T. Stapelfeldt, E. Vedmedenko, M. Bode, and R. Wiesendanger, NSS5/SP-STM2, Athens, Ohio (USA): *Observing the Thermal Switching Behavior of Superparamagnetic Nanoislands by SP-STM*

22.7.2008: R. Schmidt, C. Lazo, U. H. Pi, V. Caciuc, H. Hölscher, A. Schwarz, R. Wiesendanger and S. Heinze, International Conference on Nanoscience and Technology, Keystone, Colorado (USA): *Probing Fe/W(001) with magnetic and exchange force microscopy*

22.7.2008: M. Gyamfi, S. Meckler, O. Pietzsch, and R. Wiesendanger, International Conference on Nanoscience and Technology, Keystone, Colorado (USA): *A New Scanning Tunneling Microscope for Spin-Sensitive Measurements in a Fully Rotatable Magnetic Field*

22.7.2008: G. Herzog, S. Krause, L. Berbil-Bautista, T. Stapelfeldt, E. Vedmedenko, M. Bode, and R. Wiesendanger, International Conference on Nanoscience and Technology, Keystone, Colorado (USA): *Observing the Thermal Switching Behavior of Superparamagnetic Nanoislands by SP-STM*

11.9.2008: M. Menzel, K. von Bergmann, A. Kubetzka, M. Bode, and R. Wiesendanger, Summer School "Nanomagnetism and Spintronics", Prague (Czech Republic): *Scanning tunneling microscopy and spectroscopy of self-organized bi-atomic Fe chains on Ir(001)*

11.9.2008: G. Herzog, L. Zhou, S. Krause, F. Meier, J. Wiebe, and R. Wiesendanger, 2nd International Summer School of the GrK "Physics of Functional Micro- and Nanostructures", Hamburg (Germany): *Spin-Polarized Scanning Tunneling Microscopy and Spectroscopy*

15.9.2008: K. Lämmle, S. Fremy, A. Schwarz and R. Wiesendanger, 11th International Conference on Non-Contact Atomic Force Microscopy, Madrid (Spain): *Crystallites and Wires of Co-Salene on NaCl(001)*

21.9.2008: J. Brede, G. Hoffmann, and R. Wiesendanger, ICMM 2008 - International Conference on Molecule-based Magnets, Florence (Italy): *Local Investigation of Paramagnetic Molecular Model Systems*

28.9.2008: S. Kuck, J. Brede, S.-H. Chang, G. Hoffmann, and R. Wiesendanger, SONS Workshop Magnetism at Surfaces, Baden-Baden (Germany): *Adsorption and Agglomeration of Paramagnetic Metalloporphyrinoid.*

8.10.2008: R. Wieser, E. Y. Vedmedenko, and R. Wiesendanger, International Workshop on Quantum Transport in Nanostructures, Hamburg (Germany): *Quantized spin waves in antiferromagnetic spin systems*

24.3.2009: B. Chilian, A. Khajetoorians, J. Wiebe, and R. Wiesendanger, 73$^{\text{rd}}$ Spring Conference, Deutsche Physikalische Gesellschaft, Dresden (Germany): *Design of an XSTM head for low temperature high magnetic field studies of III-V heterostructures*

24.3.2009: A. Emmenegger, S. Krause, A. Kubetzka, G. Herzog, and R. Wiesendanger, 73$^{\text{rd}}$ Spring Conference, Deutsche Physikalische Gesellschaft, Dresden (Germany): *High Order Field Emission Resonances on W(110) and Fe/W(110) studied by Scanning Tunneling Spectroscopy*

25.3.2009: L. Lichtenstein, S. Kuck, G. Hoffmann, R. Wiesendanger, 73$^{\text{rd}}$ Spring Conference, Deutsche Physikalische Gesellschaft, Dresden (Germany): *Adsorption geometry and self assembly of corrole molecules on different copper facets*

25.3.2009: S.-H Chang, J. Brede, J. Schwöbel, S. Kuck, G. Hoffmann, R. Wiesendanger, 73$^{\text{rd}}$ Spring Conference, Deutsche Physikalische Gesellschaft, Dresden (Germany): *Adsorption of metal phthalocyanines on Cu(111) and Cu(100): A STM study*

27.3.2009: T. Stapelfeldt, E. Vedmedenko, S. Krause, G. Herzog, and R. Wiesendanger, 73$^{\text{rd}}$ Spring Conference, Deutsche Physikalische Gesellschaft, Dresden (Germany): *Superparamagnetic switching of two-dimensional magnetic islands studied by Monte Carlo simulation*

19.7.2009: S.-H. Chang, J. Brede, J. Schwöbel, S. Kuck, G. Hoffmann, and R. Wiesendanger, SPS 09, Poznan (Poland): *Adsorption of metal phthalocyanines on Cu(111) and Cu(100): A STM study*

19.7.2009: L. Lichtenstein, S. Kuck, G. Hoffmann, and R. Wiesendanger, SPS 09, Poznan (Poland): *Adsorption, self assembly, and electronic states of corrole molecules adsorbed on different copper facets*

20.7.2009: S. Pütter, N. Mikuszeit, M. Scholz, H. Stillrich, E. Y. Vedmedenko, G. Hoffmann, H. P. Oepen, 20$^{\text{th}}$ International Colloquium on Magnetic Films

and Surfaces (ICMFS), Berlin (Germany): *The influence of the real shape on the magnetostatic interaction and shape anisotropy in periodic arrays of permalloy nanostructures*

22.7.2009: S. Schroeder, M. Wasniowska, P. Ferriani and S. Heinze , 20$^{\text{th}}$ International Colloquium on Magnetic Films and Surfaces , Berlin (Germany): *Topological spin frustration of Cr monolayer on Pd(111)*

23.7.2009: R. Schmidt, C. Lazo, H. Hölscher, V. Caciuc, A. Schwarz, R. Wiesendanger, and S. Heinze, 20$^{\text{th}}$ International Colloquium on Magnetic Films and Surfaces (ICMFS), Berlin (Germany): *Probing Fe/W(001) with Magnetic Exchange Force Microscopy*

23.7.2009: M. Menzel, K. von Bergmann, A. Kubetzka, and R. Wiesendanger, 20$^{\text{th}}$ International Colloquium on Magnetic Films and Surfaces (ICMFS), Berlin (Germany): *Periodic LDOS modulations in bi-atomic Fe chains*

27.7.2009: A. Emmenegger, S. Krause, G. Herzog, A. Kubetzka, and R. Wiesendanger, International Conference on Magnetism (ICM), Karlsruhe (Germany): *Observation of Superparamagnetic Fe/W(110) Nanoislands by SP-STM in the Field Emission Mode*

28.7.2009: G. Herzog, S. Krause, L. Berbil-Bautista, M. Bode, and R. Wiesendanger, International Conference on Magnetism (ICM), Karlsruhe (Germany): *Investigation of the Thermal Switching Behavior of Superparamagnetic Nanoislands by SP-STM*

17.9.2009: G. Herzog, L. Zhou, S. Krause, F. Meier, J. Wiebe, and R. Wiesendanger, 3$^{\text{rd}}$ International Summer School of the GrK "Physics of Functional Micro- and Nanostructures", Hamburg (Germany): *Spin-Polarized Scanning Tunneling Microscopy and Spectroscopy*

20.9.2009: S. Meckler, N. Mikuszeit, A. Preßler, E. Y. Vedmedenko, O. Pietzsch, and R. Wiesendanger, Nanostructures at Surfaces, Ascona (Switzerland): *Experimental Determination of the Dzyaloshinskii-Moriya Vector by Spin-Polarized Scanning Tunneling Microscopy in a Triple Axes Vector Magnet*

9.11.2009: L. Lichtenstein, S. Kuck, G. Hoffmann, R. Wiesendanger, AVS 2009, San Jose (USA): *Adsorption, Self Assembly, and Electronic States of Corrole Molecules Adsorbed on Different Copper Facets*

9.11.2009: S.-H. Chang, J. Brede, J. Schwöbel, S. Kuck, G. Hoffmann, R. Wiesendanger, AVS 2009, San Jose (USA): *Adsorption of Metal Phthalocyanines on Cu(111) and Cu(100): A STM Study*

17.3.2010: A. DiLullo, S.-H. Chang, G. Hoffmann, R. Wiesendanger, S.-W. Hla, 2010 APS March Meeting, Portland, Oregon (USA): *Single Molecule Manipulation of Co-Salophene-Br_2*

23.3.2010: Y. Fu, G. Hoffmann, and R. Wiesendanger, 74$^{\text{th}}$ Spring Conference, Deutsche Physikalische Gesellschaft, Regensburg (Germany): *Splitting of quantum well states in Pb films induced by spin dependent confinement*

24.3.2010: A.A. Khajetoorians, B. Chilian, J. Wiebe, S. Schuwalow, F. Lechermann, R. Wiesendanger, 74$^{\text{th}}$ Spring Conference, Deutsche Physikalische Gesellschaft, Regensburg (Germany): *Probing the spin-state of individual quantum magnets embedded in a semiconductor*

24.3.2010: J. Brede, J. Schwöbel, S. Kuck, G. Hoffmann, and R. Wiesendanger, 74$^{\text{th}}$ Spring Conference, Deutsche Physikalische Gesellschaft, Regensburg (Germany): *A Scanning tunneling microscope study of single Phthalocyanine molecules on ultra thin insulating layers on different metal substrates*

24.3.2010: B. Wolter, A. Kubetzka, R. Wiesendanger, B. Schütz, J. Zhang, 74$^{\text{th}}$ Spring Conference, Deutsche Physikalische Gesellschaft, Regensburg (Germany): *Study on Automated Atom Manipulation*

24.3.2010: J. Hattendorff, A. Schwarz, R. Wiesendanger, 74$^{\text{th}}$ Spring Conference, Deutsche Physikalische Gesellschaft, Regensburg (Germany): *Growth of Co-Salen on NiO(001)*

29.3.2010: J. Wiebe, A. A. Khajetoorians, B. Chilian, S. Schuwalow, F. Lechermann, and R. Wiesendanger, International workshop on single dopant control, Lorentz Center, Leiden (The Netherlands): *Magnetization Curves and Excitation Spectra of Individual Spins on Semiconducting Substrates*

20.8.2010: S. Krause, G. Herzog, L. Berbil-Bautista, M. Bode, and R. Wiesendanger, SP-STM3, Seoul (Republic of Korea): *Magnetization Reversal of Nanoscale Islands: How Size and Shape Affect the Arrhenius Prefactor*

25.8.2010: Y. Fu, G. Hoffmann, and R. Wiesendanger, International Conference on Nanoscience and Technology, Beijing (China): *Splitting of quantum well states in Pb films induced by spin dependent confinement*

Chapter 8

Lectures and Courses at the University of Hamburg

- Nanostrukturphysik I und II
- Magnetismus und Oberflächenphysik
- Einführung in die Rastersondenmikroskopie und -spektroskopie
- Ringvorlesung Physik im Alltag
- Seminar über Nahfeldgrenzflächenphysik und Nanotechnologie
- Seminar über aktuelle Probleme der Rastersensorphysik
- Proseminar über Theorie und Praxis der Rastersensormethoden
- Proseminar über Magnetismus und Oberflächenphysik
- Übungen zur Nanostrukturphysik I und II
- Übungen zu Magnetismus und Oberflächenphysik
- Übungen zur Einführung in die Rastersondenmikroskopie und -spektroskopie
- Physikalisches Praktikum für Fortgeschrittene
- TU - Praktikum
- Studienarbeiten zur Rastersondenmikroskopie
- Schwerpunktpraktikum Grenzflächen- und Tieftemperaturphysik
- Diplompraktikum Grenzflächen- und Tieftemperaturphysik

Chapter 9

Contributions to International Organizations

- Member of the International Advisory Committee of the European Conference "Physics of Magnetism 08" (Poznan, Poland 2008)
- Member of the International Advisory Committee of the "2nd International Workshop on Spin-Polarized Scanning Tunneling Microscopy" (Athens / Ohio, USA 2008)
- Member of the International Advisory and Programme Committee of the "International Conference on Nanoscience and Technology ICN+T 2008" (Keystone / Colorado, USA 2008)
- Member of the International Advisory Committee of the "International Symposium on Surface Science and Nanotechnology ISSS-5" (Tokyo, Japan 2008)
- Member of the International Advisory Committee of the "International Nanotechnology Forum Rusnanotech" (Moscow, Russia, 2008)
- Co-Chairman of the "5th International Conference on Scanning Probe Spectroscopy SPS 09" (Poznan, Poland, 2009)
- Member of the Scientific Committee of the "Nanotech Europe '09" (Berlin, Germany, 2009)
- Member of the International Advisory Committee of the International Conference on Surfaces and Interfaces of Materials "SIM 2009" (Shenzhen, China 2009)
- Co-Chairman of the International Conference "Trends in Spintronics and Nanomagnetism" (Lecce, Italy, 2010)
- Organizer of the European Symposium on Nanospintronics (Hamburg 2010)
- Member of the International Scientific Committee of the International Conference on Nanostructures and Self-Assembly "NANOSEA 2010" (Marseilles, France, 2010)

- Member of the International Advisory Committee of the "3rd International Conference on Spin-Polarized Scanning Tunneling Microscopy SPSTM3 (Seoul, Korea, 2010)
- Member of the International Steering Committee of the 18th International Vacuum Congress (IVC-18) and International Conference on Nanoscience and Technology (ICN+T 2010) (Beijing, China, 2010)
- Member of the International Advisory Committee of the "15th International Conference on Solid Films and Surfaces ICSFS-15" (Beijing, China, 2010)
- Member of the Science Advisory Board of the "1th Annual World Congress of Nanomedicine" (Beijing, China, 2010)
- Member of the International Program Advisory Boards of the "International Symposium on Surface Science ISSS-6" (Tokyo, Japan, 2010)
- Member of the International Advisory Committee of the NANO2010-Conference (Tamil, Nadu, India, 2010)

Chapter 10

How to reach us

... by mail	write to University of Hamburg, Institute of Applied Physics, Jungiusstraße 11, D-20355 Hamburg, Germany.
... by phone	call (++49) 40 42838 5244.
... by fax	send to (++49) 40 42838 6188.
... by e-mail	send to `wiesendanger@physnet.uni-hamburg.de`
... within the WWW	`www.nanoscience.de`
... personally	


A